Optofluidic planar microreactors for the production of hydrogen and oxygen from photocatalytic water splitting

A Thesis

Submitted in Partial Fulfilment of the Requirement for the Degree of

DOCTOR OF PHILOSOPHY

By

Laxmi Prasad Rao Pala

Department of Chemical Engineering

Indian Institute of Technology Guwahati

Guwahati-781039, Assam, India

Jan, 2024

Dedicated To
my well wishers

Indian Institute of Technology Guwahati

Department of Chemical Engineering

Statement

I, hereby declare that the work contained in this thesis entitled "**Optofluidic planar microreactors for the production of hydrogen and oxygen from photocatalytic water splitting**" is original and has been done by me at the Department of Chemical Engineering, Indian Institute of Technology Guwahati, Guwahati, India, under the supervision of **Prof. Nageswara Rao Peela**. The work has not been submitted to any other Institute for any degree or diploma. I have followed the guidelines provided by the Institute in preparing the thesis. I have confirmed to the norms and guidelines given in the Ethical Code of Conduct of the Institute. Whenever I have used materials (data, theoretical analysis, figures and text) from other sources, I have given due credit to them by citing them in the text of the thesis and giving their details in the references. Further, I have taken permission from the copyright owners of the sources, whenever necessary.

Guwahati,

May, 2023

Laxmi Prasad Rao Pala

(Research scholar)

186107109

Department of Chemical Engineering

IIT Guwahati, Guwahati – 781039

Assam, India

भारतीय प्रौद्योगिकी संस्थान गुवाहाटी
Indian Institute of Technology Guwahati

Indian Institute of Technology Guwahati

Department of Chemical Engineering

Certificate

It is certified that the work described in this thesis entitled "**Optofluidic planar microreactors for the production of hydrogen and oxygen from photocatalytic water splitting**" by **Mr. Laxmi Prasad Rao Pala** for the award of degree of Doctor of Philosophy is an authentic record of the results obtained from the research work carried out under our supervision at the Department of Chemical Engineering, Indian Institute of Technology Guwahati, Guwahati, India, and this work has not been submitted elsewhere for a degree.

Prof. Nageswara Rao Peela

Thesis Supervisor

Department of Chemical Engineering

IIT Guwahati, Guwahati – 781039

Assam, India

Acknowledgement

This doctoral thesis would not be completed without the help and extended hands of several people. I take this opportunity to express my sincere thankfulness to all of them.

Firstly, I express my sincere gratitude and deepest respect to my thesis supervisor, Prof. Nageswara Rao Peela, Department of Chemical Engineering, for his continuous guidance, support, and encouragement throughout my thesis work. His valuable insights, feedback, timely assistance, and criticisms helped me gain knowledge and interest in improving the work. I am thankful to him for accepting the collaboration to widen the research area. I am honoured to work under him. Thank you very much sir, for your unforgettable help and support in my life.

I would like to thank my thesis examiners, Prof. Prakash Biswas (Department of Chemical Engineering, IIT Roorkee) and Prof. Samir H. Mushrif (Department of Chemical and Materials Engineering, University of Alberta, Canada) for their valuable suggestions and comments, which help me to improve overall quality of the thesis. I would like to also thank my doctoral committee and viva-voice members Prof. Animes Kr Golder, Prof. Tapas K Mandal, Dr. Pavan K Kancharla (Associate Prof), Dr. Partho Sarathi Gooh Pattader (Associate Prof) and Prof. Subhash Thota for their valuable suggestions and constructive criticism during all assessments of the Ph.D. program. I would also like to thank my comprehensive committee members, Prof. Vaibhav V Goud, Prof. Mahuya De, and Prof. G. Pugazhenthi.

I also thank Prof. Kaustubha Mohanty, Head, Department of Chemical Engineering, for his administrative support. Furthermore, I would like to thank other faculty members, research scholars, non-teaching staff of the Department of Chemical Engineering, IIT Guwahati for their kind cooperation in all aspects. I also thank technical staff of Central Instruments Facilities (CIF) and Center for Nanotechnology for their support during the analysis.

I thank Dr. Siddhartha Sankar Dhar (Department of Chemistry, National Institute of Technology Silchar) and his PhD student (Mr. Bishal Das) for the collaboration work.

I acknowledge Ministry of Human Resource Development (MHRD) and our institute for providing fellowship throughout the PhD program. The financial support provided by the Department of Science and Technology (DST), New Delhi, India, under the special scheme Clean Energy Research Initiative (CERI) with Grant Number: DST/TM/CERI/C19(G), and by the Ministry of Electronics and Information Technology (MEITY), India, under the project

entitled ‘Indian Nanoelectronics Users Program – Idea to Innovation (INUP i2i)’ with Grant Number: 5(1)/2021-NANO, are gratefully acknowledged.

The analytical facilities from Central Instruments Facilities (CIF), Center for Nanotechnology and analytical lab of Department of Chemical Engineering of Indian Institute of Technology Guwahati were also acknowledged.

I am grateful to my senior members from our group, Dr. Devipriya Gogoi, and Dr. Rambabu Ponnala for their cooperative assistance and suggestions in performing experiments. In addition, I sincerely acknowledge my research group members, Bharath, Alam, santosh, Anirban, Ameer, Hanumanth, Sarmistha, and Prince. I am deeply grateful to convey my sincere gratitude to my parents and family members for their sustained help and encouragement in all my personal and academic ventures. I feel proud and blessed to have such parents my mother Pala Amma Rao Lakshmi Garu and my father Pala Ramakrishna Reddy Garu. Their blessings are always with me.

I wish to thank many other people whose names are not mentioned here but this does not mean that I have forgotten their help. Above all, I am thankful to God Almighty for giving me this wonderful life.

Laxmi Prasad Rao Pala

Abstract

The depletion of fossil resources and environmental constraints have made the production of energy from renewable sources a pressing demand. Among these, utilizing solar light to generate chemical energy stands out as a highly viable green energy solution to meet the energy needs of our present-day civilization. Solar energy is an inexhaustible and renewable source, with an estimated 0.015% of the solar energy reaching earth being sufficient to meet our total energy demand - equivalent to 130 million 500 MW power plants. This makes it a highly attractive and sustainable option. While direct conversion of solar energy into electricity using photovoltaic cells is a popular technology, it faces challenges in terms of storing and distributing electricity over long distances. Consequently, immediate use after production or conversion to chemical energy, like hydrogen, becomes necessary. Converting solar energy to chemical energy, specifically hydrogen fuel, emerges as an appealing choice due to hydrogen's high gravimetric energy density and environmentally friendly nature. Presently, hydrogen production still relies heavily on fossil fuels, resulting in CO_2 emissions and environmental consequences. To reduce dependence on fossil fuels and produce clean hydrogen without releasing CO_2 into the atmosphere, there is a growing need to explore renewable sources and processes. Photocatalytic overall water splitting (POWS) is one such process that has garnered significant attention. POWS utilizes renewable resources, such as solar energy, to drive the production of hydrogen, making it a promising and sustainable solution for renewable hydrogen production.

Herein, Titanium dioxide (TiO_2) thin films are prepared on glass substrates using sol-gel spin coating method. Titanium tetraisopropoxide (TTIP) precursor is used to prepare TiO_2 sol-gels using ethanol as solvent. The acetyl acetone (AcAc) and Acetic acid (AA) are used as modifiers and cetyltrimethylammonium bromide (CTAB) surfactant as pore-forming agent. A clear transparent TiO_2 sol-gel is obtained without precipitation only when both AA and AcAc are present in the TiO_2 sol. A worm-like structure is observed in the film at 0.1 M TTIP and changed to the flake-like structure in the film at 0.4 M TTIP. The TiO_2 thin films are non-porous and porous when CTAB is below and above the concentration of 0.8 g per 0.01 mol TTIP. The critical micelle concentration is found to exist between 0.6 to 0.8 g CTAB per 0.01 mol TTIP. The grazing Incidence X-ray diffraction and Raman analysis confirm the presence of anatase phase in the 3 and 4 times coated TiO_2 thin films. The field emission scanning electron microscopy analysis shows that a highly homogeneous and uniform thin film is

obtained with TiO_2 sol-gel composition of 0.2 M TTIP, 0.1 M AcAc, 0.09 M AA and 1 g of CTAB per 0.01 mol TTIP. The photocatalytic activity of the TiO_2 films is determined by investigating the photodegradation of methylene blue (MB) in aqueous solution. The TiO_2 thin film with 110.7 nm and 145.3 nm thickness showed 42.6 % and 58.4 % degradation of MB, respectively, at 60 min of photocatalytic reaction under UV light irradiation.

As a next study, the visible light-active Pt/TiO_2 photocatalyst thin films were prepared by photo-depositing the Pt onto the sol-gel TiO_2 spin-coated films. An optofluidic planar microreactor was fabricated using the Pt/TiO_2 film coated glass substrate as bottom plate and uncoated glass substrate containing planar reaction chamber as cover plate. The Pt/TiO_2 thin films were tested for the photocatalytic water splitting activity in presence of methanol as sacrificial agent to produce hydrogen under visible/solar light irradiation. The effect of catalyst film thickness, reactant flowrate, light intensity and type of light source was studied on the rate of hydrogen production. The Pt/TiO_2 film with thickness 1650±119 nm showed a highest rate of 16.35 mmol h^{-1} g^{-1} (4.7 µmol h^{-1} cm^{-2}) hydrogen production at an optimum reactant flowrate of 0.3 mL min^{-1} under visible light (400 W metal halide lamp) irradiation. The stability study carried out for 4 cycles of 5 h runs proved that the photocatalyst was stable and the film was well adhered to the glass substrate. A hydrogen production rate of 0.766 mmol h^{-1} g^{-1} (0.22 µmol h^{-1} cm^{-2}) and a solar to hydrogen conversion efficiency (STH) of 0.015% was obtained under simulated solar light irradiation of ~100 mW cm^{-2} intensity, proving the solar light activity of Pt/TiO_2 film.

Further, an optofluidic planar microreactor has been fabricated, with the photocatalyst (IrO_2/TiO_2) film coated glass as a reactor plate and plain glass as a cover plate. A rectangular region was completely etched on plain glass and used as a spacer between catalyst coated plate and cover plates to create a planar microreaction compartment. The water splitting activity to produce oxygen using sodium iodate as a sacrificial agent (electron acceptor) is tested in the fabricated planar microreactor under visible light illumination (with 400 W metal halide lamp). The effect of catalyst coating thickness and the reactant flowrate on the rate of oxygen production is studied in detail. An oxygen evolution rate of 3.99 mmol h^{-1} g^{-1} (1.84 µmol h^{-1} cm^{-2}) was observed from the IrO_2/TiO_2 film of 3078 ± 362 nm thickness at an optimal flow rate of 0.3 mL min^{-1} in the presence of visible light. The stability study showed that the IrO_2/TiO_2 film was stable for at least 4 cycles, indicating the superior activity of the film firmly adhered to the glass substrate.

Finally, we report the successful development of a photocatalyst based on a single semiconductor, TiO_2, with Pt and IrO_2 as cocatalysts for the overall water splitting under visible/simulated light irradiation for the sustainable hydrogen production. The $2.5IrO_2/0.5Pt/TiO_2$ photocatalyst exhibited ideal POWS, producing hydrogen and oxygen from pure water with a H_2/O_2 ratio of 1.96 under visible light irradiation, and a H_2/O_2 ratio of 1.82 under simulated solar light (SSL). The rate of hydrogen and oxygen production were 9.73 and 5.32 µmol g^{-1} h^{-1}, respectively, under SSL with intensity 101.4 mW cm^{-2}. The photocatalyst showed long term stability with the POWS activity for 10 h of continuous operation. The accumulation of the generated gas on the catalyst surface and catalyst aggregation were found to be the major reasons for the decrease in the photoactivity after 10 h.

The findings of this work contributes to further the research in renewable energy and photocatalysis. The knowledge gained from the study can be utilized to optimize catalyst properties, such as bandgap engineering, for improved photocatalytic activity. Furthermore, this research provides insights for scaling up the photocatalytic water splitting process, aiding in the development of large-scale hydrogen production. The work also encourages the exploration of integrated systems that combine renewable energy sources, catalysts, and reactor technologies. Overall, this study could serve as a valuable basis for further research in the area of sustainable energy production.

Keywords: Titanium dioxide thin film; Sol-gel spin coating; Platinum and Iridium oxide cocatalysts; Photodeposition; Optofluidic planar microreactor; Hydrogen evolution; Oxygen evolution; Photocatalytic overall water splitting; Methylene blue degradation; Photocatalysis;

Table of Contents

List of Figure Captions

List of Table Captions

Chapter 1

Background of the Work and Research Objectives

1.1 Introduction

The energy production from the renewable resources is a pressing demand due to depletion of fossil resources and the environmental constraints. Solar light utilization in the form of chemical energy is considered as the most viable green energy route to meet the present day energy requirements for the human civilization because sunlight is inexhaustible and renewable energy source.[1] It is estimated that ~0.015% of solar energy reaching the earth (at any one instant equal to 130 million 500 MW power plants) is enough to meet the total energy demand, making it a viable renewable resource.[2–4] Direct conversion of solar energy into electricity through photovoltaic (solar) cells is a popular technology.[5] However, it is difficult to store and/or distribute electricity over long distances rather it must be used immediately after the production or be converted to chemical energy (to hydrogen, for example).[6] In this context, the direct conversion of solar energy to chemical energy such as hydrogen fuel is an attractive choice.[2,7–9] Hydrogen is a promising renewable energy carrier because of its high gravimetric energy density and non-polluting nature.[10] However, much of its production is still based on fossil fuels, burning of which causes environmental effects due to CO_2 emissions. Therefore, to reduce the dependence on fossil fuels for hydrogen production, there is a need to look for renewable sources and processes from which clean hydrogen can be produced without releasing any CO_2 into the atmosphere.[11] In this context, the photocatalytic overall water splitting (POWS) is gaining significant attention as a renewable process for the hydrogen production because it utilizes renewable resources such as solar energy.[12]

1.2 Photocatalytic overall water splitting (POWS)

Photocatalytic overall water splitting (POWS), wherein both hydrogen evolution (HER) and oxygen evolution (OER) reactions occur at the same time, is a practical and industrially scalable process since it avoids the usage of consumption of high cost sacrificial agents such as methanol, ethanol etc.[13]

POWS utilizes the solar energy to drive the redox reactions i.e., HER and OER simultaneously to produce H_2 and O_2 from pure water with zero carbon emissions.[14,15] During the water splitting process, photocatalyst absorbs solar energy and generates photocarriers, i.e., electron-hole pairs. These photocarriers migrate to the surface of the photocatalyst and participate in water redox (reduction and oxidation) reactions to produce H_2 and O_2.[16] A photocatalyst material with appropriate bandgap energy, band edge potentials, visible light response, and high charge separation efficiency is required to drive these redox reactions during POWS.[17]

Among the HER and OER, the OER is a sluggish (rate limiting) reaction in the POWS because of the four-electron transfer process coupled with the removal of four protons from H_2O to form O_2.[18] Therefore, developing a photocatalyst material based on a single semiconductor that can be employed for the POWS without using sacrificial agents has still remained a challenging task.[19,20] Figure 1.1 shows the schematic diagram of the POWS process under visible light irradiation.

The mechanism of the photocatalytic overall water splitting is shown in Figure 1.1

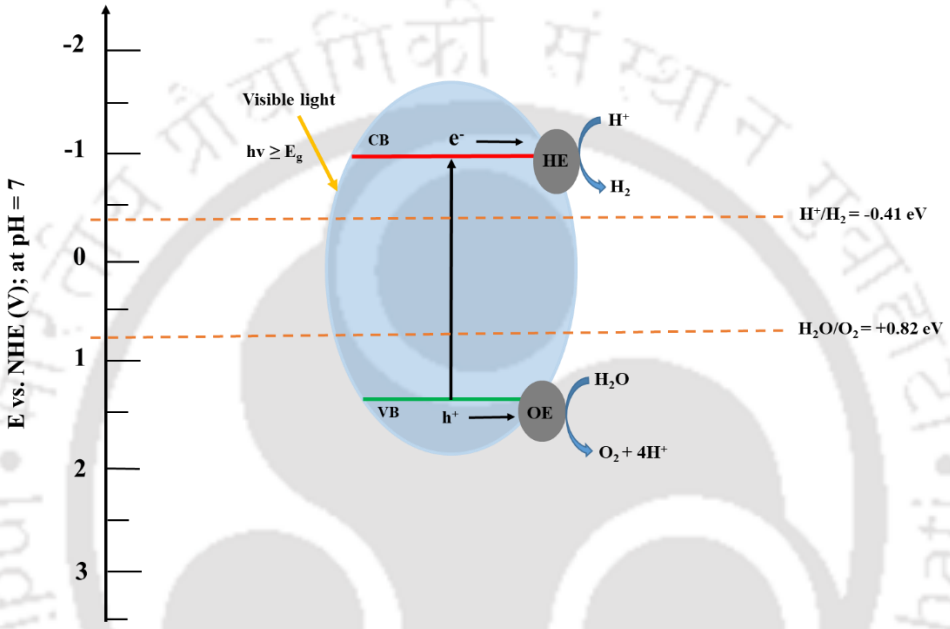

Figure 1.1: Schematic energy diagram of photocatalytic overall water splitting reaction over a single semiconductor photocatalyst with HER and OER cocatalysts

The steps involved in POWS reaction is as follow:

$$\text{Excitation: Photocatalyst} \xrightarrow{\text{Solar light}} e^- + h^+ \quad \ldots\ldots\ldots\ldots\ldots \quad (1.1)$$

$$\text{Water oxidation: } H_2O + 2h^+ \xrightarrow{\text{OER cocatalyst}} 2H^+ + 0.5O_2 \quad \ldots\ldots\ldots \quad (1.2)$$

$$\text{Water reduction: } 2H^+ + 2e^- \xrightarrow{\text{HER cocatalyst}} H_2 \quad \ldots\ldots\ldots\ldots\ldots\ldots \quad (1.3)$$

$$\text{POWS: } H_2O + h\nu \longrightarrow H_2 + 0.5O_2 \quad \Delta G_o = 237.13 \text{ kJ mol}^{-1} \ldots (1.4)$$

Upon absorbing the visible light by the photocatalyst, the electrons are excited from the valence band (VB) to conduction band (CB) of semiconductor, leaving behind vacant holes in the VB (Eq. 1.1). The OER cocatalyst captures the holes and facilitates the water (H_2O) oxidation to produce O_2 and protons (Eq. 1.2).

While, the HER cocatalyst on the photocatalyst surface captures the electrons and facilitates the H^+ reduction to produce H_2 (Eq. 1.3). The redox capability of the photocatalyst is determined by the band edge potentials of the valence band (VB) and conduction band (CB).[18] The CB should be more negative than the H_2O/H^+ reduction potential and the VB should be more positive than the H_2O/OH^- oxidation potential for the HER and OER to occur simultaneously, resulting in the POWS (Eq. 1.4).[21] Apart from constructing an effective and stable photocatalyst for POWS, there are other challenges that need attention to achieve POWS efficiency.[21]

Recent literature on the POWS is presented in Table 1.1. Different types of photocatalyst configurations have been employed for the POWS to produce H_2 and O_2 from pure water. For example, Wenlong et al.[22], developed a novel Z-scheme heterojunction, composed of a phosphatized p-type gallium indium zinc oxynitride (GIZON-P) and a n-type g-C_3N_4 (CN), with Rh as cocatalyst, for the photocatalytic pure water splitting. They reported a photocatalytic H_2 and O_2 generation rates of 1340 and 643 μmol h^{-1} g^{-1} over the GIZON-P/CN heterojunction, with the corresponding AQY 12.6% at 430 nm. Fang et al.[23], reported anatase/rutile TiO_2/g-C_3N_4 (A/R/CN) multi-heterostructure with 2.0 wt.% Pt nanoparticles as a photocatalyst for overall water splitting. They reported a rate of H_2 evolution of 374.2 μmol g^{-1} h^{-1} over the optimal A/R/CN photocatalyst, which is about 8 and 4 times that of pure g-C_3N_4 and P25. Yuan et al.[24], prepared a hybrid Pt/CuO_{1-x}/TiO_2 catalyst via an in situ photodeposition method. They reported that the prepared Pt/CuO_{1-x}/TiO_2 showed enhanced photocatalytic activity and stability in the water-splitting reaction as compared to Pt/TiO_2. This enhancement was due to the dual role of CuO_{1-x} in improving the efficiency of the Pt cocatalyst for hydrogen generation and in abating the back reaction of the photocatalytic overall water-splitting reaction.

1.3 Photocatalytic water splitting (PWS) half reactions

Due to difficulties in achieving higher POWS efficiencies, the photocatalytic water splitting (PWS) half reactions such as the only HER, and only OER are often conducted in presence of sacrificial reagents (SRs) such as methanol (electron donor), and sodium iodate (electron acceptor) thus resulting in the significant HER and OER activities, respectively.[25] However, these processes are expensive as additional sacrificial agents are needed. Moreover, the presence of sacrificial agents may release by-products that are harmful to the environment. Figure 1.2 and Figure 1.3 shows the schematic diagrams of the PWS process under visible light irradiation for the hydrogen and oxygen production, respectively.

Table 1.1: Recent literature review on the photocatalytic overall water splitting

Photocatalyst	Cocatalyst	Catalyst amount	Reactant	Light	Reactor	H_2 rate ($\mu mol\ h^{-1}\ g^{-1}$)	O_2 rate ($\mu mol\ h^{-1}\ g^{-1}$)	AQY (%)	STH (%)	Stability	Year	Ref
GIZON-P/ g-C_3N_4	1 wt.% Rh	30 mg	40 mL H_2O	300 W Xe lamp (full band)	50 mL quartz cell	1340	643	12.6% at 430 nm	-	5 cycles of 3 h	2022	22
Anatase/rutile TiO_2/g-C_3N_4	2 wt.% Pt	10 mg	100 mL H_2O	LabSolar 6 A	Pyrex glass reaction tank	374.2	187.1	0.71% at 400 nm	-	4 cycles of 3 h	2020	23
Pt/CuO_{1-x}/TiO_2	-	20 mg	200 mL H_2O	300 W xenon light with AM1.5 filter	CEL-SPH2N, China	220	110	-	0.25	4 cycles of 2 h	2018	24
Pt–Co/g-C_3N_4	3 wt.% Pt & 1 wt.% Co	200 mg	100 mL H_2O	300 W Xeon lamp ($\lambda > 420$ nm)	Pyrex top-irradiation reaction vessel	6	3	0.3% at 405 nm	-	15 cycles of 25 h	2016	26
CoO/g-C_3N_4	-	20 mg	20 mL H2O	visible light source ($\lambda > 400$ nm)	50 mL photoreactor vial	50.2	27.8	1.91% at 420 nm	-	15 cycles of 5 h	2018	27
TiO_2 Nanodots/g-C_3N_4	3 wt.% Pt	10 mg	25 mL H2O	300 W Xenon lamp ($\lambda > 300$ nm)	Three-necked flask	328.58	164.78	1.91% at 420 nm	-	4 cycles of 4 h	2022	19
MnOx/g-C_3N_4/CdS/Pt core-shell	-	50 mg	100 mL H_2O	300W Xe arc lamp ($\lambda > 400$ nm)	Pyrex glass photoreactor	1303.39	641.60	35% at 420 nm	-	6 cycles of 4 h	2021	28
$Co_3(PO_4)_2$/g-C_3N_4	-	50 mg	100 mL H_2O	Xenon lamp ($\lambda > 400$ nm)	glass photoreactor	375.6	177.4	1.32% at 420 nm		4 cycles of 3 h	2020	29
2D/2D $BiVO_4$/Ti_3C_2	-	10 mg	100 mL H_2O	300 W Xe arc lamp with AM-1.5 filter	glass photoreactor	25	12.5	-		3 cycles of 8 h	2021	30

The mechanism of the photocatalytic water splitting half reaction: HER is shown in Figure 1.2

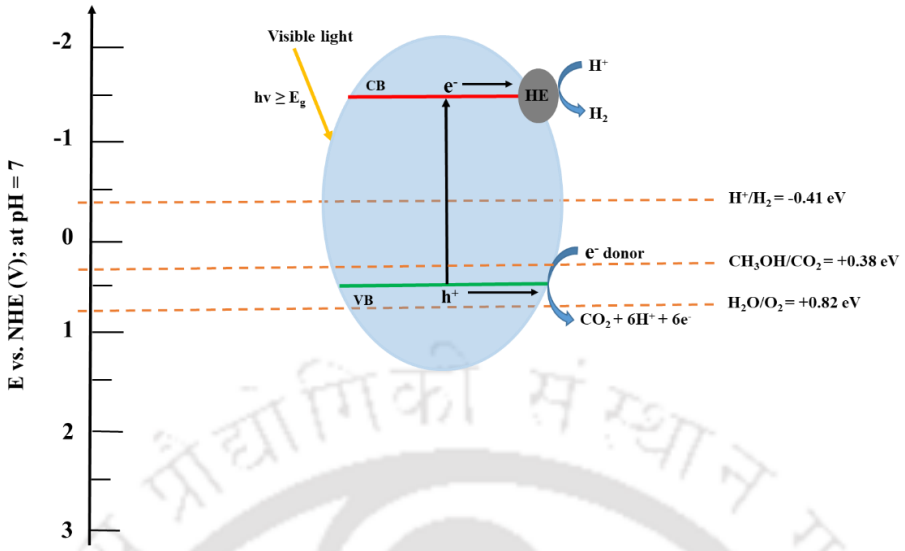

Figure 1.2: Schematic energy diagram of photocatalytic water splitting half reaction: HER over a single semiconductor photocatalyst with HER cocatalyst

The HER cocatalyst on the photocatalyst surface act as trap centers for the photo-generated CB electrons. The protons (H^+) are reduced (eq. 1.3) with the electrons accumulated on the HE cocatalyst particles to produce H_2. Whereas, the holes accumulated at the photocatalyst VB reacts with the electron donor (methanol) and water to produce oxidation products such as CO_2 and H_2 (Eq. 1.5).

Methanol oxidation[31,32]: $CH_3OH + H_2O + 3h^+ \longrightarrow CO_2 + 6H^+ + 6e^-$ …… (1.5)

In this route, the electron donor scavenges the photogenerated holes, eliminates the O_2 production (Eq. 1.2) and eliminates the backward reaction of H_2 and O_2 (reverse reaction of POWS).[33] This way, both, HER cocatalyst and methanol, helps in increasing the H_2 production rates.[34]

The isotopic labeling studies shows that the H_2 production is mainly by the reduction of protons (H^+) originated from water.[35] The role of methanol as SR is in inhibiting the electron/hole recombination and backward reaction to form H_2O resulting in higher H_2 production.[36]

A recent literature on the photocatalytic hydrogen evolution from water splitting is presented in Table 1.2. Various sacrificial agents (electron donors) have been employed to produce H_2 from PWS using different photocatalysts. For example, Zheng et al.[37], studied the performance of dye sensitized Pt/TiO_2-composite photocatalysts for HER. The photocatalyst and ascorbic

Table 1.2: Recent literature review on the photocatalytic hydrogen evolution from water splitting

Photocatalyst	(Co)catalyst method	Catalyst amount	Sacrificial agent	Light	Reactor	H_2, mmol g^{-1} h^{-1}; [a]µmol h^{-1}	AQY (%)	STH (%)	Stability	Year	Ref
Dye-sensitized Pt/TiO_2	Photodeposition	3 mg	55 mM ascorbic acid in H_2O	Xe lamp (λ > 420 nm)	photoreactor	5.41	-	-	-	2023	37
7.45 wt.% Pt/TiO_2-x USPC	sono-photo-thermo-treatment	10 mg	2 mL glycerol in 10 mL H_2O	piezoelectric transducer as an acoustic source and a 300 W Xe lamp	top-radiation reactor	225.04	-	0.89	4 cycles of 3 h	2022	38
0.5 wt.% Pt/TiO_2 PC-TC	Photodeposition	50 mg	16g methanol in 40 mL H_2O	300 W xenon light (500 mW/cm^2)	airtight reactor	20.38	-	-	-	2022	39
NC/Pt/TiO_2	hard-template method	35 mg	20 mL methanol + 80 mL H_2O	CEL-HXF 300 Xe lamp (λ = 300–400 nm); UV light	CEL-SPH2N photocatalytic instrument	23.8	11.92% at 365 nm	-	4 cycles of 10 h	2022	40
Defective Pt/TiO_{2-x} Nanorods	Crystal Facet Engineering	30 mg	50 vol.% methanol in 15 mL H_2O	500 Xe lamp (λ > 420 nm)	20 mL vial	18.75	-	-	91% activity in 2nd cycle	2022	41
0.1 wt.% Pt/TiO_2	Flame spray pyrolysis	100 mg	20 mL methanol + 80 mL H_2O	300 W Xenon lamp (λ > 300 nm)	250 mL quartz glass reactor	5.59	-	-	-	2021	42
2 wt.% Pt/TiO_2 nanosheets	Photodeposition	20 mg	20 mL ethanol + 60 mL H_2O	350 W Xe arc lamp, UV	Pyrex glass photoreactor	16.67	-	-	-	2010	43
0.5 wt% Pt/TiO_2 powder	Photodeposition	100 mg	20 vol.% methanol in 50 mL H_2O	400W Xe arc lamp, 200 to 1000	Fused silica cylindrical vessel	1.2	-	-	-	2007	44
Pt/TiO_2 thin film (21 mg/cm^2 Pt)	radio-frequency magnetron sputtering	1.5 µm thickness	50 vol.% methanol in H_2O	500 W Xe arc lamp, > 420	quartz cell	0.046 [a]	1.2% at 420 nm	-	-	2007	45

acid aqueous solution was added into a photoreactor and illuminated under xenon lamp. In the reaction process, the ascorbic acid plays a role as the sacrificial reagent, which consumes the photogenerated holes and thus inhibit the recombination of photogenerated electron-hole pairs. Therefore, ascorbic acid in the whole reaction is consumed continuously and lead to a pH increase. They reported that the Pt/TiO_2 composite sensitized with Chl-*a* type dye showed the best photocatalytic HER performance with a H_2 evolution of 5.4 mmol g^{-1} h^{-1}. Rong et al.[38], studied the thermally-enhanced sono-photocatalysis by defect and facet modulation of Pt-TiO_2 catalyst for high-efficient hydrogen evolution. The Pt species loaded defect-rich TiO_2 (Pt-TiO_{2-x}) catalyst was synthesized by facile *in situ* sono-photo-thermo-treatment. Glycerol was used as sacrificial reagent due to its high boiling point and renewable properties. They reported a hydrogen evolution rate of 225 mmol g^{-1} h^{-1} with the light-to-hydrogen efficiency of 0.89%. Masaaki et al.[45], synthesized visible light-responsive TiO_2 thin films (Vis-TiO_2) by a radio-frequency magnetron sputtering method and tested the efficiency of the Pt-loaded Vis-TiO_2 thin films for the photocatalytic splitting of water in presence of methanol. They reported an H_2 production rate of 0.046 µmol g^{-1} and an apparent quantum yield of 1.2% at 420 nm.

The mechanism of the photocatalytic water splitting half reaction: OER is shown in Figure 1.3

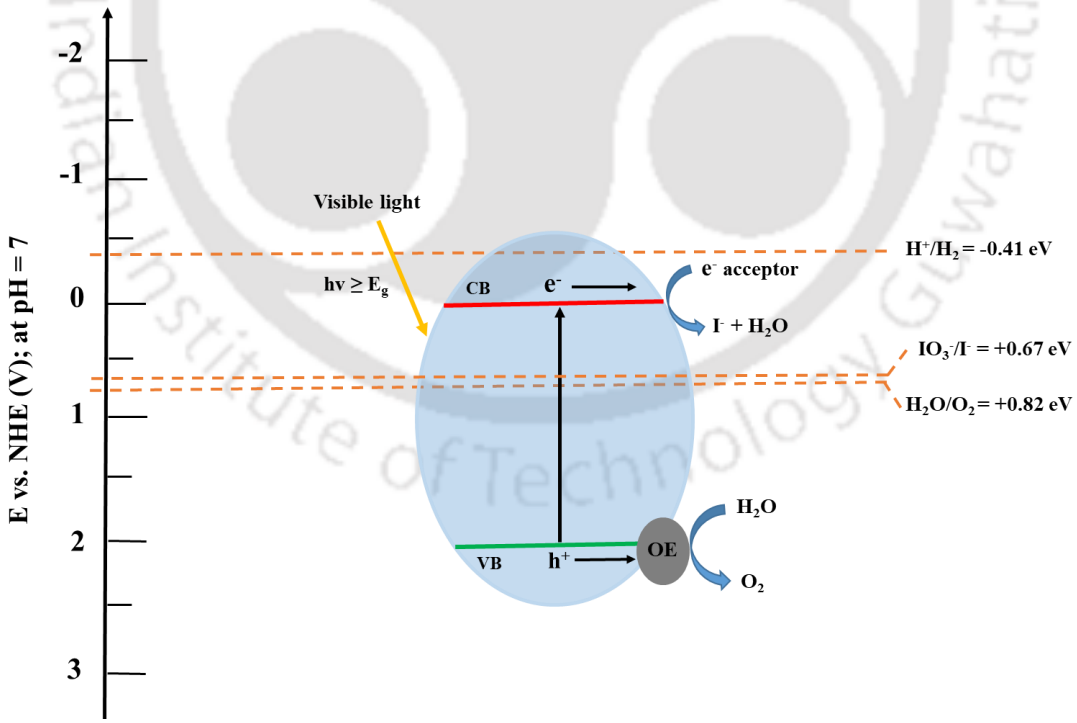

Figure 1.3: Schematic energy diagram of photocatalytic water splitting half reaction: OER over a single semiconductor photocatalyst with OER cocatalyst

The OER cocatalyst sites on the photocatalyst surface act as trap centers for the vacant holes at VB. The captured holes participate in the water oxidation to form oxygen and protons (H^+) on the OER co-catalyst surface (Eq. 1.2). The excited electrons along with H^+ ions participate in the electron acceptor (sodium iodate) reduction (Eq. 1.6).

Iodate reduction[46,47]: $IO_3^- + 6H^+ + 6e^- \longrightarrow I^- + 3H_2O$ …… (1.6)

This way, both, OER cocatalyst and electron acceptor, helps in increasing the O_2 production rates. Similar to electron donor, the role of electron acceptor as SR is to inhibit the electron/hole recombination and backward reaction to form H_2O resulting in higher O_2 production.

Recent literature on the photocatalytic oxygen evolution from water splitting is presented in Table 1.3. Jasmin et al.[48], prepared Mn, Co, and Fe-based co-catalysts immobilized on TiO_2 nanoparticles (NPs) by wet impregnation route and systematically investigated their prospects in photocatalytic water splitting reactions for OER with $AgNO_3$ (0.1 M) as electron acceptor. They reported that the CoO_x-TiO_2 exhibited the highest oxygen evolution rate of 34.3 mmol g^{-1} h^{-1}. Masaaki et al.[45], tested Pt-loaded visible light-responsive TiO_2 thin films (Pt/Vis-TiO_2), prepared by radio-frequency magnetron sputtering method for the photocatalytic oxygen evolution in presence of $AgNO_3$ as sacrificial agent. They reported an O_2 production rate of 0.277 µmol g^{-1} with an apparent quantum yield of 2.43% at 420 nm. However, utilizing $AgNO_3$ as sacrificial agent greatly reduces the activity for photocatalytic oxygen evolution with time because of the photodeposition of metallic Ag from the sacrificial agent on the photocatalyst surface thereby blocking the incident light absorption.[49]

1.4 Titanium dioxide photocatalyst: Powder vs thin film for photocatalytic applications

Titanium dioxide (TiO_2), a well-studied semiconductor, found its uses as a catalyst support material and in photocatalytic reactions because of the advantages such as low cost, non-toxicity, resistance to photo-induced corrosion and ease of handling.[50] The TiO_2 exists as anatase, rutile, and brookite phases among which anatase TiO_2 reported to be more efficient photocatalyst because of the lower recombination rate and longer lifetime of the photo-generated electrons and holes over this phase.[51] The TiO_2 nano-powders are generally employed as suspensions in the aqueous phase. Their practical use is limited due to the separation issue during the purification stage. This issue can be eliminated by immobilizing the nanoparticles on a steady substrate. This has attracted a large scientific interest in the development of immobilized TiO_2 thin films. The thin films show good electrochemical and photocatalytic properties for photocatalysis applications.[52]

Table 1.3: Recent literature review on the photocatalytic oxygen evolution from water splitting

Photocatalyst	(Co)catalyst method	Catalyst amount	Sacrificial agent	Light	Reactor	O_2, μmol g^{-1} h^{-1}; [a]μmol h^{-1}	AQY (%)	Stability	Year	Ref
$TiZrNbTaWO_{12}$	high-pressure torsion method	30 mg	20 mM $AgNO_3$ in 30 mL H_2O	300 Xe lamp ($\lambda > 420$ nm)	photoreactor	0.01	-	-	2022	53
$BiVO_4$ NPs	homogeneous co-precipitation process	100 mg	0.05 M $AgNO_3$ in 100 mL H_2O	300 Xe lamp ($\lambda > 420$ nm)	Pyrex glass reactor	141.6	-	-	2008	54
$Y_2Ti_{1.94}Rh_{0.06}O_7$	solid-state reactions	100 mg	0.05 M $AgNO_3$ in 20 mL H_2O	300 Xe lamp ($\lambda > 420$ nm)	quartz cuvette cell	73	53 % at 400 nm	3 cycles of 20 h	2014	55
Ag_3PO_4/MoS_2	ultrasonic treatment	300 mg	10mg $AgNO_3$ in 100 mL H_2O	visible light	photoreactor	20.1	-	-	2018	56
Mo-doped $BiVO_4$	liquid–solid state reaction	100 mg	10mM $AgNO_3$ in 100 mL H_2O	300 W Xe lamp ($510 < \lambda < 600$ nm)	Pyrex top-irradiation reactor	4.9	0.01 % at 430 nm	-	2021	57
TiO_2-700	sol–gel method	120 mg	5 mM $Fe(NO_3)_3 \cdot 9H_2O$ in 120 mL H_2O	4 LEDs system (λ_{max} = 384 nm	slurry glass-immersion reactor	537	0.6 % at 384 nm	-	2021	58
$Fe_3O_4/SiO_2/TiO$ 2-CoPcS	co-precipitation	100 mg	100mg $AgNO_3$ in 100 mL H_2O	blue LED visible light	Pyrex glass cell	4560	-	3 cycles	2023	59
CoO_x-TiO_2 powder	wet impregnation	1 mg	0.1 M $AgNO_3$ in 2 mL H_2O	LED lamp (λ = 365 nm	top illumination closed reactor	34420	-	-	2019	48
Pt/TiO_2 thin film (21 mg/cm^2 Pt)	radio-frequency magnetron sputtering	1.5 μm thickness	0.05 M silver nitrate in H_2O	500 W Xe arc lamp, > 420	quartz cell	0.277 [a]	2.43% at 420 nm	-	2007	45

Similarly, various other catalyst materials can be prepared in the form of thin films. The materials in the form of thin films can be employed for different photocatalytic applications including environmental such as air and water treatment, and energy conversion such as solar cells and water splitting for hydrogen production.[60,61]

1.5 Preparation of thin films by Sol-gel spin coating

The photocatalytic activity of the TiO_2 thin films depends on the textural properties such as thickness, grain or particle size, pore size distribution and porosity of the films.[52] These textural characteristics of the thin films depend on the sol properties such as sol reactivity, viscosity, water-to-alkoxide ratio, precursor concentration, solvent type, chelating agent and surfactant.[62,63] The sol properties can be controlled by varying its composition. The spin-coating of TiO_2 sol-gel is a common deposition method used to coat TiO_2 thin films on the glass substrates due to its low cost, easy handling and experimental simplicity.[64] It is also very well established, simple and cheaper method and gives uniform coating.

In the sol-gel method, hydrolysis of metal alkoxides occurs first followed by the polycondensation of hydroxyl and/or alkoxy groups thus forming the oxide polymer network of TiO_2 via Ti–O–Ti route.[65] The hydrolysis and condensation reactions in the sol-gel process are as shown below:

$$Ti(OPr^i)_4 + x(H_2O) \rightarrow Ti(OPr^i)_{4-x}(OH)_x + xPr^iOH \quad (1.7)$$

$$2[Ti(OPr^i)_{4-x}(OH)_x] \rightarrow Ti(OPr^i)_{4-x}(OH)_{x-1} - O - Ti(OPr^i)_{4-x-1}(OH)_x + Pr^iOH \quad (1.8)$$

where equation 1.7 represents hydrolysis of TTIP with water and equation 1.8 represents condensation of hydrolyzed TTIP.

The faster hydrolysis of the TTIP with water results in the rapid precipitation of hydrolyzed TTIP due to high reactivity, which in turn leads to non-homogeneity in the films. Therefore, the hydrolysis rate needs to be controlled in order to avoid precipitation and to achieve sol-gels with desired properties to obtain highly homogeneous TiO_2 thin films.[66] The sol-gel spin coating method can be employed to prepare several other catalyst thin films, i.e., CdS thin films.[67] Researchers have also used advanced coating methods such as physical vapor deposition (including thermal evaporation, reactive sputtering, ion or electron beam evaporation), chemical vapor deposition techniques, electrodeposition, electrophoresis and wet chemical deposition methods (dip-coating and spray coating) for making the TiO_2 thin films.[68–70] However, these methods are complex and require costly equipment.

1.6 Photocatalytic applications using thin film form of catalysts

Of the various photocatalytic applications, the photocatalytic degradation of Methylene blue (MB) is suggested as a standard by the international organization for standardization (ISO), namely, "Determination of photocatalytic activity of surfaces in the aqueous medium by degradation of methylene blue (10678:2010)" to assess the photocatalytic activity of thin films.[71] Therefore, the performance of the thin film-based catalyst can be tested by the photo-degradation of MB. Of the other photocatalytic applications, photocatalytic water splitting is gaining rapid attention since it is an environmentally friendly process as it involves only water, solar light and catalyst materials to generate H_2 and O_2.[72] Recently, the thin film photocatalyst outperformed the powder form photocatalyst in water splitting.[73] In the solar hydrogen generation, the H_2 production rate is higher using the thin film form as compared to that using the powder form, with the same (amount of) catalyst in both the cases.[73–75] This improved activity of the thin film is attributed to enhanced solar light absorption, effective charge separation and utilization, and enhanced mass transfer of reactants/sacrificial agents and photon transfer because of high surface to volume ratio. Thus, proving the superiority of applying thin film form over powder form of photocatalysts.

Several studies reported the preparation of TiO_2 thin films by sol-gel method and their performance tests by photocatalytic degradation of MB dye. Shilpa et al.[76] studied the degradation of methylene blue in aqueous solution under direct sun light using the carbon quantum dots (CQD)/TiO_2 thin films. The CQD/TiO_2 film was synthesized using facile, and low-temperature hydrothermal synthesis approach using CQD derived from sugarcane juice and ethanol. They reported that CQD/TiO_2 thin films exhibited 82.6% MB degradation, with good reusability, under the noon sunlight radiation. Dulian et al.[77] studied the photocatalytic MB degradation under UV light on the multilayer TiO_2 coatings prepared by sol-gel dip coating method. The TiO_2 coated glass substrates were dipped into the MB solution horizontally. The authors reported that the reaction rate of MB degradation is strongly related to the thickness of the layer, the number of layers and its morphology. The film with 1150 nm thick exhibited the highest degradation rate. Komaraiah et al.[78] studied the photocatalytic degradation of MB using Fe doped TiO_2 thin films synthesized by the sol-gel spin coating technique under visible light irradiance. The enhancement of photocatalytic activity with the doping of Fe was ascribed to the high specific surface area, lower bandgap energy and expanded absorption of the visible light. Table 1.4 shows the recent literature review on the use of TiO_2 based photocatalysts for standardized test of methylene blue degradation.

Table 1.4: Recent literature review on the use of TiO_2 based photocatalysts for standardized test of methylene blue degradation

Photocatalyst	(Co)catalyst method	Catalyst Amount/ thickness	Dye solution	Light	Reactor	% degradation	Time (min)	Stability	Year	Ref
CQDs/TiO_2 thin films	hydrothermal	-	3 mg L^{-1} MB in 100 mL H_2O	direct sunlight	200 ml beaker	82.6	240	3 cycles	2023	[76]
TiO_2-coated PAN-glass flat membrane	tape casting/dip coating	1000 mg	20 mg L^{-1} MB in 10 mL H_2O	UV lamp	self-made photoreactor	98.5	480	5 cycles of 8 h	2023	[79]
TiO_2 thin films	metal–organic chemical vapor deposition	203 nm	10 ppm MB solution	sunlight	photoreactor	97.5	120	5 runs	2023	[80]
Fe_3O_4/TiO_2 Thin Film	hydrothermal	-	3 mg L^{-1} MB in 100 mL H_2O	direct sunlight	beaker	84	240	3 cycles	2023	[81]
ZnO-TiO_2 multilayer thin films	sol-gel spin coating	-	100 µM MB solution	100 W incandescent visible bulb	jacketed transparent vessel	50	180	-	2023	[82]
flowerlike rutile-phase TiO_2 film	hydrothermal method	-	100 mL of 5 ppm MB solution	300 W Xenon lamp (300–600 nm)	photoreactor	42	300	5 runs	2022	[83]
TiO_2: Fe^{3+} films	sol-gel spin coating	358 nm	3 mg L^{-1} MB in 25 mL H_2O	200W tungsten visible irradiation	beaker	96.7	240	-	2019	[78]
Thin TiO_2 films	sol-gel/dip-coating	1150 nm	2.5 mM MB	mercury lamp (λ = 254 nm)	photoreactor	100	480	-	2019	[77]

1.7 Visible light driven photocatalytic water splitting

Anatase TiO_2 usually has a bandgap energy of 3.2 eV, allowing it to absorb the photon energy in the UV region only. However, the majority of the solar spectrum consists of 40–45% photon energy in the visible region. Therefore, the visible light assisted photocatalytic process is of great importance to convert a major part of the solar energy received on earth into hydrogen energy.

Various strategies such as surface modification (e.g., cocatalyst loading), morphology control, and heterojunction formation are extensively attempted in order to improve the visible light absorption efficiency of the existing photocatalysts. Among them, the cocatalyst loading has still been an effective method.[84] The Pt and IrO_2 are very well-known cocatalysts for the HER and OER because of their good activity and stability.[85,86] However, a semiconductor photocatalyst is often required to utilize the Pt and IrO_2 cocatalysts because the platinum and iridium are noble metals, expensive and rare.[87] Therefore, doping Pt and IrO_2 nanoparticles as cocatalyst onto the wide bandgap semiconductor such as TiO_2 is a feasible choice for extending absorption into visible light region, as well as acting as HER and OER cocatalysts.[88] Other than modification of TiO_2, exploration and development of novel semiconductor materials capable of absorbing visible light is underway. For example, CdS, WO_3, Ag_3PO_4, $BiVO_4$, and g-C_3N_4 are discovered to be some novel and efficient non-TiO_2 photocatalyst for visible light photocatalysis.[89]

The TiO_2 is still the most studied and well-established semiconductor for photocatalytic applications. Different techniques such as metal doping (Pt, Ag, Au etc.,), non-metal doping (N, C, S etc.,) and semiconductor doping to form heterojunction or Z-scheme (ZnO, CdS etc.,) have been employed to make the TiO_2 visible active, as mentioned above. However, metal doping is very efficient because of the enhanced photocarriers (electron-hole pairs) separation and also shifting to visible light absorbance, thereby improving the photocatalytic activity.

1.8 Photocatalytic reactors: conventional batch reactor vs Optofluidic microreactor

Optofluidic technology, a synergy between optics and microfluidics, has been gaining interest in recent times for testing the photocatalytic systems for various applications because of the fine control of the interaction between light and fluid inside the microscale structures.[90,91] Optofluidic microdevice improves the process efficiency because of the large surface area to volume ratio, compact size and enhanced mass and photon transfer.[92,93] The shorter optical length and diffusion times enable the uniform distribution of the irradiated light and reactants/products on catalyst surface, which in turn enhances the rate of the photocatalytic

reactions.[94] The photocatalyst immobilized (as thin films of less than a few μm thick) onto the microreactor walls have higher illuminated specific surface area than conventional batch reactors.[95] The self-refreshing nature of the catalyst surface inside the microreactor because of the continuous reactant flow results in higher activity and longer photocatalyst durability.[96,97] The optofluidic devices have been tested for various photocatalytic applications such as water treatment[96,98–100], organic synthesis[95], CO_2 reduction[101] and water-splitting[102,103].

Various optofluidic configurations such as microcapillary, single- and multi-channel, and planar have been explored in the literature.[97] The planar configuration is more efficient among the four due to the large photon receiving area, and higher throughput. The former characteristic helps in improving the quantum yield and the latter characteristic in the easy scalability.[100,101] Various studies compared the photocatalysis in planar and bulk reactors and proved that the planar microreactors achieved higher reaction rates.[96,98] Optofluidic planar microreactors are attaining considerable interest because of their easy scalability apart from the advantages induced by microfluidics.

Reports on optofluidic microreactors for the photocatalytic water-splitting reaction are scarce (Table 1.5). For the first time, Ahsan et al.[103], demonstrated I^-/IO_3^- redox-mediated water-splitting in an optofluidic planar microreactor over the Pt/TiO_2 using UV light irradiation. The planar reactor was fabricated using glass slides for catalyst plate and cover plate, with parafilm in between to bond them together as well as to create the space for fluid movement. The authors reported a two-fold increase in the reaction rate with changing the reaction conditions due to enhancement of transport properties. Chen and group[102,104] developed a planar reactor with SU-8 micropillars (to create high surface area) on the Si substrate and with PDMS/glass as reaction chamber as well as cover plate for water splitting. The reaction was carried out in presence of I^-/IO_3^- redox-mediators and under UV light illumination and reported a higher reaction rate in planar microreactor with micropillars as compared to that in flat planar microreactor.

A drawback of above studies is the use of change in I^-/IO_3^- redox-mediators' concentration as a measure of hydrogen production and also the use of UV light for illumination. If the I^-/IO_3^- redox-mediators undergo side reactions during water splitting, then the rate of hydrogen production may not be directly correlated to the I^-/IO_3^- depleted. Moreover, due to the corrosive and toxic nature of the I^-/IO_3^-, their presence especially at higher concentrations seriously hinders the prospects of commercialization.[103] Usage of UV radiation as light source greatly limits the utilization of solar power as it constitutes only 4% UV radiation.

Table 1.5: Recent literature review on the optofluidic planar microreactors for different photocatalytic applications

Application	Photocatalyst	(Co)catalyst method	Coating method	Catalyst amount	Feed	Light	Reactor dimensions	performance	AQY (%)	Stability	Year	Ref
CO_2 photo-reduction	$Cu_2O/Mo_2C/TiO_2$	physically mixing	airbrush	2 mg·cm^{-2}	0.5 M $KHCO_3$ aqueous solution	visible (450 nm)	Reaction microchamber of 1 cm^2 and 75 µL	CH_3OH – 36.3 µmol g^{-1} h^{-1}	0.64	7 h continuous operation	2023	105
EE2 degradation	Pd-TiO_2	sol–gel	dip-coating	0.1 mg·cm^{-2}	4.7 mg L^{-1} EE2 aqueous solution	solar simulator	reactor volume - 209 µL	99.5 % degradation	0.66	-	2023	106
MB degradation	Ag/AgCl	-	-	10.5 mg/cm^3	10 mg/L solution	300 W xe lamp (≥ 400 nm)	area of 2 cm X 6 cm	40 % degradation	-	10 runs of 40h	2023	107
Cephalexin removal	chitosan/Bi_2WO_6/CNT/TiO_2 nanofibers	hydrothermal	electro-spinning	6.5 µm thickness	29 mg/L solution	20 W Xe lamp	volume = 300 µL	99.9 % removal efficiency	-	25 h continuous operation	2022	108
Rh6G degradation	TiO_2 nanohelix film	-	GLAD technique	450 nm thickness	0.05 M solution	UV-light (310–390 nm)	volume = 45 µL	90 % degradation	-	-	2022	109
Water splitting: H_2 production	Pt/TiO_2	Photo-chemical reduction	sol–gel	150 µg. cm^{-2}	80 µM iodide solution	50-W mercury UV lamp	volume = 45 µL	2.4% depleted efficiency	-	-	2015	104
Water splitting: O_2 production	Pt/TiO_2	Photo-chemical reduction	sol–gel	150 µg. cm^{-2}	80 µM iodate solutio	50-W mercury UV lamp	volume = 45 µL	1.1% depleted efficiency	-	-	2015	104
Water splitting: H_2 production	Pt/TiO_2	NaBH4 reduction	sol–gel	-	200 µM NaI solution	100 W UV Hg lamp	3.75 cm X 1.25 cm	0.06% depleted efficiency	-	-	2013	103

1.9 Knowledge gap and hypothesis

Although the TiO_2 thin films are widely used in the field of photocatalysis, the detailed study of the effect of sol-gel composition on the surface morphology and topography of the TiO_2 thin film to achieve uniform and well adhered catalyst coatings is scarce in the literature. Once uniform and adherent TiO_2-coated film on glass substrate is developed, optofluidic microreactors can be constructed and be used for photocatalytic applications such as water splitting for hydrogen production. Optofluidic planar microreactor is a novel photocatalytic reactor which offers high reaction rates compared to that of conventional batch reactors because of advantages such as large surface to volume ratio and enhanced mass and photon transfer efficiency. To our knowledge, there are no literature studies available for the photocatalytic water splitting in the optofluidic planar microreactor for the production of hydrogen and oxygen in the presence of sacrificial agents, respectively, under visible light illumination. Photocatalytic overall water splitting (POWS) to form both hydrogen and oxygen is attracting considerable attention as a potential means of clean, renewable and large-scale energy conversion process with no dependence on fossil fuels and carbon dioxide emissions. The OER is a sluggish reaction in the POWS because of the four-electron transfer process coupled with the removal of four protons from H_2O to form O_2. Developing an efficient and highly active photocatalyst for OER is critical for successful implementation of POWS for large scale practical applications. Therefore, it is still a challenge to successfully synthesize a single semiconductor doped with metal cocatalysts to meet the required conduction and valence band potentials for simultaneous HER and OER to occur resulting in POWS from pure water without using any sacrificial agents.

1.10 Objectives of the work

The objectives of the thesis, deduced from knowledge gaps, are as follows:

- Preparation of uniform and adherent TiO_2 thin films on glass by sol-gel spin coating method and photo-deposition of Pt and IrO_2 onto these films.
- Characterization of the synthesized photocatalyst films and powders using various techniques such as X-ray diffraction, Ultraviolet-Visible spectroscopy, Photoluminescence spectroscopy, Field emission transmission electron microscopy, Field emission scanning electron microscopy, Energy dispersive X-ray spectroscopy, and X-ray photoelectron spectroscopy.

- Fabrication and testing of an optofluidic planar microreactors for the hydrogen and oxygen production from the photocatalytic water splitting (PWS) over Pt/TiO_2 (sacrificial reagent (SR): methanol) and IrO_2/TiO_2 (SR: sodium iodate) thin films, respectively, under visible/simulated solar light (SSL) irradiation.
- Synthesis of a TiO_2 based photocatalyst using Pt and IrO_2 as cocatalysts and testing the activity for the photocatalytic overall water splitting (POWS) under visible/SSL irradiation using the particle suspension (batch) reactor without using any SR.
- Study of the effect of the various parameters such as photocatalyst film thickness, reactant flowrate, catalyst loading, cocatalyst loading, stirring speed, solar light intensity, and long-term stability test on the rate of hydrogen and oxygen production.

1.11 Organization of the thesis

The following chapters of the thesis document on development of TiO_2 based photocatalysts for the photocatalytic water splitting reactions using the planar microreactor and batch reactor.

Chapter 1: Background of the work and research objectives

This chapter introduces the problem, includes literature survey and outlines the research objectives. A glimpse of this chapter is outlined at the beginning of this report.

Chapter 2: Materials and methods

This chapter describes the procedures for the preparation of TiO_2 based photocatalysts and testing these catalysts for the production of hydrogen and oxygen from the photocatalytic water splitting in the planar microreactor and batch reactor. The analytical procedures for catalysts characterizations and product analyses are also detailed.

Physicochemical properties of TiO_2 catalysts were determined by various techniques including X-ray diffraction (XRD), Raman spectroscopy, UV-Visible (UV-Vis) spectroscopy, Photoluminescence (PL) spectroscopy, field emission transmission electron microscopy (FETEM), field emission scanning electron microscopy (FESEM), Electron dispersive X-ray (EDX) spectroscopy and X-ray photoelectron spectroscopy (XPS). The identification of reaction products was carried out using gas chromatography (GC).

For the preparation of TiO_2 thin films, TiO_2 sol-gels with varying concentrations of reagents were prepared. These sols were spin coated on the glass substrate and film structures were

characterized. The obtained uniform films were tested for the photo activity by methylene blue degradation.

The planar microreactors were fabricated using Pt/TiO_2 and IrO_2/TiO_2 films which were prepared by the photo-deposition method. The photocatalytic water splitting (PWS) reactions were conducted using the fabricated planar reactors. For the photocatalytic overall water splitting (POWS), $IrO_2/Pt/TiO_2$ photocatalysts were synthesized and characterized using various techniques. The catalyst performance tests were conducted using the batch reactor. The generated products (hydrogen and oxygen) were quantified using GC.

Chapter 3: Surface and photocatalytic properties of TiO_2 thin films prepared by non-aqueous surfactant assisted sol-gel method

In this chapter, the titanium dioxide (TiO_2) thin films are prepared on glass substrates using sol-gel spin coating method. The photocatalytic activity of the TiO_2 films is determined by investigating the photodegradation of methylene blue (MB) in aqueous solution. The TiO_2 thin films with 3 and 4 coatings showed 42.6 % and 58.4 % degradation of MB, respectively, in 60 min of photocatalytic reaction under UV light irradiation.

Chapter 4: Green hydrogen production in an optofluidic planar microreactor via photocatalytic water splitting under visible/simulated sun light irradiation

In this chapter, the visible light-active Pt/TiO_2 photocatalyst thin films were prepared by photo-depositing the Pt onto the sol-gel TiO_2 spin-coated films. An optofluidic planar microreactor was fabricated using the Pt/TiO_2 film coated glass substrate as bottom plate and uncoated glass substrate containing planar reaction chamber as cover plate. The Pt/TiO_2 thin films were tested for the photocatalytic water splitting activity in presence of methanol as sacrificial agent to produce hydrogen under visible/SSL irradiation. The Pt/TiO_2 film with thickness of 1650±119 nm showed a highest rate of 16.35 mmol h^{-1} g^{-1} (4.7 µmol h^{-1} cm^{-2}) hydrogen production at an optimum reactant flowrate of 0.3 mL min^{-1} under visible light (400 W metal halide lamp) irradiation.

Chapter 5: Visible light active IrO_2/TiO_2 films for oxygen evolution from photocatalytic water splitting in an optofluidic planar microreactor

In this chapter, an optofluidic planar microreactor was fabricated with the photocatalyst (IrO_2/TiO_2) film coated glass as a reactor plate and plain glass as a cover plate. The water splitting activity to produce oxygen using sodium iodate as a sacrificial agent (electron acceptor) was tested in the fabricated planar microreactor under visible light illumination (with

400 W metal halide lamp). An oxygen evolution rate of 3.99 mmol h^{-1} g^{-1} (1.84 µmol h^{-1} cm^{-2}) was observed over the IrO_2/TiO_2 film of 3078 ± 362 nm thickness at an optimal flow rate of 0.3 mL min^{-1} in the presence of visible light.

Chapter 6: Green hydrogen and oxygen production over $IrO_2/Pt/TiO_2$ via photocatalytic overall water splitting under visible light illumination

In this chapter, a photocatalyst was developed based on a single semiconductor (TiO_2) by employing Pt and IrO_2 as cocatalysts that showed activity for the photocatalytic overall water splitting under visible/SSL irradiation. The rate of hydrogen and oxygen production were 9.73 and 5.32 µmol g^{-1} h^{-1} under the SSL intensity of 101.4 mW cm^{-2} over the $2.5IrO_2/0.5Pt/TiO_2$ photocatalyst, resulting in the H_2/O_2 ratio of 1.82.

Chapter 7: Thesis conclusions and recommendations of future scope of work

This chapter summarizes the significant findings based on the investigations in the overall work. Furthermore, the recommendations for future work were added along with a few limitations observed in the thesis work.

References

(1) Zong, S.; Tian, L.; Guan, X.; Cheng, C.; Shi, J.; Guo, L. Photocatalytic Overall Water Splitting without Noble-Metal: Decorating CoP on Al-Doped SrTiO3. *J. Colloid Interface Sci.* **2022**, *606*, 491–499. https://doi.org/10.1016/j.jcis.2021.08.049.

(2) Yuan, L.; Han, C.; Yang, M. Q.; Xu, Y. J. Photocatalytic Water Splitting for Solar Hydrogen Generation: Fundamentals and Recent Advancements. *Int. Rev. Phys. Chem.* **2016**, *35* (1), 1–36. https://doi.org/10.1080/0144235X.2015.1127027.

(3) Walter, M. G.; Warren, E. L.; McKone, J. R.; Boettcher, S. W.; Mi, Q.; Santori, E. A.; Lewis, N. S. Solar Water Splitting Cells. *Chem. Rev.* **2010**, *110* (11), 6446–6473. https://doi.org/10.1021/cr1002326.

(4) Crabtree, G. W.; Lewis, N. S. Solar Energy Conversion. *Phys. Today* **2007**, *60* (3), 37–42. https://doi.org/10.1063/1.2718755.

(5) Sivaranjani, K.; Agarkar, S.; Ogale, S. B.; Gopinath, C. S. Toward a Quantitative Correlation between Microstructure and DSSC Efficiency: A Case Study of TiO2-XNx Nanoparticles in a Disordered Mesoporous Framework. *J. Phys. Chem. C* **2012**, *116* (3), 2581–2587. https://doi.org/10.1021/jp210677d.

(6) Ran, J.; Zhang, J.; Yu, J.; Jaroniec, M.; Qiao, S. Z. Earth-Abundant Cocatalysts for Semiconductor-Based Photocatalytic Water Splitting. *Chem. Soc. Rev.* **2014**, *43* (22), 7787–7812. https://doi.org/10.1039/C3CS60425J.

(7) Patra, K. K.; Bhuskute, B. D.; Gopinath, C. S. Possibly Scalable Solar Hydrogen Generation with Quasi-Artificial Leaf Approach. *Sci. Rep.* **2017**, *7* (1), 6515. https://doi.org/10.1038/s41598-017-06849-x.

(8) Li, R. Latest Progress in Hydrogen Production from Solar Water Splitting via Photocatalysis, Photoelectrochemical, and Photovoltaic-Photoelectrochemical Solutions. *Chinese J. Catal.* **2017**, *38* (1), 5–12. https://doi.org/10.1016/S1872-2067(16)62552-4.

(9) Li, R.; Li, C. Photocatalytic Water Splitting on Semiconductor-Based Photocatalysts. In *Advances in Catalysis*; 2017; Vol. 60, pp 1–57. https://doi.org/10.1016/bs.acat.2017.09.001.

(10) Melián, E. P.; Díaz, O. G.; Méndez, A. O.; López, C. R.; Suárez, M. N.; Rodríguez, J. M. D.; Navío, J. A.; Hevia, D. F.; Peña, J. P. Efficient and Affordable Hydrogen Production by Water Photo-Splitting Using TiO2-Based Photocatalysts. *Int. J. Hydrogen Energy* **2013**, *38* (5), 2144–2155. https://doi.org/10.1016/j.ijhydene.2012.12.005.

(11) Pareek, A.; Dom, R.; Gupta, J.; Chandran, J.; Adepu, V.; Borse, P. H. Insights into Renewable Hydrogen Energy: Recent Advances and Prospects. *Mater. Sci. Energy Technol.* **2020**, *3*, 319–327. https://doi.org/10.1016/j.mset.2019.12.002.

(12) Hagiwara, H.; Nozawa, I.; Hayakawa, K.; Ishihara, T. Hydrogen Production by Photocatalytic Water Splitting of Aqueous Hydrogen Iodide over Pt/Alkali Metal Tantalates. *Sustain. Energy Fuels* **2019**, *3* (11), 3021–3028. https://doi.org/10.1039/c9se00355j.

(13) Yang, L.; Gao, P.; Lu, J.; Guo, W.; Zhuang, Z.; Wang, Q.; Li, W.; Feng, Z. Mechanism Analysis of Au, Ru Noble Metal Clusters Modified on TiO2(101) to Intensify Overall

Photocatalytic Water Splitting. *RSC Adv.* **2020**, *10* (35), 20654–20664. https://doi.org/10.1039/d0ra01996h.

(14) Jiang, Z.; Ye, Z.; Shangguan, W. Recent Advances of Hydrogen Production through Particulate Semiconductor Photocatalytic Overall Water Splitting. *Front. Energy* **2022**, *16* (1), 49–63. https://doi.org/10.1007/s11708-022-0817-9.

(15) Drmosh, Q. A.; Alade, I. O.; Alkanad, K.; Alnaggar, G.; Khan, A.; Khan, M. Y.; Elsayed, K. A.; Manda, A. A.; Onaizi, S. A. Fabrication of Z-Scheme TiO2/BP/g-C3N4 Nanocomposite via Pulsed Laser Ablation in Liquid for Photocatalytic Overall Water Splitting. *Opt. Mater. (Amst).* **2022**, *128*, 112428. https://doi.org/10.1016/j.optmat.2022.112428.

(16) Lin, L.; Wang, C.; Ren, W.; Ou, H.; Zhang, Y.; Wang, X. Photocatalytic Overall Water Splitting by Conjugated Semiconductors with Crystalline Poly(Triazine Imide) Frameworks. *Chem. Sci.* **2017**, *8* (8), 5506–5511. https://doi.org/10.1039/c7sc00900c.

(17) Lin, Y.; Wang, X.; Fu, X.; Su, W. In Situ Growth of Crystalline Carbon Nitride on LaOCl for Photocatalytic Overall Water Splitting. *J. Mater. Chem. A* **2022**, *10* (15), 8252–8257. https://doi.org/10.1039/D2TA00068G.

(18) Pala, L. P. R.; Peela, N. R. Visible Light Active IrO2/TiO2 Films for Oxygen Evolution from Photocatalytic Water Splitting in an Optofluidic Planar Microreactor. *Renew. Energy* **2022**, *197*, 902–910. https://doi.org/10.1016/j.renene.2022.08.017.

(19) Jiang, Y.; Sun, Z.; Chen, Q.; Cao, C.; Zhao, Y.; Yang, W.; Zeng, L.; Huang, L. Fabrication of 0D/2D TiO2 Nanodots/g-C3N4 S-Scheme Heterojunction Photocatalyst for Efficient Photocatalytic Overall Water Splitting. *Appl. Surf. Sci.* **2022**, *571*, 151287. https://doi.org/10.1016/j.apsusc.2021.151287.

(20) Wan, G.; Yin, L.; Chen, X.; Xu, X.; Huang, J.; Zhen, C.; Zhu, H.; Huang, B.; Hu, W.; Ren, Z.; Tian, H.; Wang, L.; Liu, G.; Cheng, H.-M. Photocatalytic Overall Water Splitting over PbTiO3 Modulated by Oxygen Vacancy and Ferroelectric Polarization. *J. Am. Chem. Soc.* **2022**, *144* (44), 20342–20350. https://doi.org/10.1021/jacs.2c08177.

(21) Bie, C.; Wang, L.; Yu, J. Challenges for Photocatalytic Overall Water Splitting. *Chem* **2022**, *8* (6), 1567–1574. https://doi.org/10.1016/j.chempr.2022.04.013.

(22) Fu, W.; Guan, X.; Wu, H.; Liu, M. Switching from Two-Electron to Four-Electron Photocatalytic Pure Water Splitting via Band Bending Engineering with Boosted Activity. *Appl. Catal. B Environ.* **2022**, *305*, 121054. https://doi.org/10.1016/j.apcatb.2021.121054.

(23) Fang, Y.; Huang, W.; Yang, S.; Zhou, X.; Ge, C.; Gao, Q.; Fang, Y.; Zhang, S. Facile Synthesis of Anatase/Rutile TiO2/g-C3N4 Multi-Heterostructure for Efficient Photocatalytic Overall Water Splitting. *Int. J. Hydrogen Energy* **2020**, *45* (35), 17378–17387. https://doi.org/10.1016/j.ijhydene.2020.04.214.

(24) Lin, Y.; Liu, Y.; Li, Y.; Cao, Y.; Huang, J.; Wang, H.; Yu, H.; Liang, H.; Peng, F. Dual Functional CuO1–x Clusters for Enhanced Photocatalytic Activity and Stability of a Pt Cocatalyst in an Overall Water-Splitting Reaction. *ACS Sustain. Chem. Eng.* **2018**, *6* (12), 17340–17351. https://doi.org/10.1021/acssuschemeng.8b04889.

(25) Galinska, A.; Walendziewski, J. Photocatalytic Water Splitting over Pt - TiO2 in the Presence of Sacrificial Reagents. *Energy & Fuels* **2005**, *19*, 1143–1147.

https://doi.org/10.1021/ef0400619.

(26) Zhang, G.; Lan, Z. A.; Lin, L.; Lin, S.; Wang, X. Overall Water Splitting by Pt/g-C3N4 Photocatalysts without Using Sacrificial Agents. *Chem. Sci.* **2016**, *7* (5), 3062–3066. https://doi.org/10.1039/c5sc04572j.

(27) Guo, F.; Shi, W.; Zhu, C.; Li, H.; Kang, Z. CoO and G-C3N4 Complement Each Other for Highly Efficient Overall Water Splitting under Visible Light. *Appl. Catal. B Environ.* **2018**, *226*, 412–420. https://doi.org/10.1016/j.apcatb.2017.12.064.

(28) Pan, J.; Wang, P.; Wang, P.; Yu, Q.; Wang, J.; Song, C.; Zheng, Y.; Li, C. The Photocatalytic Overall Water Splitting Hydrogen Production of G-C3N4/CdS Hollow Core–Shell Heterojunction via the HER/OER Matching of Pt/MnOx. *Chem. Eng. J.* **2021**, *405*, 126622. https://doi.org/10.1016/j.cej.2020.126622.

(29) Shi, W.; Li, M.; Huang, X.; Ren, H.; Yan, C.; Guo, F. Facile Synthesis of 2D/2D Co3(PO4)2/g-C3N4 Heterojunction for Highly Photocatalytic Overall Water Splitting under Visible Light. *Chem. Eng. J.* **2020**, *382*, 122960. https://doi.org/10.1016/j.cej.2019.122960.

(30) Li, Y.; Liu, Y.; Xing, D.; Wang, J.; Zheng, L.; Wang, Z.; Wang, P.; Zheng, Z.; Cheng, H.; Dai, Y.; Huang, B. 2D/2D Heterostructure of Ultrathin BiVO4/Ti3C2 Nanosheets for Photocatalytic Overall Water Splitting. *Appl. Catal. B Environ.* **2021**, *285*, 119855. https://doi.org/10.1016/j.apcatb.2020.119855.

(31) Pérez-Larios, A.; Rico, J. L.; Anaya-Esparza, L. M.; Vargas, O. A. G.; González-Silva, N.; Gómez, R. Hydrogen Production from Aqueous Methanol Solutions Using Ti–Zr Mixed Oxides as Photocatalysts under UV Irradiation. *Catalysts* **2019**, *9* (11). https://doi.org/10.3390/catal9110938.

(32) Li, K.; Teng, C.; Wang, S.; Min, Q. Recent Advances in TiO2-Based Heterojunctions for Photocatalytic CO2 Reduction With Water Oxidation: A Review. *Front. Chem.* **2021**, *9*. https://doi.org/10.3389/fchem.2021.637501.

(33) Rico-Oller, B.; Boudjemaa, A.; Bahruji, H.; Kebir, M.; Prashar, S.; Bachari, K.; Fajardo, M.; Gómez-Ruiz, S. Photodegradation of Organic Pollutants in Water and Green Hydrogen Production via Methanol Photoreforming of Doped Titanium Oxide Nanoparticles. *Sci. Total Environ.* **2016**, *563–564*, 921–932. https://doi.org/10.1016/j.scitotenv.2015.10.101.

(34) Hakamizadeh, M.; Afshar, S.; Tadjarodi, A.; Ruhollah, K.; Mohammad, R. F.; Babak, B. b. Improving Hydrogen Production via Water Splitting over Pt/TiO2/Activated Carbon Nanocomposite. *Int. J. Hydrogen Energy* **2014**, *39*, 7262–7269. https://doi.org/10.1016/j.ijhydene.2014.03.048.

(35) Kandiel, T. A.; Ivanova, I.; Bahnemann, D. W. Long-Term Investigation of the Photocatalytic Hydrogen Production on Platinized TiO2: An Isotopic Study. *Energy Environ. Sci.* **2014**, *7* (4), 1420–1425. https://doi.org/10.1039/c3ee41511b.

(36) Guzman, F.; Chuang, S. S. C.; Yang, C. Role of Methanol Sacrificing Reagent in the Photocatalytic Evolution of Hydrogen. *Ind. Eng. Chem. Res.* **2013**, *52* (1), 61–65. https://doi.org/10.1021/ie301177s.

(37) Zheng, T.; Liu, Y.; Li, Y.; Yang, L.; Ren, H.; Wang, X.-F.; Fujii, R.; Kitao, O.; Nakamura, T.; Sasaki, S. Panchromatic Pt/TiO2-Based Photocatalysts Sensitized with

Carboxylated Chlorin Dyads for Water Splitting Hydrogen Evolution. *Appl. Surf. Sci.* **2023**, *619*, 156570. https://doi.org/10.1016/j.apsusc.2023.156570.

(38) Ma, R.; Su, H.; Sun, J.; Li, D.; Zhang, Z.; Wei, J. Thermally-Enhanced Sono-Photo-Catalysis by Defect and Facet Modulation of Pt-TiO2 Catalyst for High-Efficient Hydrogen Evolution. *Ultrason. Sonochem.* **2022**, *90*, 106222. https://doi.org/10.1016/j.ultsonch.2022.106222.

(39) Li, L.; Ouyang, W.; Zheng, Z.; Ye, K.; Guo, Y.; Qin, Y.; Wu, Z.; Lin, Z.; Wang, T.; Zhang, S. Synergetic Photocatalytic and Thermocatalytic Reforming of Methanol for Hydrogen Production Based on Pt@TiO2 Catalyst. *Chinese J. Catal.* **2022**, *43* (5), 1258–1266. https://doi.org/10.1016/S1872-2067(21)63963-3.

(40) Cao, S.; Zhou, Y.; Wang, R.; Jiao, W. Enhanced Photocatalytic Activity by Pt Confined within N-Doped Carbon on TiO2 Inner Surface. *Ind. Eng. Chem. Res.* **2022**, *61* (6), 2494–2501. https://doi.org/10.1021/acs.iecr.1c04431.

(41) Yamazaki, Y.; Toyonaga, T.; Doshita, N.; Mori, K.; Kuwahara, Y.; Yamazaki, S.; Yamashita, H. Crystal Facet Engineering and Hydrogen Spillover-Assisted Synthesis of Defective Pt/TiO2–x Nanorods with Enhanced Visible Light-Driven Photocatalytic Activity. *ACS Appl. Mater. Interfaces* **2022**, *14* (1), 2291–2300. https://doi.org/10.1021/acsami.1c20148.

(42) Gao, F.; Xu, Z.; Zhao, H. Flame Spray Pyrolysis Made Pt/TiO2 Photocatalysts with Ultralow Platinum Loading and High Hydrogen Production Activity. *Proc. Combust. Inst.* **2021**, *38* (4), 6503–6511. https://doi.org/10.1016/j.proci.2020.06.330.

(43) Yu, J.; Qi, L.; Jaroniec, M. Hydrogen Production by Photocatalytic Water Splitting over Pt/TiO2 Nanosheets with Exposed (001) Facets. *J. Phys. Chem. C* **2010**, *114* (30), 13118–13125. https://doi.org/10.1021/jp104488b.

(44) Zhang, Z.; Maggard, P. A. Investigation of Photocatalytically-Active Hydrated Forms of Amorphous Titania, TiO2·nH2O. *J. Photochem. Photobiol. A Chem.* **2007**, *186* (1), 8–13. https://doi.org/10.1016/j.jphotochem.2006.07.004.

(45) Kitano, M.; Takeuchi, M.; Matsuoka, M.; Thomas, J. M.; Anpo, M. Photocatalytic Water Splitting Using Pt-Loaded Visible Light-Responsive TiO2 Thin Film Photocatalysts. *Catal. Today* **2007**, *120*, 133–138. https://doi.org/10.1016/j.cattod.2006.07.043.

(46) Nadeem, M. A.; Khan, M. A.; Ziani, A. A.; Idriss, H. An Overview of the Photocatalytic Water Splitting over Suspended Particles. *Catalysts* **2021**, *11* (1), 1–25. https://doi.org/10.3390/catal11010060.

(47) Qureshi, M.; Shinagawa, T.; Tsiapis, N.; Takanabe, K. Exclusive Hydrogen Generation by Electrocatalysts Coated with an Amorphous Chromium-Based Layer Achieving Efficient Overall Water Splitting. *ACS Sustain. Chem. Eng.* **2017**, *5* (9), 8079–8088. https://doi.org/10.1021/acssuschemeng.7b01704.

(48) Schubert, J. S.; Popovic, J.; Haselmann, G. M.; Nandan, S. P.; Wang, J.; Giesriegl, A.; Cherevan, A. S.; Eder, D. Immobilization of Co, Mn, Ni and Fe Oxide Co-Catalysts on TiO2 for Photocatalytic Water Splitting Reactions. *J. Mater. Chem. A* **2019**, *7* (31), 18568–18579. https://doi.org/10.1039/C9TA05637H.

(49) Wu, T.; Niu, P.; Yang, Y.; Yin, L.-C.; Tan, J.; Zhu, H.; Irvine, J. T. S.; Wang, L.; Liu, G.; Cheng, H.-M. Homogeneous Doping of Substitutional Nitrogen/Carbon in TiO2

Plates for Visible Light Photocatalytic Water Oxidation. *Adv. Funct. Mater.* **2019**, *29* (25), 1901943. https://doi.org/10.1002/adfm.201901943.

(50) Calleja, G.; Serrano, D. P.; Sanz, R.; Pizarro, P.; García, A. Study on the Synthesis of High-Surface-Area Mesoporous TiO 2 in the Presence of Nonionic Surfactants. *Ind. Eng. Chem. Res.* **2004**, *43* (10), 2485–2492. https://doi.org/10.1021/ie030646a.

(51) Zhang, J.; Zhou, P.; Liu, J.; Yu, J. New Understanding of the Difference of Photocatalytic Activity among Anatase, Rutile and Brookite TiO 2. *Phys. Chem. Chem. Phys.* **2014**, *16* (38), 20382–20386. https://doi.org/10.1039/C4CP02201G.

(52) Kenanakis, G.; Katsarakis, N. Chemically Grown TiO2on Glass with Superior Photocatalytic Properties. *J. Environ. Chem. Eng.* **2014**, *2* (3), 1748–1755. https://doi.org/10.1016/j.jece.2014.07.015.

(53) Edalati, P.; Itagoe, Y.; Ishihara, H.; Ishihara, T.; Emami, H.; Arita, M.; Fuji, M.; Edalati, K. Visible-Light Photocatalytic Oxygen Production on a High-Entropy Oxide by Multiple-Heterojunction Introduction. *J. Photochem. Photobiol. A Chem.* **2022**, *433*, 114167. https://doi.org/10.1016/j.jphotochem.2022.114167.

(54) Ke, D.; Peng, T.; Ma, L.; Cai, P.; Jiang, P. Photocatalytic Water Splitting for O2 Production under Visible-Light Irradiation on BiVO4 Nanoparticles in Different Sacrificial Reagent Solutions. *Appl. Catal. A Gen.* **2008**, *350* (1), 111–117. https://doi.org/10.1016/j.apcata.2008.08.003.

(55) Kiss, B.; Didier, C.; Johnson, T.; Manning, T. D.; Dyer, M. S.; Cowan, A. J.; Claridge, J. B.; Darwent, J. R.; Rosseinsky, M. J. Photocatalytic Water Oxidation by a Pyrochlore Oxide upon Irradiation with Visible Light: Rhodium Substitution Into Yttrium Titanate. *Angew. Chemie Int. Ed.* **2014**, *53* (52), 14480–14484. https://doi.org/10.1002/anie.201407179.

(56) Cui, X.; Yang, X.; Xian, X.; Tian, L.; Tang, H.; Liu, Q. Insights into Highly Improved Solar-Driven Photocatalytic Oxygen Evolution over Integrated Ag3PO4/MoS2 Heterostructures. *Front. Chem.* **2018**, *6* (APR), 1–8. https://doi.org/10.3389/fchem.2018.00123.

(57) Kageshima, Y.; Tateyama, S.; Kishimoto, F.; Teshima, K.; Domen, K.; Nishikiori, H. Photocatalytic Oxygen Evolution Triggered by Photon Upconverted Emission Based on Triplet–Triplet Annihilation. *Phys. Chem. Chem. Phys.* **2021**, *23* (9), 5673–5679. https://doi.org/10.1039/D0CP06139E.

(58) Sampaio, M. J.; Yu, Z.; Lopes, J. C.; Tavares, P. B.; Silva, C. G.; Liu, L.; Faria, J. L. Light-Driven Oxygen Evolution from Water Oxidation with Immobilised TiO2 Engineered for High Performance. *Sci. Rep.* **2021**, *11* (1), 21306. https://doi.org/10.1038/s41598-021-99841-5.

(59) Amouzad, S.; Monadi, N. Sensitization of Magnetite@SiO2@TiO2 by Cobalt Sulfophthalocyanine and Investigation of Photocatalytic Activity of Oxygen Evolution under Visible Light. *Inorg. Chem. Commun.* **2023**, *149*, 110401. https://doi.org/10.1016/j.inoche.2023.110401.

(60) Nakata, K.; Fujishima, A. TiO2 Photocatalysis: Design and Applications. *J. Photochem. Photobiol. C Photochem. Rev.* **2012**, *13* (3), 169–189. https://doi.org/10.1016/j.jphotochemrev.2012.06.001.

(61) Hwang, K. J.; Lee, J. W.; Shim, W. G.; Jang, H. D.; Lee, S. Il; Yoo, S. J. Adsorption and Photocatalysis of Nanocrystalline TiO2particles Prepared by Sol-Gel Method for Methylene Blue Degradation. *Adv. Powder Technol.* **2012**, *23* (3), 414–418. https://doi.org/10.1016/j.apt.2011.05.010.

(62) Alzamani, M.; Shokuhfar, A.; Eghdam, E.; Mastali, S. Influence of Catalyst on Structural and Morphological Properties of TiO2nanostructured Films Prepared by Sol–Gel on Glass. *Prog. Nat. Sci. Mater. Int.* **2013**, *23* (1), 77–84. https://doi.org/10.1016/j.pnsc.2013.01.012.

(63) Arconada, N.; Castro, Y.; Durán, A. Photocatalytic Properties in Aqueous Solution of Porous TiO2-Anatase Films Prepared by Sol-Gel Process. *Appl. Catal. A Gen.* **2010**, *385* (1–2), 101–107. https://doi.org/10.1016/j.apcata.2010.06.051.

(64) Anderson, A.-L.; Binions, R. The Effect of Tween® Surfactants in Sol-Gel Processing for the Production of TiO2 Thin Films. *Coatings* **2014**, *4* (4), 796–809. https://doi.org/10.3390/coatings4040796.

(65) Medina-Valtierra, J.; Sánchez-Cárdenas, M.; Frausto-Reyes, C.; Calixto, S. Formation of Smooth and Rough TiO2 Thin Films on Fiberglass by Sol-Gel Method. *Chem. Soc* **2006**, *50* (1), 8–13.

(66) Dunuwila, D. D.; Gagliardi, C. D.; Berglund, K. A. Application of Controlled Hydrolysis of Titanium(IV) Isopropoxide to Produce Sol-Gel-Derived Thin Films. *Chem. Mater.* **1994**, *6* (9), 1556–1562. https://doi.org/10.1021/cm00045a013.

(67) Munaga, V. V. P.; Krishnan, T.; Borra, R. K. Structural, Surface Morphological, Optical and Thermoelectric Properties of Sol–Gel Spin Coated Zn Doped CdS Thin Films. *SN Appl. Sci.* **2020**, *2* (4), 1–12. https://doi.org/10.1007/s42452-020-2358-3.

(68) Soni, K.; Sheikh, A.; Lakshmi, N. Thiourea Doped TiO2: Structural, Optical and Electrochemical Properties. *Mater. Today Proc.* **2022**, *49*, 1861–1864. https://doi.org/10.1016/j.matpr.2021.08.058.

(69) Schuster, J. M.; Vera, M. L.; Schvezov, C. E.; Rosenberger, M. R. Smooth Semicompact Multilayer Coating of TiO2 Obtained by Combining Anodic Oxidation and Sol-Gel Techniques. *Surf. Coatings Technol.* **2022**, *451*, 129035. https://doi.org/10.1016/j.surfcoat.2022.129035.

(70) Vahl, A.; Veziroglu, S.; Henkel, B.; Strunskus, T.; Polonskyi, O.; Aktas, O. C.; Faupel, F. Pathways to Tailor Photocatalytic Performance of TiO(2) Thin Films Deposited by Reactive Magnetron Sputtering. *Mater. (Basel, Switzerland)* **2019**, *12* (17). https://doi.org/10.3390/ma12172840.

(71) Díaz-Uribe, C.; Viloria, J.; Cervantes, L.; Vallejo, W.; Navarro, K.; Romero, E.; Quiñones, C. Photocatalytic Activity of Ag-TiO_2 Composites Deposited by Photoreduction under UV Irradiation. *Int. J. Photoenergy* **2018**, *2018*, 6080432. https://doi.org/10.1155/2018/6080432.

(72) Ahmad, H.; Kamarudin, S. K.; Minggu, L. J.; Kassim, M. Hydrogen from Photo-Catalytic Water Splitting Process: A Review. *Renew. Sustain. Energy Rev.* **2015**, *43*, 599–610. https://doi.org/10.1016/j.rser.2014.10.101.

(73) Nalajala, N.; Patra, K. K.; Bharad, P. A.; Gopinath, C. S. Why the Thin Film Form of a Photocatalyst Is Better than the Particulate Form for Direct Solar-to-Hydrogen

Conversion: A Poor Man's Approach. *RSC Adv.* **2019**, *9* (11), 6094–6100. https://doi.org/10.1039/c8ra09982k.

(74) Tudu, B.; Nalajala, N.; Reddy, K.; Saikia, P.; Gopinath, C. S. Electronic Integration and Thin Film Aspects of Au-Pd/RGO/TiO2 for Improved Solar Hydrogen Generation. *ACS Appl. Mater. Interfaces* **2019**, *11* (36), 32869–32878. https://doi.org/10.1021/acsami.9b07070.

(75) Tudu, B.; Nalajala, N.; Saikia, P.; Gopinath, C. S. Cu–Ni Bimetal Integrated TiO2 Thin Film for Enhanced Solar Hydrogen Generation. *Sol. RRL* **2020**, *4* (5), 1900557. https://doi.org/10.1002/solr.201900557.

(76) Shilpa, G.; P, M. K.; Deepthi, P. R.; Balan, R.; Sukhdev, A.; Bhaskar, P.; Kumar D, K. Enhanced Photocatalytic Activity of Orientationally Grown CQD/TiO2 Thin Film on FTO Substrate. *Ceram. Int.* **2023**. https://doi.org/10.1016/j.ceramint.2023.03.035.

(77) Dulian, P.; Nachit, W.; Jaglarz, J.; Zięba, P.; Kanak, J.; Żukowski, W. Photocatalytic Methylene Blue Degradation on Multilayer Transparent TiO2 Coatings. *Opt. Mater. (Amst).* **2019**, *90*, 264–272. https://doi.org/10.1016/j.optmat.2019.02.041.

(78) Komaraiah, D.; Radha, E.; Sivakumar, J.; Ramana Reddy, M. V.; Sayanna, R. Structural, Optical Properties and Photocatalytic Activity of Fe3+ Doped TiO2 Thin Films Deposited by Sol-Gel Spin Coating. *Surfaces and Interfaces* **2019**, *17*, 100368. https://doi.org/10.1016/j.surfin.2019.100368.

(79) Tan, H.; Zhang, Y.; Li, B.; Yang, H.; Hou, H.; Huang, Q. Preparation of TiO2-Coated Glass Flat Membrane and Its Photocatalytic Degradation of Methylene Blue. *Ceram. Int.* **2023**. https://doi.org/10.1016/j.ceramint.2023.02.089.

(80) Khalifa, Z. S.; Shaban, M.; Ahmed, I. A. Photocatalytic Degradation of Methyl Orange and Methylene Blue Dyes by Engineering the Surface Nano-Textures of TiO2 Thin Films Deposited at Different Temperatures via MOCVD. *Molecules*. 2023. https://doi.org/10.3390/molecules28031160.

(81) Shilpa, G.; Kumar, P. M.; Deepthi, P. R.; Sukhdev, A.; Bhaskar, P.; Kumar, D. K. Improved Photocatalytic Performance of Fe3O4/TiO2 Thin Film in the Degradation of MB Dye Under Sunlight Radiation. *Brazilian J. Phys.* **2023**, *53* (2), 38. https://doi.org/10.1007/s13538-022-01243-z.

(82) Yadawa, Y.; Singh, S.; Ranjan, A. Processing Induced Morphology Change in ZnO-TiO2 Multilayer Thin Films and Its Effect on Their Photocatalytic Activity under Visible Light Irradiation. *Mater. Sci. Eng. B* **2023**, *288*, 116164. https://doi.org/10.1016/j.mseb.2022.116164.

(83) Hamed, N. K. A.; Ahmad, M. K.; Hairom, N. H. H.; Faridah, A. B.; Mamat, M. H.; Mohamed, A.; Suriani, A. B.; Soon, C. F.; Fazli, F. I. M.; Mokhtar, S. M.; Shimomura, M. Photocatalytic Degradation of Methylene Blue by Flowerlike Rutile-Phase TiO2 Film Grown via Hydrothermal Method. *J. Sol-Gel Sci. Technol.* **2022**, *102* (3), 637–648. https://doi.org/10.1007/s10971-021-05691-y.

(84) Iwase, Y.; Tomita, O.; Higashi, M.; Abe, R. Enhanced Oxygen Evolution on Visible Light Responsive TaON Photocatalysts Co-Loaded with Highly Active Ru Species for IO3- Reduction and Co Species for Water Oxidation. *Sustain. Energy Fuels* **2017**, *1* (4), 748–754. https://doi.org/10.1039/c7se00110j.

(85) Wang, Z. M.; Liu, P.; Cao, Y. P.; Ye, F.; Xu, C.; Du, X. Z. Characterization and Electrocatalytic Properties of Electrospun Pt-IrO2 Nanofiber Catalysts for Oxygen Evolution Reaction. *Int. J. Energy Res.* **2021**, *45* (4), 5841–5851. https://doi.org/10.1002/er.6204.

(86) Exner, K. S.; Over, H. Beyond the Rate-Determining Step in the Oxygen Evolution Reaction over a Single-Crystalline IrO2(110) Model Electrode: Kinetic Scaling Relations. *ACS Catal.* **2019**, *9* (8), 6755–6765. https://doi.org/10.1021/acscatal.9b01564.

(87) Park, Y. J.; Lee, J.; Park, Y. S.; Yang, J.; Jang, M. J.; Jeong, J.; Choe, S.; Lee, J. W.; Kwon, J.-D.; Choi, S. M. Electrodeposition of High-Surface-Area IrO2 Films on Ti Felt as an Efficient Catalyst for the Oxygen Evolution Reaction. *Front. Chem.* **2020**, *8* (October), 1–9. https://doi.org/10.3389/fchem.2020.593272.

(88) Oakton, E.; Lebedev, D.; Povia, M.; Abbott, D. F.; Fabbri, E.; Fedorov, A.; Nachtegaal, M.; Copéret, C.; Schmidt, T. J. IrO2-TiO2: A High-Surface-Area, Active, and Stable Electrocatalyst for the Oxygen Evolution Reaction. *ACS Catal.* **2017**, *7* (4), 2346–2352. https://doi.org/10.1021/acscatal.6b03246.

(89) Dong, P.; Xinguo, X.; Guihua, H. Typical Non–TiO2-Based Visible-Light Photocatalysts. In *Semiconductor Photocatalysis - Materials, Mechanisms and Applications*; IntechOpen, 2016; p Ch. 8. https://doi.org/10.5772/62889.

(90) Erickson, D.; Sinton, D.; Psaltis, D. Optofluidics for Energy Applications. *Nat. Photonics* **2011**, *5* (10), 583–590. https://doi.org/10.1038/nphoton.2011.209.

(91) Cambié, D.; Bottecchia, C.; Straathof, N. J. W.; Hessel, V.; Noël, T. Applications of Continuous-Flow Photochemistry in Organic Synthesis, Material Science, and Water Treatment. *Chemical Reviews*. American Chemical Society September 2016, pp 10276–10341. https://doi.org/10.1021/acs.chemrev.5b00707.

(92) Li, L.; Chen, R.; Zhu, X.; Wang, H.; Wang, Y.; Liao, Q.; Wang, D. Optofluidic Microreactors with TiO2-Coated Fiberglass. *ACS Appl. Mater. Interfaces* **2013**, *5* (23), 12548–12553. https://doi.org/10.1021/am403842b.

(93) Li, L.; Tang, D.; Song, Y.; Jiang, B. Dual-Film Optofluidic Microreactor with Enhanced Light-Harvesting for Photocatalytic Applications. *Chem. Eng. J.* **2018**, *339* (November 2017), 71–77. https://doi.org/10.1016/j.cej.2018.01.074.

(94) Huang, X.; Wang, J.; Li, T.; Wang, J.; Xu, M.; Yu, W.; El Abed, A.; Zhang, X. Review on Optofluidic Microreactors for Artificial Photosynthesis. *Beilstein J. Nanotechnol.* **2018**, *9* (1), 30–41. https://doi.org/10.3762/bjnano.9.5.

(95) Matsushita, Y.; Ohba, N.; Kumada, S.; Sakeda, K.; Suzuki, T.; Ichimura, T. Photocatalytic Reactions in Microreactors. *Chem. Eng. J.* **2008**, *135S*, 303–308. https://doi.org/10.1016/j.cej.2007.07.045.

(96) Wang, N.; Tan, F.; Wan, L.; Wu, M. Microfluidic Reactors for Visible-Light Photocatalytic Water Purification Assisted with Thermolysis. *Biomicrofluidics* **2014**, *8*, 054122. https://doi.org/10.1063/1.4899883.

(97) Wang, N.; Zhang, X.; Wang, Y.; Yu, W.; Chan, H. L. W. Microfluidic Reactors for Photocatalytic Water Purification. *Lab Chip* **2014**, *14* (6), 1074–1082. https://doi.org/10.1039/C3LC51233A.

(98) Lei, L.; Wang, N.; Zhang, X. M.; Tai, Q.; Tsai, D. P.; Chan, H. L. W. Optofluidic Planar Reactors for Photocatalytic Water Treatment Using Solar Energy. *Biomicrofluidics* **2010**, *4* (4), 043004. https://doi.org/10.1063/1.3491471.

(99) Zhao, P.; Qin, N.; Wen, J. Z.; Ren, C. L. Photocatalytic Performances of ZnO Nanoparticle Film and Vertically Aligned Nanorods in Chamber-Based Microfluidic Reactors: Reaction Kinetics and Flow Effects. *Appl. Catal. B Environ.* **2017**, *209*, 468–475. https://doi.org/10.1016/j.apcatb.2017.03.020.

(100) Liao, W.; Wang, N.; Wang, T.; Xu, J.; Han, X.; Liu, Z.; Zhang, X.; Yu, W. Biomimetic Microchannels of Planar Reactors for Optimized Photocatalytic Efficiency of Water Purification. *Biomicrofluidics* **2016**, *10* (1), 014123. https://doi.org/10.1063/1.4942947.

(101) Cheng, X.; Chen, R.; Zhu, X.; Liao, Q.; An, L.; Ye, D.; He, X.; Li, S.; Li, L. An Optofluidic Planar Microreactor for Photocatalytic Reduction of CO2 in Alkaline Environment. *Energy* **2017**, *120*, 276–282. https://doi.org/10.1016/j.energy.2016.11.081.

(102) Li, L.; Chen, R.; Liao, Q.; Zhu, X.; Wang, G. High Surface Area Optofluidic Microreactor for Redox Mediated Photocatalytic Water Splitting. *Int. J. Hydrogen Energy* **2014**, *39*, 19270–19276. https://doi.org/10.1016/j.ijhydene.2014.05.098.

(103) Ahsan, S. S.; Gumus, A.; Erickson, D. Redox Mediated Photocatalytic Water-Splitting in Optofluidic Microreactors. *Lab Chip* **2013**, *13*, 409–414. https://doi.org/10.1039/c2lc41129f.

(104) Chen, R.; Li, L.; Zhu, X.; Wang, H.; Liao, Q.; Zhang, M. X. Highly-Durable Optofluidic Microreactor for Photocatalytic Water Splitting. *Energy* **2015**, *83*, 797–804. https://doi.org/10.1016/j.energy.2015.02.097.

(105) Merino-Garcia, I.; García, G.; Hernández, I.; Albo, J. An Optofluidic Planar Microreactor with Photoactive Cu2O/Mo2C/TiO2 Heterostructures for Enhanced Visible Light-Driven CO2 Conversion to Methanol. *J. CO2 Util.* **2023**, *67*, 102340. https://doi.org/10.1016/j.jcou.2022.102340.

(106) Martin, M. V; Rossi, L.; Rosso, J. A.; Villabrille, P. I.; Alfano, O. M.; Satuf, M. L. Palladium-Modified TiO2 Films in a Photocatalytic Microreactor: Evaluation of Radiation Absorption Properties and Pollutant Degradation Efficiency. *Photochem. Photobiol. Sci.* **2023**, *22* (1), 47–58. https://doi.org/10.1007/s43630-022-00296-y.

(107) Duan, J.; Fang, X.; Li, C.; Qu, J.; Guo, L.; Zou, Y.; Xiang, M.; Wang, W. Efficient and Stable Monolithic Microreactor with Ag/AgCl Photocatalysts Coated on Polydopamine Modified Melamine Sponge for Photocatalytic Water Purification. *Colloids Surfaces A Physicochem. Eng. Asp.* **2023**, *659*, 130759. https://doi.org/10.1016/j.colsurfa.2022.130759.

(108) Rabanimehr, F.; Farhadian, M.; Nazar, A. R. S. A High-Performance Microreactor Integrated with Chitosan/ Bi2WO6/CNT/TiO2 Nanofibers for Adsorptive/Photocatalytic Removal of Cephalexin from Aqueous Solution. *Int. J. Biol. Macromol.* **2022**, *208*, 260–274. https://doi.org/https://doi.org/10.1016/j.ijbiomac.2022.03.108.

(109) Kim, H.; Kwon, H.; Song, R.; Shin, S.; Ham, S.-Y.; Park, H.-D.; Lee, J.; Fischer, P.; Bodenschatz, E. Hierarchical Optofluidic Microreactor for Water Purification Using an Array of TiO2 Nanostructures. *npj Clean Water* **2022**, *5* (1), 62.

https://doi.org/10.1038/s41545-022-00204-y.

Chapter 2

Materials and Methodology

2.1 Materials and reagents

All the materials were used as obtained without any further purification. The materials used in this research work are summarized in Table 2.1. The distilled water used in all the experiments was obtained from the Millipore unit (Model: Elix 3, Make: Millipore, USA), present in the analytical lab of the Department of Chemical Engineering, IIT Guwahati.

Table 2.1: List of chemicals/reagents and materials used for the photocatalysts synthesis and testing

S. No	Reagents/Chemicals/Materials	code	Purity (%)	Make & Origin	Role
1	Titanium (IV) isopropoxide	TTIP	95	Alfa Aesar, England	TiO_2 precursor
2	glacial Acetic Acid	AA	99	Himedia, India	Acid catalyst
3	Acetyl acetone	AcAc	-	Merck, India	Stabilizing agent
4	absolute Ethanol AR	-	99.9	Merck, India	Solvent
5	Cetyltrimethylammonium Bromide	CTAB	-	Himedia, India	Surfactant
6	Hydrofluoric acid	HF	40; 48	Himedia, India	Glass etching
7	Methylene blue	MB	-	Loba chemie, India	For TiO_2 film activity
8	Potassium tetrachloroplatinate	K_2PtCl_4	99.9	Sigma Aldrich, US	Platinum precursor
9	Sodium citrate	-	-	HiMedia, India	Ligand
10	Sodium hexachloroiridate (IV) hexahydrate	$Na_2IrCl_6.6H_2O$	99.9	Sigma Aldrich, US	Iridium precursor
11	Hydrogen peroxide	H_2O_2	50	Himedia, India	Chemical oxidizer

12	Sodium Iodate	$NaIO_3$	-	Himedia, India	Electron acceptor
13	Methanol	CH_3OH	-	Himedia, India	Hole scavenger
14	microscope glass slides: 76 mm × 25 mm × 1 mm; 76 mm × 52 mm × 1 mm	MGS	-	Microlife; TedPella	Microreactor fabrication
15	UV curable glue	-	-	NOA 81, Edmund Optics, India	bonding
16	self-adhesive tape	-	-	Rayan plast, India	Glass mask
17	PTFE tube: 1/16" O.D. × 1/32" I.D.	-	-	Merck, India	Reactor inlet/outlet
18	Titanium dioxide, anatase	-	99.7	Sigma Aldrich, England	Catalyst support
19	100 mL borosilicate glass volumetric flask	-	-	JSGW, India	Batch reactor
20	Rubber Suba Seal Stopper, OD 15 mm	-	-	JSGW, India	To use with volumetric flask
21	Silicon grease	-	-	HiMedia, India	To use on rubber stopper

2.2 Methodology

2.2.1 Photocatalysts synthesis and coating (TiO_2, Pt/TiO_2, IrO_2/TiO_2 and $IrO_2/Pt/TiO_2$)

2.2.1.1 TiO_2 sol-gel preparation

First, TiO_2 sol was prepared by taking ethanol in a glass beaker and AA, AcAc, TTIP and finally CTAB were added slowly and sequentially, under vigorous stirring. This sequential addition helped in achieving clear TiO_2 sol without any precipitation. Then, the prepared sol was kept under stirring at 600 rpm for 20 h. Finally, a clear transparent yellowish TiO_2 sol-gel was obtained after ageing for 24 h. The total weight of the solution, in all the experiments, was maintained constant (4 g). The amounts of each reagent used in sol-gel preparation are presented in Table 2.2.

Table 2.2: The composition of sol-gel

S. No.	Nominal Composition				Sample name
	TTIP, M (g)	AcAc, M (g)	AA, M (g)	CTAB, g/0.01mole TTIP (g)	
1	0.2 (0.28)	0.1 (0.05)	0.09 (0.03)	1.0 (0.1)	$Ti_{0.2}AcAc_{0.1}AA_{0.09}CTAB_1$
2	0.2 (0.28)	0.1 (0.05)	0	1.0 (0.1)	$Ti_{0.2}AcAc_{0.1}CTAB_1$
3	0.2 (0.28)	0	0.09 (0.03)	1.0 (0.1)	$Ti_{0.2}AA_{0.09}CTAB_1$
4	0.2 (0.28)	0.1 (0.05)	0.09 (0.03)	0	$Ti_{0.2}AcAc_{0.1}AA_{0.09}$
5	0.1 (0.14)	0.1 (0.05)	0.09 (0.03)	1.0 (0.05)	$Ti_{0.1}AcAc_{0.1}AA_{0.09}CTAB_1$
6	0.4 (0.57)	0.1 (0.05)	0.09 (0.03)	1.0 (0.2)	$Ti_{0.4}AcAc_{0.1}AA_{0.09}CTAB_1$
7	0.2 (0.28)	0.1 (0.05)	0.09 (0.03)	0.6 (0.06)	$Ti_{0.2}AcAc_{0.1}AA_{0.09}CTAB_{0.6}$
8	0.2 (0.28)	0.1 (0.05)	0.09 (0.03)	0.8 (0.08)	$Ti_{0.2}AcAc_{0.1}AA_{0.09}CTAB_{0.8}$
9	0.2 (0.28)	0.1 (0.05)	0.09 (0.03)	1.2 (0.12)	$Ti_{0.2}AcAc_{0.1}AA_{0.09}CTAB_{1.2}$
10	0.2 (0.28)	0.1 (0.05)	0.09 (0.03)	1.4 (0.14)	$Ti_{0.2}AcAc_{0.1}AA_{0.09}CTAB_{1.4}$

2.2.1.2 TiO_2 thin film preparation

Borosilicate microscopic glass slides were used as substrates to coat TiO_2 films. Glass slides were cleaned by sonication in acetone and in DI water for 30 min each. After sonication, glass slides were kept for drying in a hot air oven at 110°C for 15 min. A few drops of the precursor solution was deposited on to the clean glass substrates and spin coated by rotating it on a spin coater (Model: SpinNXG-P1, Make: Apex Instruments, India) at 1000 rpm for 15 s. Coated films were first dried at room temperature then at 110°C for 60 min and finally calcined in a muffle furnace at 500°C for 2 h with temperature ramp rate of 2°C/min. This heat treatment allowed the films to firmly adhere on the glass substrates. The effect of presence and change in concentrations of AA, AcAc, TTIP and CTAB on the surface morphology and topography of the formed thin films was studied.

The above spin coating procedure was repeated to make 2, 3, and 4 coatings and thereby to increase the thickness of the films. Amount of TiO_2 deposited after three (3x) and four (4x) coatings on the glass slides was determined by measuring the weights of glass slides before and after coatings. Weights were found to be 0.4 mg and 0.5 mg for 3x and 4x coatings of TiO_2.

The thickness of the 3x and 4x films were found to be 110.7 nm and 145.3 nm, calculated using the relation $t = m/(d \times A)$[1], where m is mass of the film deposited on glass in grams, A is surface area of the film in cm^2, and d is the density of the deposited material (density of anatase TiO_2 = 3.9 g/cm^3). The 3x- and 4x- TiO_2 films were tested for methylene blue degradation activity. The multicoated (up to 24x) TiO_2 films were prepared using optimum sol-gel composition at which uniform and adherent coatings were obtained.

2.2.1.3 Synthesis of IrO_2 nanoparticle (NP) hydrosol

Synthesis of IrO_2 NPs hydrosol was employed from the literature.[2] 84 mg of sodium citrate was dissolved in 30 mL DI water under stirring. Then, 25 mg of sodium hexachloroiridate (IV) hexahydrate was dissolved in the above mixture and was heated at 90 ºC for 4 h under stirring. After 4 h, the solution was cooled down to room temperature and diluted to a final volume of 10 mL. A few drops of H_2O_2 were added dropwise to the above solution under stirring for 1 h. The H_2O_2 concentration was maintained at 2 vol.% in the final solution. The solution was finally aged for at least 24 h to allow the formation of IrO_2 NP hydrosol. The formation of IrO_2 NPs was confirmed by the characteristic blue color appearance and a broad absorption peak at ~ 570 nm, observed from UV-Vis spectroscopy (Fig. A.1 in Appendix A). This peak is because of the transition among t_{2g} and e_g orbital of the Ir^{4+} ion in the octahedral coordinated environment.[3] The IrO_2 NPs hydrosol solution was used for the photodeposition of the IrO_2 NPs onto the TiO_2.

2.2.1.4 Synthesis of Pt/TiO_2 films, IrO_2/TiO_2 films and $IrO_2/Pt/TiO_2$ powders by photodeposition method

Photo-reduction process was used to deposit the platinum and Iridium oxide onto the TiO_2 films and onto commercial TiO_2 powder. A required amount of K_2PtCl_4 aqueous solution, corresponding to 1 wt.% Pt (with respect to the weight of TiO_2 film) was spread on to the TiO_2 films, coated on 76 mm * 25 mm glass substrates. Similarly, a required amount of IrO_2 hydrosol (5 wt.% IrO_2 with respect to the TiO_2 film weight) was spread onto the TiO_2 films, coated on 76 mm * 52 mm glass substrates. After drying in air for 1 h, the TiO_2 film immersed in the 100 mL DI water was illuminated with UV light (365 nm) for 2 h for the photo-reduction process.[4,5] Finally, the Pt/TiO_2 and IrO_2/TiO_2 films were dried in oven at 80 °C and 60 °C, respectively, for 1 h and then used for reactors fabrication. The Pt and IrO_2 was photo-deposited on the spin coated TiO_2 films with varying number of coatings, and named them as Pt/TiO_2-nx and IrO_2/TiO_2-nx, where n indicates number of coatings. The weight and average thickness of the TiO_2 films are presented in Table 2.3.

Table 2.3: Weight and Thickness of the TiO_2 thin films

S. No.	Number of Coatings, n	Sample name	Weight, mg	Avg. Thickness, nm
1	2	Pt/TiO_2-2x	0.65	640 ± 50
2	4	Pt/TiO_2-4x	1.17	1150 ± 106
3	6	Pt/TiO_2-6x	1.76	1380 ± 321
4	8	Pt/TiO_2-8x	2.15	1650 ± 119
5	6	IrO_2/TiO_2-6x	1 ± 0.04	728 ± 20
6	12	IrO_2/TiO_2-12x	2 ± 0.12	1958 ± 92
7	18	IrO_2/TiO_2-18x	3 ± 0.2	2269 ± 146
8	24	IrO_2/TiO_2-24x	4 ± 0.5	3078 ± 362

The average thickness of the films was obtained from the field emission scanning electron microscopy (FESEM) (Fig. A.2 in Appendix A).

For $IrO_2/Pt/TiO_2$ synthesis, Pt and IrO_2 NPs were photodeposited sequentially onto the commercial TiO_2. The anatase phase TiO_2 is chosen because it is a n-type semiconductor with an indirect bandgap transition and has lower recombination rate and longer lifetime of the photocarriers.[6–8] First, TiO_2 powder was dispersed in DI water under stirring at 500 rpm. A desired amount of K_2PtCl_4 precursor was added to the above solution. Then, the solution was irradiated under 365 nm UV light for 2 h. After 2 h, IrO_2 hydrosol was added to the solution and continued photodeposition for another 2 h. After photodeposition, UV light and stirring were stopped and solution was dried at 80°C until dry powder was obtained. Thus, synthesis of $IrO_2/Pt/TiO_2$ photocatalyst was completed. The Pt and IrO_2 loadings were varied from 0.5 to 2.5 wt.% and 0.5 to 5 wt.%, respectively, with respect to the weight of TiO_2 powder.

2.2.2 Characterization of photocatalyst film and powder samples

All the photocatalyst film and powder samples were characterized to determine their physico-chemical and morphological properties. The analysis procedure of each technique was mentioned below.

The crystal structures of the TiO_2 films, Pt/TiO_2 (8x coating), IrO_2/TiO_2 film (24x coating) and $IrO_2/Pt/TiO_2$ powders was identified using X-ray diffractometer ((Model: X'Pert Pro, Make: Phillips, USA) with Cu K_α (λ=0.15418 nm) and (Model: Smartlab; Make: Rigaku, Japan)) using Cu K_α radiation (λ= 0.1578 nm) under an applied voltage of 40 and 45 kV, a

current of 35 and 200 mA, a grazing incidence angle of 1 and 0.5˚, and 0.02º/sec and 6˚/min scan rate in the region of 20-80˚ diffraction angle (2θ). Raman spectra of the TiO_2 films were collected using Raman spectrometer (Model: LabRAM HR evolution, Make: Horiba scientific, India) by mounting the TiO_2 films on a flat stage in a 180º backscattering geometry and irradiated with an Argon ion laser of 532 nm excitation wavelength and in the Raman shift range of 50–700 cm^{-1}. The surface morphology of the TiO_2 films was observed by the field emission scanning electron microscopy (FESEM) (Model: JSM-7610F, Make: Jeol, USA) at a voltage of 15 kV. Before FESEM analysis, the samples were coated with platinum using Auto fine coater (Model: JEC-3000FC, Make: Jeol, USA) to avoid the sample charging. The average particle size and porosity of the TiO_2 films were estimated using ImageJ 1.51j8 software from FESEM images.[9,10] The porosity corresponds to the void space formed after calcination of the TiO_2 films. FESEM (Model: Sigma; Make: Zeiss, Germany) was used to obtain the surface morphology of the Pt/TiO_2 (8x coating), IrO_2/TiO_2 film (24x coating) and IrO_2/Pt/TiO_2 powders photocatalysts. The TiO_2 film roughness was examined by atomic force microscopy (AFM) (Model: Innova, Make: Bruker, India) and was estimated using Nanoscope analysis 1.5 software from AFM images. The UV-Vis absorbance of the photocatalysts was obtained using UV-Vis spectrophotometer (Model: UV-2600; Make: Shimadzu, Japan) in the wavelength range of 200-700 nm using $BaSO_4$ as reference standard. Photoluminescence (PL) emission spectra of the photocatalysts was recorded on the fluorescence spectrophotometer (Model: Fluoromax-4; Make: Horiba Jobin Yvon, Japan) under 325 nm excitation wavelength. The average particles size and actual concentration of Pt and IrO_2 deposited on TiO_2 support was determined from FETEM and EDX. FETEM (Model: JEM-2100F; Make: JEOL, Japan) analysis was conducted at an accelerating voltage of 200 kV to determine the particle size and the morphology of the samples. The composition and elemental mapping of the sample was analyzed by the EDX analyzer connected to FESEM (Model: Sigma; Make: Zeiss, Germany). The X-ray photoelectron spectroscopy (XPS) with monochromatic X-ray source ((Model: ESCALAB; Make: ThermoFisher Scientific Co., U.K.) and (Model: PHI 5000 Versa Probe III; Make: M/s Physical electronics, USA)) was used to determine the chemical states present in the photocatalysts. The XPSPEAK 4.1 software was used to perform the peak fitting of the XPS spectra. Spectral output of MH lamp was recorded on the fluorescence spectrophotometer (Model: Fluoromax-4; Make: Horiba Jobin Yvon, Japan). The illuminated MH lamp was set as reference lamp while the other lamps were kept off and emission from the lamp was recorded by the spectrophotometer.

List of instruments used in this thesis with their specifications and availability are presented in Table 2.4.

Table 2.4: List of instruments used in this thesis with their specifications and availability

S. No	Instrument Name	Make, model and origin	Specifications	Pre-treatment conditions	Availability
1	X-ray powder diffraction (XRD)	Smartlab,Rigaku, Japan	CuKα source; scan speed – 6°/min	Dried at 110°C	Center for Instruments facility (CIF), IITG
2	Raman Spectroscopy	CPX100, Labram HR Evolution, HORIBA, Japan	Argon ion laser of 532 nm excitation wavelength	Dried at 110°C	Centre for Nano technology (CNT), IITG
3	Field Emission Scanning Electron Microscope (FESEM)	JSM-7610F, JEOL, Japan	15KW Current and 7V probe voltage	-	CNT, IITG
4	Auto fine coater	JEC-3000FC, Jeol, USA	-	Dried at 110°C	CNT, IITG
5	Atomic force microscopy	Innova, Bruker, India	-	Dried at 110°C	CNT, IITG
6	UV-Vis spectrophotometry	UV-2600, Shimadzu, Japan	-	Dried at 110°C	Analytical lab, Chemical Engg. Dept., IITG
7	Fluorescence spectrophotometry	Fluoromax-4, Horiba Jobin Yvon, Japan	325 nm excitation wavelength	Dried at 110°C	Physics Dept., IITG
8	Field Emission Transmission Electron	JEM-2100F, JEOL, Japan	voltage of 200 kV	Sonicated with ethanol and drop casted	CIF, IITG

	Microscope (FETEM)			over the copper grid	
9	EDX analyzer connected to FESEM	Sigma 300, Zeiss, Germany	-	-	CIF, IITG
10	X-ray powder diffraction (XRD)	X'Pert Pro, Phillips, USA	CuKα source; scan speed – 0.02°/sec	Dried at 110°C	SAIF, Guwahati University
11	X-Ray Photoelectro Spectroscopy (XPS)	ESCALAB Xi+, Thermoscientific, UK	$\sim 3 \times 10^{-9}$ mbar, 20 eV, and 55°	-	CSIR-NEIST, Jorhat
12	X-Ray Photoelectro Spectroscopy (XPS)	PHI 5000 Versa Probe III, M/s Physical electronics, USA	Monochromated k-Apha X-ray source (1486.7 eV)	-	CIF, IITG

2.2.3 Experimental procedures of photocatalyst testing

2.2.3.1 Fabrication of optofluidic planar microreactors (OFPMRs)

Figure 2.1 shows the steps involved in the fabrication of the OFPMR used to perform HER.The planar rectangular reaction chamber, along with the inlet and outlet manifolds, (Fig. 2.1b) on the glass slide was formed by HF wet etching process. The clean glass slide was covered with self-adhesive tape, resistant to HF, on both sides. Usage of tape as mask for the acid etching was as reported earlier.[11] Then, the area to be etched on the glass slide was marked on one side of the tape and removed the tape in that area using a sharp surgical knife. The glass slide was dipped completely in the plastic beaker containing 50 ml of 40% HF and DI water in the 1:1 volume ratio, and left it for etching for 1 h. After 1 h, the etched glass slide was taken out and cleaned under running tape water. A clear transparent reaction chamber was obtained after etching such that light can pass through easily. The surface area of the reaction chamber of the cover plate (Fig. 2.1b) was same as that of the catalyst coated surface of the reaction plate (Fig. 2.1a). The area of the catalyst coated region was 7.5 cm^2. The PTFE tube was joined at the inlet and the outlet of the cover plate (Fig. 2.1c) using UV curable glue. Glass strips with holes were used to provide additional support and strength to inlet/outlet tubing (Fig. 2.1c and

2.1d). Finally, the optofluidic planar microreactor (Fig. 2.1d) was fabricated by bonding the cover plate and the catalyst plate together using UV curable glue, cured by 365 nm UV lamp in 5-10 min. The volume of the reaction chamber in the microreactor was 75 µL. Fig. 2.1(b)-(d) represent the fabrication process described above, once Pt/TiO_2 film coated on glass slide (Fig. 2.1a).

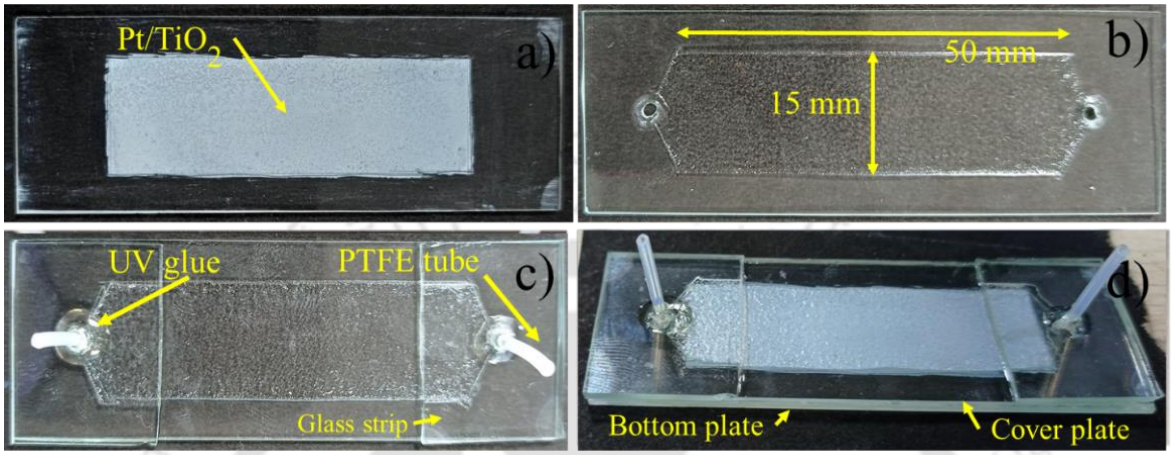

Figure 2.1: a) Bottom plate with catalyst coating; b) Planar chamber with inlet and outlet holes; c) Cover plate with inlet and outlet tubes; d) Fabricated planar microreactor with bottom and cover plate

Figure 2.2 shows the steps involved in the fabrication of the OFPMR used to perform OER. A bottom plate consisting of catalyst thin film is shown in Fig. 2.2a. A middle plate (spacer) with a hollow rectangular reaction chamber (Fig. 2.2b) was fabricated using wet chemical etching method with an adhesive tape as a mask. Initially, the adhesive tape was applied to cover the entire glass substrate and then the unwanted portion of the tape were removed using a sharp surgical knife. Finally, the glass substrate was completely dipped in 48% HF solution for 2 h. The cover plate (Fig. 2.2c) was also obtained using the wet chemical etching method as described above. Finally, the cover, middle, and bottom plates were bonded together using 365 nm UV curable glue. The fabricated OFPMR is shown in Fig. 2.2d. The catalyst coated region has an area of 8.75 cm^2, and the microreactor has a reaction volume of 875 µL. The inlet and outlet of the fabricated planar microreactors (Fig.s 2.1d and 2.2d) were connected to a syringe pump and a liquid collecting reservoir through PTFE tubing, respectively (Fig.s 2.4 and 2.5).

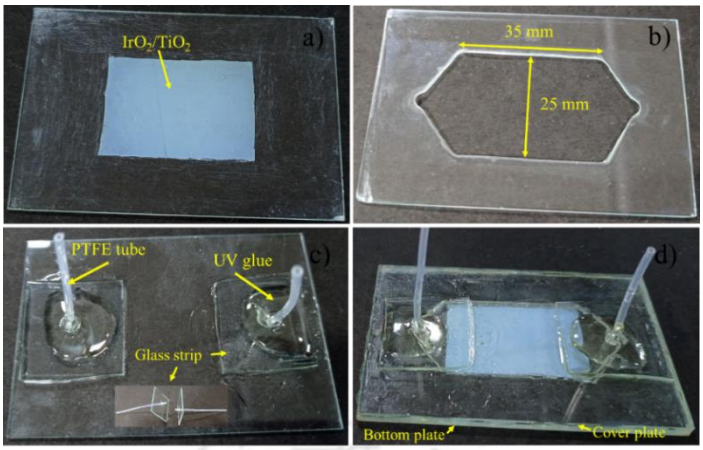

Figure 2.2: (a) Bottom plate, (b) middle plate, (c) Cover plate, (d) Fabricated planar microreactor

2.2.3.2 Photocatalytic activity of TiO_2 thin films by Methylene blue degradation

The photocatalytic activity of TiO_2 thin films was studied by investigating the photo-degradation of MB in aqueous solution under UV light illumination. A standard MB solution with concentration of ~1 ppm was used as model dye pollutant to determine the photocatalytic efficiency of TiO_2 films. A beaker containing 50 ml of prepared MB solution was placed on a magnetic stirrer inside a dark chamber equipped with 365 nm UV-A type lamp. The photocatalyst-coated glass substrate was immersed in the MB solution. The mixture was stirred for 60 min in the absence of light to ensure the equilibrium of MB adsorption-desorption on the TiO_2 films. Photocatalysis experiment was started by illuminating the UV light, vertically hung over the top of the stirrer at a distance of 5 cm above the solution. The UV radiation reaches the film surface through the dye solution thereby causing the photocatalytic oxidation on the film surface. The pollutant concentration was analyzed at every 15 min till the completion of the experiment using UV-Vis spectroscopy (Model: UV-2600, Make: Shimadzu, Singapore), at a wavelength of 664 nm with DI water as reference. For comparison, experiments with aqueous MB solution under UV light (photolysis), and with uncoated glass substrate are also performed. The schematic diagram of the experimental setup for MB degradation over TiO_2 thin films is shown in Figure 2.3.

The percentage degradation of MB is calculated by using the formula:

$$\% \text{ Degradation} = \frac{(A_0 - A_t)}{A_0} X\ 100 = \frac{(C_0 - C_t)}{C_0} X\ 100 \text{..... (2.1)}$$

where A_0 and A_t were the absorbance and C_0 and C_t were the concentrations of the initial and at time t MB, respectively.[12,13]

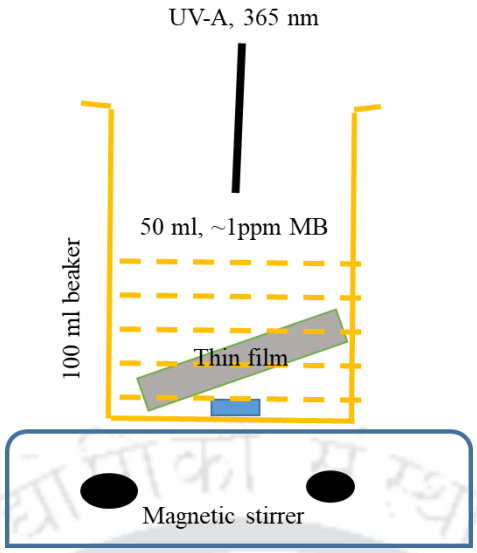

Figure 2.3: Schematic diagram of the experimental setup for photodegradation of Methylene blue

All experiments were performed at room temperature and atmospheric pressure inside dark chamber. The MB was selected as model compound to assess the photocatalytic activity of thin films because it is suggested as standard (10678:2010) by international organization for standardization (ISO), namely, "Determination of photocatalytic activity of surfaces in the aqueous medium by degradation of methylene blue".[14]

2.2.3.3 Photocatalytic activity testing for hydrogen and oxygen production using OFPMRs

The photocatalytic activity of Pt/TiO_2 thin films was tested for water splitting using methanol as electron donor (sacrificial agent, SR) to produce hydrogen in the OFPMR (Fig. 2.1d) and the photocatalytic activity of IrO_2/TiO_2 thin films was investigated using $NaIO_3$ as electron acceptor[15] (sacrificial agent, SR) to produce oxygen in the OFPMR (Fig. 2.2d). The reactant solution containing 20 vol.% methanol in DI water was pumped using a syringe pump through the inlet of the planar microreactor (Fig. 2.1d) (Model: PHD Ultra; Make: Harvard Apparatus, USA). While the reactant solution containing 10 mM $NaIO_3$ in DI water was passed through the inlet of the planar microreactor (Fig. 2.2d). The flow rate of the reactant solutions was varied between 0.1 to 0.5 mL/min (The corresponding residence time varies from 45 to 9 s). It is recommended to employ the optimal flow rate range for microreactors because the product gas rate might be negligible due to large mass transfer resistance at very low flow rates. At very high flow rates, the shorter residence time can limit the reaction efficiency. Additionally, uniform flow distribution may not occur at too low flow rates, resulting in the insufficient use of catalyst. Moreover, pumping costs might become excessively high, and

pressure inside the microreactor could lead to leakage at very high flow rates. Based on the above arguments and literature reports, the flowrates employed in our work are chosen.[16]

A 400 W metal halide (MH) lamp (Specifications: Daylight, 5000K, 38000 lm; Model: MH BT; Make: Halonix Technologies Pvt. Ltd., India) with inbuilt UV blocking was used as visible light source. The MH lamp emission spectrum is given in Fig. A.3 in Appendix A. The solar spectrum consists mainly of 44.7% visible radiation (380–780 nm), 6.6% UV radiation (<380nm) and 48.7% IR radiation (>780nm).[17] The MH lamp used in this study emits 96.8% visible and 3.2% IR and no UV radiation. The MH lamp was positioned at a fixed distance of 10 cm vertically above the planar microreactor, so the MH light intensity at the microreactor surface was maintained constant in all experiments. The MH intensity at the surface of the microreactor was calculated and obtained ~318.5 mW cm^{-2} (See MH intensity calculation in Appendix A).

In addition, some tests were also carried out using solar simulator (Model: SLB300A; Make: Sciencetech, Canada) consisting of 300 W Xenon lamp with spectral range of 350–2000 nm with AM 1.5G filter (which simulates the global radiation that reaches the earth's ground) to calculate solar to hydrogen conversion efficiency (STH). The STH is a practical standard to measure the performance of photocatalyst under simulated sun light (SSL).[18] The SSL intensities were measured at various points along the catalyst coating area using a handheld optical power meter (Model: UNO; Make: Gentec-eo, Canada). The water-splitting tests were conducted at two different (99.7 and 341.3 mW cm^{-2}) SSL average intensities. The average intensity 99.7 mW cm^{-2} was obtained at the power output of 63% and at distance of 15 cm between lamp and the microreactor surface. Similarly, the average intensity of 341.3 mWcm^{-2} was obtained at the power output of 103% and at distance of 10 cm.

The incident light falls on the catalyst film inside the reaction chamber of planar microreactor through the cover glass and liquid reactant. The outlet of the reactor was connected to a collector flask through a rubber septum, where the outlet stream was collected. Before each experiment, the optofluidic planar microreactor and collector were made leak-proof and degassed with nitrogen at a flow rate of 25 ml min^{-1} for 30 min to evacuate air.

In case of oxygen production experiments, the reactant solution was also purged (degassed) under nitrogen flow to eliminate dissolved oxygen in order to maintain the reactor system under anaerobic conditions before starting the experiment.[19,20] The oxygen detected at the start of the lamp (zero time) was taken as base oxygen concentration (This was the residual

oxygen from the N_2 cylinder used for purging). Considering the residual oxygen as a baseline at zero time was found to be an effective method for the measurement of molecular oxygen produced during experiments.[21] In order to calculate the volume percentage of the oxygen generated during the reaction, the oxygen calibration was performed to determine the oxygen response factor [22] and given in Fig. A.4 in Appendix A.

The gas collected in the collector was analyzed using a gas chromatograph (GC, Model: 7820A; Make: Agilent, The USA) at every 60 min for 5 h using a gas tight syringe (Model: 1001; Make: Hamilton, Switzerland). The GC was equipped with a thermal conductivity detector and CP-molecular sieves column for the separation of hydrogen, oxygen and nitrogen.[23] The reactor temperature during the photocatalytic activity test experiments was monitored using a K-type thermocouple. All experiments were conducted inside a dark enclosure (black box) at atmospheric pressure.

The schematic diagram of the experimental setup and testrig is shown in Figure 2.4.

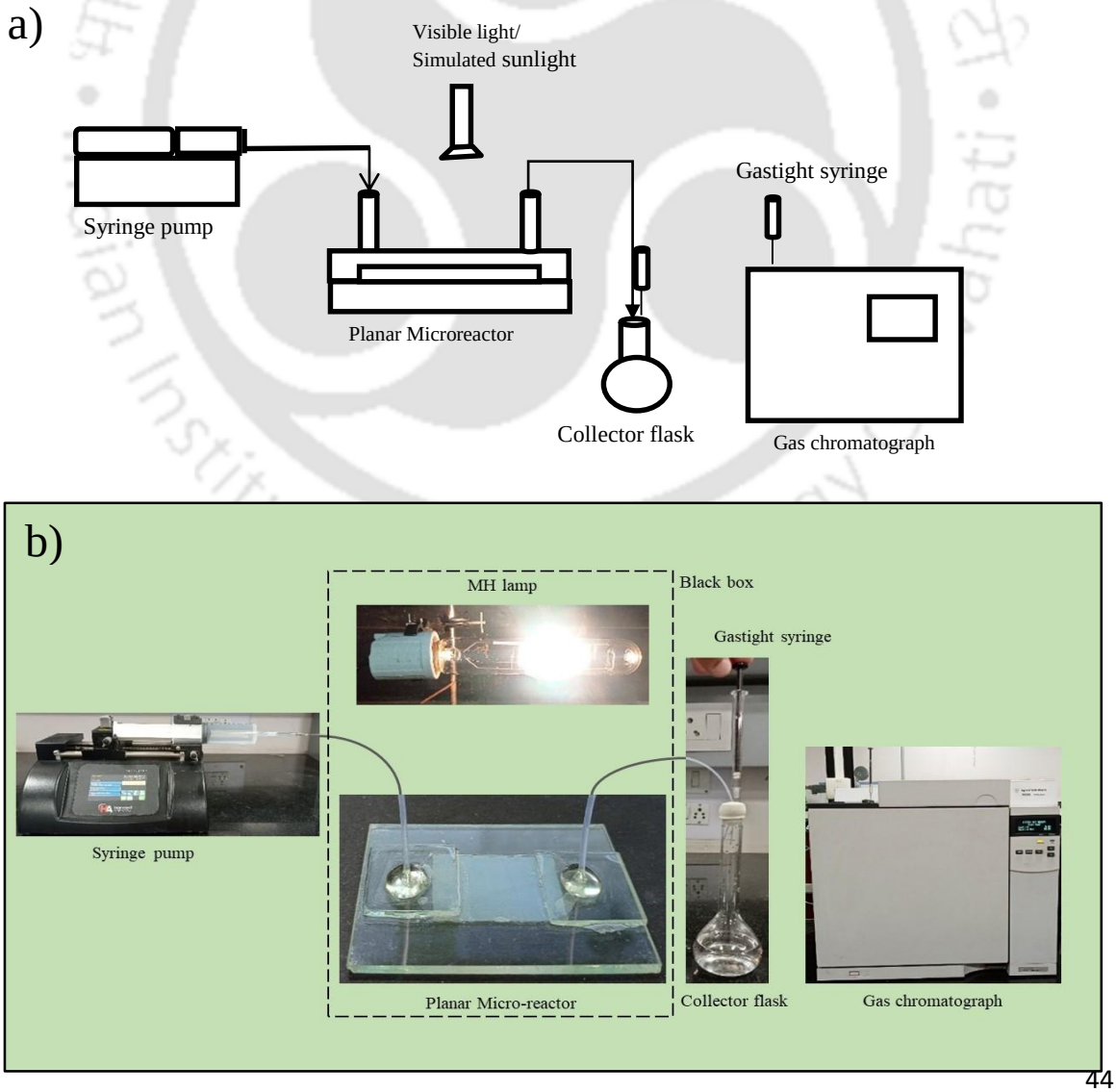

Figure 2.4: a) Schematic diagram of the experimental setup; and b) Experimental test rig for photocatalytic water splitting reactions in an optofluidic planar microreactors

2.2.3.4 Photocatalytic overall water splitting (POWS) experimentation

The activity of $IrO_2/Pt/TiO_2$ photocatalysts was tested for the POWS to produce hydrogen (H_2) and oxygen (O_2) from pure water. A flat bottom flask with total volume of 110 mL was served as a batch reactor. 100 mL DI water as reactant solution was taken in above flask (sacrificial agents were not added in DI water). A desired amount of photocatalyst powder (catalyst loading was varied) was dispersed in DI water and flask was closed with rubber stopper, thus making it a closed reactor system. The above solution was kept under continuous stirring (stirring speed was varied). Then, the air inside the reactor was replaced with inert nitrogen by flowing nitrogen gas at 25 mL min^{-1} for 30 min. The activity test was performed by starting the 400 W metal halide (MH) lamp, which was kept adjacent to the reactor at a distance of ~10 cm, generating an intensity of 99.3 mW cm^{-2}. The MH lamp (with inbuilt UV blocking) has no emission in UV region and mostly emits visible light with a small fraction of IR light emission.[24]

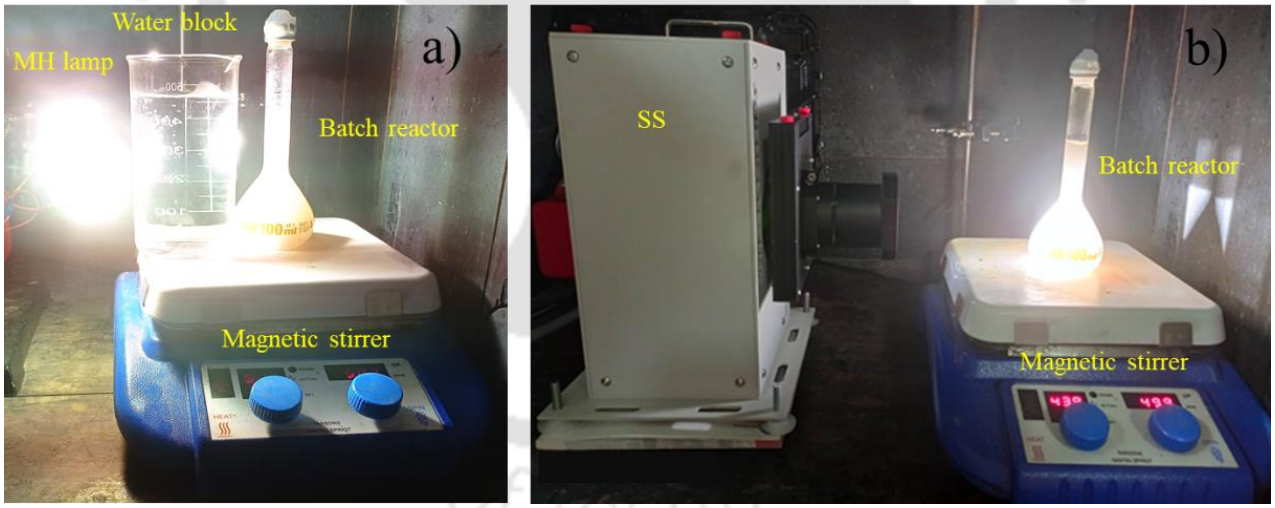

Figure 2.5: Experimental test rig for POWS reactions: a) under MH lamp; b) under solar simulator (SS)

The product gas generated was collected from the reactor head space at every 60 min in a gas tight syringe and analyzed using gas chromatography (GC). Collection and injection of reaction gas mixture using a gas tight syringe avoids the contamination of the sample with the atmospheric air. The temperature of the reactor was stabilized at ~ 60ºC within 10 min of the start of the MH lamp during the reactions. All the experiments were conducted at atmospheric

pressure inside the black box. Additionally, activity tests were also conducted using a solar simulator (SS) at the intensities of 101.4 (obtained at a distance of 15 cm and power output of 63%) and 336.1 mW cm^{-2} (at a distance of 10 cm and power output of 103%) away from the reactor, respectively, in order to estimate the solar to hydrogen conversion efficiency (STH) for the POWS. The schematic of the experimental test rig is shown in Figure 2.5. The chromatograms are shown in Fig. A.5 in Appendix A. The nitrogen peak areas from zero to five-hour injection into GC remained similar indicating that air leaks into the system did not occur.

Precaution during experiment: Nitrogen gas was bubbled through the bottom of the reactor suspension by connecting inlet and outlet tubes via rubber septum. After purging for 30 min, the tubing was removed and applied silicon grease on top of rubber septa holes. Then, the reaction was started by switching on the light source. The gas from the reactor headspace was collected into gas tight syringe by dipping the needle through the septa hole into the headspace. The silicon grease was removed and applied while collecting gas into syringe.

References

(1) Komaraiah, D.; Madhukar, P.; Vijayakumar, Y.; Ramana Reddy, M. V.; Sayanna, R. Photocatalytic Degradation Study of Methylene Blue by Brookite TiO2thin Film under Visible Light Irradiation. *Mater. Today Proc.* **2016**, *3* (10), 3770–3778. https://doi.org/10.1016/j.matpr.2016.11.026.

(2) Nam, Y. S.; Magyar, A. P.; Lee, D.; Kim, J. W.; Yun, D. S.; Park, H.; Pollom, T. S.; Weitz, D. A.; Belcher, A. M. Biologically Templated Photocatalytic Nanostructures for Sustained Light-Driven Water Oxidation. *Nat. Nanotechnol.* **2010**, *5* (5), 340–344. https://doi.org/10.1038/nnano.2010.57.

(3) Frame, F. A.; Townsend, T. K.; Chamousis, R. L.; Sabio, E. M.; Dittrich, T.; Browning, N. D.; Osterloh, F. E. Photocatalytic Water Oxidation with Nonsensitized IrO2 Nanocrystals under Visible and UV Light. *J. Am. Chem. Soc.* **2011**, *133* (19), 7264–7267. https://doi.org/10.1021/ja200144w.

(4) Zhu, D.; Long, L.; Sun, J.; Wan, H.; Zheng, S. Highly Active and Selective Catalytic Hydrogenation of P-Chloronitrobenzene to p-Chloroaniline on Pt@Cu/TiO2. *Appl. Surf. Sci.* **2020**, *504*, 144329. https://doi.org/10.1016/j.apsusc.2019.144329.

(5) Kim, S. C.; Heo, M. C.; Hahn, S. H.; Lee, C. W.; Joo, J. H.; Kim, J. S.; Yoo, I. K.; Kim, E. J. Optical and Photocatalytic Properties of Pt-Photodeposited Sol-Gel TiO2 Thin Films. *Mater. Lett.* **2005**, *59* (16), 2059–2063. https://doi.org/10.1016/j.matlet.2005.02.016.

(6) Hayes, O. R.; Awad Ibrahim, A.; Samra, S. E.; El-Hakam, S. A.; Ahmed, A. I. CuO Decorated Graphene TiO2 Derived MIL-125 Nanocomposite with Enhanced Photo-Response as a Highly Efficient Indirect Sunlight Driven Photocatalyst. *J. Photochem. Photobiol. A Chem.* **2023**, 114800. https://doi.org/10.1016/j.jphotochem.2023.114800.

(7) Zhang, D.; Dong, S. Challenges in Band Alignment between Semiconducting Materials: A Case of Rutile and Anatase TiO2. *Prog. Nat. Sci. Mater. Int.* **2019**, *29* (3), 277–284. https://doi.org/10.1016/j.pnsc.2019.03.012.

(8) Pala, L. P. R.; Uday, V.; Gogoi, D.; Peela, N. R. Surface and Photocatalytic Properties of TiO2thin Films Prepared by Non-Aqueous Surfactant Assisted Sol-Gel Method. *J. Environ. Chem. Eng.* **2020**, *8* (5), 104267. https://doi.org/10.1016/j.jece.2020.104267.

(9) Anderson, A.-L.; Binions, R. The Effect of Tween® Surfactants in Sol-Gel Processing for the Production of TiO2 Thin Films. *Coatings* **2014**, *4* (4), 796–809. https://doi.org/10.3390/coatings4040796.

(10) Eliceiri, K.; Schneider, C. A.; Rasband, W. S.; Eliceiri, K. W. NIH Image to ImageJ : 25 Years of Image Analysis HISTORICAL Commentary NIH Image to ImageJ : 25 Years of Image Analysis. *Nat. Methods* **2012**, *9* (7), 671–675. https://doi.org/10.1038/nmeth.2089.

(11) Beard, P. *Resist and Masking Techniques*, illustrate.; Ceramics Handbooks; University of Pennsylvania Press, Incorporated, 1996.

(12) Wang, C.; Yao, J. Decolorization of Methylene Blue with TiO2 Sol via UV Irradiation Photocatalytic Degradation. *Int. J. Photoenergy* **2010**, *2010*. https://doi.org/10.1155/2010/643182.

(13) Siwińska-Stefańska, K.; Zdarta, J.; Paukszta, D.; Jesionowski, T. The Influence of Addition of a Catalyst and Chelating Agent on the Properties of Titanium Dioxide Synthesized via the Sol–Gel Method. *J. Sol-Gel Sci. Technol.* **2015**, *75* (2), 264–278. https://doi.org/10.1007/s10971-015-3696-2.

(14) Díaz-Uribe, C.; Viloria, J.; Cervantes, L.; Vallejo, W.; Navarro, K.; Romero, E.; Quiñones, C. Photocatalytic Activity of Ag-TiO_2 Composites Deposited by Photoreduction under UV Irradiation. *Int. J. Photoenergy* **2018**, *2018*, 6080432. https://doi.org/10.1155/2018/6080432.

(15) Nakada, A.; Nishioka, S.; Vequizo, J. J. M.; Muraoka, K.; Kanazawa, T.; Yamakata, A.; Nozawa, S.; Kumagai, H.; Adachi, S.; Ishitani, O.; Maeda, K. Solar-Driven Z-Scheme Water Splitting Using Tantalum/Nitrogen Co-Doped Rutile Titania Nanorod as an Oxygen Evolution Photocatalyst. *J. Mater. Chem. A* **2017**, *5* (23), 11710–11719. https://doi.org/10.1039/C6TA10541F.

(16) Lei, L.; Wang, N.; Zhang, X. M.; Tai, Q.; Tsai, D. P.; Chan, H. L. W. Optofluidic Planar Reactors for Photocatalytic Water Treatment Using Solar Energy. *Biomicrofluidics* **2010**, *4* (4), 043004. https://doi.org/10.1063/1.3491471.

(17) Fu, S. C.; Zhong, X. L.; Zhang, Y.; Lai, T. W.; Chan, K. C.; Lee, K. Y.; Chao, C. Y. H. Bio-Inspired Cooling Technologies and the Applications in Buildings. *Energy Build.*

2020, *225*, 110313. https://doi.org/10.1016/j.enbuild.2020.110313.

(18) Hisatomi, T.; Takanabe, K.; Domen, K. Photocatalytic Water-Splitting Reaction from Catalytic and Kinetic Perspectives. *Catal. Letters* **2015**, *145* (1), 95–108. https://doi.org/10.1007/s10562-014-1397-z.

(19) Yu, J.; Qi, L.; Jaroniec, M. Hydrogen Production by Photocatalytic Water Splitting over Pt/TiO2 Nanosheets with Exposed (001) Facets. *J. Phys. Chem. C* **2010**, *114* (30), 13118–13125. https://doi.org/10.1021/jp104488b.

(20) Kim, S.; Hwang, S.-J.; Choi, W. Visible Light Active Platinum-Ion-Doped TiO2 Photocatalyst. *J. Phys. Chem. B* **2005**, *109* (51), 24260–24267. https://doi.org/10.1021/jp055278y.

(21) Alrushaid, M.; Nadeem, M. A.; Wahab, K. A.; Idriss, H. Extracting Turnover Frequencies of Electron Transfer in Heterogeneous Catalysis: A Study of IrO2-TiO2 Anatase for Water Oxidation Using Ce4+ Cations. *Catalysts* **2021**, *11* (9), 1030. https://doi.org/10.3390/catal11091030.

(22) Lourdes C. Fuller. Analysis of Oxygen Enriched Air Samples by Gas Chromatography. *Nav. AIR Syst. Command. Dep. Navy Washingt.* **1978**. https://doi.org/ADA062664.

(23) He, G.; Yang, W.; Zheng, W.; Gong, L.; Wang, X.; An, Y.; Tian, M. Facile Controlled Synthesis of Ag3PO4 with Various Morphologies for Enhanced Photocatalytic Oxygen Evolution from Water Splitting. *RSC Adv.* **2019**, *9* (32), 18222–18231. https://doi.org/10.1039/c9ra01306g.

(24) Pala, L. P. R.; Peela, N. R. Green Hydrogen Production in an Optofluidic Planar Microreactor via Photocatalytic Water Splitting under Visible/Simulated Sunlight Irradiation. *Energy & Fuels* **2021**, *35* (23), 19737–19747. https://doi.org/10.1021/acs.energyfuels.1c02686.

Chapter 3

Surface and photocatalytic properties of TiO_2 thin films prepared by non-aqueous surfactant assisted sol-gel method

Laxmi Prasad Rao Pala, Uday V, Gogoi D, Nageswara Rao Peela, J Environ Chem Eng (2020) 8:104267. https://doi.org/10.1016/j.jece.2020.104267

3.1 Objectives

In the present work, TiO_2 sol-gels with different concentrations of each of the components such as titania precursor, acid catalyst, stabilizing agent and surfactant is prepared in the alcohol medium. The effect of concentration of the components in the sol-gel on the surface morphology and topography of the TiO_2 films to achieve uniform and well adhered catalyst coatings is studied. Finally, the photocatalytic activity of the TiO_2 thin films is assessed by investigating the photo-degradation of methylene blue in aqueous solution by UV light illumination and the kinetics of the MB degradation are determined.

3.2 Results and discussion

3.2.1 Characterization of TiO_2 thin films

3.2.1.1 Effect of addition of each component in the sol on the surface morphology

To study the effect of the addition of each component in the sol on the surface morphology, the sols with and without that particular component were prepared by keeping the concentration of all other components constant (Table 2.2, composition numbers: 1 – 4). The AA, AcAc, and CTAB each have their specific effect on the morphology of the final TiO_2 thin film formed (Figure 3.1).

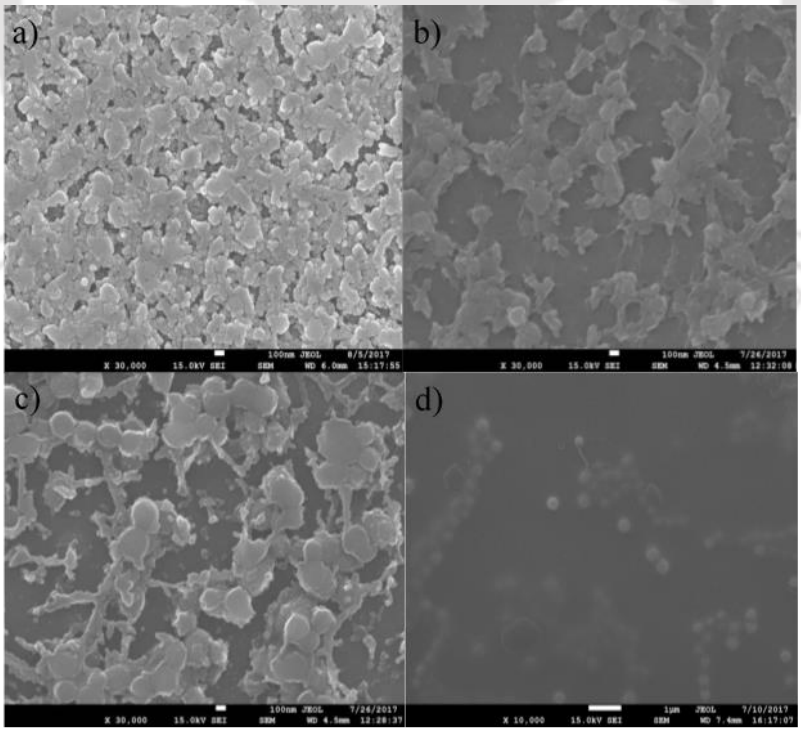

Figure 3.1: Effect of components in the sol compositions on the morphology of films: a) TiO_2 film; b) TiO_2 film without AA; c) TiO_2 film without AcAc; d) TiO_2 film without CTAB [Sol composition: 0.2M TTIP, 0.1M AcAc, 0.09M AA and 1g CTAB/0.01 mol TTIP]

A uniform layer of aggregated TiO_2 spherical particles (Fig. 3.1a) was formed with sol composition of 0.2 M TTIP, 0.1M AcAc, 0.09M AA and 1g of CTAB per 0.01mol TTIP (composition 1 of Table 2.2). In the absence of either AA or AcAc in the sol, a non-uniform film with large aggregates was formed (Fig. 3.1b and 3.1c). A non-porous smooth film with lumps of bigger particles was observed when CTAB was not used in the sol (Fig. 3.1d).

Table 3.1 shows the influence of sol composition on particle size, porosity and surface roughness of the TiO_2 thin films. The particle size was lower for the TiO_2 thin film formed from the sol with all the 3 components (AcAc, AA, and CTAB) present. This indicates that a denser uniform film was formed in presence of AcAc, AA, and CTAB.

Table 3.1: Influence of sol components on TiO_2 thin films properties

S. No.	Nominal Composition	Roughness, nm	Particle size, nm	Porosity, %
1	$Ti_{0.2}AcAc_{0.1}AA_{0.09}CTAB_1$	7.9	10.4	14.8
2	$Ti_{0.2}AcAc_{0.1}CTAB_1$	11.2	18.5	25.2
3	$Ti_{0.2}AA_{0.09}CTAB_1$	18.2	27.5	45.6
4	$Ti_{0.2}AcAc_{0.1}AA_{0.09}$	0.3	26.4	0.95

When CTAB was not present in the TiO_2 sol, the surface roughness and the porosities were 0.3 nm and 0.95 %, respectively, indicating the formation of the non-porous smooth film. With the addition of CTAB, a uniform continuous porous TiO_2 thin film was achieved with the roughness value of 7.9 nm and the porosity of ~15 %. The roughness, particle size, and porosity were lower for the film formed from the sol containing AcAc as compared to that formed from sol containing AA, thus indicating that AcAc acted as a better modifier than AA. However, a uniform film was obtained only when both AcAc and AA were present in the TiO_2 sol along with CTAB (Fig. 3.1a).

When AcAc was added to TTIP, the hydroxyl group present in the enol form of AcAc easily reacts with the TTIP and causes the transfer of an acidic proton from the AcAc to an alkoxy group of TTIP. This results in the formation of the corresponding alcohol and a modified complex, as follows:

$$Ti(OPr^i)_4 + x(AcAcH) \rightarrow Ti(OPr^i)_{4-x}(AcAc)_x + xPr^iOH \quad \text{..... (3.1)}$$

This modified complex ($Ti\left(OPr^i\right)_{4-x}(AcAc)_x$) generally has lower reactivity compared to hydrolyzed TTIP ($Ti\left(OPr^i\right)_{4-x}(OH)_x$), formed when TTIP reacts with water. Therefore, AcAc controls the hydrolysis and thereby condensation rates of TTIP through the formation of less reactive modified TTIP.[1,2]

Similarly, when AA is added to TTIP, it also forms a new molecular complex through the following exothermic reaction:

$$Ti(OPr^i)_4 + x(AA) \rightarrow Ti\left(OPr^i\right)_{4-x}(OAc)_x + xPr^iOH \ldots\ldots\ldots\ldots\ldots\ldots \quad (3.2)$$

This modified complex ($Ti\left(OPr^i\right)_{4-x}(OAc)_x$) also has less reactivity and thus hydrolysis and condensation rates of TTIP are controlled.[1]

The TiO_2 thin films obtained using either AcAc or AA in the sol were not completely uniform (Fig. 3.1b and 3.1c). This could be due to the inadequate control of hydrolysis and condensation rates as some degree of precipitation is still observed in the sols containing either AcAc or AA but not both. When both AA and AcAc were present in the TiO_2 sol, a completely homogeneous thin film was formed (Fig. 3.1d). In this case, a clear transparent TiO_2 sol-gel was obtained without precipitation which could be due to the sufficient control of hydrolysis and condensation rates. This further control of hydrolysis and condensation is achieved by forming a new network of Ti-O-Ti in presence of AcAc and AA.[3] Therefore, co-existence of AcAc and AA as modifiers of TTIP in the TiO_2 sol is essential for controlling the hydrolysis and condensation reactions by occupying the coordination sites of TTIP to avoid the precipitation of undesirable phases and to produce clear transparent TiO_2 sol-gels.

On comparing the TiO_2 films formed with (Fig. 3.1a) and without CTAB (Fig. 3.1d), a highly porous film with uniform grain like structure having aggregated particles was formed after the addition of CTAB. The presence of CTAB in the sol induces a porous TiO_2 inorganic framework because of the capping effect of CTAB around the precursor. It plays a minor role in further reducing the hydrolysis and condensation rates.[4]

3.2.1.2 Effect of the concentration of TTIP on the surface morphology

The effect of concentration of TTIP (in the range of 0.1 to 0.4 M) on the thin film morphology was studied and presented in Figure 3.2. At a concentration of 0.1 M TTIP, a thin film containing well dispersed and finely aggregated TiO_2 particles was formed (Fig. 3.2a).

The TiO_2 aggregates increased with the TTIP concentration, although the films were uniform (Fig. 3.2b and 3.2c).

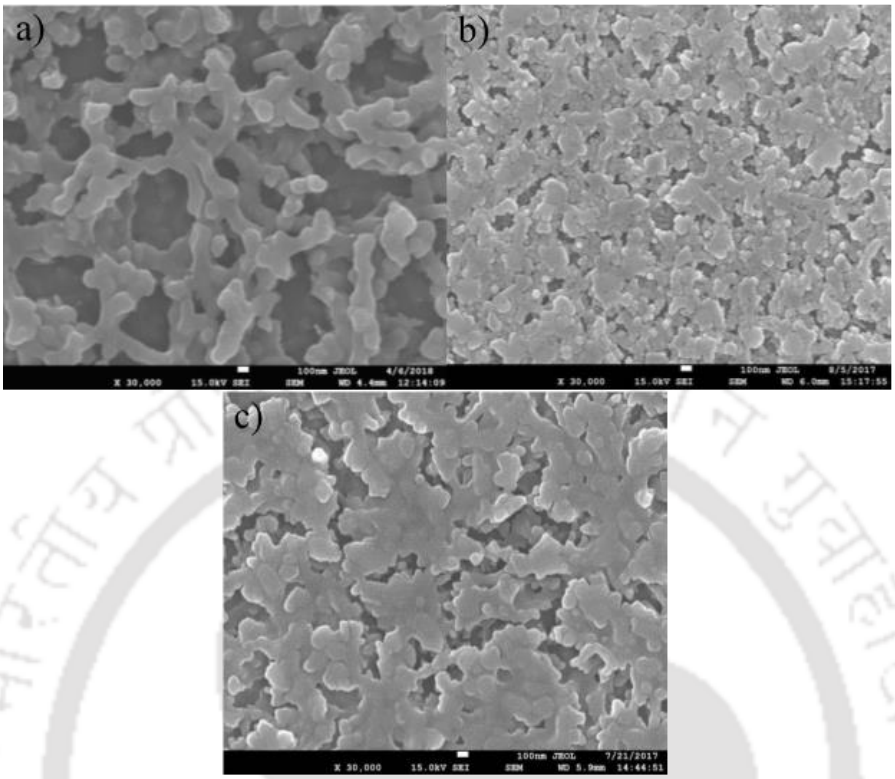

Figure 3.2: Effect of varying TTIP concentration on the morphology of films: a) 0.1M; b) 0.2M; c) 0.4M [Sol composition: xM TTIP, 0.1M AcAc, 0.09M AA and 1g CTAB/0.01 mol TTIP]

Table 3.2 shows the influence of the concentration of TTIP on the surface roughness, particle size and porosity of TiO_2 thin films. The surface roughness, particle size, and porosity were the highest with the 0.1 M TTIP concentration. It can be noticed that the particle size almost remained constant i.e., from 10.4 to 10.5 nm with increasing TTIP from 0.2M to 0.4M. The surface roughness and porosity of the films decreased and then increased with increasing the TTIP concentration. Higher surface roughness results in the higher active surface area of the films for the dye degradation.[5]

Table 3.2: Influence of TTIP concentrations on TiO_2 thin films properties

Nominal Composition	Roughness, nm	Particle size, nm	Porosity, %
$Ti_{0.1}AcAc_{0.1}AA_{0.09}CTAB_1$	42.9	12.3	17.5
$Ti_{0.2}AcAc_{0.1}AA_{0.09}CTAB_1$	7.9	10.4	14.8
$Ti_{0.4}AcAc_{0.1}AA_{0.09}CTAB_1$	13.5	10.5	17.3

Cheng et al.[6] studied the morphologies obtained at the different concentrations of TTIP with PS-b-PEO block copolymer as structure directing agent. They reported structural change from clustered nanoparticles to isolated flake-like structures with increasing TTIP concentration. In the present work, at the lowest concentration of TTIP of 0.1 M, a worm-like structure was observed. With increasing TTIP from 0.1 to 0.2 M, the thickness of the nano-worms increases with the deposition of new spherical particles around it. As the TTIP concentration was further increased from 0.2 to 0.4 M, the size of the worm-like structure increased and finally transformed into the flake-like structure. This morphology transition (from worm-like to flake-like structure) could be due to the increase in the condensation of Ti-O nanostructures inside the micelles by increasing the TTIP concentration. Bishnu et al.[7] also observed a similar effect of an increase in the thickness of the TiO_2 wall from 10 to 50 nm with increasing the TTIP concentration from 25 to 200 µL and attributed this effect to the deposition of more TTIP over the polystyrene core.

3.2.1.3 Effect of the Concentration of CTAB on the surface morphology

CTAB is a cationic surfactant with a hydrophilic polar head group and hydrophobic carbon tail. It forms spherical micelles above the critical micelle concentration (CMC). Due to its amphiphilic nature, CTAB acts as a pore-forming agent which enables the formation of highly porous materials with specific pore size and structure by inhibiting the crystallite growth and aggregation of adjacent primary particles.[4,8]

The effect of concentration of CTAB (in the range of 0–1.4 g per 0.01mol TTIP) in the sol on the formed thin film morphology was studied and presented in Figure 3.3.

The highly porous TiO_2 thin films with uniform grain like structure were formed above the concentration of 0.8 g per 0.01mol TTIP (Fig. 3.3c-f). The surface of the TiO_2 thin films was non-porous and smooth below the concentration of 0.8 g per 0.01mol TTIP (Fig. 3.3a, b). Mariquit et al.[9] studied the effect of adding CTAB surfactant to the TiO_2 solution for immobilizing TiO_2 films on glass substrate. From surface morphology study using FESEM, they observed that the porous thin film structure was formed when the TiO_2 films were prepared with CTAB. The TiO_2 particles bond with CTAB surfactant micelles during the sol-gel process and then these micelles were subsequently burned off during film calcination, thus forming a porous thin TiO_2 film.

Figure 3.4 shows the variation of particle size, roughness and porosity of the films obtained with changing concentrations of CTAB. The surface roughness varied unevenly and the particle

size remained nearly constant with increasing the CTAB concentration. While the porosity increased when CTAB concentration increased from 0.6 to 0.8g/0.01 mol TTIP and then decreased with CTAB concentration.

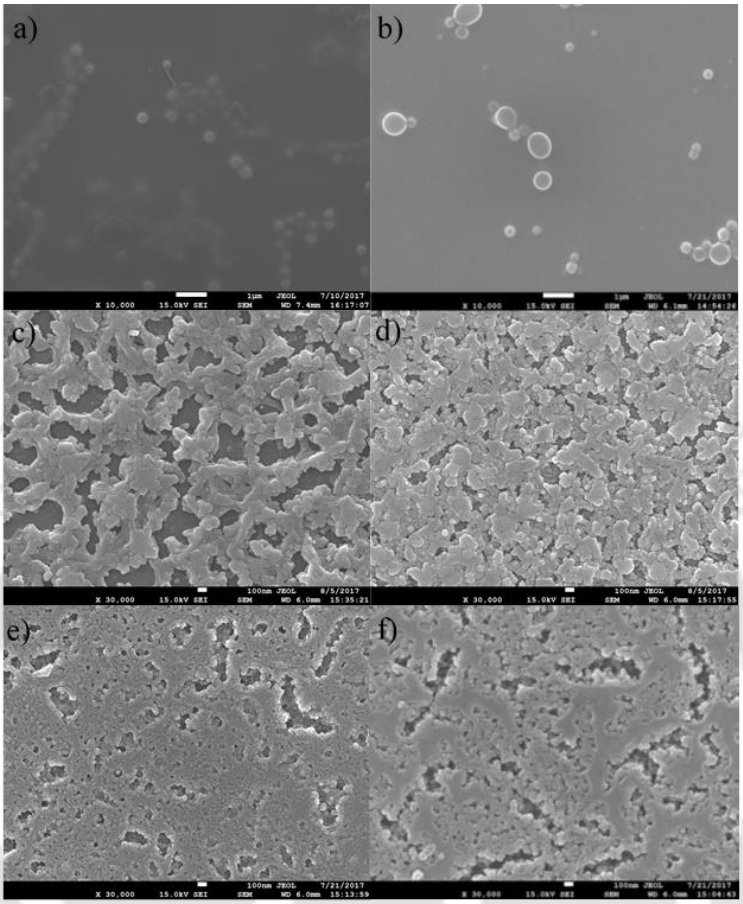

Figure 3.3: Effect of change in the CTAB weight on the morphology of films; a) 0g; b) 0.6g; c) 0.8g; d) 1g; e) 1.2g; f) 1.4g [Sol composition: 0.2M TTIP, 0.1M AcAc, 0.09M AA and Xg CTAB/0.01 mol TTIP]

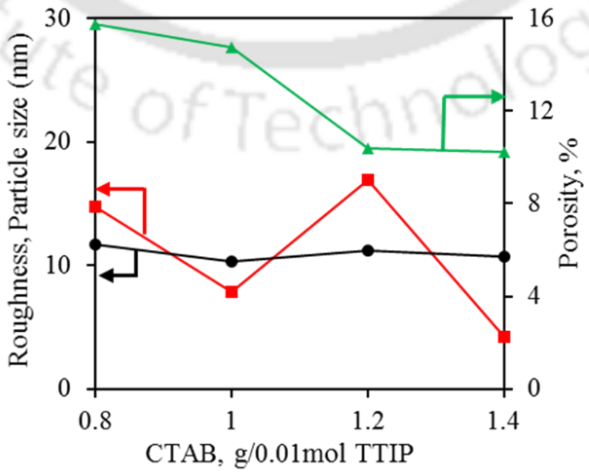

Figure 3.4: Variation of surface roughness, particle size and porosity with CTAB concentration

It is known that the CMC is the concentration of the surfactant above which micelles are formed spontaneously. The TiO_2 thin film morphology changed from non-porous to porous when the CTAB concentration was increased from 0.6 to 0.8 g/0.01 mol TTIP, therefore it can be considered that the CMC exists between these concentrations of CTAB. As the CTAB concentration increased from 0.6 to 0.8g/0.01 mol TTIP, the surfactant concentration exceeded the CMC and the spherically shaped micelles are formed. These spherical micelles transformed into rod-like micelles with increasing CTAB concentration in the solution. The size of the rod-like micelles increased with increasing CTAB concentration, leading to an increase in pore size, and porosity and thus forming porous TiO_2 films after calcination.[10,11] However, with further increasing CTAB concentration between 0.8 and 1.4 g/0.01 mol TTIP, the TiO_2 framework around the rod-like micelles collapses during calcination due to the decrease in the mechanical strength since more number of micelles are present per unit volume in the solution. This leads to the particle agglomeration resulting in the decrease of porosity in the TiO_2 films.[12] The collapse of the TiO_2 structure is more pronounced in the range of 1–1.2 g/0.01 mol TTIP CTAB concentration.

3.2.1.4 Effect of number of coatings on the surface morphology

Effect of number of coatings was studied by obtaining the TiO_2 films with 1, 2, 3 and 4 times coating (1x, 2x, 3x and 4x) using the sol containing 0.1 M TTIP, 0.1 M AcAc, 0.09 M AA and 1 g CTAB/0.01 mol TTIP (Table 2.2, Composition 5).

3.2.1.4.1 GIXRD and Raman analysis

Figure 3.5 shows the GIXRD and Raman spectra of the TiO_2 thin films. Fig. 3.5a shows the GIXRD pattern of the TiO_2 thin films obtained with 1x, 2x, 3x and 4x coatings. The GIXRD pattern of the TiO_2 thin films of 2x, 3x and 4x coatings showed the diffraction peaks corresponding to the anatase phase of TiO_2 and no others phases of TiO_2 were observed. An increase in the crystallinity of the TiO_2 thin films was observed with increasing number of coatings from 2 to 4. It can be seen that the first coating (1x) exhibit amorphous phase as no peaks were observed and a broad hump was formed which corresponds to the glass substrate. The other possible reason for the amorphous nature of 1x coating could be that the film may be too thin to show any peaks corresponding to crystallinity at the calcination temperature of 500 ˚C. The initial coating act as buffer layer thus blocking the diffusion of atoms from the glass substrate.[13] This resulted in the crystallization of TiO_2 films with increasing the film thickness with 2x, 3x, and 4x coatings.

The average grain size of TiO_2 anatase is estimated using Scherrer's equation in the spherical shape[14]:

Scherrer's equation: $$D = \frac{K\lambda}{\beta \cos\theta} \quad \ldots\ldots\ldots\ldots\ldots\ldots (3.3)$$

where D is the average crystallite size, K is a shape factor taken as 0.94, λ is the wavelength of X-ray radiation (CuK_α = 0.15418 nm), β is the full width at half maximum (FWHM) after making the appropriate base line correction, and θ is the diffraction angle at the position of the peaks. The average grain size of anatase TiO_2 was found to be 2.1 nm and 9.6 nm for 3 and 4 coatings.

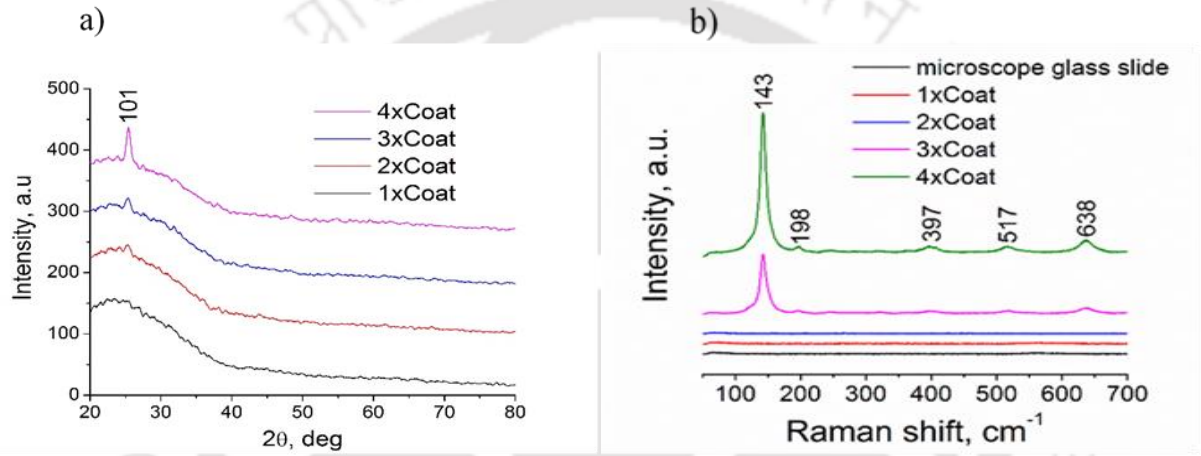

Figure 3.5: (a) GIXRD patterns of the TiO_2 thin films; (b) Raman Spectra of the TiO_2 thin films: 1xCoat, 2xCoat, 3xCoat, and 4xCoat; Ref: Raman spectrum of microscope glass slide

Fig. 3.5b shows the Raman spectra of the TiO_2 thin films obtained at different coatings. Raman spectrum of the glass substrate is also included for reference. The effect of the glass substrate on Raman spectra of the film was negligible, as can be seen from Fig. 3.5b. It can be seen that the characteristic TiO_2 phonon structure was present in 3 and 4 times coated samples while it was absent in 1 and 2 times coated samples. This suggests that TiO_2 is present in the anatase phase in 3 and 4 times coated samples and in amorphous phase in 1 and 2 times coated samples. The observed phonon bands for anatase TiO_2 at 143 ($E_g(1)$), 198 ($E_g(2)$), 397 ($B_{1g}(1)$), 517 ($A_{1g}+B_{1g}(2)$) and 638 ($E_g(3)$) cm^{-1} were in close matching with the literature reports.[15,16] The slight deviations between band frequencies obtained in this work and literature could be because of intra-grain defects or the structural distortions in the thin films. The E_g peak is mainly caused by the symmetric stretching vibration of the O-Ti-O, the B_{1g} peak is caused by the symmetric bending vibration of the O-Ti-O and the A_{1g} peak by the anti-symmetric bending vibration of the O-Ti-O in the TiO_2.[7]

3.2.1.4.2 Surface morphology and Topology by FESEM and AFM

Figure 3.6 shows the FESEM images of the TiO_2 thin films obtained after 1x, 2x, 3x and 4x times coatings. The TiO_2 thin film uniformity increased with number of coatings. Interestingly, a homogeneous smoother film with smaller TiO_2 spherical particles was formed on 3 times coated sample.

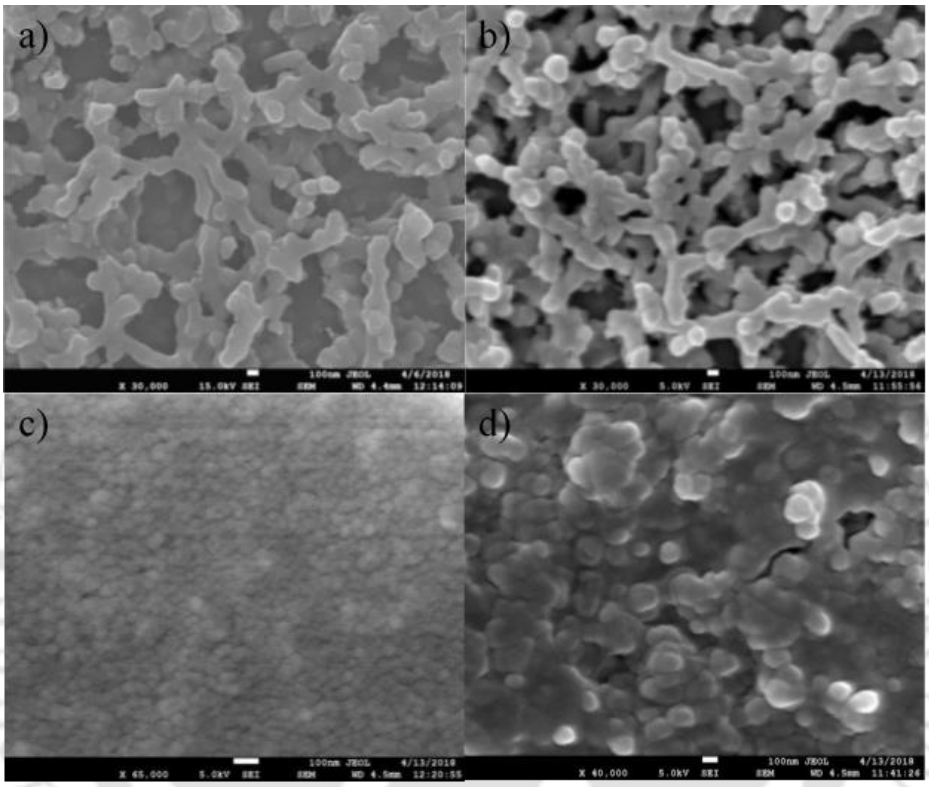

Figure 3.6: Effect of number of film coatings on the morphology of films a) 1x; b) 2x; c) 3x; d) 4x [Sol composition: 0.1M TTIP, 0.1M AcAc, 0.09M AA and 1g CTAB/0.01 mol TTIP]

Figure 3.7 shows the variation of film thickness, surface roughness, particle size and porosity against number of coatings. It was found that the film thickness increased almost linearly with number of coatings. The roughness, particle size, and porosity decreased to 3 coatings and then increased. The decrease in porosity with increasing thickness could be attributed to the film densification and the pore filling.[17] The lower roughness with 3 coatings represents good homogeneity of TiO_2 particles on the surface. The decrease in the particle size until 3 times coatings is attributed to the increase in the nucleation sites in the initial layers of the film.[14] These initial layers act as particle nucleation sites wherein the agglomerates transform into nanoparticles. Smaller particle size with increasing thickness results in more surface area to absorb free radicals.[18]

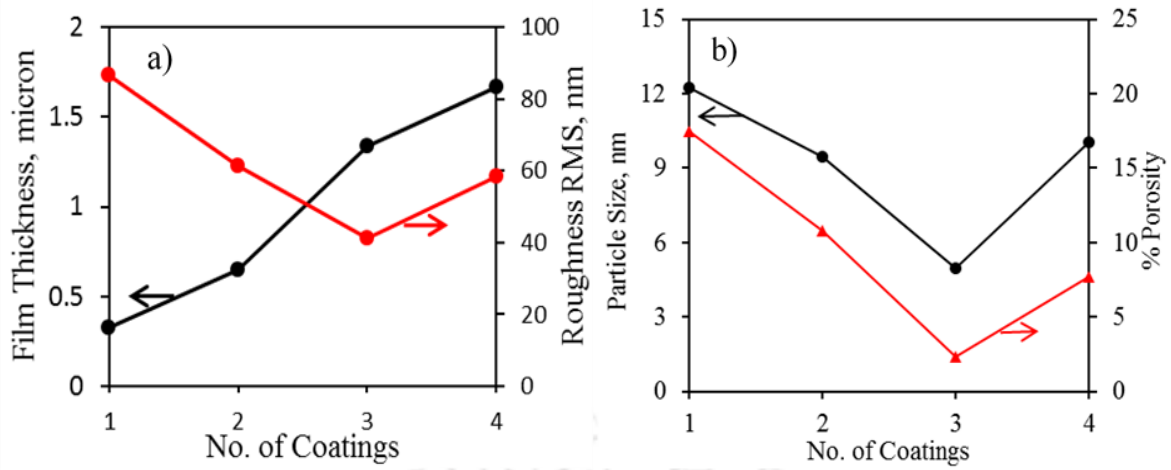

Figure 3.7: a) Variation of film thickness and roughness with number of coatings; b) Variation of particle size and porosity with number of coatings

From Figure 3.6, a single coating film (1x) has a coarse microstructure with relatively low regularity. With increasing the number of coatings, the films exhibited good microstructure with improved homogeneity. Toktam et al.[19] studied the microstructure and surface characteristics evolution of the mesoporous TiO_2 multi-spin coated films. The authors reported that the high lattice mismatch between the TiO_2 and glass substrate resulted in the coarse structure of single layer film. With increasing number of coatings above 1, the lattice mismatch gets eliminated and closely packed microstructure films with more uniformity are obtained. Increased nucleation sites in the initial layers resulted in the fine nanoparticle structures. They also reported that the high lattice mismatch between the glass substrate and TiO_2 film induced significant stress and roughness in the first TiO_2 layer. Higher roughness for the first layer was also witnessed in our study. Another reason for the formation of nanoparticle structure with increasing number of coatings is the surface reorganization in the structures further away from the substrate. This surface reorganization is because of the anisotropic stresses occurring during calcination as reported by Cheng et al.[6]

AFM images from which the roughness was determined for the 1x, 2x, 3x and 4x coatings are shown in Figure 3.8.

The AFM images were consistent with the FESEM images of the 1x, 2x, 3x and 4x coatings presented in the Figure 3.6. A uniform film with smoother surface from 3x coating can also be observed by the AFM imaging (Fig. 3.8c).

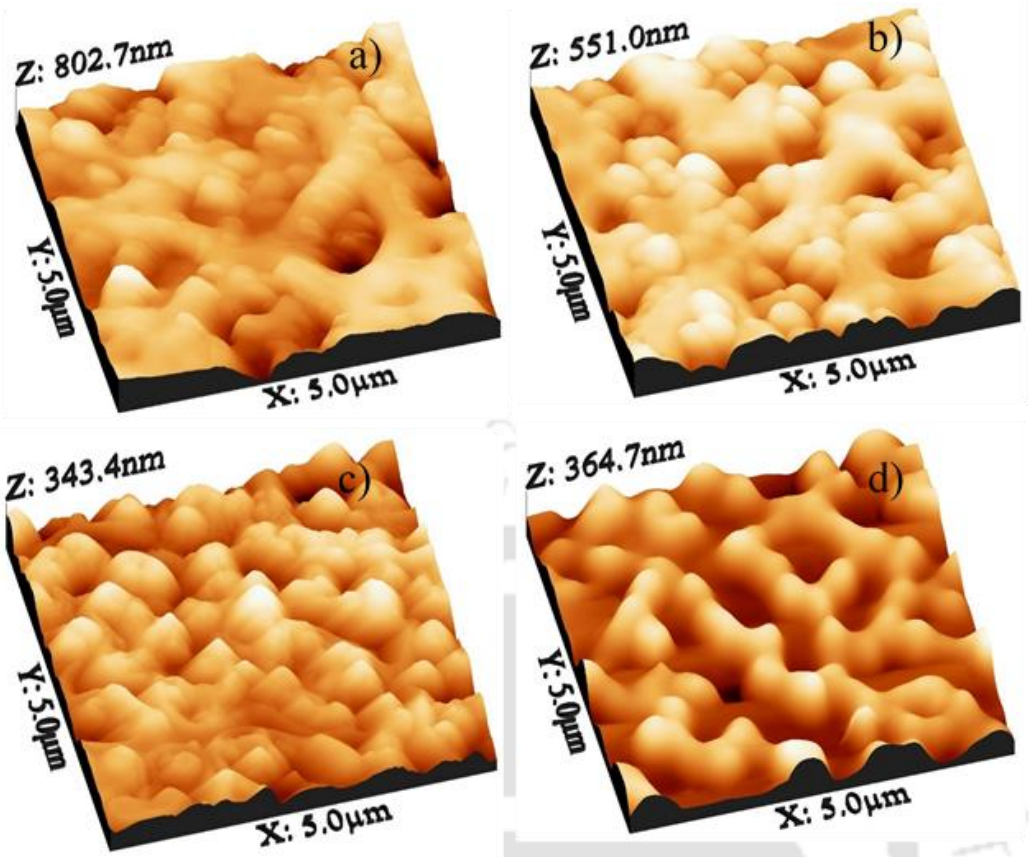

Figure 3.8: AFM images of films obtained with variable number of coatings a) 1x; b) 2x; c) 3x; d) 4x [Sol composition: 0.1M TTIP, 0.1M AcAc, 0.09M AA and 1g CTAB/0.01 mol TTIP]

3.2.1.4.3 Optical absorbance by UV-Vis spectroscopy

The UV-Vis spectra are shown in the Figure 3.9. The absorption edges were red-shifted when the film thickness was increased (Fig. 3.9a), which could be due to the quantum-size effect that depends on the particle size.[20] It can be seen from XRD that the particle size increased with film thickness. The absorption edges for the TiO_2-3x and TiO_2-4x films were found to be 380 and 410 nm and their bandgap energies (E_g) were 3.16 and 3.02 eV. The E_g was calculated from the Tauc plots (Fig. 3.9b), using the relationship $\alpha h\nu = A(h\nu - E_g)^{\eta}$, where α, hν and A are the absorption coefficient, energy of the incident photon and the proportionality constant, respectively. η is a constant which depends on the nature of the transition (η = 2 for the indirect band gap of anatase TiO_2)[21]. The indirect bandgap decreased with film thickness, due to the changes in the barrier height at grain boundaries, which in turn increases the localized density of states near the band edges. The decrease of indirect bandgap with increasing film thickness can be attributed also to the increase of particle size, decrease of strain and increase of lattice constants.[22,23] With decrease in bandgap, the minimum energy

required to excite electrons from the valence to conduction band also decreases and improves the photocatalytic performance.[24]

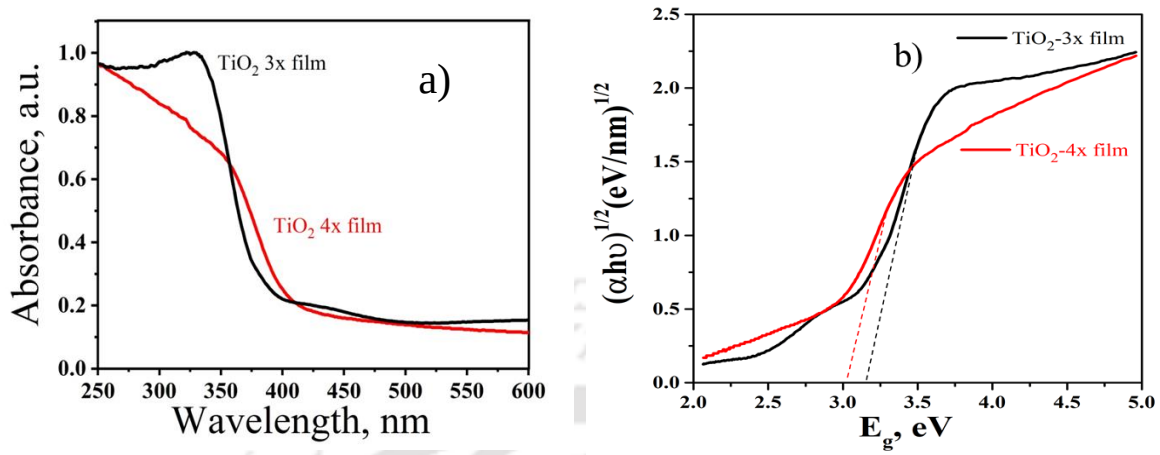

Figure 3.9: a) UV-Vis spectra and b) Tauc plots of TiO_2 thin films

3.3 Catalytic Performance of TiO_2 thin films

3.3.1 Photo-degradation of MB

The degradation of MB on the TiO_2 thin films under UV light illumination with time is presented in Figure 3.10. In the UV-Vis absorbance spectra of the samples collected after photo-irradiation for different times, the intensities of all the peaks with maxima at 664 nm for MB were decreased gradually with time, thus indicating the degradation of the MB occurred over TiO_2 films.[25,26] During the photocatalytic process, the TiO_2 photocatalyst gets excited, thereby generating photoelectrons. These photoelectrons are transferred to the nearby MB and participate in the redox reactions, which leads to the decomposition of MB into CO_2 and H_2O.[16]

A negligible photocatalytic degradation of MB in the absence of TiO_2 films (UV and UV+Glass conditions) under UV light illumination was noticed, which was as expected.[27] The catalytic performance of 1x and 2x coated films was not significantly different in MB degradation obtained with no film (UV+glass). This could be due to the amount of TiO_2 deposited for 1x and 2x films being too low to show considerable MB degradation. There was a significant MB degradation in case of 3 times and 4 times coated TiO_2 thin films indicating that these films were photocatalytically active and thereby faster decomposition of MB. The 3 times coated (110.7 nm thick) and the 4 times coated (145.3 nm thick) films showed 42.6% and 58.4% MB degradation, respectively, after 60 min of reaction time. The photocatalytic activity of TiO_2 thin films is due to the formation of highly oxidative radicals such as hydroxyl ($HO^{\cdot}$), hydrogen

peroxides ($HO_2^{\cdot}$) and superoxide (O_2^{-}) generated on the TiO_2 catalyst surface during UV light irradiation and then the reaction with dye molecules. [28,29]

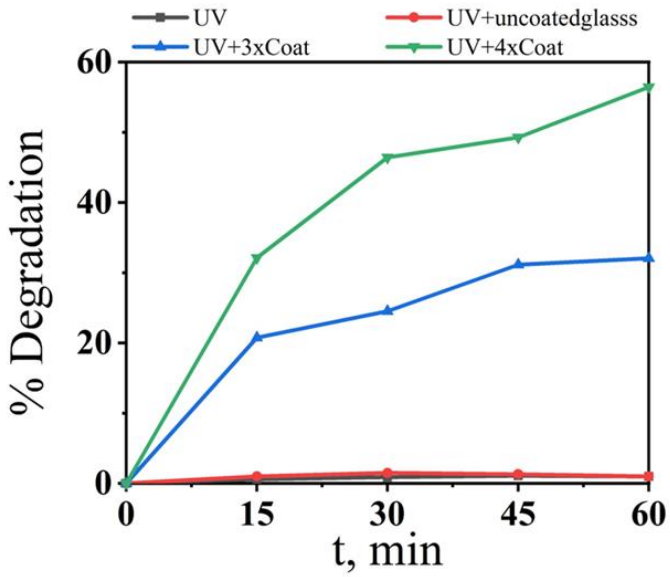

Figure 3.10: Degradation percentage of MB with reaction time

3.3.2 Proposed mechanism of photocatalytic degradation of MB

The proposed mechanism of MB degradation on TiO_2 film surface under UV light is shown in Figure 3.11.

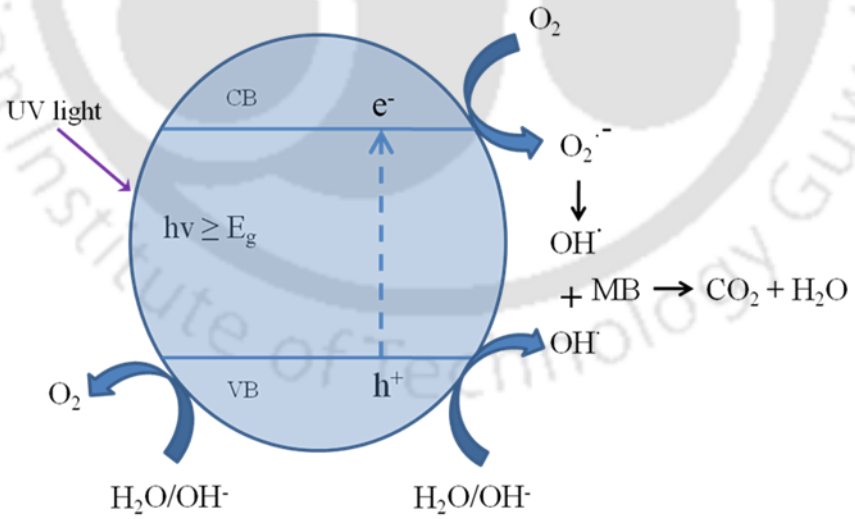

Figure 3.11: Mechanism of MB degradation on TiO_2 film surface under UV light

The relevant equations involved in the mechanism from TiO_2 activation to MB degradation is as follow [29–33]:

$$TiO_2 + hv \rightarrow e_{CB}^- + h_{VB}^+ \quad \ldots\ldots (3.4)$$

$$h_{VB}^+ + H_2O \rightarrow OH^\bullet + H^+ \ldots\ldots (3.5)$$

$$h_{VB}^+ + OH^- \rightarrow OH^\bullet \ldots\ldots (3.6)$$

$$O_2 + e_{CB}^- \rightarrow O_2^{\bullet -} \ldots\ldots (3.7)$$

$$O_2^{\bullet -} + H^+ \rightarrow HO_2^\bullet \ldots\ldots (3.8)$$

$$2\,HO_2^\bullet \rightarrow H_2O_2 + O_2 \ldots\ldots (3.9)$$

$$H_2O_2 \rightarrow 2OH^\bullet \ldots\ldots (3.10)$$

$$MB + OH^\bullet \rightarrow degradation products \rightarrow CO_2 + H_2O \ldots\ldots (3.11)$$

$$MB + 25.5\,O_2 \rightarrow 16CO_2 + 6H_2O + HCl + H_2SO_4 + 3HNO_3 \ldots\ldots (3.12)$$

TiO_2 generates electron-holes pairs by absorbing photons possessing energy greater than the bandgap energy according to the Eq. (3.4). Photogenerated holes oxidize water molecules or OH^- ions on the TiO_2 film surface to form highly reactive hydroxyl radicals ($OH^\bullet$) according to Eq. (3.5) and (3.6). These hydroxyl radicals ($OH^\bullet$) are also produced via reduction of oxygen molecules adsorbed on the Ti(III) surface or dissolved in water to superoxide radical ($O_2^{\bullet -}$) according to Eq. (3.7), protonation of superoxide radical to hydroperoxyl radical ($HO_2^\bullet$) according to Eq. (3.8) and subsequently formation of H_2O_2 according to Eq. (3.9), which further dissociates to form $OH^\bullet$ according to Eq. (3.10). The $OH^\bullet$ radical, being a very strong oxidizing agent (standard redox potential +2.8 eV), degrades MB dye molecules adsorbed on the TiO_2 film surface to the mineral products before forming CO_2 and H_2O according to Eq. (3.11). The Eq. 3.12 represents the overall decomposition reaction of MB.[34,35] The major products formed during the photocatalytic degradation of MB under UV light irradiation are CO_2, H_2O, HNO_3, HCl and H_2SO_4.[28,36,37] Though the acids HNO_3, HCl and H_2SO_4 were formed during the degradation, the concentration of these acids is very small (> 10 ppm) as the amount of MB itself is very small (usually in ppm levels). The rate of degradation of MB is proportional to the concentration of surface hydroxyl radicals produced, which in turn depends on the rate of generation of stable electron-hole pairs. Nagaveni et al.[38] observed a better performance with anatase TiO_2, prepared by solution combustion, as compared to commercial Degussa TiO_2 in

degradation of MB and attributed to the large amount of surface hydroxyl radicals and lower bandgap. Bensouici et al.[39] noticed that the photocatalytic activity and apparent rate constant increased with TiO_2 film thickness and ascribed this behavior to the increase in the surface hydroxyl radicals. The decrease in the optical bandgap and increase in the MB degradation rate with anatase TiO_2 film thickness was also observed in the present study.

The MB degradation rates using TiO_2 thin films from this work are compared to those obtained in the literature (Table 3.3).

Table 3.3: Comparative study of degradation of MB using TiO_2 photocatalyst

S. No.	Catalyst	Synthesis method	Light source, wavelength (nm)	C_{dye} (ppm)	Catalyst dosage (g/l)	Thickness (nm)	Time (min)	% degradation	Ref
1	Anatase TiO_2 powder	Sol-gel	UV, 365	10	1	-	60	50	[40]
2.	Anatase TiO_2 powder	Sol-gel	UV, 365	15	0.1	-	720	25	[41]
3	Anatase TiO_2 powder	Sol-gel	UV, 254	0.355	0.5	-	60	97	[25]
4	Anatase TiO_2 powder	Sol-gel	Xenon lamp	10	1	-	180	25	[42]
5	Anatase TiO_2 powder	Ultrasonic-assisted Sol-gel	UV, 254	85	0.1	-	60	70	[43]
6	Anatase TiO_2 powder	Sol-gel	UV-vis, 350-450	20	0.33	-	150	58	[44]
7	Anatase TiO_2 powder	EISA method	UV, 254	20	0.2	-	100	65	[45]
8	Anatase TiO_2 nanotubes	Hydrothermal	Mercury lamp, 200-1000	20	0.5	-	180	73	[46]
9	Anatase TiO_2 thin film	Magnetron sputtering	Xenon lamp, 300-600	15	-	500	120	40	[47]
10	Anatase TiO_2 thin film	Sol-gel dip-coating	UV, 365	10	-	240	80	20	[48]
11	Anatase TiO_2 thin film (3x)	Sol-gel spin-coating	UV, 365	1	-	110.7	60	43	This work

12	Anatase TiO_2 thin film (4x)	Sol-gel spin-coating	UV, 365	1	-	145.3	60	58	This work

The MB degradation performance of 3x and 4x TiO_2 thin films were lower compared to that reported in Ref 25 of Table 3.3. The reason for this could be the lower MB concentration treated with higher amount of catalyst at higher energy UV light (254 nm) in their study as compared to ours.

TiO_2 powders were used more often in comparison to thin films for the photo-degradation of MB. Generally, Sol-gel method was employed to synthesize the TiO_2 powder with anatase phase. However, as mentioned earlier, usage of powders poses problem such as improper separation during the purification process from the water suspensions, which lead to the use of TiO_2 in the form of thin films. Different methods were used to prepare the thin films such as sol-gel spin coating, sol-gel dip coating and magnetron sputtering. It can be observed that the TiO_2 thin films prepared using sol-gel spin coating method in the present work showed better photo-degradation compared to those reported in literature. This could be attributed to the uniform thin films obtained in this study which resulted in the higher degradation due to the availability of more active surface sites to convert absorbed water molecules to active hydroxyl and superoxide radicals. [40]

3.3.3 Kinetics of photocatalytic degradation of MB

Kinetics of the photocatalytic degradation of MB over TiO_2 photocatalysts was estimated using the following zero, first and the second order rate equations [49]:

$$C_t = -k_0 t + C_0 \quad \ldots\ldots\ldots\ldots\ldots (3.13)$$

$$\ln(C_t) = -k_1 t + \ln(C_0) \quad \ldots\ldots (3.14)$$

$$\frac{1}{C_t} = k_2 t + \frac{1}{C_0} \quad \ldots\ldots\ldots\ldots\ldots (3.15)$$

where k_0, k_1, and k_2 are the zero, first and second order rate constants and t is UV illumination time.

The plot between $C_t \; vs \; t$,$\ln(C_t) \; vs \; t$ and $\frac{1}{C_t} vs \; t$ for the 3x and 4x TiO_2 thin films are shown in Figure 3.12.

The calculated rate constants and the corresponding R^2 values for the 3x and 4x TiO_2 films are presented in Table 3.4. From the Table 3.4, the second order equation best fits to the experimental data with the better R^2 values than zero and first order indicating that the MB

degradation kinetics follows the second order model. It can be observed that rate constant increased with increasing the TiO_2 film thickness, thereby indicating the increasing rate of degradation of MB. The observed difference in R^2 value for zeroth, first and second order kinetics is very small, making the judgment of second order kinetic model fit difficult based on linear regression fitting. Damian et al.[50], performed the kinetics of the MB degradation on the catalyst plate by fitting the first and second order kinetic models. They reported that a downward concave curvature is observed thereby ruling out the first order kinetics and confirmed the applicability of the second order kinetic model by fitting straight line with R^2 value of 0.9975. In our work, upon observation, downward concave curvatures can be seen for the data sets of zeroth and first order models, whereas the data set of second order model is much closer to straight line. Hence, the second order kinetic model better fits the MB degradation kinetics.

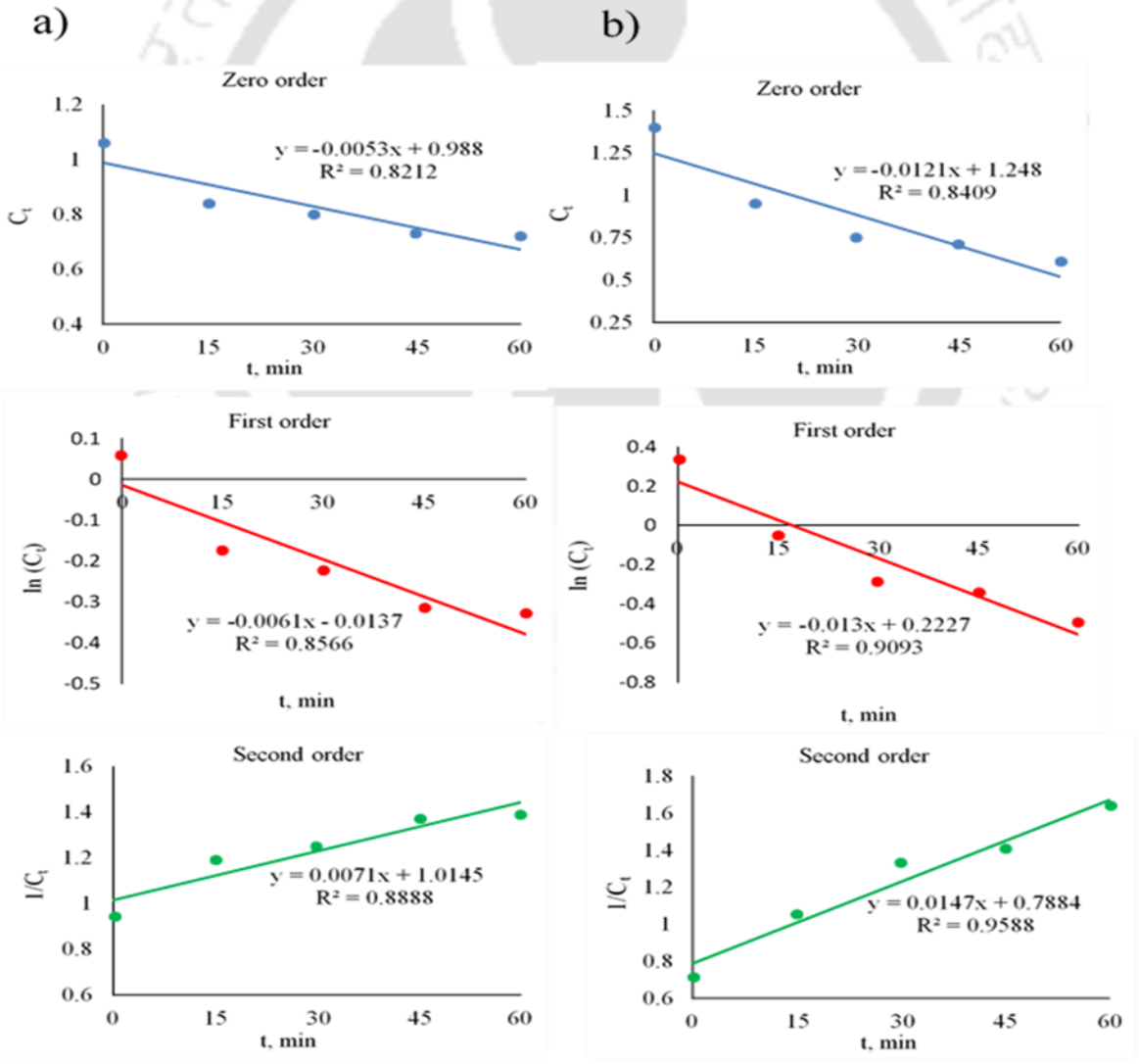

Figure 3.12: Estimation of rate constants for TiO_2 films: a) 3xCoat; b) 4xCoat

Second order kinetics were also reported for the photodegradation of congo red dye using chromite catalyst [49], photodegradation of dodecyl benzene sulphonate using TiO_2 Degussa P25 [51], photodegradation of toluene and acetone using modified TiO_2/activated carbon composite catalyst [52], and photodegradation of MB using polymeric complex of silver catalyst [50].

Table 3.4: Kinetic parameters of the TiO_2 films

TiO_2 Film	Zero order		First order		Second order	
	k_0, ppm min^{-1}	R^2	k_1, min^{-1}	R^2	k_2, $ppm^{-1}min^{-1}$	R^2
3x	0.005	0.82	0.006	0.86	0.007	0.89
4x	0.012	0.84	0.013	0.91	0.015	0.96

In the future work, the TiO_2 thin films on glass prepared in this work will be used to fabricate the optofluidic planar microreactors.

The prepared TiO_2-3x and 4x thin films, having high uniformity, good adhesion and high photocatalytic activity, are very promising for several practical applications such as photocatalytic water-splitting and CO_2 reduction. By impregnating with co-catalysts such as Ag, Au, Pt, etc., these TiO_2 thin films can be used for visible-light irradiated photocatalytic water-splitting (ongoing work in our research group). Optofluidic devices can be constructed using these thin film coated transparent substrates such as glass and be used for various applications including photocatalytic applications (another ongoing work in our research group).

3.4 Conclusions

In summary, TiO_2 thin films on the glass substrate are successfully prepared by using sol-gels containing TTIP, AcAc, AA, and CTAB. The GIXRD of the 3 and 4 times coated TiO_2 thin films show the diffraction peaks of the anatase phase of TiO_2. Raman spectra confirm the presence of anatase phase in the 3 and 4 times coated TiO_2 thin films. A clear transparent TiO_2 sol-gel is obtained without precipitation when both AA and AcAc are present in the TiO_2 sol. A worm-like structure forms at lower TTIP concentrations and transforms into a flake-like structure with increasing the concentration of TTIP from 0.1 to 0.4 M. The TiO_2 thin films are non-porous below 0.8 g CTAB per 0.01mol TTIP and are porous above 0.8 g CTAB per 0.01mol TTIP. The CMC is found to exist between 0.6 to 0.8 g CTAB per 0.01mol TTIP. A

highly homogeneous TiO_2 thin film is obtained with a sol-gel containing 0.2 M TTIP, 0.1 M AcAc, 0.09 M AA and 1 g of CTAB per 0.01 mol TTIP and the roughness, particle size and porosity of the thin film are estimated to be 7.9 nm, 10.4 nm and 14.8 %. FESEM and AFM images are consistent with each other for the 1x, 2x, 3x and 4x coatings. A homogeneous film with smaller TiO_2 spherical particles is formed on 3 times coated sample. The 3 times coated TiO_2 thin film with thickness 110.7 nm shows 42.6 % degradation of MB whereas 4 times coated TiO_2 thin film with thickness 145.3 nm shows 58.4 % MB degradation at 60 min of photocatalytic reaction. The kinetic study shows that MB degradation follows the second order kinetics.

References

(1) Attar, A. S.; Ghamsari, M. S.; Hajiesmaeilbaigi, F.; Mirdamadi, S. Modifier Ligands Effects on the Synthesized TiO2nanocrystals. *J. Mater. Sci.* **2008**, *43* (5), 1723–1729. https://doi.org/10.1007/s10853-007-2244-z.

(2) Siwińska-Stefańska, K.; Zdarta, J.; Paukszta, D.; Jesionowski, T. The Influence of Addition of a Catalyst and Chelating Agent on the Properties of Titanium Dioxide Synthesized via the Sol–Gel Method. *J. Sol-Gel Sci. Technol.* **2015**, *75* (2), 264–278. https://doi.org/10.1007/s10971-015-3696-2.

(3) Okunaka, S.; Tokudome, H.; Hitomi, Y.; Abe, R. Facile Preparation of Stable Aqueous Titania Sols for Fabrication of Highly Active TiO_2 Photocatalyst Films. *J. Mater. Chem. A* **2015**, *3* (4), 1688–1695. https://doi.org/10.1039/C4TA04680C.

(4) Choi, H.; Stathatos, E.; Dionysiou, D. D. Synthesis of Nanocrystalline Photocatalytic TiO2 Thin Films and Particles Using Sol-Gel Method Modified with Nonionic Surfactants. *Thin Solid Films* **2006**, *510* (1–2), 107–114. https://doi.org/10.1016/j.tsf.2005.12.217.

(5) Hosseini, A.; Içli, K.; Özenbaş, M.; Erçelebi. Fabrication and Characterization of Spin-Coated TiO2films. *Energy Procedia* **2014**, *60* (C), 191–198. https://doi.org/10.1016/j.egypro.2014.12.332.

(6) Cheng, Y. J.; Gutmann, J. S. Morphology Phase Diagram of Ultrathin Anatase TiO2films Templated by a Single PS-b-PEO Block Copolymer. *J. Am. Chem. Soc.* **2006**, *128* (14), 4658–4674. https://doi.org/10.1021/ja0562853.

(7) Bastakoti, B. P.; Ishihara, S.; Leo, S. Y.; Ariga, K.; Wu, K. C. W.; Yamauchi, Y. Polymeric Micelle Assembly for Preparation of Large-Sized Mesoporous Metal Oxides with Various Compositions. *Langmuir* **2014**, *30* (2), 651–659. https://doi.org/10.1021/la403901x.

(8) Anderson, A.-L.; Binions, R. The Effect of Tween® Surfactants in Sol-Gel Processing for the Production of TiO2 Thin Films. *Coatings* **2014**, *4* (4), 796–809. https://doi.org/10.3390/coatings4040796.

(9) Mariquit, E. G.; Kurniawan, W.; Miyauchi, M.; Hinode, H. Effect of Addition of Surfactant to the Surface Hydrophilicity and Photocatalytic Activity of Immobilized

Nano-TiO2 Thin Films. *J. Chem. Eng. Japan* **2015**, *48* (10), 856–861. https://doi.org/10.1252/jcej.14we421.

(10) Peikani, H. F.; Salehtash, F.; Fard, F. G.; Rezaie, H. The Synthesis of Mesoporous Sio2/Tio2 Composite Particles by Sol-Gel Method and Effect of Hexane on Its Structural Properties. *J. Bioeng. Biomed. Sci.* **2016**, *06* (02), 179. https://doi.org/10.4172/2155-9538.1000179.

(11) Lin, L.; Chen, C.; Bai, H. Synthesis of Nanoscale Adsorbents and Catalysts via Aerosol Route and Air Pollution Control Applications. *Earozoru Kenkyu* **2010**, *25* (2), 121–133.

(12) Hilonga, A.; Kim, J. K.; Sarawade, P. B.; Kim, H. T. Mesoporous Titania-Silica Composite from Sodium Silicate and Titanium Oxychloride. Part I: Grafting Method. *J. Mater. Sci.* **2010**, *45* (5), 1255–1263. https://doi.org/10.1007/s10853-009-4076-5.

(13) Bouachiba, Y.; Bouabellou, A.; Hanini, F.; Kermiche, F.; Taabouche, A.; Boukheddaden, K. Structural and Optical Properties of TiO 2 Thin Films Grown by Sol-Gel Dip Coating Process. *Mater. Sci.* **2014**, *32* (1), 1–6. https://doi.org/10.2478/s13536-013-0147-z.

(14) Sta, I.; Jlassi, M.; Hajji, M.; Boujmil, M. F.; Jerbi, R.; Kandyla, M.; Kompitsas, M.; Ezzaouia, H. Structural and Optical Properties of TiO2 Thin Films Prepared by Spin Coating. *J. Sol-Gel Sci. Technol.* **2014**, *72* (2), 421–427. https://doi.org/10.1007/s10971-014-3452-z.

(15) Kenanakis, G.; Katsarakis, N. Chemically Grown TiO2on Glass with Superior Photocatalytic Properties. *J. Environ. Chem. Eng.* **2014**, *2* (3), 1748–1755. https://doi.org/10.1016/j.jece.2014.07.015.

(16) Atout, H.; Álvarez, M. G.; Chebli, D.; Bouguettoucha, A.; Tichit, D.; Llorca, J.; Medina, F. Enhanced Photocatalytic Degradation of Methylene Blue: Preparation of TiO2/Reduced Graphene Oxide Nanocomposites by Direct Sol-Gel and Hydrothermal Methods. *Mater. Res. Bull.* **2017**, *95* (July), 578–587. https://doi.org/10.1016/j.materresbull.2017.08.029.

(17) Mechiakh, R.; Bensaha, R. Variation of the Structural and Optical Properties of Sol-Gel TiO2 Thin Films with Different Treatment Temperatures. *Comptes Rendus Phys.* **2006**, *7* (3–4), 464–470. https://doi.org/10.1016/j.crhy.2006.05.002.

(18) Nandang Mufti, Ifa K R Laila, A. F. The Effect of TiO 2 Thin Film Thickness on Self Cleaning Glass Properties. *Int. Conf. Phys. Instrum. Adv. Mater* **2017**, *853* (1), 0–6.

(19) Geramipour, T.; Oveisi, H. Microstruture and Surface Characteristics Evolution of Mesoporous Multiple Spin-Coated Titania Films. *Thin Solid Films* **2016**, *619*, 353–358. https://doi.org/10.1016/j.tsf.2016.10.030.

(20) Wei, C.-H.; Chang, C.-M. Polycrystalline TiO2 Thin Films with Different Thicknesses Deposited on Unheated Substrates Using RF Magnetron Sputtering. *Mater. Trans.* **2011**, *52* (3), 554–559. https://doi.org/10.2320/matertrans.M2010358.

(21) Gogoi, D.; Namdeo, A.; Golder, A. K.; Peela, N. R. Ag-Doped TiO2 Photocatalysts with Effective Charge Transfer for Highly Efficient Hydrogen Production through Water Splitting. *Int. J. Hydrogen Energy* **2020**, *45* (4), 2729–2744. https://doi.org/10.1016/j.ijhydene.2019.11.127.

(22) Cheng, X.; Gotoh, K.; Mochizuki, T.; Usami, N. Controllable Optical and Electrical Properties of Nb Doped TiO Films by RF Sputtering. *2018 IEEE 7th World Conf. Photovolt. Energy Conversion, WCPEC 2018 - A Jt. Conf. 45th IEEE PVSC, 28th PVSEC 34th EU PVSEC* **2018**, No. 1, 1986–1990. https://doi.org/10.1109/PVSC.2018.8548205.

(23) Aly, S. A.; Akl, A. A. Influence of Film Thickness on Optical Absorption and Energy Gap of Thermally Evaporated CdS0.1Se0.9 Thin Films. *Chalcogenide Lett.* **2015**, *12* (10), 489–496.

(24) Dhanapandian, S.; Arunachalam, A.; Manoharan, C. Highly Oriented and Physical Properties of Sprayed Anatase Sn-Doped TiO2 Thin Films with an Enhanced Antibacterial Activity. *Appl. Nanosci.* **2016**, *6* (3), 387–397. https://doi.org/10.1007/s13204-015-0450-6.

(25) Majeed, J.; Nayak, C.; Jha, S. N.; Bhattacharyya, K.; Bhattacharyya, D.; Tripathi, A. K. Correlation of Mo Dopant and Photocatalytic Properties of Mo Incorporated TiO2: An EXAFS and Photocatalytic Study. *RSC Adv.* **2015**, *5* (110), 90932–90940. https://doi.org/10.1039/c5ra14613e.

(26) Rauf, M. A.; Meetani, M. A.; Khaleel, A.; Ahmed, A. Photocatalytic Degradation of Methylene Blue Using a Mixed Catalyst and Product Analysis by LC/MS. *Chem. Eng.*

J. **2010**, *157* (2–3), 373–378. https://doi.org/10.1016/j.cej.2009.11.017.

(27) Komaraiah, D.; Madhukar, P.; Vijayakumar, Y.; Ramana Reddy, M. V.; Sayanna, R. Photocatalytic Degradation Study of Methylene Blue by Brookite TiO2thin Film under Visible Light Irradiation. *Mater. Today Proc.* **2016**, *3* (10), 3770–3778. https://doi.org/10.1016/j.matpr.2016.11.026.

(28) Zuo, R.; Du, G.; Zhang, W.; Liu, L.; Liu, Y.; Mei, L.; Li, Z. Photocatalytic Degradation of Methylene Blue Using TiO 2 Impregnated Diatomite. *Adv. Mater. Sci. Eng.* **2014**, No. 170148, 7.

(29) Konstantinou, I. K.; Albanis, T. A. TiO2-Assisted Photocatalytic Degradation of Azo Dyes in Aqueous Solution: Kinetic and Mechanistic Investigations: A Review. *Appl. Catal. B Environ.* **2004**, *49* (1), 1–14. https://doi.org/10.1016/j.apcatb.2003.11.010.

(30) Woods, R. M.; Searle, J. R.; Pursglove, A.; Worsley, D. A. Comparison of the Photoactivity of TiO2 Coatings Using a Flat Panel Reactor and FTIR to Monitor the CO2 Evolution Rate. *J. Environ. Chem. Eng.* **2019**, *7* (5), 103336. https://doi.org/10.1016/j.jece.2019.103336.

(31) Wang, N.; Zhang, X.; Wang, Y.; Yu, W.; Chan, H. L. W. Microfluidic Reactors for Photocatalytic Water Purification. *Lab Chip* **2014**, *14* (6), 1074–1082. https://doi.org/10.1039/C3LC51233A.

(32) Söyleyici Cergel, M.; Demir, E.; Atay, F. The Effect of the Structural, Optical, and Surface Properties of Anatase-TiO2 Film on Photocatalytic Degradation of Methylene Blue Organic Contaminant. *Ionics (Kiel).* **2019**, *25* (9), 4481–4492. https://doi.org/10.1007/s11581-019-02986-7.

(33) Ajmal, A.; Majeed, I.; Malik, R. N.; Idriss, H.; Nadeem, M. A. Principles and Mechanisms of Photocatalytic Dye Degradation on TiO2 Based Photocatalysts: A Comparative Overview. *RSC Advances*. Royal Society of Chemistry August 20, 2014, pp 37003–37026. https://doi.org/10.1039/c4ra06658h.

(34) Chang, H.; Su, C.; Lo, C. H.; Chen, L. C.; Tsung, T. T.; Jwo, C. S. Photodecomposition and Surface Adsorption of Methylene Blue on TiO2 Nanofluid Prepared by ASNSS. *Mater. Trans.* **2004**, *45* (12), 3334–3337. https://doi.org/10.2320/matertrans.45.3334.

(35) Sangpour, P.; Hashemi, F.; Moshfegh, A. Z. Photoenhanced Degradation of Methylene

Blue on Cosputtered M:TiO2 (M = Au, Ag, Cu) Nanocomposite Systems: A Comparative Study. *J. Phys. Chem. C* **2010**, *114* (33), 13955–13961. https://doi.org/10.1021/jp910454r.

(36) Dariani, R. S.; Esmaeili, A.; Mortezaali, A.; Dehghanpour, S. Photocatalytic Reaction and Degradation of Methylene Blue on TiO2nano-Sized Particles. *Optik (Stuttg).* **2016**, *127* (18), 7143–7154. https://doi.org/10.1016/j.ijleo.2016.04.026.

(37) Zhang, T.; Oyama, T.; Aoshima, A.; Hidaka, H.; Zhao, J.; Serpone, N. Photooxidative N-Demethylation of Methylene Blue in Aqueous TiO2 Dispersions under UV Irradiation. *J. Photochem. Photobiol. A Chem.* **2001**, *140* (2), 163–172. https://doi.org/10.1016/S1010-6030(01)00398-7.

(38) Nagaveni, K.; Hegde, M. S.; Ravishankar, N.; Subbanna, G. N.; Madras, G. Synthesis and Structure of Nanocrystalline TiO2 with Lower Band Gap Showing High Photocatalytic Activity. *Langmuir* **2004**, *20* (7), 2900–2907. https://doi.org/10.1021/la035777v.

(39) Bensouici, F.; Bououdina, M.; Iratni, A.; Tala-ighil, R. Z. Effect of Thickness on Photocatalytic Activity of TiO2 Thin Films Chapter 56 Effect of Thickness on Photocatalytic Activity of TiO 2 Thin Films. **2015**, No. November. https://doi.org/10.1007/978-3-319-16709-1.

(40) Chaudhari, S. M.; Gawal, P. M.; Sane, P. K.; Sontakke, S. M.; Nemade, P. R. Solar Light-Assisted Photocatalytic Degradation of Methylene Blue with Mo/TiO2: A Comparison with Cr- and Ni-Doped TiO2. *Res. Chem. Intermed.* **2018**, *44* (5), 3115–3134. https://doi.org/10.1007/s11164-018-3296-1.

(41) Wei, Y.-L.; Chen, K.-W.; Wang, H. P. Study of Chromium Modified TiO2 Nano Catalyst Under Visible Light Irradiation. *J. Nanosci. Nanotechnol.* **2010**, *10* (8), 5456–5460. https://doi.org/10.1166/jnn.2010.1944.

(42) Tan, K.; Zhang, H.; Xie, C.; Zheng, H.; Gu, Y.; Zhang, W. F. Visible-Light Absorption and Photocatalytic Activity in Molybdenum- and Nitrogen-Codoped TiO2. *Catal. Commun.* **2010**, *11* (5), 331–335. https://doi.org/10.1016/j.catcom.2009.10.025.

(43) Khan, H.; Berk, D. Characterization and Mechanistic Study of Mo+6 and V+5 Codoped TiO2 as a Photocatalyst. *J. Photochem. Photobiol. A Chem.* **2014**, *294*, 96–109.

https://doi.org/10.1016/j.jphotochem.2014.08.007.

(44) Wang, S.; Bai, L. N.; Sun, H. M.; Jiang, Q.; Lian, J. S. Structure and Photocatalytic Property of Mo-Doped TiO2 Nanoparticles. *Powder Technol.* **2013**, *244*, 9–15. https://doi.org/10.1016/j.powtec.2013.03.054.

(45) Avilés-García, O.; Espino-Valencia, J.; Romero, R.; Rico-Cerda, J. L.; Arroyo-Albiter, M.; Natividad, R. W and Mo Doped TiO2: Synthesis, Characterization and Photocatalytic Activity. *Fuel* **2017**, *198*, 31–41. https://doi.org/10.1016/j.fuel.2016.10.005.

(46) Zhang, S.; Chen, Y.; Yu, Y.; Wu, H.; Wang, S.; Zhu, B.; Huang, W.; Wu, S. Synthesis, Characterization of Cr-Doped TiO 2 Nanotubes with High Photocatalytic Activity. *J. Nanoparticle Res.* **2008**, *10* (5), 871–875. https://doi.org/10.1007/s11051-007-9309-4.

(47) Luo, S. Y.; Yan, B. X.; Shen, J. Enhancement of Photoelectric and Photocatalytic Activities: Mo Doped TiO 2 Thin Films Deposited by Sputtering. *Thin Solid Films* **2012**, *522*, 361–365. https://doi.org/10.1016/j.tsf.2012.07.121.

(48) Yang, Y.; Li, X. J.; Chen, J. T.; Wang, L. Y. Effect of Doping Mode on the Photocatalytic Activities of Mo/TiO2. *J. Photochem. Photobiol. A Chem.* **2004**, *163* (3), 517–522. https://doi.org/10.1016/j.jphotochem.2004.02.008.

(49) Shaban, M.; Abukhadra, M. R.; Ibrahim, S. S.; Shahien, M. . G. Photocatalytic Degradation and Photo-Fenton Oxidation of Congo Red Dye Pollutants in Water Using Natural Chromite—Response Surface Optimization. *Appl. Water Sci.* **2017**, *7* (8), 4743–4756. https://doi.org/10.1007/s13201-017-0637-y.

(50) Marcinkowski, D.; Wałęsa-Chorab, M.; Patroniak, V.; Kubicki, M.; Kądziołka, G.; Michalkiewicz, B. A New Polymeric Complex of Silver(I) with a Hybrid Pyrazine-Bipyridine Ligand - Synthesis, Crystal Structure and Its Photocatalytic Activity. *New J. Chem.* **2014**, *38* (2), 604–610. https://doi.org/10.1039/c3nj01187a.

(51) Sanchez, M.; Rivero, M. J.; Ortiz, I. Kinetics of Dodecylbenzenesulphonate Mineralisation by TiO2 Photocatalysis. *Appl. Catal. B Environ.* **2011**, *101* (3–4), 515–521. https://doi.org/10.1016/j.apcatb.2010.10.023.

(52) Yang, Q.; Liao, Y.; Mao, L. Kinetics of Photocatalytic Degradation of Gaseous Organic Compounds on Modified TiO 2/AC Composite Photocatalyst. *Chinese J. Chem. Eng.*

2012, *20* (3), 572–576. https://doi.org/10.1016/S1004-9541(11)60221-8.

Chapter 4

Green Hydrogen Production in an Optofluidic Planar Microreactor via Photocatalytic Water Splitting under Visible/Simulated Sun Light Irradiation

Laxmi Prasad Rao Pala, Nageswara Rao Peela, ACS Energy & Fuels (2021) 35:19737–19747.
https://doi.org/10.1021/acs.energyfuels.1c02686

4.1 Objectives

Here, in this work, an optofluidic planar microreactor for the hydrogen generation from the photocatalytic water splitting in presence of methanol as sacrificial agent using TiO_2 with platinum co-catalyst under visible/simulated-solar light irradiation was developed. The TiO_2 films were prepared by sol-gel spin coating method and deposited Pt onto these films by photochemical deposition technique. The optofluidic planar microreactor was fabricated using Pt/TiO_2 photocatalyst film coated glass substrate. The effect of parameters such as photocatalyst film thickness, reactant flow rate, solar light intensity and type of light source on the rate of hydrogen production was studied. The recycle stability of Pt/TiO_2 film in the optofluidic planar microreactor was also conducted.

4.2 Results and discussion

4.2.1 Characterization of TiO_2 and Pt/TiO_2

Figure 4.1 shows the XRD, UV-Vis and Photoluminescence spectra of the TiO_2 and Pt/TiO_2 film.

4.2.1.1 X-ray diffraction of the TiO_2 and Pt/TiO_2

The XRD patterns of undoped TiO_2 and Pt/TiO_2 are shown in Fig. 4.1a. The diffraction pattern of the TiO_2 indicated that the synthesized film contained only the anatase phase and no others phases of TiO_2. The Pt/TiO_2 possessed an additional peak at 40° 2θ angle, corresponding to Pt (111) lattice plane, which is consistent with face-centered cubic metallic phase Pt^0 [ICDD card No. 04-0802].[1] This indicates the successful deposition and reduction of Pt on TiO_2 surface. The observed diffraction peak at 40° was weak due to low loading and/or good dispersion of Pt. The dominant reason being good dispersion. This is because the good dispersion eliminates the agglomeration, which can occur even at low loading.[2] Thammanoon et.[3], photo-deposited 0.9 wt.% Pt onto the mesoporous TiO_2 particles prepared using sol-gel method and reported a similar XRD pattern.

The average crystallite size of TiO_2 and Pt/TiO_2 nanoparticles (NPs) were estimated using Scherrer's equation for the spherical shaped particles [4]:

Scherrer's equation: $$D=\frac{K\lambda}{\beta\cos\theta} \quad \text{.....(4.1)}$$

Here D, crystallite size; K, shape factor (=0.94); λ, wavelength of X-ray radiation (CuK_α = 0.15418 nm); β, full width at half maximum (FWHM) after the base line correction; and θ,

diffraction angle at the peak position. The crystallite sizes of TiO_2 and Pt/TiO_2 were estimated to be 10.43 nm and 9.94 nm.

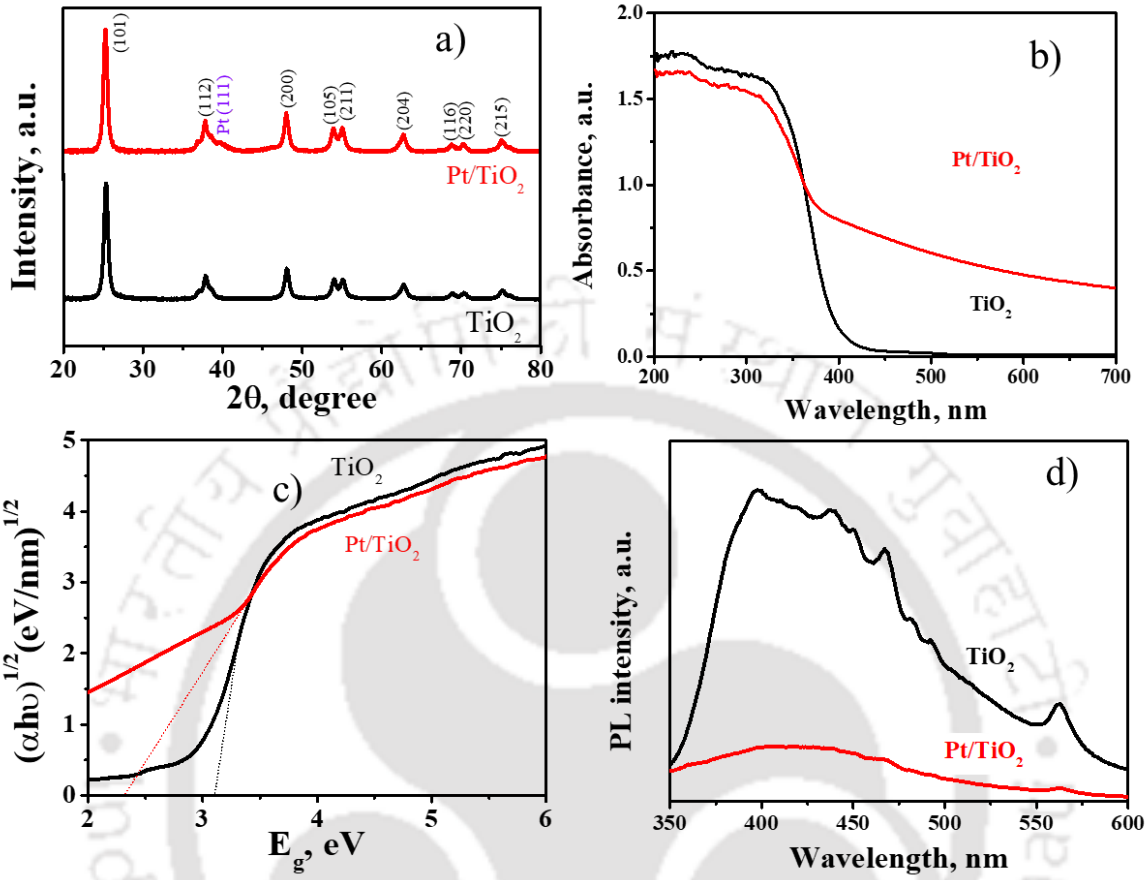

Figure 4.1: a) XRD; b) UV-Vis absorbance spectra; c) Tauc plots; and d) PL spectra of the TiO_2 and Pt/TiO_2 film

4.2.1.2 UV-Vis spectroscopy of the TiO_2 and Pt/TiO_2

The UV-Vis optical absorbance spectra of the TiO_2 and Pt/TiO_2 are shown in Fig. 4.1b. The TiO_2 has absorbance at wavelengths lower than 400 nm (UV region), and the absorbance of Pt/TiO_2 was extended into visible region. The optical absorbance of Pt/TiO_2 increased significantly in the wavelength range of 350–700 nm as compared to that of bare TiO_2. The absorption edges for the TiO_2 and Pt/TiO_2 were 396 and 438 nm, indicating that the optical absorption edge red-shifted with Pt deposition on TiO_2 surface. The observed red-shift in the absorption edge suggests that Pt/TiO_2 enhances the light utilization efficiency to split water to produce hydrogen under visible light irradiation.[5] The strong absorbance of visible light with the Pt photodeposited on TiO_2 was also reported by other researchers [6,7]. The bandgap energies (E_g) of the TiO_2 and Pt/TiO_2 were calculated to be 3.10 and 2.31 eV using the Tauc plots (Fig. 4.1c), from the relationship $\alpha h\nu = A(h\nu - E_g)^{\eta}$, [8]. Here α, absorption

coefficient; hν, energy of incident photon; A, proportionality constant; and η = 2 for the indirect band gap of anatase TiO_2.[9] The narrowing of TiO_2 bandgap with addition of Pt also indicates the light absorption of Pt/TiO_2 extends into visible region. The minimum energy required to excite electrons from valence band to conduction band of TiO_2 decreases with the decrease in bandgap of Pt/TiO_2 and improves the photocatalytic performance by transferring photoexcited electrons to Pt under visible light irradiation. The transfer of photoexcited electrons from the conduction band of TiO_2 to Pt NPs would occur until the fermi level attains an equilibrium; the formed Schottky barrier between the TiO_2 and Pt NPs leads to higher separation of generated electron-hole pairs thereby decreasing its recombination (also confirmed from photoluminescence spectroscopy), resulting in the improved photocatalytic efficiency.[10]

4.2.1.3 Photoluminescence (PL) analysis of the TiO_2 and Pt/TiO_2

The PL spectra for the TiO_2 and Pt/TiO_2 are shown in Fig. 4.1d. The PL analysis gives qualitative information on the recombination rate of the electron-hole pairs. The broad PL peak obtained with TiO_2 at wavelength 395 nm corresponds to the band-band PL (emission of the light from the recombination of electron-hole charge carriers that are created due to photon absorption by the TiO_2). The smaller peaks (at wavelengths 438, 450, 468, 482, 490, and 565 nm) are due to excitonic PL. These peaks give information about the defects, oxygen vacancies and surface states present in the photocatalyst. The excitonic PL peaks at 450 and 468 nm are due to band edge free excitons and the peaks at 482 and 490 nm correspond to bound excitons.[11] The PL intensity of Pt/TiO_2 was lower as compared to that of TiO_2. Upon photo-deposition of Pt onto TiO_2, both band-band and excitonic PL intensities were suppressed largely. This can be attributed to the transport of the conduction band electrons (e^-) of TiO_2 to Pt and also excellent interaction between Pt nanoparticles and TiO_2 photocatalyst.[12] The Pt acts as sink or trap sites for the e^- and lowers the recombination rate of electrons and holes.[13] The suppression of the excitonic PL with Pt addition can be viewed as the capability of Pt to capture the photo-induced electrons is higher as compared to that of defects/oxygen vacancies of TiO_2.[14]

4.2.1.4 X-ray photoelectron spectroscopy (XPS) of the TiO_2 and Pt/TiO_2

The XPS analysis was carried to determine the chemical phases present in the Pt/TiO_2 and shown in Figure 4.2. Fig. 4.2a shows the survey spectra of the TiO_2 and Pt/TiO_2, confirming the presence of (Ti2p and O1s) and (Pt4f, Ti2p and O1s) in TiO_2 and Pt/TiO_2, respectively. Fig. 4.2b shows the Pt 4f spectra and corresponding peaks fitted according to the XPS peak fitting procedure reported elsewhere[15]. The broadening and small valley between the

spin-orbit components indicates the presence of two different Pt species.[16] The deconvolution shows the peaks at binding energies 71.9 and 75.2 eV correspond to 4f $_{7/2}$ and 4f $_{5/2}$ of Pt metallic phase, and those at 72.9 and 76.2 eV correspond to 4f $_{7/2}$ and 4f $_{5/2}$ of Pt oxide phases, such as PtO and $Pt(OH)_2$. The amounts of Pt^0 and Pt^{2+} phases present in the Pt/TiO_2 were 43.3 and 56.7%, respectively. The percentage of oxidized Pt phase was higher than that of Pt metallic phase. The presence of Pt oxide phases along with the metallic Pt causes the photosensitization of Pt/TiO_2 samples to absorb visible light,[17–19] which was reflected in the optical absorbance of Pt/TiO_2, as observed from UV-Vis spectra.[20] Overall, the Pt present in Pt/TiO_2 existed in two chemical states namely, Pt metallic, and PtO and/or $Pt(OH)_2$. Similar observations were reported in the literature. For example, the photodeposition of Pt on TiO_2 in the absence of hole scavenger (e.g., methanol) leads to formation of Pt oxides predominantly along with metallic Pt.[21,22] The amount of metallic Pt or Pt oxide phase formed is dependent on the duration of the photodeposition carried out. The degree of formation of metallic platinum increases with increasing the photodeposition time and vice versa.[21,22] When the Pt is present only in metallic phase, the Pt/TiO_2 samples show photocatalytic activity under UV light only.[23]

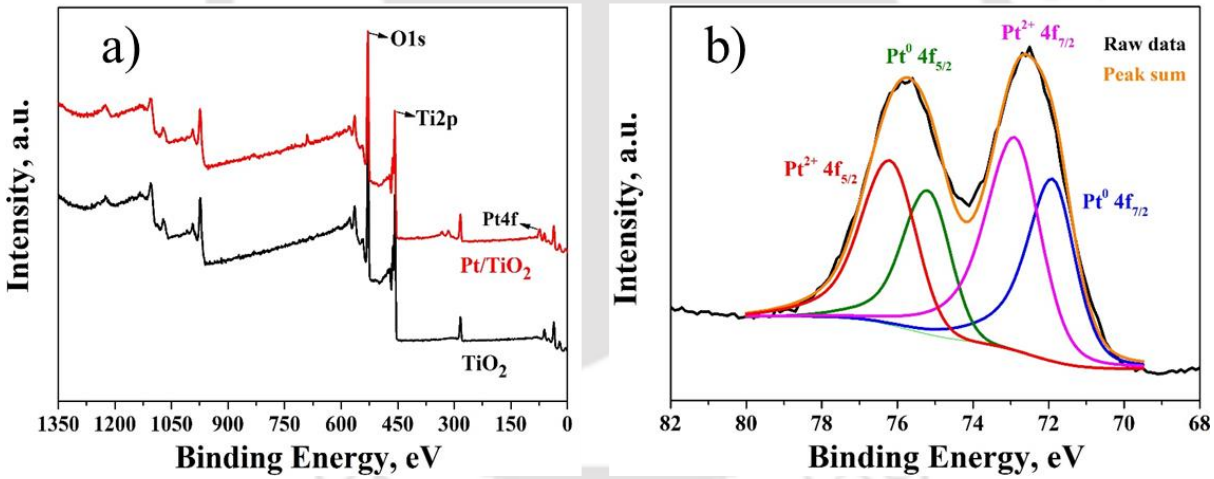

Figure 4.2: XPS Spectra of the TiO_2 and Pt/TiO_2: a) Survey spectrum and b) Pt 4f

4.2.1.5 FETEM and EDX of the Pt/TiO_2

The FETEM images and composition analysis by EDX of the Pt/TiO_2 are shown in Figure 4.3. The Pt NPs (appeared as spherical black dots as the electron density of Pt is higher compared to that of TiO_2) are well dispersed on the TiO_2 surface with the formation of a few aggregates (Fig. 4.3a and b). The particle size of Pt NPs deposited on TiO_2 was estimated to be in the range of 2-5 nm from the TEM image using Image analysis for approximately 1150 particles. The Fig. 4.3b inset shows the particle size distribution. The Pt usually disperses well

on the TiO_2 surface due to the strong metal-support interaction (SMSI).[24] The amount of Pt deposited onto the TiO_2 film was estimated to be 0.9 wt. %, from EDX analysis (Fig. 4.3d). The FESEM image (Fig. 4.3c) of the Pt/TiO_2 film shows homogeneous smoother film with smaller TiO_2 spherical particles.

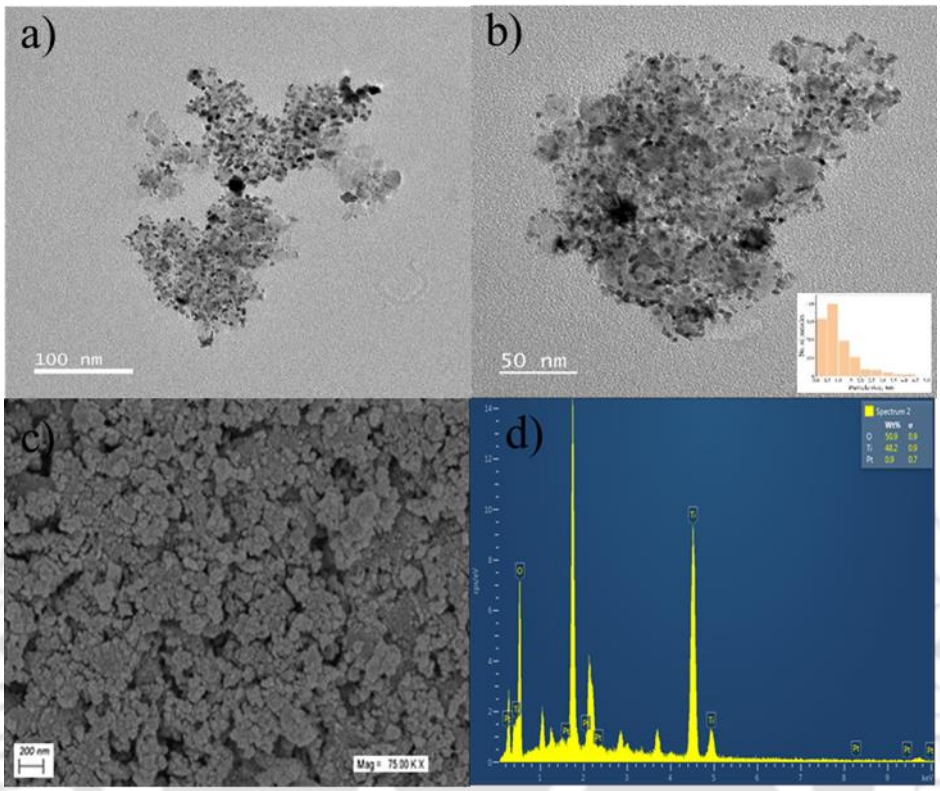

Figure 4.3: FETEM images (a and b); FESEM (c) and EDX (d) of the fresh Pt/TiO_2-8x film; Inset in Fig. 4.3b: Particle size distribution

4.2.2 Catalytic testing: Hydrogen production over Pt/TiO_2 films through photocatalytic water splitting in presence of methanol

In control experiments with and without bare TiO_2 film in the planar microreactor and in presence of methanol (SR), under visible light illumination, no hydrogen production was observed. The control experiments with Pt/TiO_2 film did not show any activity for overall water splitting into H_2 and O_2 (in the absence of methanol) under visible light irradiation. Therefore, water splitting experiments presented hereafter were conducted using 20 vol.% methanol in DI water reactant solution in the optofluidic planar microreactor over Pt/TiO_2 films under visible light irradiation.

4.2.2.1 Effect of reactant flow rate

The variation of hydrogen produced and its production rate as a function of flowrate (0.1-0.5 mL min^{-1}), with MH lamp illumination, are presented in Figure 4.4. The amount of hydrogen produced was increased with the run time up to 5 h, for all the flowrates (Fig. 4.4a).

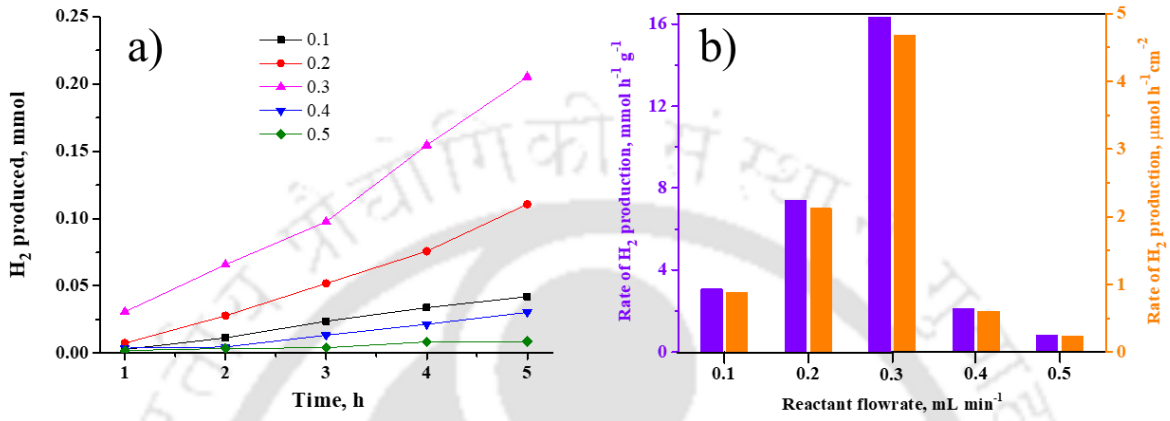

Figure 4.4: a) Hydrogen produced with run time; b) Rate of hydrogen production as a function of reactant flowrate; at reactant flowrates between 0.1-0.5 mL min^{-1} in the planar microreactor. (Reaction conditions: 20 vol.% methanol in DI water, Catalyst film Pt/TiO_2-8x (1650 nm thick) and 400 W MH lamp for visible light illumination)

The rate of hydrogen production increased with reactant flowrate reaching a maximum at 0.3 mL min^{-1} and then decreased (Fig. 4.4b). At lower flowrates, due to the laminar flow in the planar optofluidic device, the external mass transfer resistance limits the overall reaction.[25–28] Therefore, the hydrogen production rate increased with increasing flowrate till 0.3 mL min^{-1}. However, as the flowrate was increased beyond 0.3 mL min^{-1}, the hydrogen production rate significantly decreased even though the external mass transfer resistances were completely eliminated. This significant decrease in the hydrogen production rate was due to decrease in the residence times.[29–31] Therefore, 0.3 mL min^{-1} was the optimum flowrate to obtain the maximum hydrogen production rate and was used in the further studies.

4.2.2.2 Effect of catalyst coating thickness

The hydrogen produced as a function of time and its production rate, over the Pt/TiO_2 films of different thicknesses (Table 2.3), are presented in Figure 4.5. The reactant flowrate of 0.3 mL min^{-1} was used for these experiments and the reactor was illuminated with 400 W MH lamp.

All Pt doped TiO_2 thin films showed significant amount of hydrogen generation compared to bare TiO_2 indicating that these films were photocatalytically active under visible light irradiation. The photocatalytic activity of Pt/TiO_2 under visible light irradiation was because of the visible light absorption by this photocatalyst.

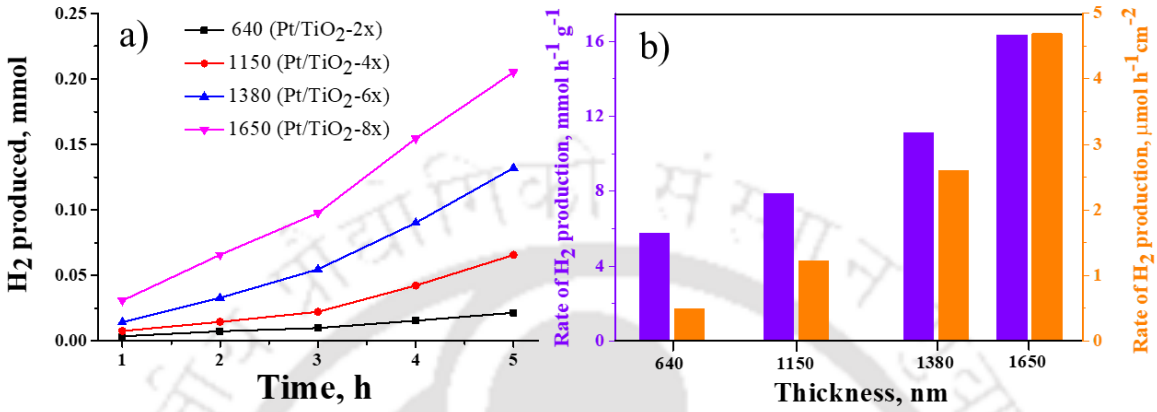

Figure 4.5: a) Hydrogen produced with run time; b) Rate of hydrogen production as a function of thickness; over Pt/TiO_2 films with varying thickness in the planar microreactor. (Reaction conditions: 20 vol.% methanol in DI water, 0.3 mL min^{-1} flowrate and 400 W MH lamp for visible light illumination)

This could be attributed to the presence of Pt oxide phase along with metallic Pt, as observed from XPS analysis (Figure 4.2). The Pt oxide phase acts as a photosensitizer to enhance the optical absorbance of Pt/TiO_2 in the visible region. The amount of hydrogen produced increased nearly linearly with time up to 5 h, over all the films (Fig. 4.5a). The rate of hydrogen production increased with increasing the thickness of the photocatalyst film (Fig. 4.5b). This could be attributed to the increase of the photogenerated carriers (e^--h^+ pairs) with film thickness, through the absorption of more photons.[27,29,32] These photogenerated holes react with water molecules and generate more protons, which eventually react with electrons resulting in the increased hydrogen production rate. The Pt/TiO_2-8x film with thickness of 1650±119 nm showed the highest photocatalytic activity with a hydrogen production rate of 16.35 mmol h^{-1} g^{-1} and 4.7 µmol h^{-1} cm^{-2}. Table 1.2 (Page 7) shows the recent literature on the photocatalytic hydrogen evolution from water splitting. It can be observed that the Pt/TiO_2 catalyst configuration showed a highest H_2 production rate of 225.04 mmol g^{-1} h^{-1} for a batch reactor system. The higher loading of Pt cocatalyst as well as catalyst was employed, compared to our study. Apart from this, piezoelectric transducer as an acoustic source was used along with the xenon lamp irradiation which has resulted in the significant activity for H_2 production

with rate of 225.04 mmol g^{-1} h^{-1}. However, the planar microreactor offers the scalability of the process thereby allowing for the further improvement of the reaction efficiencies.

The two H_2 production rates presented in Fig. 4.5b were converged to each other at higher photocatalyst thickness because the coating weight increased with thickness but the geometric area of photocatalyst film remained the same. Thus, the rate of increase of hydrogen production rate with respect to geometric area (with units µmol h^{-1} cm^{-2}) was higher than that with respect to weight of the photocatalyst (units mmol h^{-1} g^{-1}) with thickness. The absorption of incident light and internal mass transfer resistance are the important factors, which vary with varying the film thickness. With increasing the film thickness, the absorption of the incident light increases and thus the hydrogen production rate increases, reaching maximum at a particular thickness. Beyond this thickness, the rate decreases.[25,33] The internal mass transfer (diffusional) resistance, plays a significant role by limiting utilization of the deeper catalyst layers, particularly at higher film thicknesses.[25] The rate of hydrogen production increased with increasing the thickness of the photocatalyst film up to 1650 ± 119 nm, indicating an increase of absorption of incident light and negligible internal diffusional resistances [25,26] in the range of thicknesses studied. Lei et al.[27], studied the effect of TiO_2 film thickness of the top and bottom films in a planar microreactor. The authors reported an increase in the effective surface area with thickness, particularly when the film is very thin, due to the porous morphology of TiO_2 film. This results in the increase of reaction efficiency with the TiO_2 thickness. Whereas, when the film becomes very thick, the pores in the inner part are not exposed to the solution and/or light absorption decreases and thus decrease in the photoreactivity. The optimum bottom and top film thicknesses were reported to be 2 µm and 1 µm, through methylene blue photodegradation studies. The film thickness needs to further varied beyond 8x coatings in order to reach optimum thickness w.r.t the hydrogen production activity in our study.

4.2.2.3 Recycle stability of catalyst coating

The recycle stability and characterization of the spent Pt/TiO_2-8x film is shown in Figure 4.6. The recycle stability of the Pt/TiO_2-8x film in the optofluidic planar microreactor is presented in Fig. 4.6a. The water splitting recycle experiments were conducted using 20 vol.% methanol in DI water reactant solution pumped at flowrate of 0.3 mL min^{-1} under visible light illumination. After every 5 h of recycle experiment, the methanol free DI water is pumped through the microreactor for 10 min to refresh the catalyst coating.

A marginal decrease in the activity was observed after 2 cycles. To understand the reasons for the decrease in activity during recycle study, the spent photocatalyst was characterized using FESEM and EDX (Fig. 4.6b and c). The Pt content of fresh and spent photocatalysts were 0.9 and 0.8 wt.%, respectively (Fig. 4.3d and Fig. 4.6c), based on EDX analysis. Before and after the recycle test, the Pt contents were approximately the same, indicating that the Pt nanoparticles are intact in the photocatalyst. The FESEM images of the Pt/TiO_2-8x catalyst film, before and after recycle stability test are shown in Fig. 4.3c and Fig. 4.6b, respectively. From Fig. 4.6b, it can be observed that there is a slight aggregation of the Pt/TiO_2 composite particles in the spent catalyst after 4 cycles of stability runs, which could be the reason for the marginal decrease in the hydrogen production rate after 2nd cycle.[34]

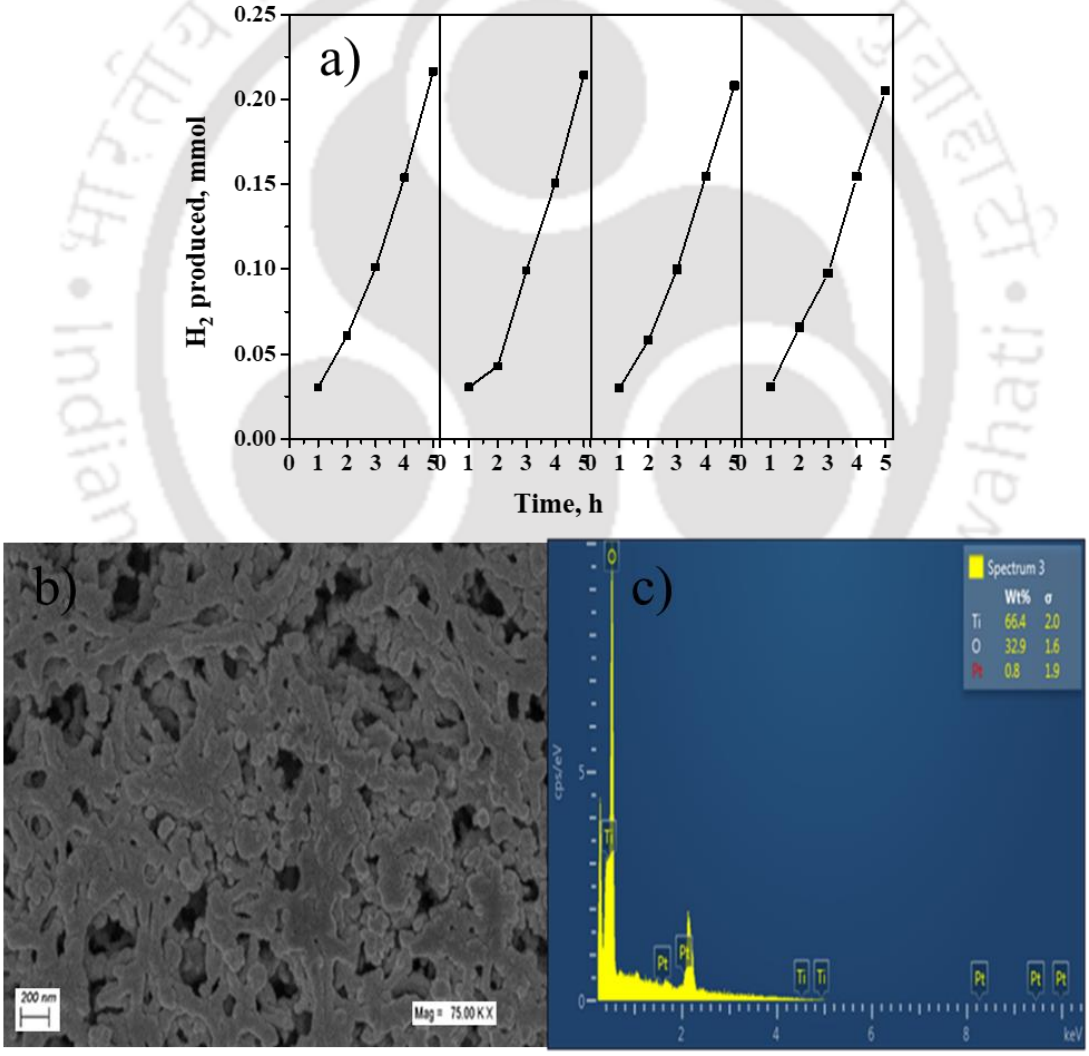

Figure 4.6: a) Catalyst stability test of Pt/TiO_2-8x film in the planar microreactor (The reaction conditions were similar to those used in Fig. 4.4); (b) FESEM and (c) EDX of the spent Pt/TiO_2-8x for recycle stability

Overall, the recycle stability tests showed that the activity of Pt/TiO_2-8x coating was maintained nearly constant for the 4 cycles of 5 h run which means that neither adsorption of reactive intermediates onto the active sites nor leaching of catalyst coating occurred that can cause catalyst deactivation and/or activity decrease.[32,35] This also confirms the stability, robustness and durability of this system.[36] Good recycle stability indicates the strong adherence of the catalyst films on the glass substrate. This helps in easy scalability of the optofluidic planar microreactor for practical applications.

4.2.2.4 Effect of simulated solar light (SSL) intensity

The effect of the SSL intensity (99.7 and 341.3 mW cm^{-2}) on the hydrogen production and its rate, over Pt/TiO_2-8x film, is shown in Figure 4.7. The water splitting experiments were conducted at a reactant flowrate of 0.3 mL min^{-1} using solar simulator with AM 1.5G filter as light source.

The amount of hydrogen produced was increased nearly linearly with time up to 5 h, over the Pt/TiO_2-8x film, for both the SSL intensities (Fig. 4.7a). The hydrogen production rate was increased with solar intensity (Fig. 4.7b). This could be attributed to the absorption of more photons at higher intensity leading to the generation of more electron-hole pairs.[29,32,35,37] The Pt/TiO_2-8x film with thickness 1650±119 nm showed a hydrogen production rate of 766 µmol h^{-1} g^{-1} and 0.22 µmol h^{-1} cm^{-2} at an avg. intensity of 99.7 mW cm^{-2}. The inset in Fig. 4.7b shows the image of planar microreactor with gas evolution over Pt/TiO_2-8x film under solar irradiation at 99.7 mW cm^{-2} intensity. The H_2 production rate increased by 3.9 times with increasing the SSL intensity from 99.7 to 341.3 mW cm^{-2} (3.4 times), indicating a linear increase in H_2 production rate with the light intensity.

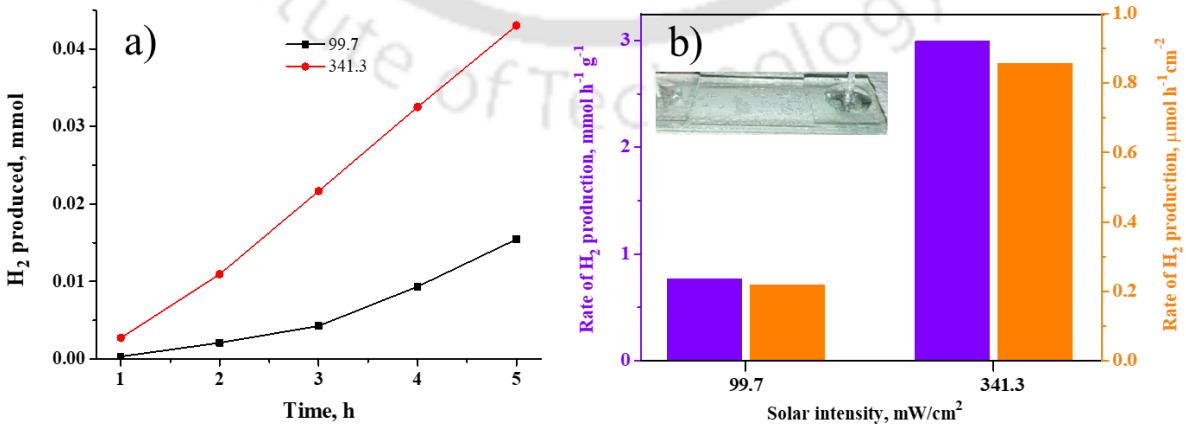

Figure 4.7: a) Hydrogen produced with run time; b) Rate of hydrogen production; at SSL intensities of 99.7 and 341.3 mW/cm^2 in the planar microreactor (Reaction conditions: Pt/TiO_2-

8x (1650 nm thick) catalyst, 20 vol.% methanol in DI water, 0.3 mL min^{-1} flowrate and 300 W xenon lamp with AM 1.5G filter as SSL source). The inset image shows gas evolution inside planar microreactor

In the experiments conducted with light irradiation from solar simulator, the reaction temperatures were 45 and 60 °C at the SSL intensities 99.7 and 341.3 mW cm^{-2}, respectively. While, the reaction temperature was 60 °C with MH lamp having an intensity of 318.5 mW cm^{-2}. The mentioned reaction temperatures were reached within 10 min of the start of experiment and remained constant thereafter. The increase in the H_2 production rate with increasing SSL intensity and with associated temperature increase is connected to the adsorption/desorption equilibria at the active sites of TiO_2 and also to the diffusion rates to and from the surface.[38,39] Velázquez et al.,[38] studied the effect of reaction temperature in the range of 5 to 60 °C on the photocatalytic hydrogen production via water splitting using Pt/TiO_2 powder catalyst under UV irradiance. They reported that the hydrogen production rate increased by a factor of 5.5 as the temperature increased from 5 to 60 °C, indicating the positive effect of reaction temperature on the photocatalytic water splitting. Zhang and Maggard.,[39] also reported that the photocatalytic reaction rate of H_2 evolution on Pt/TiO_2 measured at 58 °C was up to 2 times higher than the rate measured at room temperature. In this study, the H_2 production rate was increased by 3.9 times with increasing the SSL intensity from 99.7 to 341.3 mW cm^{-2} (3.4 times), along with a reaction temperature increase of 15 °C (from ~45 to 60 °C). The optimum temperature range for photocatalytic reactions is reported to be in the range of 20–80 °C.[40]

4.2.2.5 Effect of type of light source

In terms of hydrogen production rate, the 400 W MH lamp outperformed 300 W xenon based solar simulator by at least 5 times. The increase in the lamp power (or intensity) results in the increased number of visible light photons incident per unit area, which in turn generates more electron-hole pairs, leading to higher H_2 production. [41,42] To understand the reasons for higher activity with MH lamp, the intensity of MH lamp was calculated and the emission spectra of MH lamp compared with solar simulator [43]. The intensity of MH lamp at the microreactor surface was 318.5 mW cm^{-2}. The activity with MH lamp was higher even at the similar intensity as that of solar simulator (341.3 mW cm^{-2}). This could be because the MH lamp emits a high quality spectrum distribution [44], with strong peak at lower wavelength (~ 467 nm) as compared to that with solar simulator (~ 490 nm). The solar simulator spectrum is distributed broadly throughout the visible range. Moreover, the contribution of IR radiation

with the solar simulator was higher. Similar observations were reported in the literature. For example, Hisatomi et al.[45], studied the photocatalytic water splitting on $Rh_{2-y}Cr_yO_3$/Zn-Ga_2O_3 and reported at least 100 times higher photon absorption under irradiation by 450 W Hg lamp than that under 300 W Xe lamp.

4.2.2.6 Solar to hydrogen energy conversion efficiency (STH)

The solar to hydrogen energy conversion efficiency (STH) was calculated based on the following equation[46–48]:

$$\text{STH (\%)} = \frac{R_H \Delta G^0}{PS} \times 100 \quad \text{.....(4.2)}$$

where R_H, ΔG^0, P and S are the rate of hydrogen production (mmol s^{-1}), Gibbs free energy (237 kJ mol^{-1}), intensity of the light (mW cm^{-2}) and irradiated area (7.5 cm^2).

The calculated STH at the solar intensity of 99.7 mW cm^{-2} was 0.015%. The STH value increased slightly with increasing the solar light intensity (0.017% at 341.3 mW cm^{-2}). This STH value is within the range of the STH values (<0.1%) reported so far for most of the particulate photocatalysis (PC) systems.[49,50] The presence of methanol as SR eliminates the need of H_2/O_2 separation since it avoids the formation of O_2 and increases the safety of the process. The planar microreactor, being a continuous reaction system, has a great potential for large scale applications.

The united states department of energy (DOE) estimated the targeted threshold cost of hydrogen to be $ 4.0 per kg H_2, produced from photocatalytic water splitting process in presence of methanol. Zhao et al.[48] reviewed the feasibility of using methanol as SR. They reported that a hydrogen production rate of 1.29 mol h^{-1} m^{-2} under AM 1.5G light conditions is needed for the process to be economical at commercial scale, with a cost price of $ 4.0 per kg H_2. A hydrogen production rate of 0.22 µmol h^{-1} cm^{-2} (0.0022 mol h^{-1} m^{-2}) was obtained in this work. The production rate may further be improved by developing an effective photocatalyst with more solar light absorption and optimizing the catalyst amount. A maximum STH efficiency of 0.12% was reported for a large scale (~1 m^2) panel photoreactor using Pt/mesoporous carbon nitride coating under natural sunlight irradiation in presence of Triethanolamine as SR, untill now.[35] The thin film based reactors are easily scalable and preparation of large size panel (planar) reactors could be cheaper. This type of reactors even with the lower STH (3–5%) can economically compete with photo electrochemical (PEC) technology that has 10% STH.[51]

4.3 Conclusions

An optofluidic planar microreactor was fabricated and tested successfully for the photocatalytic water splitting in presence of methanol as sacrificial agent under visible light (400 W metal halide lamp) and simulated sun light (SSL, 300 W xenon lamp with AM1.5G filter) illumination. The rate of hydrogen production linearly increased with increasing catalyst coating thickness and solar light intensity. While it reached a maximum with increasing reactant flowrate. The highest rate of 16.35 mmol h^{-1} g^{-1} (4.7 µmol h^{-1} cm^{-2}) hydrogen production was obtained on the Pt/TiO_2 film of thickness 1650±119 nm at an optimum reactant flowrate of 0.3 mL min^{-1} using 20 vol.% methanol in DI water under visible light illumination. The recycle stability test proved the strong adherence of 1650±119 nm thick Pt/TiO_2 film, which is essential for scale up of planar microreactor. A SSL driven hydrogen production rate of 0.766 mmol h^{-1} g^{-1} (0.22 µmol h^{-1} cm^{-2}) with STH of 0.015% was obtained at ~100 mW cm^{-2} intensity.

References

(1) Larimi, A.; Rahimi, M.; Khorasheh, F. Carbonaceous Supports Decorated with Pt-TiO2 Nanoparticles Using Electrostatic Self-Assembly Method as a Highly Visible-Light Active Photocatalyst for CO2 Photoreduction. *Renew. Energy* **2020**, *145*, 1862–1869. https://doi.org/10.1016/j.renene.2019.07.105.

(2) Li, Z.; Li, B.; Hu, Y.; Wang, S.; Yu, C. Highly-Dispersed and High-Metal-Density Electrocatalysts on Carbon Supports for the Oxygen Reduction Reaction: From Nanoparticles to Atomic-Level Architectures. *Mater. Adv.* **2022**, *3* (2), 779–809. https://doi.org/10.1039/D1MA00858G.

(3) Sreethawong, T.; Yoshikawa, S. Enhanced Photocatalytic Hydrogen Evolution over Pt Supported on Mesoporous TiO2 Prepared by Single-Step Sol-Gel Process with Surfactant Template. *Int. J. Hydrogen Energy* **2006**, *31*, 786–796. https://doi.org/10.1016/j.ijhydene.2005.06.015.

(4) Sta, I.; Jlassi, M.; Hajji, M.; Boujmil, M. F.; Jerbi, R.; Kandyla, M.; Kompitsas, M.; Ezzaouia, H. Structural and Optical Properties of TiO2 Thin Films Prepared by Spin Coating. *J. Sol-Gel Sci. Technol.* **2014**, *72* (2), 421–427. https://doi.org/10.1007/s10971-014-3452-z.

(5) Zhu, Z.; Chen, J.; Su, K.; Wu, R. Efficient Hydrogen Production by Water-Splitting over Pt-Deposited C-HS-TiO2 Hollow Spheres under Visible Light. *J. Taiwan Inst. Chem. Eng.* **2016**, *60*, 222–228. https://doi.org/10.1016/j.jtice.2015.10.001.

(6) Kim, S.; Hwang, S.-J.; Choi, W. Visible Light Active Platinum-Ion-Doped TiO2 Photocatalyst. *J. Phys. Chem. B* **2005**, *109* (51), 24260–24267. https://doi.org/10.1021/jp055278y.

(7) Galeano, L.; Valencia, S.; Marín, J. M.; Restrepo, G.; Navío, J. A.; Hidalgo, M. C. Comparison of the Effects Generated by the Dry-Soft Grinding and the Photodeposition of Au and Pt Processes on the Visible Light Absorption and Photoactivity of TiO2. *Mater. Res. Express* **2019**, *6* (10). https://doi.org/10.1088/2053-1591/ab4316.

(8) Gogoi, D.; Namdeo, A.; Golder, A. K.; Peela, N. R. Ag-Doped TiO2 Photocatalysts with Effective Charge Transfer for Highly Efficient Hydrogen Production through Water Splitting. *Int. J. Hydrogen Energy* **2020**, *45* (4), 2729–2744. https://doi.org/10.1016/j.ijhydene.2019.11.127.

(9) Prathan, A.; Bhoomanee, C.; Ruankham, P.; Choopun, S.; Gardchareon, A.; Phadungdhitidhada, S.; Wongratanaphisan, D. Hydrothermal Growth of Well-Aligned TiO2 Nanorods on Fluorine-Doped Tin Oxide Glass. *Mater. Today Proc.* **2019**, *17*, 1514–1520. https://doi.org/10.1016/j.matpr.2019.06.176.

(10) Yang, Z.; Lu, J.; Ye, W.; Yu, C.; Chang, Y. Preparation of Pt/TiO2 Hollow Nanofibers with Highly Visible Light Photocatalytic Activity. *Appl. Surf. Sci.* **2017**, *392*, 472–480. https://doi.org/10.1016/j.apsusc.2016.09.065.

(11) Yu, J.; Yue, L.; Liu, S.; Huang, B.; Zhang, X. Hydrothermal Preparation and Photocatalytic Activity of Mesoporous Au-TiO2 Nanocomposite Microspheres. *J. Colloid Interface Sci.* **2009**, *334* (1), 58–64. https://doi.org/10.1016/j.jcis.2009.03.034.

(12) Antony, R. P.; Mathews, T.; Ramesh, C.; Murugesan, N.; Dasgupta, A.; Dhara, S.; Dash, S.; Tyagi, A. K. Efficient Photocatalytic Hydrogen Generation by Pt Modified TiO2

Nanotubes Fabricated by Rapid Breakdown Anodization. *Int. J. Hydrogen Energy* **2012**, *37*, 8268–8276. https://doi.org/10.1016/j.ijhydene.2012.02.089.

(13) Yu, J.; Qi, L.; Jaroniec, M. Hydrogen Production by Photocatalytic Water Splitting over Pt/TiO2 Nanosheets with Exposed (001) Facets. *J. Phys. Chem. C* **2010**, *114* (30), 13118–13125. https://doi.org/10.1021/jp104488b.

(14) Liqiang, J.; Yichun, Q.; Baiqi, W.; Shudan, L.; Baojiang, J.; Libin, Y.; Wei, F.; Honggang, F.; Jiazhong, S. Review of Photoluminescence Performance of Nano-Sized Semiconductor Materials and Its Relationships with Photocatalytic Activity. *Sol. Energy Mater. Sol. Cells* **2006**, *90* (12), 1773–1787. https://doi.org/10.1016/j.solmat.2005.11.007.

(15) Beatty, M. E. S.; Chen, H.; Labrador, N. Y.; Lee, B. J.; Esposito, D. V. Structure–Property Relationships Describing the Buried Interface between Silicon Oxide Overlayers and Electrocatalytic Platinum Thin Films. *J. Mater. Chem. A* **2018**, *6* (44), 22287–22300. https://doi.org/10.1039/C8TA06969G.

(16) Basu, S.; Paul, H.; Gopinath, C. S.; Bhaduri, S.; Lahiri, G. K. A MCM-41-Supported Platinum Carbonyl Cluster-Derived Asymmetric Hydrogenation Catalyst. *J. Catal.* **2005**, *229* (2), 298–302. https://doi.org/10.1016/j.jcat.2004.11.010.

(17) Wang, Y.; Lai, Q.; Zhang, F.; Shen, X.; Fan, M.; He, Y.; Ren, S. High Efficiency Photocatalytic Conversion of CO2 with H2O over Pt/TiO2 Nanoparticles. *RSC Adv.* **2014**, *4* (84), 44442–44451. https://doi.org/10.1039/C4RA07457B.

(18) Li, F. B.; Li, X. Z. The Enhancement of Photodegradation Efficiency Using Pt–TiO2 Catalyst. *Chemosphere* **2002**, *48* (10), 1103–1111. https://doi.org/10.1016/S0045-6535(02)00201-1.

(19) Nguyen, C.-C.; Nguyen, D. T.; Do, T.-O. A Novel Route to Synthesize C/Pt/TiO2 Phase Tunable Anatase–Rutile TiO2 for Efficient Sunlight-Driven Photocatalytic Applications. *Appl. Catal. B Environ.* **2018**, *226*, 46–52. https://doi.org/10.1016/j.apcatb.2017.12.038.

(20) Cubillos-Lobo, J. A.; Murcia-Mesa, J. J.; Guarín-Romero, J. R.; Rojas-Sarmiento, H. A.; Hidalgo-López, M. del C.; Navío-Santos, J. A. Study of the Visible Light Activity of Pt and Au-TiO2 Photocatalysts in Organic Pollutants Degradation. *Rev. Fac. Ing. Univ. Antioquia* **2017**, *0* (83 SE-Articles). https://doi.org/10.17533/udea.redin.n83a03.

(21) Jiang, Z.; Zhang, Z. Y.; Shangguan, W.; Isaacs, M. A.; Durndell, L. J.; Parlett, C. M. A.; Lee, A. F. Photodeposition as a Facile Route to Tunable Pt Photocatalysts for Hydrogen Production: On the Role of Methanol. *Catal. Sci. Technol.* **2016**, *6* (1), 81–88. https://doi.org/10.1039/c5cy01364j.

(22) Wenderich, K.; Han, K.; Mul, G. The Effect of Methanol on the Photodeposition of Pt Nanoparticles on Tungsten Oxide. *Part. Part. Syst. Charact.* **2018**, *35* (1), 1700250. https://doi.org/10.1002/ppsc.201700250.

(23) Matsubara, K.; Inoue, M.; Hagiwara, H.; Abe, T. Photocatalytic Water Splitting over Pt-Loaded TiO2 (Pt/TiO2) Catalysts Prepared by the Polygonal Barrel-Sputtering Method. *Appl. Catal. B Environ.* **2019**, *254* (April), 7–14. https://doi.org/10.1016/j.apcatb.2019.04.075.

(24) Filippo, E.; Carlucci, C.; Capodilupo, A. L.; Perulli, P.; Conciauro, F.; Corrente, G. A.;

Gigli, G.; Ciccarella, G. Enhanced Photocatalytic Activity of Pure Anatase Tio 2 and Pt-Tio 2 Nanoparticles Synthesized by Green Microwave Assisted Route. *Mater. Res.* **2015**, *18* (3), 473–481. http://dx.doi.org/10.1590/1516-1439.301914.

(25) Chen, D.; Li, F.; Ray, A. K. External and Internal Mass Transfer Effect on Photocatalytic Degradation. *Catal. Today* **2001**, *66* (2–4), 475–485. https://doi.org/10.1016/S0920-5861(01)00256-5.

(26) Zhan, X.; Yan, C.; Zhang, Y.; Rinke, G.; Rabsch, G.; Klumpp, M.; Schäfer, A. I.; Dittmeyer, R. Investigation of the Reaction Kinetics of Photocatalytic Pollutant Degradation under Defined Conditions with Inkjet-Printed TiO2 Films – from Batch to a Novel Continuous-Flow Microreactor. *React. Chem. Eng.* **2020**, *5* (9), 1658–1670. https://doi.org/10.1039/D0RE00238K.

(27) Lei, L.; Wang, N.; Zhang, X. M.; Tai, Q.; Tsai, D. P.; Chan, H. L. W. Optofluidic Planar Reactors for Photocatalytic Water Treatment Using Solar Energy. *Biomicrofluidics* **2010**, *4* (4), 043004. https://doi.org/10.1063/1.3491471.

(28) Ahsan, S. S.; Gumus, A.; Erickson, D. Redox Mediated Photocatalytic Water-Splitting in Optofluidic Microreactors. *Lab Chip* **2013**, *13*, 409–414. https://doi.org/10.1039/c2lc41129f.

(29) Cheng, X.; Chen, R.; Zhu, X.; Liao, Q.; An, L.; Ye, D.; He, X.; Li, S.; Li, L. An Optofluidic Planar Microreactor for Photocatalytic Reduction of CO2 in Alkaline Environment. *Energy* **2017**, *120*, 276–282. https://doi.org/10.1016/j.energy.2016.11.081.

(30) Li, L.; Chen, R.; Liao, Q.; Zhu, X.; Wang, G. High Surface Area Optofluidic Microreactor for Redox Mediated Photocatalytic Water Splitting. *Int. J. Hydrogen Energy* **2014**, *39*, 19270–19276. https://doi.org/10.1016/j.ijhydene.2014.05.098.

(31) Cheng, M.; Yang, S.; Chen, R.; Zhu, X.; Liao, Q.; Huang, Y. Copper-Decorated TiO2 Nanorod Thin Films in Optofluidic Planar Reactors for Efficient Photocatalytic Reduction of CO2. *Int. J. Hydrogen Energy* **2017**, *42* (15), 9722–9732. https://doi.org/10.1016/j.ijhydene.2017.01.126.

(32) Castedo, A.; Mendoza, E.; Angurell, I.; Llorca, J. Silicone Microreactors for the Photocatalytic Generation of Hydrogen. *Catal. Today* **2016**, *273*, 106–111. https://doi.org/10.1016/j.cattod.2016.02.053.

(33) Dundar, I.; Mere, A.; Mikli, V.; Krunks, M.; Oja Acik, I. Thickness Effect on Photocatalytic Activity of TiO2 Thin Films Fabricated by Ultrasonic Spray Pyrolysis. *Catalysts* **2020**, *10* (9), 1058. https://doi.org/10.3390/catal10091058.

(34) Yang, C.; Dong, W.; Cui, G.; Zhao, Y.; Shi, X.; Xia, X.; Tang, B.; Wang, W. Highly-Efficient Photocatalytic Degradation of Methylene Blue by PoPD-Modified TiO2nanocomposites Due to Photosensitization-Synergetic Effect of TiO2 with PoPD. *Sci. Rep.* **2017**, *7* (1), 3973. https://doi.org/10.1038/s41598-017-04398-x.

(35) Schrçder, M.; Kailasam, K.; Borgmeyer, J.; Neumann, M.; Thomas, A.; Schomäcker, R.; Schwarze, M. Hydrogen Evolution Reaction in a Large-Scale Reactor Using a Carbon Nitride Photocatalyst under Natural Sunlight Irradiation. *Energy Technol.* **2015**, *3* (10), 1014–1017. https://doi.org/10.1002/ente.201500142.

(36) Yousaf, A. Bin; Imran, M.; Zaidi, S. J.; Kasak, P. Highly Efficient Photocatalytic Z-

Scheme Hydrogen Production over Oxygen-Deficient WO3–x Nanorods Supported Zn0.3Cd0.7S Heterostructure. *Sci. Rep.* **2017**, *7* (1), 6574. https://doi.org/10.1038/s41598-017-06808-6.

(37) Cheng, X.; Chen, R.; Zhu, X.; Liao, Q.; He, X.; Li, S.; Li, L. Optofluidic Membrane Microreactor for Photocatalytic Reduction of CO2. *Int. J. Hydrogen Energy* **2016**, *41* (4), 2457–2465. https://doi.org/10.1016/j.ijhydene.2015.12.066.

(38) Velázquez, J. J.; Fernández-González, R.; Díaz, L.; Pulido Melián, E.; Rodríguez, V. D.; Núñez, P. Effect of Reaction Temperature and Sacrificial Agent on the Photocatalytic H2-Production of Pt-TiO2. *J. Alloys Compd.* **2017**, *721*, 405–410. https://doi.org/10.1016/j.jallcom.2017.05.314.

(39) Zhang, Z.; Maggard, P. A. Investigation of Photocatalytically-Active Hydrated Forms of Amorphous Titania, TiO2·nH2O. *J. Photochem. Photobiol. A Chem.* **2007**, *186* (1), 8–13. https://doi.org/10.1016/j.jphotochem.2006.07.004.

(40) Yang, Y.; Jing, D.; Zhao, L. Computational Fluid Dynamics Modeling of Reactive Multiphase Flow for Suspended Photocatalytic Water Splitting of Hydrogen Production System. *Appl. Therm. Eng.* **2020**, *173* (October 2019), 115220. https://doi.org/10.1016/j.applthermaleng.2020.115220.

(41) Ravichandran, K.; Sindhuja, E.; Uma, R.; Arun, T. Photocatalytic Efficacy of ZnO Films – Light Intensity and Thickness Effects. *Surf. Eng.* **2017**, *33* (7), 512–520. https://doi.org/10.1080/02670844.2016.1270797.

(42) Sampath, S.; Sellappa, K. Visible-Light-Driven Photocatalysts for Hydrogen Production by Water Splitting. *Energy Sources, Part A Recover. Util. Environ. Eff.* **2020**, *42* (6), 719–729. https://doi.org/10.1080/15567036.2019.1602194.

(43) Solar Spectrum, AM 1.5 G. *Scientech*. https://doi.org/http://www.sciencetech-inc.com/low-cost-solar-sim.

(44) Tawfik, M.; Tonnellier, X.; Sansom, C. Light Source Selection for a Solar Simulator for Thermal Applications: A Review. *Renew. Sustain. Energy Rev.* **2018**, *90*, 802–813. https://doi.org/10.1016/j.rser.2018.03.059.

(45) Hisatomi, T.; Miyazaki, K.; Takanabe, K.; Maeda, K.; Kubota, J.; Sakata, Y.; Domen, K. Isotopic and Kinetic Assessment of Photocatalytic Water Splitting on Zn-Added Ga2O3 Photocatalyst Loaded with Rh2−yCryO3 Cocatalyst. *Chem. Phys. Lett.* **2010**, *486* (4), 144–146. https://doi.org/10.1016/j.cplett.2010.01.006.

(46) Song, X.; Wei, G.; Sun, J.; Peng, C.; Yin, J.; Zhang, X.; Jiang, Y.; Fei, H. Overall Photocatalytic Water Splitting by an Organolead Iodide Crystalline Material. *Nat. Catal.* **2020**, *3* (12), 1027–1033. https://doi.org/10.1038/s41929-020-00543-4.

(47) Nishioka, S.; Yanagisawa, K. I.; Lu, D.; Vequizo, J. J. M.; Yamakata, A.; Kimoto, K.; Inada, M.; Maeda, K. Enhanced Water Splitting through Two-Step Photoexcitation by Sunlight Using Tantalum/Nitrogen-Codoped Rutile Titania as a Water Oxidation Photocatalyst. *Sustain. Energy Fuels* **2019**, *3* (9), 2337–2346. https://doi.org/10.1039/c9se00289h.

(48) Zhao, J.; Shi, R.; Li, Z.; Zhou, C.; Zhang, T. How to Make Use of Methanol in Green Catalytic Hydrogen Production? *Nano Sel.* **2020**, *1* (1), 12–29. https://doi.org/10.1002/nano.202000010.

(49) Yang, L.; Gao, P.; Lu, J.; Guo, W.; Zhuang, Z.; Wang, Q.; Li, W.; Feng, Z. Mechanism Analysis of Au, Ru Noble Metal Clusters Modified on TiO2(101) to Intensify Overall Photocatalytic Water Splitting. *RSC Adv.* **2020**, *10* (35), 20654–20664. https://doi.org/10.1039/d0ra01996h.

(50) Li, R.; Li, C. Photocatalytic Water Splitting on Semiconductor-Based Photocatalysts. In *Advances in Catalysis*; 2017; Vol. 60, pp 1–57. https://doi.org/10.1016/bs.acat.2017.09.001.

(51) Gopinath, C. S.; Nalajala, N. A Scalable and Thin Film Approach for Solar Hydrogen Generation: A Review on Enhanced Photocatalytic Water Splitting. *J. Mater. Chem. A* **2021**, *9* (3), 1353–1371. https://doi.org/10.1039/D0TA09619A.

Chapter 5

Visible Light Active IrO_2/TiO_2 films for Oxygen Evolution from Photocatalytic Water Splitting in an Optofluidic Planar Microreactor

Laxmi Prasad Rao Pala, Nageswara Rao Peela, Renewable Energy (2022) 197:902–910. https://doi.org/10.1016/j.renene.2022.08.017

5.1 Objectives

The current study focus on the fabrication of the optofluidic planar microreactor using TiO_2 coated glass with IrO_2 as co-catalyst and then photocatalytic water splitting is conducted using the planar microreactor for oxygen production with sodium iodate ($NaIO_3$) sacrificial agent (electron acceptor) in the presence of visible light. The IrO_2 hydrosol, an aqueous solution of nanoparticles was prepared and photo-deposited onto TiO_2 films, prepared using sol-gel spin coating technique. The effect of the photocatalyst film thicknesses and reactant flow rates on the oxygen evolution rates was studied. Recycle stability tests of IrO_2/TiO_2 film in the optofluidic planar microreactor were also conducted.

5.2 Results and discussion

5.2.1 Characterization of TiO_2 and IrO_2/TiO_2 films

The physicochemical and morphological properties of TiO_2 and IrO_2/TiO_2 photocatalysts was deduced in detail by characterizing the samples thoroughly using XRD, UV-vis spectroscopy, Photoluminescence spectroscopy, X-ray photoelectron spectroscopy, FESEM, FETEM, and EDX, and shown in Figure 5.1 and Figure 5.2.

5.2.1.1 X-ray diffraction pattern of the TiO_2 and IrO_2/TiO_2

The X-ray diffraction patterns of the TiO_2 and IrO_2/TiO_2 (Fig. 5.1a) showed that the peaks correspond to the anatase phase of TiO_2 only (JCPDS file no. 21-1272).[1,2] The diffraction peaks corresponding to IrO_2 were not observed due to either good dispersion of IrO_2 NPs on TiO_2 support or its lower content.[3,4] The crystallite sizes of TiO_2 and IrO_2/TiO_2, as estimated from Scherrer's equation, were 10.43 and 9.48 nm, respectively.[5]

5.2.1.2 Optical absorbance of the TiO_2 and IrO_2/TiO_2

The optical absorbance spectra of the TiO_2 and IrO_2/TiO_2, obtained from UV-Vis spectroscopy, are shown in Fig. 5.1b. The absorbance decreased in the UV region (<350 nm) and increased in the visible region (>380 nm) with the deposition of IrO_2 NPs onto TiO_2 surface. The absorption edges were red-shifted from 396 nm for TiO_2 to 410 nm for IrO_2/TiO_2. The TiO_2 has bandgap energy (E_g) of 3.10 eV and the IrO_2/TiO_2 of 2.84 eV as estimated from the Tauc plot (Fig. 5.1c).[6] The decrease in TiO_2 bandgap after IrO_2 deposition indicates the reduction in the minimum energy required to generate photocarriers (electron-holes pairs). This in turn enhances the photocatalytic performance by transferring the photogenerated holes from the TiO_2 valence band to IrO_2 NPs under visible light irradiation.[7,8]

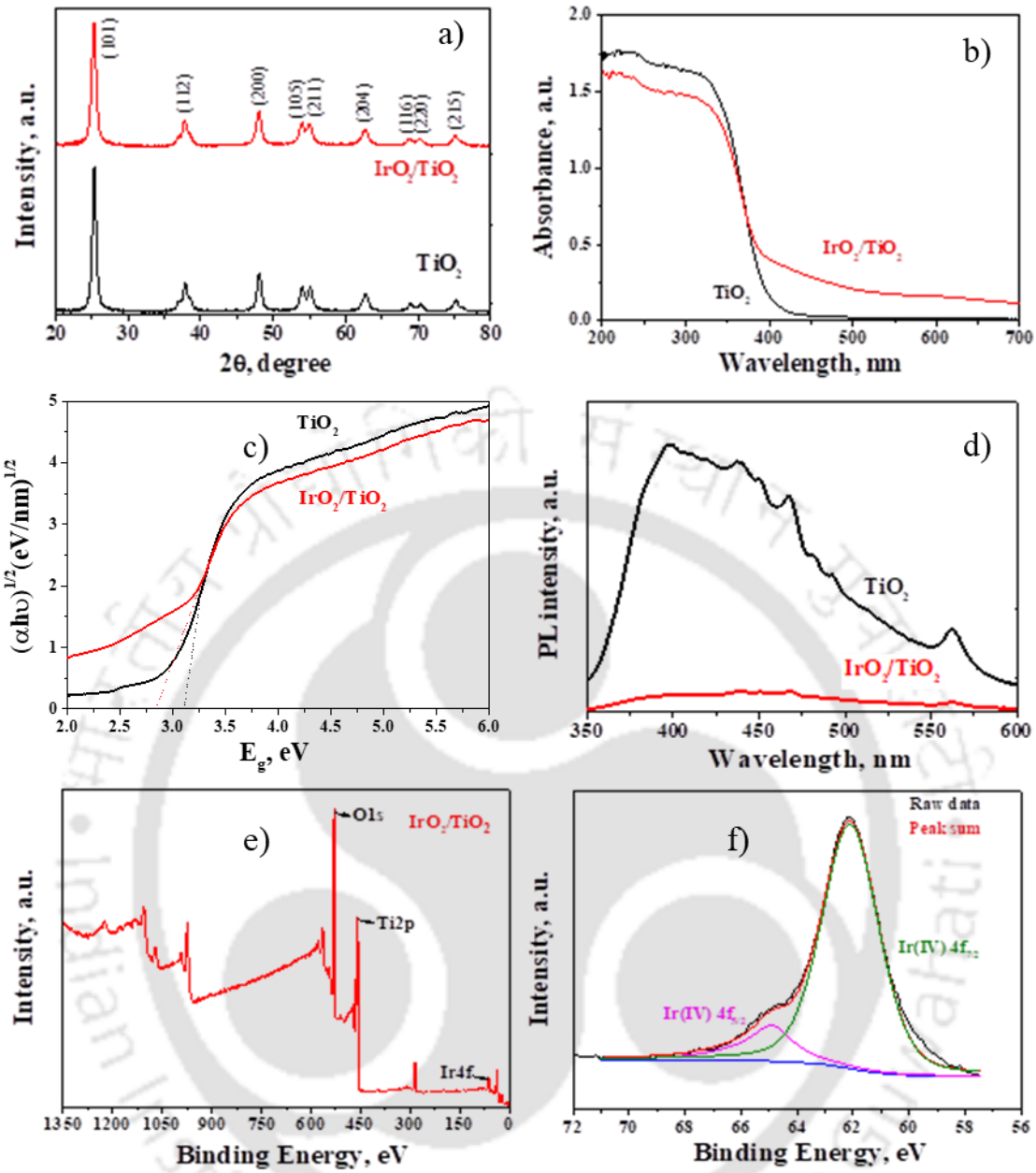

Figure 5.1: X-ray Diffraction (a), UV-Visible spectra (b), Tauc plot (c), Photoluminescence spectra (d) of the TiO_2 and IrO_2/TiO_2; X-ray photoelectron Survey spectrum (e) and high resolution Ir 4f (f)

5.2.1.3 Photoluminescence (PL) spectra for the TiO_2 and IrO_2/TiO_2

The photoluminescence (PL) study provides qualitative information on the electron-hole pair recombination rate. The PL spectra for the TiO_2 and IrO_2/TiO_2 are shown in Fig. 5.1d. The PL intensity of TiO_2 decreased significantly with the deposition of IrO_2 NPs. The reduction in intensity indicates an enhancement in the photogenerated electron-hole pair separation and a decrease in the recombination rate, which in turn improves the photocatalytic efficiency of the IrO_2/TiO_2.[9]

5.2.1.4 Chemical states of the IrO_2/TiO_2 catalyst by XPS

The chemical states of the IrO_2/TiO_2 catalyst were determined using X-ray photoelectron spectroscopy (XPS). Fig. 5.1e shows the survey spectrum of the IrO_2/TiO_2, confirming the presence of Ir, Ti, and O elements in IrO_2/TiO_2. Fig. 5.1f shows the peak fitting of the high resolution Ir 4f spectrum. The peaks corresponding to Ir $4f_{7/2}$ and Ir $4f_{5/2}$ were obtained at binding energies 62.1 and 64.9 eV, respectively[2], which are characteristic of the Ir^{4+} state[10], corresponding to the rutile phase of IrO_2.[11] The rutile phase of IrO_2 is known to be the best electrocatalyst for the water oxidation reaction.[12,13] Similar Ir 4f XPS spectra were reported in Ref. [14] The XPS data confirmed that the synthesis method followed in this work resulted in pure IrO_2 NPs without forming any other phase.

5.2.1.5 FETEM and EDX analysis of the IrO_2/TiO_2

The FETEM and EDX analysis of the IrO_2/TiO_2 are shown in Figure 5.2. A good dispersion of IrO_2 NPs on the TiO_2 surface was observed with only a few agglomerates. The particle size distribution (PSD) of IrO_2 NPs was in the range of 1–3 nm (Fig. 5.2b inset). The particle size was estimated considering approximately 1325 particles from the TEM image using the ImageJ analysis software. The fresh IrO_2/TiO_2 film was homogeneous and smooth, containing spherical shaped TiO_2 particles as observed from the FESEM images (Fig. 5.2c). The EDX analysis indicates that the IrO_2 concentration on TiO_2 film was ~ 5 wt.% (Fig. 5.2d), which was similar to the nominal concentration taken during the synthesis.

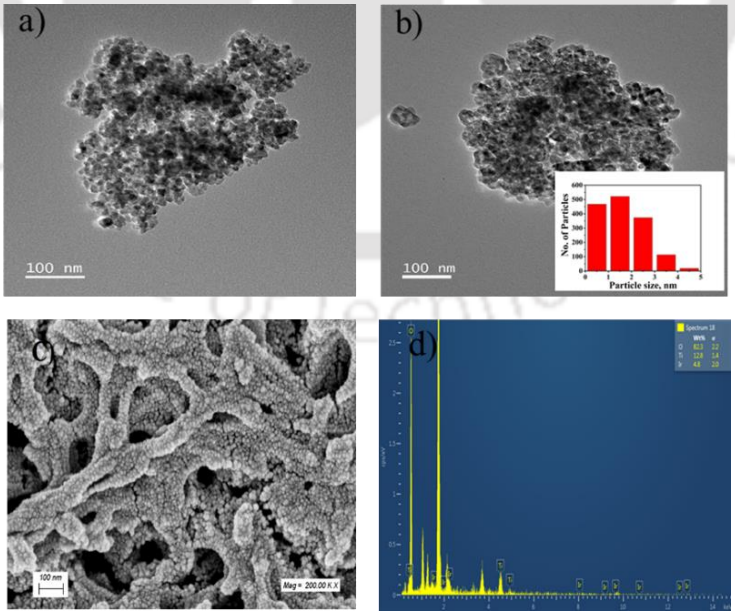

Figure 5.2: (a, b) Field Emission Transmission Electron Microscopic images, (c) Field Emission Scanning Electron Microscopic image, and (d) Energy Dispersive X-ray spectra of the fresh IrO_2/TiO_2-24x film; Fig. 5.2b inset: Particle Size Distribution

5.2.2 Catalytic testing: Oxygen production over IrO_2/TiO_2 films via photocatalytic water splitting

The oxygen evolution was not observed during the control experiments performed in the presence and absence of bare TiO_2 film in the planar microreactor under visible light illumination using 10 mM $NaIO_3$ aqueous solution. The control experiments with IrO_2/TiO_2 film resulted in no hydrogen production activity in the presence of visible light. Hence, the following water-splitting reactions were performed with 10 mM $NaIO_3$ aqueous solution as a reactant in the optofluidic planar microreactor over IrO_2/TiO_2 films under visible light illumination using a metal halide (MH) lamp.

The effect of parametric variation on the oxygen evolution is shown in Figure 5.3. The evolved oxygen increased with the run time at different reactant flowrates and film thicknesses (Fig.s 5.3a and b). All IrO_2 doped TiO_2 thin films showed a significant oxygen production rate (Fig. 5.3b), indicating that the films were photocatalytically active for OER in the presence of visible light illumination. The activity of IrO_2/TiO_2 films under visible light illumination was due to the absorption of visible light by the films as observed from UV-Vis spectroscopy (Fig.s 5.1b and c).

The effect of flowrate on oxygen evolution rate was studied over IrO_2/TiO_2-24x films. A maximum in the rate of oxygen production was obtained with the increase of flow rate (Fig. 5.3c), i.e., the oxygen production rate was increased up to 0.3 mL min^{-1} and then decreased slowly. The increase in the rate of oxygen production up to 0.3 mL min^{-1} indicates that the process was intruded by the external mass transfer resistance in the optofluidic planar microreactor at lower flow rates. Beyond 0.3 mL min^{-1}, the decrease in the oxygen production rate could be due to the decrease in the reactant residence times. Therefore, 0.3 mL min^{-1} was the optimal reactant flowrate where the maximum oxygen production rate was obtained.

The oxygen production rate was increased with the thickness of the films up to 3078 ± 362 nm (Fig. 5.3d). With an increase in the film thickness, more photogenerated carriers (e^--h^+ pairs) are generated by the absorption of more photons.[15–17] The photogenerated holes oxidize the water molecules, thereby increasing the oxygen production rate.

In the case of immobilized photocatalytic film, the three competing factors that determine the optimum film thickness are the catalyst surface area, internal mass transfer/diffusion, and absorption of incident light.

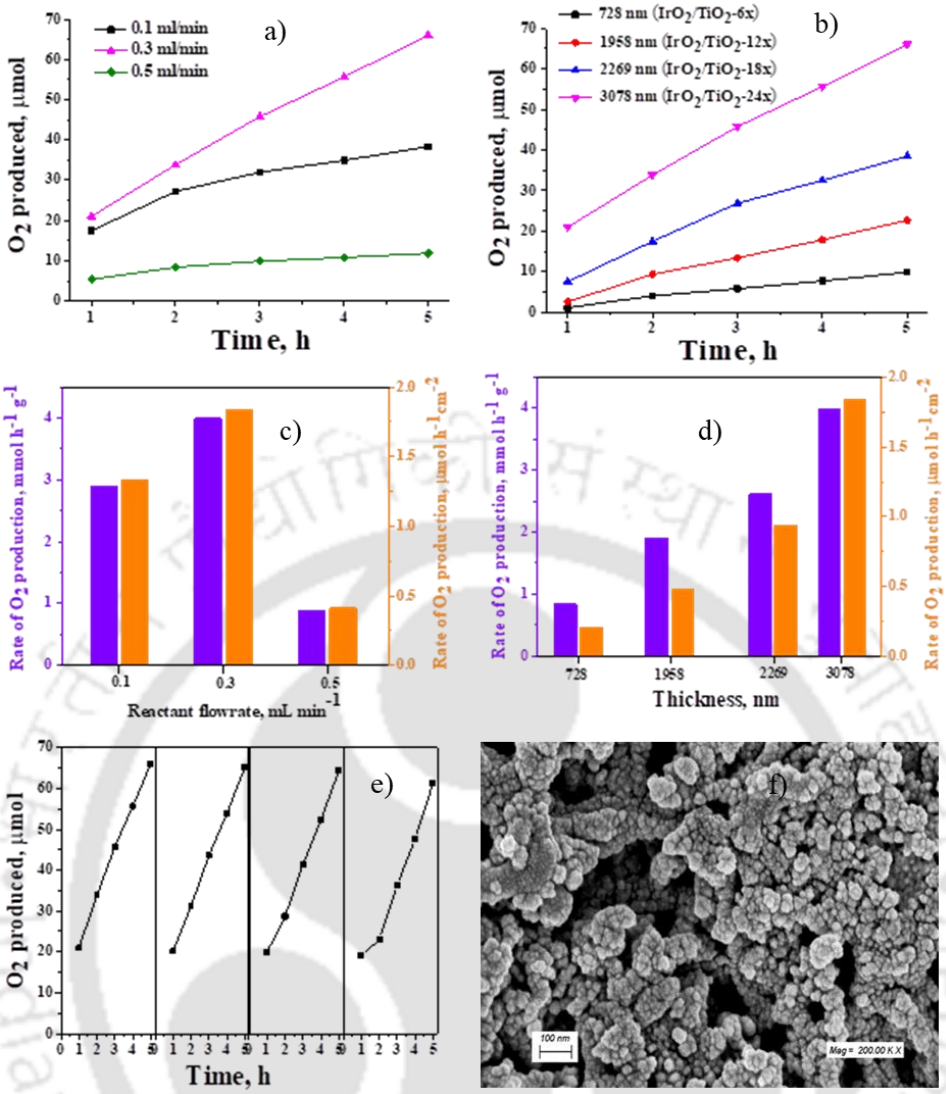

Figure 5.3: (a, b) Amount of oxygen produced against run time; (c, d) Rate of oxygen production with the variation of reactant flowrate and film thickness; e) Recycle stability of IrO_2/TiO_2-24x film, and f) FESEM image of IrO_2/TiO_2-24x film after recycle test

The initial increase in reaction rate with increasing the film thickness is because of the increase in the active surface area and light absorption. With further increasing the thickness, the reaction rate reaches a maximum at a certain value and then decreases. The decrease in the reaction rate is because of the dominance of the internal mass transfer resistance, which reduces the utilization of deeper layers. Moreover, the light absorption also decreases with the increase of film thickness.[18,19] The increased oxygen production rate with an increase in the thickness means that the light absorption increased and internal diffusional resistance was negligible [20–22] in the range of thicknesses studied here. The thickness studies were performed at the reactant flow rate of 0.3 mL min^{-1}. The IrO_2/TiO_2-24x film of 3078 ± 362 nm thickness exhibited the highest oxygen evolution with the photocatalytic activity of 3.99 mmol h^{-1} g^{-1} and 1.84 µmol

h^{-1} cm^{-2}. The optimum film thickness range for the maximum light absorption and hence solar water splitting activity is reported to be 8-12 µm for the TiO_2 films. [23] The TiO_2 film prepared by sol-gel spin coating, employed in this work, requires oven drying followed by high temperature calcination after every coating, which was very time consuming (Approximately one day is required for completing one coating cycle). A film with a thickness of 3 µm was obtained after 24 coating cycles, taking a very long time (approximately 24 days) to complete the coating process. Therefore, only the film thicknesses up to 3 µm were tested, even though an increase in the activity with thickness was observed up to this coating thickness. However, we are attempting different coating techniques to achieve thicker TiO_2 films with fewer coating cycles and good adherence (an ongoing work in our research group).

Recycle stability of the IrO_2/TiO_2-24x film in the planar microreactor is shown in Fig. 5.3e. Recycle experiment was performed using $NaIO_3$ aqueous solution, pumped at a flow rate of 0.3 mL min^{-1} in the presence of visible light. The catalyst film was refreshed after each cycle by feeding the fresh DI water through the microreactor for 10 min in the absence of light. A slight decrease in the activity after the 4^{th} cycle was observed as compared to that in the 1^{st} cycle. The slight decline in activity could be due to the TiO_2 catalyst particle aggregation, which increases particle size and thereby decreases active surface area.[24] The nanoparticles tend to form aggregates because of their high surface energy.[25] The FESEM images of the fresh and utilized IrO_2/TiO_2 film for recycle test are shown in Figs. 5.2c and 5.3f. Yasun et al.[26] reported that the higher the thickness of the layer, the more the TiO_2 particles in the film, and hence the higher the particle aggregation. On comparing the FESEM images of the Pt/TiO_2-8x [27] and IrO_2/TiO_2-24x films after recycle stability tests, the degree of TiO_2 particle aggregation increased with increasing the thickness, and thus the decrease in activity was more pronounced after 4 cycles for IrO_2/TiO_2-24x film. The EDX of the spent catalyst showed a similar Ir content as that of the fresh catalyst (Fig. 5.2d). Good recycle stability indicates that the catalyst films were adhered firmly onto glass, which is important for the scalability of the planar microreactor.[27]

In our previous work, we have developed Pt/TiO_2 films for hydrogen generation in the optofluidic planar microreactor using methanol as a sacrificial agent under visible light irradiation.[27] With IrO_2/TiO_2 film showing significant oxygen evolution in the present work, the scope for the further work will be to develop an overall water splitting photocatalyst, which will produce both hydrogen and oxygen simultaneously from the DI water only (without using any sacrificial agent) in the presence of visible light.

5.2.3 Proposed mechanism of photocatalytic water splitting over IrO_2/TiO_2 catalyst under visible light irradiation for oxygen evolution

The band structures of the IrO_2/TiO_2 and Pt/TiO_2 were examined from XPS valence band (VB) spectra. Determining the band edge positions of the valence band (VB) and conduction band (CB) is crucial as the edge positions signify the redox capability of the photocatalysts.[28] Figure 5.4 shows the VB spectra, bandedge diagram and oxygen evolution mechanism.

The XPS VB spectra of the IrO_2/TiO_2 and Pt/TiO_2 are shown in Fig. 5.4a. The Pt/TiO_2, a hydrogen evolution reaction photocatalyst employed in our previous work [27], was also included for reference. The VB edge potentials were obtained from the XPS VB spectra by extrapolating the intersection onto the binding energy (BE) axis (shown in orange). The CB edge potentials were obtained from the equation ($E_{CB} = E_{VB} – E_g$).[29] Table 5.1 shows the band edge potentials and bandgap energies of the samples.

Table 5.1: Band edge potentials and bandgap energies

Photocatalyst	Bandgap energy (E_g)	Valence band edge potential (E_{VB})	Conduction band edge potential (E_{CB})
IrO_2/TiO_2	2.84 eV	3.10 eV	0.26 eV
Pt/TiO_2	2.31 eV [27]	0.84 eV	-1.47 eV

Based on the VB and CB edge potentials, the band alignment diagram was constructed as shown in Fig. 5.4b. From the diagram, it can be observed that the IrO_2/TiO_2 has a VB potential more positive than the water oxidation potential, thereby making it capable of producing oxygen under visible light illumination. The Pt/TiO_2 has CB potential more negative than the water reduction potential, favoring a significant amount of hydrogen production in the presence of visible light irradiation.[27]

The mechanism for the photocatalytic oxygen production over IrO_2/TiO_2 was postulated based on the band edge position analysis and is shown in Fig. 5.4c. The TiO_2, with a bandgap of 3.10 eV (from UV-Vis analysis), produces electron-hole pairs under UV light only. After the photo-deposition of IrO_2 NPs, the bandgap of TiO_2 was narrowed down to 2.92 eV, indicating that the IrO_2/TiO_2 could generate electron-hole pairs under visible light illumination. The electrons are excited to the TiO_2 conduction band (CB), while the IrO_2 NPs capture the vacant holes at the TiO_2 valence band (VB). The captured holes participate in the water oxidation to form

oxygen and protons (H^+) on the IrO_2 co-catalyst surface. The excited electrons along with H^+ ions participate in the iodate reduction to iodine via iodide ion formation.

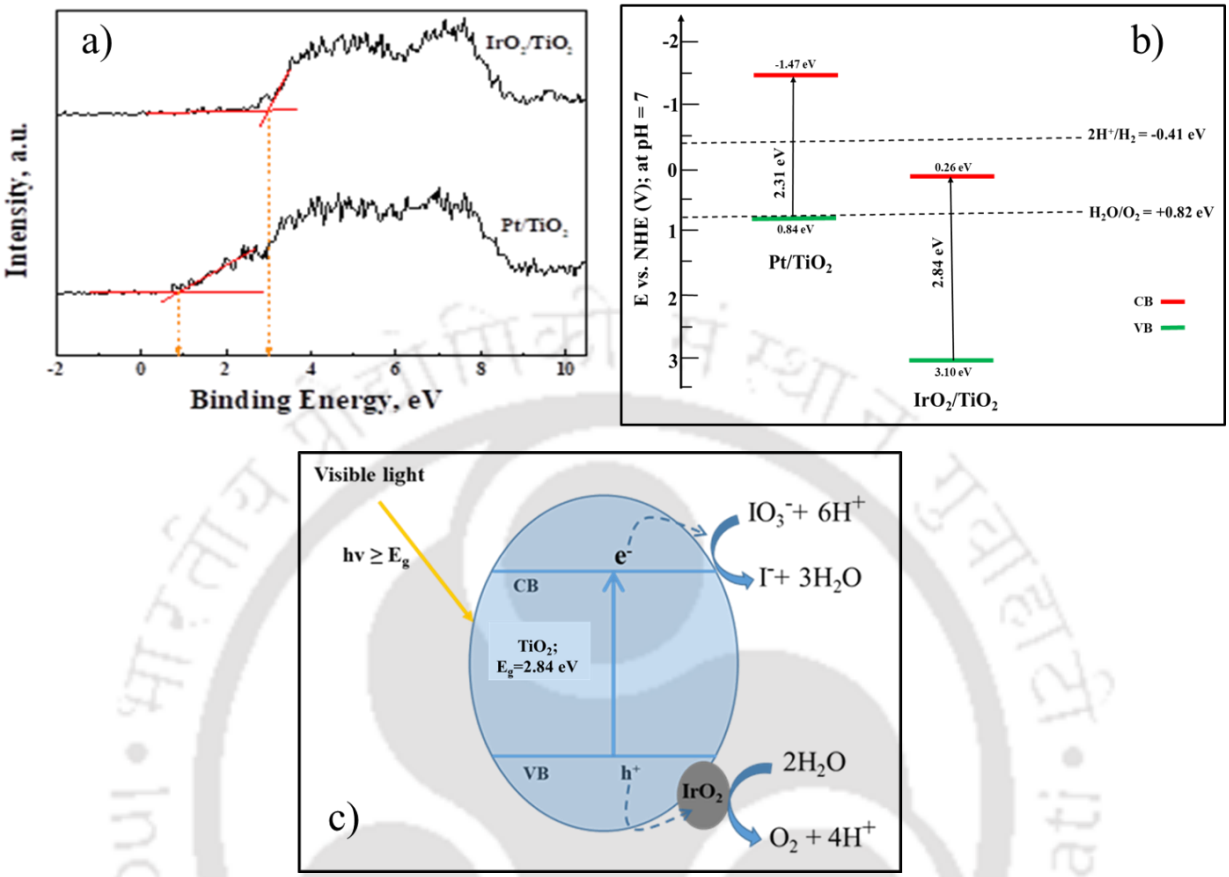

Figure 5.4: a) XPS valence band spectra; b) Band edge positions (Redox potentials of water at pH = 7; [30]); and c) Schematic diagram of oxygen evolution mechanism

The following are the reactions for consumption of $NaIO_3$ and oxygen evolution [31]:

$$IrO_2/TiO_2 \xrightarrow{hv>Eg} e^- + h^+(IrO_2) \quad (5.1)$$

$$2H_2O + 4h^+ \rightarrow O_2 + 4H^+ \quad (5.2)$$

$$IO_3^- + 5e^- + 6H^+ \rightarrow \frac{1}{2}I_2 + 3H_2O \quad (5.3)$$

The pH of the product solution after reactions was measured using a pH meter and found to be almost neutral. This indicates that the H^+ ions produced during OER were consumed in sodium iodate reduction.

5.3 Conclusions

The fabricated optofluidic planar microreactor, with IrO_2/TiO_2 film as photocatalyst, has been tested successfully for photocatalytic water splitting using sodium iodate as a sacrificial agent (electron acceptor) to produce oxygen under visible light irradiation. The oxygen production rate linearly increased with the increase in catalyst coating thickness and passed through a maximum with the increase in the reactant flowrate. An oxygen evolution rate of ~ 4 mmol h^{-1} g^{-1} and 1.84 µmol h^{-1} cm^{-2} was achieved on the IrO_2/TiO_2 film with a thickness of 3078 ± 362 nm at an optimal reactant (10 mM $NaIO_3$ in DI water) flowrate of 0.3 mL min^{-1} in the presence of visible light irradiation. The recycle study showed that the IrO_2/TiO_2 film was stable for 4 cycles of 5 h each. This indicates that the films were strongly adhered to the glass substrate, which is crucial for the long run use of the planar microreactor.

References

(1) Rui, Z.; Chen, L.; Chen, H.; Ji, H. Strong Metal-Support Interaction in Pt/TiO2 Induced by Mild HCHO and NaBH4 Solution Reduction and Its Effect on Catalytic Toluene Combustion. *Ind. Eng. Chem. Res.* **2014**, *53* (41), 15879–15888. https://doi.org/10.1021/ie5029107.

(2) Tian, J.; Zhao, P.; Zhang, S.; Huo, G.; Suo, Z.; Yue, Z.; Zhang, S.; Huang, W.; Zhu, B. Platinum and Iridium Oxide Co-Modified TiO2 Nanotubes Array Based Photoelectrochemical Sensors for Glutathione. *Nanomaterials* **2020**, *10* (3), 522. https://doi.org/10.3390/nano10030522.

(3) Ramadan, W.; Feldhoff, A.; Bahnemann, D. Assessing the Photocatalytic Oxygen Evolution Reaction of BiFeO3 Loaded with IrO2 Nanoparticles as Cocatalyst. *Sol. Energy Mater. Sol. Cells* **2021**, *232*, 111349. https://doi.org/10.1016/j.solmat.2021.111349.

(4) Dimitrova, N.; Banti, A.; Spyridou, O.-N.; Papaderakis, A.; Georgieva, J.; Sotiropoulos, S.; Valova, E.; Armyanov, S.; Tatchev, D.; Hubin, A.; Baert, K. Photodeposited IrO2 on TiO2 Support as a Catalyst for Oxygen Evolution Reaction. *J. Electroanal. Chem.* **2021**, *900*, 115720. https://doi.org/10.1016/j.jelechem.2021.115720.

(5) Sta, I.; Jlassi, M.; Hajji, M.; Boujmil, M. F.; Jerbi, R.; Kandyla, M.; Kompitsas, M.; Ezzaouia, H. Structural and Optical Properties of TiO2 Thin Films Prepared by Spin Coating. *J. Sol-Gel Sci. Technol.* **2014**, *72* (2), 421–427. https://doi.org/10.1007/s10971-014-3452-z.

(6) Prathan, A.; Bhoomanee, C.; Ruankham, P.; Choopun, S.; Gardchareon, A.; Phadungdhitidhada, S.; Wongratanaphisan, D. Hydrothermal Growth of Well-Aligned TiO2 Nanorods on Fluorine-Doped Tin Oxide Glass. *Mater. Today Proc.* **2019**, *17*, 1514–1520. https://doi.org/10.1016/j.matpr.2019.06.176.

(7) Ryu, W.-H.; Lee, Y. W.; Nam, Y. S.; Youn, D.-Y.; Park, C. B.; Kim, I.-D. Crystalline IrO2-Decorated TiO2 Nanofiber Scaffolds for Robust and Sustainable Solar Water Oxidation. *J. Mater. Chem. A* **2014**, *2* (16), 5610–5615. https://doi.org/10.1039/C4TA00339J.

(8) Zhu, Z.; Chen, J.; Su, K.; Wu, R. Efficient Hydrogen Production by Water-Splitting over Pt-Deposited C-HS-TiO2 Hollow Spheres under Visible Light. *J. Taiwan Inst. Chem. Eng.* **2016**, *60*, 222–228. https://doi.org/10.1016/j.jtice.2015.10.001.

(9) Yang, Z.; Lu, J.; Ye, W.; Yu, C.; Chang, Y. Preparation of Pt/TiO2 Hollow Nanofibers with Highly Visible Light Photocatalytic Activity. *Appl. Surf. Sci.* **2017**, *392*, 472–480. https://doi.org/10.1016/j.apsusc.2016.09.065.

(10) Bhanja, P.; Mohanty, B.; Patra, A. K.; Ghosh, S.; Jena, B. K.; Bhaumik, A. IrO2 and Pt Doped Mesoporous SnO2 Nanospheres as Efficient Electrocatalysts for the Facile OER and HER. *ChemCatChem* **2019**, *11* (1), 583–592. https://doi.org/10.1002/cctc.201801312.

(11) Pfeifer, V.; Jones, T. E.; Velasco Vélez, J. J.; Massué, C.; Arrigo, R.; Teschner, D.; Girgsdies, F.; Scherzer, M.; Greiner, M. T.; Allan, J.; Hashagen, M.; Weinberg, G.; Piccinin, S.; Hävecker, M.; Knop-Gericke, A.; Schlögl, R. The Electronic Structure of Iridium and Its Oxides. *Surf. Interface Anal.* **2016**, *48* (5), 261–273. https://doi.org/10.1002/sia.5895.

(12) Lee, Y.; Suntivich, J.; May, K. J.; Perry, E. E.; Shao-Horn, Y. Synthesis and Activities of Rutile IrO2 and RuO2 Nanoparticles for Oxygen Evolution in Acid and Alkaline Solutions. *J. Phys. Chem. Lett.* **2012**, *3* (3), 399–404. https://doi.org/10.1021/jz2016507.

(13) Frame, F. A.; Townsend, T. K.; Chamousis, R. L.; Sabio, E. M.; Dittrich, T.; Browning, N. D.; Osterloh, F. E. Photocatalytic Water Oxidation with Nonsensitized IrO2 Nanocrystals under Visible and UV Light. *J. Am. Chem. Soc.* **2011**, *133* (19), 7264–7267. https://doi.org/10.1021/ja200144w.

(14) Ma, Y.; Chong, R.; Zhang, F.; Xu, Q.; Shen, S.; Han, H.; Li, C. Synergetic Effect of Dual Cocatalysts in Photocatalytic H2 Production on Pd-IrOx/TiO2: A New Insight into Dual Cocatalyst Location. *Phys. Chem. Chem. Phys.* **2014**, *16* (33), 17734–17742. https://doi.org/10.1039/c4cp02567a.

(15) Lei, L.; Wang, N.; Zhang, X. M.; Tai, Q.; Tsai, D. P.; Chan, H. L. W. Optofluidic Planar Reactors for Photocatalytic Water Treatment Using Solar Energy. *Biomicrofluidics* **2010**, *4* (4), 043004. https://doi.org/10.1063/1.3491471.

(16) Castedo, A.; Mendoza, E.; Angurell, I.; Llorca, J. Silicone Microreactors for the Photocatalytic Generation of Hydrogen. *Catal. Today* **2016**, *273*, 106–111. https://doi.org/10.1016/j.cattod.2016.02.053.

(17) Cheng, X.; Chen, R.; Zhu, X.; Liao, Q.; An, L.; Ye, D.; He, X.; Li, S.; Li, L. An Optofluidic Planar Microreactor for Photocatalytic Reduction of CO2 in Alkaline Environment. *Energy* **2017**, *120*, 276–282. https://doi.org/10.1016/j.energy.2016.11.081.

(18) Padoin, N.; Soares, C. An Explicit Correlation for Optimal TiO2 Film Thickness in Immobilized Photocatalytic Reaction Systems. *Chem. Eng. J.* **2017**, *310*, 381–388. https://doi.org/10.1016/j.cej.2016.06.013.

(19) Kleiman, A.; Meichtry, J. M.; Vega, D.; Litter, M. I.; Márquez, A. Photocatalytic Activity of TiO2 Films Prepared by Cathodic Arc Deposition: Dependence on Thickness and Reuse of the Photocatalysts. *Surf. Coatings Technol.* **2020**, *382*, 125154. https://doi.org/10.1016/j.surfcoat.2019.125154.

(20) Dundar, I.; Mere, A.; Mikli, V.; Krunks, M.; Oja Acik, I. Thickness Effect on Photocatalytic Activity of TiO2 Thin Films Fabricated by Ultrasonic Spray Pyrolysis. *Catalysts* **2020**, *10* (9), 1058. https://doi.org/10.3390/catal10091058.

(21) Zhan, X.; Yan, C.; Zhang, Y.; Rinke, G.; Rabsch, G.; Klumpp, M.; Schäfer, A. I.; Dittmeyer, R. Investigation of the Reaction Kinetics of Photocatalytic Pollutant Degradation under Defined Conditions with Inkjet-Printed TiO2 Films – from Batch to a Novel Continuous-Flow Microreactor. *React. Chem. Eng.* **2020**, *5* (9), 1658–1670. https://doi.org/10.1039/D0RE00238K.

(22) Chen, D.; Li, F.; Ray, A. K. External and Internal Mass Transfer Effect on Photocatalytic Degradation. *Catal. Today* **2001**, *66* (2–4), 475–485. https://doi.org/10.1016/S0920-5861(01)00256-5.

(23) Gopinath, C. S.; Nalajala, N. A Scalable and Thin Film Approach for Solar Hydrogen Generation: A Review on Enhanced Photocatalytic Water Splitting. *J. Mater. Chem. A* **2021**, *9* (3), 1353–1371. https://doi.org/10.1039/D0TA09619A.

(24) Yang, C.; Dong, W.; Cui, G.; Zhao, Y.; Shi, X.; Xia, X.; Tang, B.; Wang, W. Highly-

Efficient Photocatalytic Degradation of Methylene Blue by PoPD-Modified TiO2nanocomposites Due to Photosensitization-Synergetic Effect of TiO2 with PoPD. *Sci. Rep.* **2017**, *7* (1), 3973. https://doi.org/10.1038/s41598-017-04398-x.

(25) Luo, B.; Song, R.; Jing, D. Particle Aggregation Behavior during Photocatalytic Ethanol Reforming Reaction and Its Correlation with the Activity of H2 Production. *Colloids Surfaces A Physicochem. Eng. Asp.* **2017**, *535*, 114–120. https://doi.org/10.1016/j.colsurfa.2017.09.035.

(26) Kannangara, Y. Y.; Wijesena, R.; Rajapakse, R. M. G.; de Silva, K. M. N. Heterogeneous Photocatalytic Degradation of Toluene in Static Environment Employing Thin Films of Nitrogen-Doped Nano-Titanium Dioxide. *Int. Nano Lett.* **2018**, *8* (1), 31–39. https://doi.org/10.1007/s40089-018-0230-x.

(27) Pala, L. P. R.; Peela, N. R. Green Hydrogen Production in an Optofluidic Planar Microreactor via Photocatalytic Water Splitting under Visible/Simulated Sunlight Irradiation. *Energy & Fuels* **2021**, *35* (23), 19737–19747. https://doi.org/10.1021/acs.energyfuels.1c02686.

(28) Cui, X.; Yang, X.; Xian, X.; Tian, L.; Tang, H.; Liu, Q. Insights into Highly Improved Solar-Driven Photocatalytic Oxygen Evolution over Integrated Ag3PO4/MoS2 Heterostructures. *Front. Chem.* **2018**, *6* (APR), 1–8. https://doi.org/10.3389/fchem.2018.00123.

(29) Gogoi, D.; Shah, A. K.; Rambabu, P.; Qureshi, M.; Golder, A. K.; Peela, N. R. Step-Scheme Heterojunction between CdS Nanowires and Facet-Selective Assembly of MnOx-BiVO4 for an Efficient Visible-Light-Driven Overall Water Splitting. *ACS Appl. Mater. Interfaces* **2021**, *13* (38), 45475–45487. https://doi.org/10.1021/acsami.1c11740.

(30) Li, X.; Yu, J.; Low, J.; Fang, Y.; Xiao, J.; Chen, X. Engineering Heterogeneous Semiconductors for Solar Water Splitting. *J. Mater. Chem. A* **2015**, *3* (6), 2485–2534. https://doi.org/10.1039/C4TA04461D.

(31) Iwase, Y.; Tomita, O.; Higashi, M.; Abe, R. Enhanced Oxygen Evolution on Visible Light Responsive TaON Photocatalysts Co-Loaded with Highly Active Ru Species for IO3- Reduction and Co Species for Water Oxidation. *Sustain. Energy Fuels* **2017**, *1* (4), 748–754. https://doi.org/10.1039/c7se00110j.

Chapter 6

Green hydrogen and oxygen production over $IrO_2/Pt/TiO_2$ via photocatalytic overall water splitting under visible light illumination

Laxmi Prasad Rao Pala, Nageswara Rao Peela (Renewable Energy, under review 2023)

6.1 Objectives

In the previous chapters 4 and 5, we have developed a Pt/TiO_2 photocatalyst for the hydrogen production and IrO_2/TiO_2 photocatalyst for the oxygen production under visible light irradiation. The activity of these photocatalysts was observed only when sacrificial agents such as methanol and sodium iodate were present in the water. The POWS activity was not observed using either Pt/TiO_2 or IrO_2/TiO_2 from pure water. Therefore, in the present work, we have attempted to develop a TiO_2 based photocatalyst using Pt and IrO_2 as cocatalysts for hydrogen and oxygen production from pure water without any sacrificial agents in presence of the visible light and simulated sunlight illumination. The effect of the various parameters such as catalyst loading, cocatalyst loading, stirring speed and solar light intensity on the rate of hydrogen and oxygen production from POWS was studied in detail. The catalyst performance tests were conducted using the particle suspension (batch) reactor. In addition, long term stability test was conducted to understand the durability of the photocatalyst.

6.2 Results and discussion

6.2.1 Characterization of $IrO_2/Pt/TiO_2$ photocatalysts

6.2.1.1 X-ray diffraction (XRD) of the $IrO_2/Pt/TiO_2$

Figure 6.1 shows the XRD patterns of the $IrO_2/Pt/TiO_2$ photocatalysts. The XRD peaks corresponding to the TiO_2 anatase phase were observed for all the synthesized catalysts (Fig. 6.1a, b).[1,2] A small shift to higher 2θ values was observed for the IrO_2/Pt impregnated/doped TiO_2 as compared to those of bare TiO_2, indicating the lattice deformation of doped TiO_2 samples.[3] The increase in shift to higher 2θ values with increasing the IrO_2 and Pt loadings suggests the migration of IrO_2 and Pt into TiO_2 lattice from its surface.[4] The smaller atomic radius of Pt (1.35 Å) and Ir (1.35 Å) than Ti (1.40 Å) could be the reason for the peak shift to higher 2θ.[5,6] It is possible that the migration of IrO_2 or Pt into TiO_2 lattice could have occurred when doped individually (Chapter 4 and 5). However, the degree in shift to higher 2θ values might be too small to notice any difference. Soundarya et al.[7], prepared the Pt doped TiO_2 nanotubes and studied photocatalytic H_2 generation through water splitting using ethanol sacrificial agent. They reported the shift in (101) peak to higher diffraction angle and attributed to the lattice distortion caused by the migration of the Pt into TiO_2 lattice.

The XRD peaks corresponding to IrO_2 were not observed at IrO_2 loading below 1 wt.%, because of either low content or good dispersion.[8,9] Two additional peaks at 2θ 31.8 and 45.5° were observed with increasing the IrO_2 loading above 1 wt.%, at a Pt loading of 0.5 wt.% (Fig. 6.1c). These peaks correspond closely with the rutile structure of IrO_2.[10] Similarly, two

additional peaks at 2θ of 56.5 and 66.2° were observed with increasing the Pt loading above 0.5 wt.%, at the IrO_2 loading of 2.5 wt.% (Fig. 6.1d). These peaks correspond closely to the Pt oxide (PtO) phase and metallic platinum (Pt), respectively.[11] The crystallite size of $IrO_2/Pt/TiO_2$ catalysts (Table B.1 in Appendix B) was estimated from Scherrer's equation.[12] All the synthesized catalysts have crystallite sizes smaller than that of TiO_2 (13.66 nm). The crystallite size increased with increasing the IrO_2 loading and decreased with increasing the Pt loading, up to 2.5 wt.%. A similar trend was reported in Ref[13,14]. The variation of crystallite size of the synthesized catalysts is related to the location and incorporation of Pt(IV) and Ir(IV) in the TiO_2 lattice. It was reported that the optimal crystallite size is required to balance activity and stability because smaller nanoparticles are prone to faster dissolution/deactivation and thus not beneficial.[15]

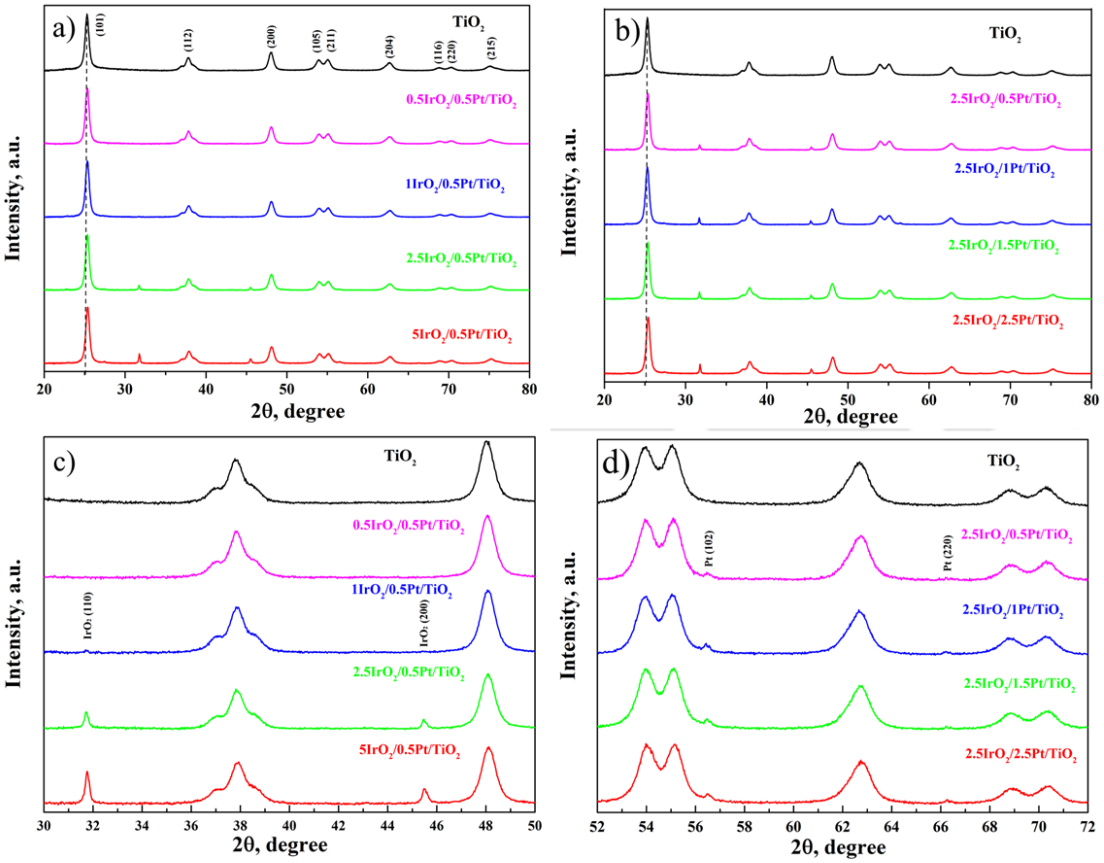

Figure 6.1: XRD patterns of the $IrO_2/Pt/TiO_2$ photocatalysts: a) IrO_2 loading; b) Pt loading; c) IrO_2 loading-enlarged; and d) Pt loading- enlarged;

6.2.1.2 UV-Vis spectroscopy of the $IrO_2/Pt/TiO_2$

Figure 6.2 shows the UV-Vis spectra, Tauc plots and PL spectra of the $IrO_2/Pt/TiO_2$ photocatalysts. The absorbance in the visible region with the wavelength range 350–700 nm

was significantly increased for the TiO_2 upon the addition of IrO_2 and Pt (Fig. 6.2a, b). The red shift in absorption edges was observed with the deposition of IrO_2 and Pt NPs onto TiO_2, indicating that synthesized photocatalysts have enhanced visible light utilization efficiency for splitting the water to produce H_2 and O_2.[16] The Pt oxide phase (i.e., PtO) along with the metallic Pt contributes to the visible light absorption by the photosensitization of Pt/TiO_2 samples.[17,18] The IrO_2 NPs when loaded on to TiO_2 caused the absorption edge to shift to higher wavelength and resulted in the decrease of the bandgap energy, thereby allowing IrO_2/TiO_2 samples to absorb visible light.[19] Therefore, the visible light absorption of the $IrO_2/Pt/TiO_2$ photocatalysts is caused by the presence of Pt, PtO and IrO_2 phases. The absorption edges for the photocatalysts are given in Table B.1 in Appendix B. The indirect bandgap energies (E_g) of the photocatalysts were estimated from the Tauc plots (Fig. 6.2c, d) and presented in Table B.1 in Appendix B. The bandgaps were obtained from the Tauc plots by extrapolating the tangent line to the wavelength axis at zero absorbance.

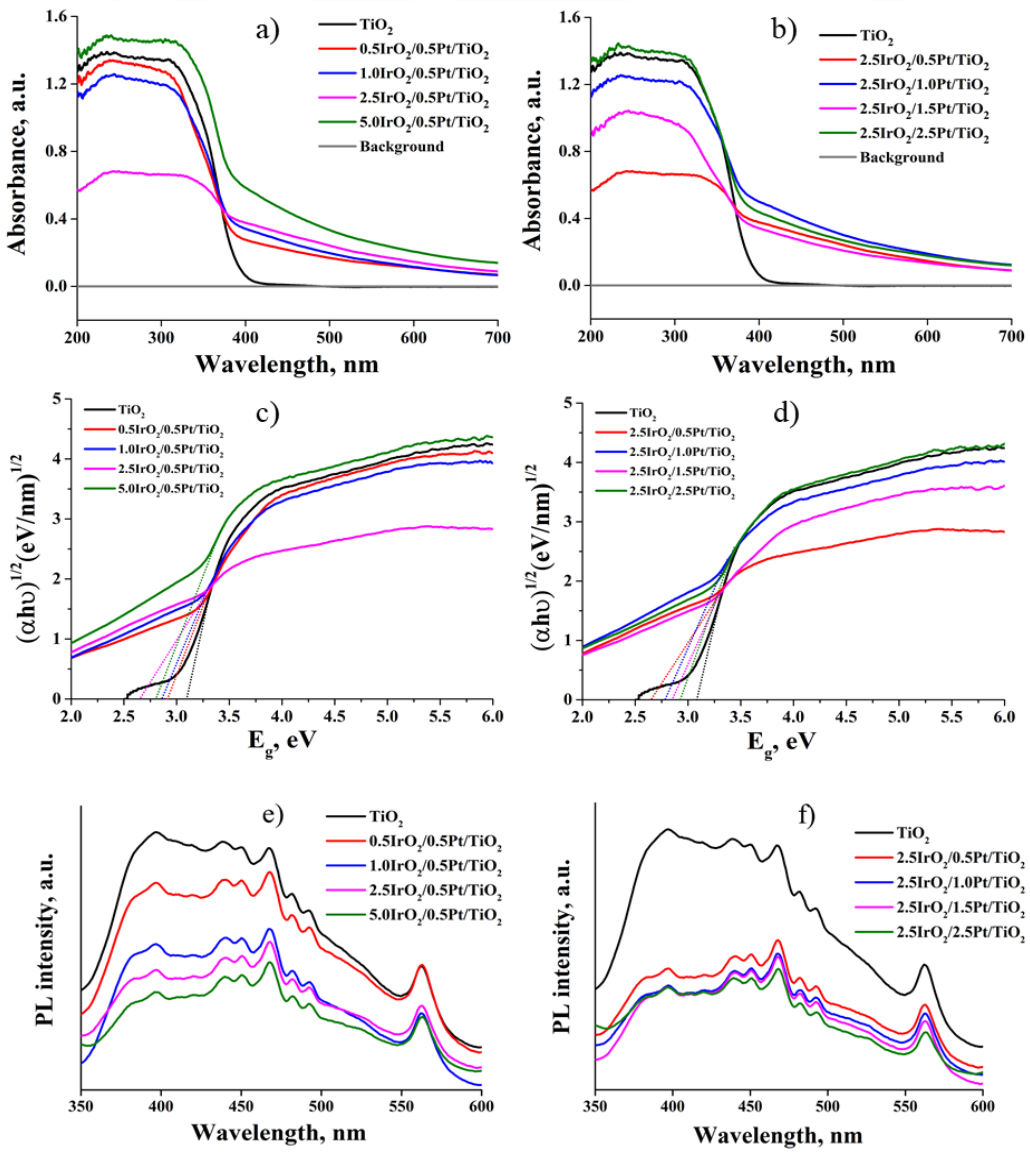

Figure 6.2: (a, b) UV-Vis absorbance spectra, (c, d) Tauc plots and (e, f) PL spectra of the $IrO_2/Pt/TiO_2$ photocatalysts, with variation of IrO_2 and Pt loading

All cocatalyst loaded TiO_2 photocatalysts have bandgap energies lower than that of bare TiO_2 (3.10 eV). The bandgap energy decreased with increasing IrO_2 loading up to 2.5 wt.% (from 2.91 to 2.66 eV) at the Pt loading of 0.5 wt.%, while the bandgap energy increased with increasing Pt loading (from 2.66 to 2.93 eV) at the IrO_2 loading of 2.5 wt.%. The bandgap energy increases with the decrease in crystallite size and vice versa.[20,21] The same trend was observed with the variation of IrO_2 and Pt loadings. The photocatalyst, $2.5IrO_2/0.5Pt/TiO_2$, exhibited the lowest bandgap energy of 2.66 eV. The smaller bandgap energy indicates the increased light absorption in the visible range.[22,23] The reduction in bandgap energy for the cocatalyst loaded TiO_2 photocatalysts, compared to bare TiO_2, indicates that the minimum energy required for the generation of the electron-hole pairs significantly decreased and photoexcitation occurs easily.

6.2.1.3 Photoluminescence (PL) analysis of the $IrO_2/Pt/TiO_2$

The PL spectroscopic study gives the qualitative information on the recombination rate of the electron-hole pairs. The PL spectra for the $IrO_2/Pt/TiO_2$ photocatalysts are shown in Fig. 6.2(e, f). The PL intensity decreased significantly for the $IrO_2/Pt/TiO_2$ photocatalysts, compared to that of bare TiO_2 support. The reduction in PL intensity indicates that the separation of the photogenerated electron-hole pair enhanced considerably and results in the decrease of the recombination rates. The electrons and holes generated on TiO_2 photocatalyst upon incidence of light will be transferred to its surface. Then, the Pt cocatalyst captures electrons from the TiO_2 conduction band (CB) and the IrO_2 cocatalyst captures holes from the TiO_2 valence band (VB). Thus, the charge transfer is effective and the recombination rate is lower. The captured electrons and holes participate in the water redox reactions to produce H_2 and O_2, in higher number, resulting in the improved photocatalytic efficiency of the $IrO_2/Pt/TiO_2$.[24] The transfer pathway of electrons and holes to Pt and IrO_2 cocatalysts was established in our previous works [17,19] and also reported in Refs [2,25].

6.2.1.4 X-ray photoelectron spectroscopy (XPS) of the $IrO_2/Pt/TiO_2$

The XPS analysis gives the information about the chemical phases present in the $IrO_2/Pt/TiO_2$ photocatalysts.[2] The XPS survey spectra confirmed the presence of Ir4f, Pt4f, Ti2p and O1s in all the synthesized $IrO_2/Pt/TiO_2$ photocatalysts (Figure 6.3). The Ir4f and Pt4f peak intensities increased with increasing the IrO_2 and Pt loadings.

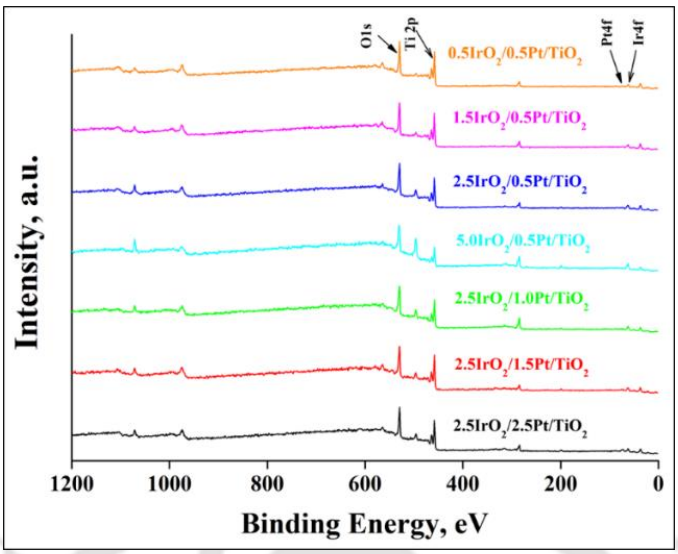

Figure 6.3: XPS survey spectra of the $IrO_2/Pt/TiO_2$ photocatalysts

High resolution XPS spectra of the Ir4f (a), Pt4f (b), Ti2p (c), and O1s (d) regions for the $IrO_2/Pt/TiO_2$ photocatalysts is shown in Figure 6.4. The XPS peak fitting for the high resolution Ir4f, Pt4f, Ti2p, and O1s spectral regions of the $IrO_2/Pt/TiO_2$ catalysts is shown in Fig. 6.4(a-d). The high resolution XPS spectra for the TiO_2, 1wt.%Pt/TiO_2 [17], and 5wt.%IrO_2/TiO_2 [19] from our previous works were included for reference. The binding energies (BE) obtained from the peak fitting analysis for all the synthesized photocatalysts are shown in Table B.2 in Appendix B. The high-resolution spectra of Pt4f and Ir4f regions show the presence of Pt^0, Pt^{2+} and Ir^{4+} phases in all the synthesized $IrO_2/Pt/TiO_2$ catalysts (Fig. 6.4a, b). Compared to BEs of the bulk metal Pt, PtO, and rutile IrO_2 [10,11], the observed BEs for the Pt^0, Pt^{2+} and Ir^{4+} phases were positive shifted to the higher values in the synthesized $IrO_2/Pt/TiO_2$ catalysts. This demonstrates the strong interaction of Pt and IrO_2 with the TiO_2 support.[26,27] On comparing with IrO_2/TiO_2 catalyst, all the $IrO_2/Pt/TiO_2$ catalysts exhibited similar BE indicating the rutile structure of IrO_2. A small shift in BE to higher values was observed for the catalysts at 5 wt.% IrO_2 loading and Pt loadings of 1 and 1.5 wt.% (Table B.2 in Appendix B). This shift to higher BE for the Ir^{4+} state indicates that the electronic charge density of Ir is decreased rather than forming Ir^{3+} with a reverse core level shift.[28,29] On comparing with Pt/TiO_2 catalyst, the BEs for the Pt^0 phase for the $IrO_2/Pt/TiO_2$ catalysts remained the same indicating that the electronic configuration of the metallic Pt remained unaffected. A slight shift in BEs of the Pt^{2+} phase to lower values was observed for the catalysts with IrO_2 loading below 2.5 wt.% (Table B.2 in Appendix B). This shift to lower BE for the Pt^{2+} state indicates that the electronic charge density

of Pt^{2+} could have improved.[30,31] The BE of Pt^{2+}4f decreased, Ir^{4+}4f increased, and Pt^{0}4f unaltered for the $IrO_2/Pt/TiO_2$ catalysts compared to Pt/TiO_2 and IrO_2/TiO_2. The reason could be that the Pt-IrO_2 particle-particle interactions were significant in the $IrO_2/Pt/TiO_2$ catalysts.[32]

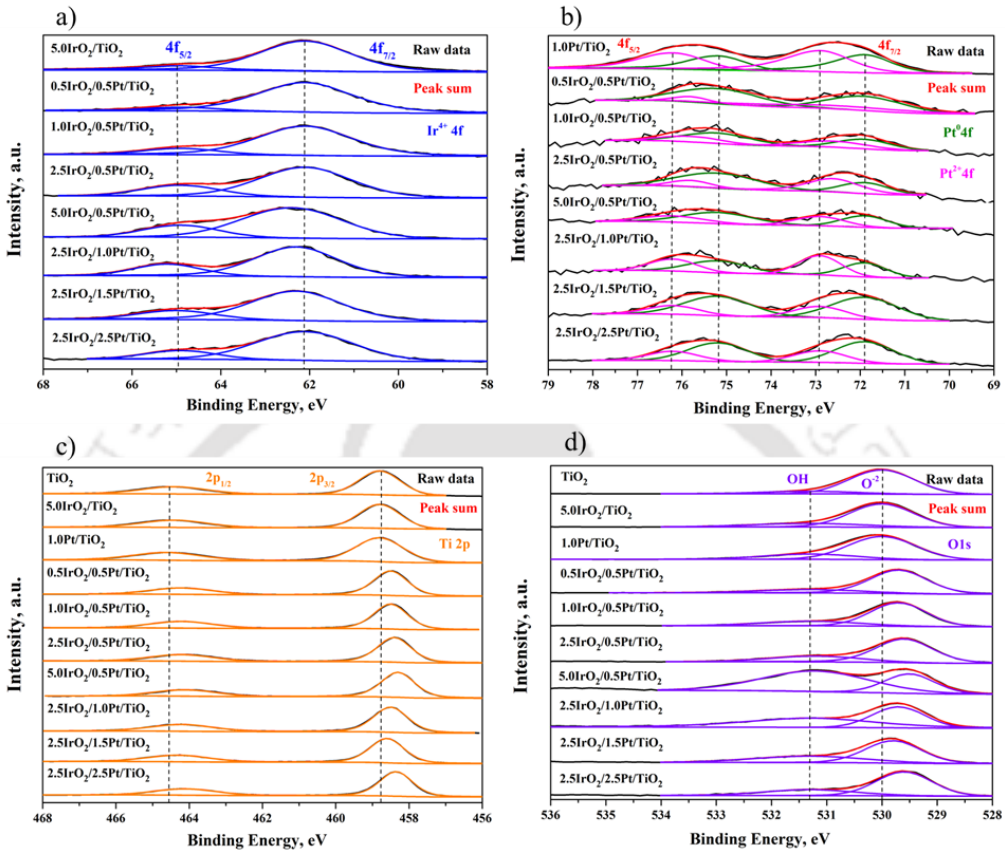

Figure 6.4: High resolution XPS spectra of the Ir4f (a), Pt4f (b), Ti2p (c), and O1s (d) regions for the $IrO_2/Pt/TiO_2$ photocatalysts

The Ti2p peak fitting (Fig. 6.4c) shows that the obtained BE correspond to the presence of Ti^{4+} state with the spin orbital splitting energy of 5.6 – 5.8 eV. The BE of Ti2p were shifted to lower values for the $IrO_2/Pt/TiO_2$ catalysts compared to TiO_2, Pt/TiO_2 and IrO_2/TiO_2, indicating that the Pt and IrO_2 cocatalysts are doped into TiO_2 lattice.[33] The O1s peak fitting (Fig. 6.4d) shows the presence of the lattice oxygen (O^{2-}) and hydroxyl group (OH^{-}) for all the catalysts. Similar to Ti2p, the BE of lattice oxygen shifted to lower values for the $IrO_2/Pt/TiO_2$ catalysts compared to TiO_2, Pt/TiO_2 and IrO_2/TiO_2, which also indicates that the incorporation of Pt and IrO_2 cocatalysts into TiO_2 lattice was by doping.[34]

The surface composition of Pt^{0}, Pt^{2+}, Ir^{4+}, Ti2p and O1s phases present in the $IrO_2/Pt/TiO_2$ are presented in Table B.3 in Appendix B. An increase in the Ir4f and Pt4f amounts was observed with increasing the IrO_2 and Pt loading on TiO_2, respectively. The ratio of Ir4f/IrO_2 loading

was decreased, whereas the ratio of Pt4f/Pt loading remained nearly constant. The observed decrease in the ratio of Ir4f/IrO_2 loading could indicate the migration of IrO_2 from the surface to the lattice of TiO_2 with increasing the IrO_2 loading. It is to be noted that the Pt and IrO_2 were sequentially deposited on TiO_2, with Pt deposited first.

The O^{2-}/Ti^{4+} ratios for the $IrO_2/Pt/TiO_2$ catalysts were lowered compared to bare TiO_2 (2.19). Interestingly, the O^{2-}/Ti^{4+} ratio of 2 was obtained for the $2.5IrO_2/0.5Pt/TiO_2$ catalyst, which is of the stoichiometric TiO_2.[35–37] The total O1s/Ti2p ratios for the $IrO_2/Pt/TiO_2$ catalysts were significantly varied compared to bare TiO_2 (2.52). This can be ascribed to the presence of Pt and IrO_2 doped onto TiO_2.[38] The O1s/Ti2p ratio for bare TiO_2 (2.52) was higher than the stoichiometric value of 2. This could be due to the moisture (absorbed water) presence on the commercial TiO_2.

6.2.1.5 Band structures of the $IrO_2/Pt/TiO_2$ photocatalysts

The redox capability of the photocatalyst is determined by the band edge potentials of the valence band (VB) and conduction band (CB).[19] The CB should be more negative than the proton (H^+) reduction (PR) potential (E = -0.41V) and the VB should be more positive than the water oxidation (WO) potential (E = +0.82V) for the hydrogen and oxygen evolution to occur.[39] The VB potentials obtained from the XPS VB spectra and the CB potentials obtained from the equation ($E_{CB} = E_{VB} - E_g$), were given in Table B.1 in Appendix B. The band alignment diagram (Figure 6.5) was developed based on the CB and VB edge potentials.

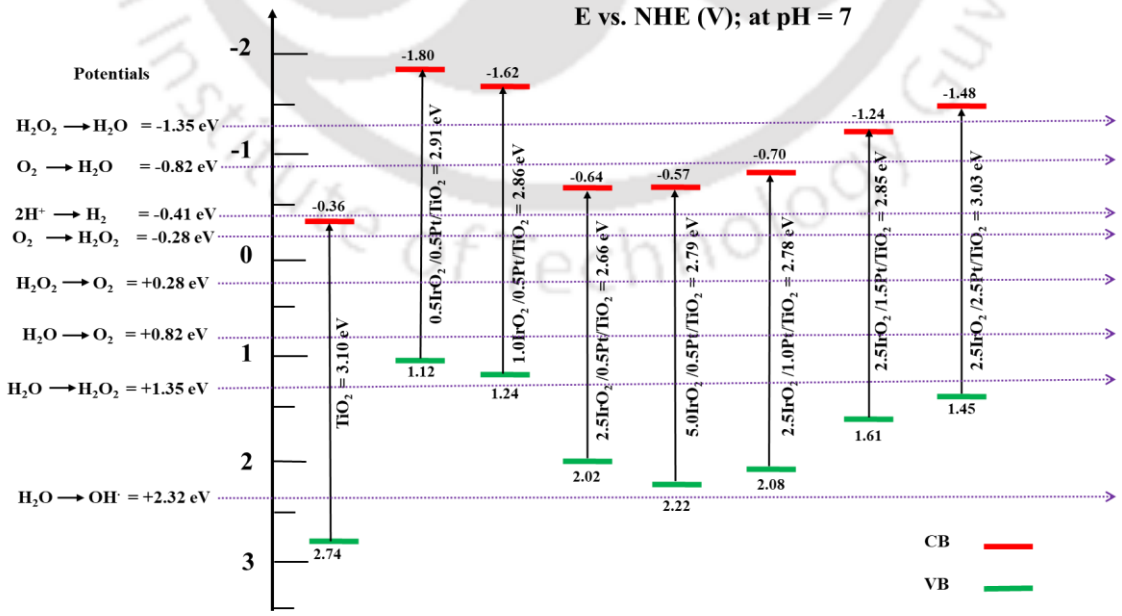

Figure 6.5: Band structures of the $IrO_2/Pt/TiO_2$ photocatalysts (Redox potentials at pH = 7)

It can be seen that all the synthesized photocatalysts have desirable band edge potentials favoring the POWS for the hydrogen and oxygen production under visible light irradiation. Additionally, the water partial oxidation (WPO) potential (E = +1.35V), the hydrogen peroxide oxidation (HPO) potential (E = +0.28V), the oxygen partial reduction (OPR) potential (E = -0.28V), the oxygen reduction (OR) potential (E = -0.82V), the hydrogen peroxide reduction (HPR) potential (E = -1.35V), and the OH radical formation (ORF) potential (E = +2.32V) are also included for reference.[40,41]

The following are the reactions that could be taking place during POWS [39,40,42]:

Water oxidation (WO): $[2H_2O + 4h^+ \longrightarrow O_2 + 4H^+ + 4e^-]$ E = +0.82 eV .. (6.1)

OR reaction: $[O_2 + 4H^+ + 4e^- \longrightarrow 2H_2O + 4h^+]$ E = -0.82 eV .. (6.2)

WPO reaction: $[2H_2O + 2h^+ \longrightarrow H_2O_2 + 2H^+ + 2e^-]$ E = +1.35 eV .. (6.3)

HPR reaction: $[H_2O_2 + 2H^+ + 2e^- \longrightarrow 2H_2O + 2h^+]$ E = -1.35 eV .. (6.4)

HPO reaction: $[H_2O_2 + 2h^+ \longrightarrow O_2 + 2H^+ + 2e^-]$ E = +0.28 eV .. (6.5)

OPR reaction: $[O_2 + 2H^+ + 2e^- \longrightarrow H_2O_2 + 2h^+]$ E = -0.28 eV .. (6.6)

PR reaction: $[2H^+ + 2e^- \longrightarrow H_2]$ E = -0.41 eV .. (6.7)

ORF reaction: $[H_2O + h^+ \longrightarrow OH^{\cdot} + H^+ + e^-]$ E = +2.32 eV .. (6.8)

POWS: $[2H_2O \longrightarrow 2H_2 + O_2]$ E = +1.23 eV .. (6.9)

Additionally, the hydrogen peroxide could decompose to produce oxygen as follows:

Hydrogen peroxide decomposition (HPD): $[H_2O_2 \longrightarrow H_2O + 0.5O_2]$ ….. (6.10)

6.2.1.6 FETEM, FESEM and EDX analysis of the $IrO_2/Pt/TiO_2$

The FETEM, particle size distribution (PSD), FESEM and EDS of the $2.5IrO_2/0.5Pt/TiO_2$ are shown in Figure 6.6. The Pt and IrO_2 NPs were well dispersed on the TiO_2 surface with the formation of a few agglomerates (Fig. 6.6a). The PSD (Fig. 6.6b) shows that the cocatalysts have average particle size in the range of 0.5 – 2 nm, obtained from the TEM image (Fig. 6.6a) using Image analysis for approximately 135 particles. The good dispersion of the Pt and IrO_2 NPs on the TiO_2 surface indicate that the metal (oxide) has strong interaction with the support [43,44], which was observed from XPS analysis. The FESEM image (Fig. 6.6c) of the fresh $IrO_2/Pt/TiO_2$ catalyst shows the uniform and homogeneous tiny Pt or

IrO_2 spherical particles on TiO_2 support. The EDX survey spectrum (Fig. 6.6d) confirms the presence of the Pt and IrO_2 NPs on the TiO_2 surface. The elemental mapping (Fig. 6.6e) shows the uniform distribution of the Pt and IrO_2 NPs on the TiO_2 support. All mapping images have same scale of 10 µm, taken over same area of catalyst sample. Wang et al.[25], synthesized spatially separated Pt and IrO_2 deposited on micro-SiC surface using an in-situ photodeposition method. The authors confirmed the spatial separation of Pt and IrO_2 cocatalysts on SiC surface by SEM and EDS elemental mapping characterizations. They observed that the Pt NPs appeared as dark dots and IrO_2 NPs as bright dots, with deposition at different locations. Therefore, the bright dots observed in Fig. 6.6c corresponds to IrO_2 NPs, while the dark dots could not be identified due to lower concentration of Pt NPs (0.5 wt.%) compared to IrO_2 NPs (2.5 wt.%) and/or doped into TiO_2 lattice as evidenced from XRD and XPS studies. Thus, the FESEM and elemental mapping confirmed that the Pt and IrO_2 cocatalysts were separately deposited on to TiO_2 support. This spatial separation of Pt and IrO_2 cocatalysts on TiO_2 reduces the photogenerated electron – hole recombination rate, evidenced from PL analysis.

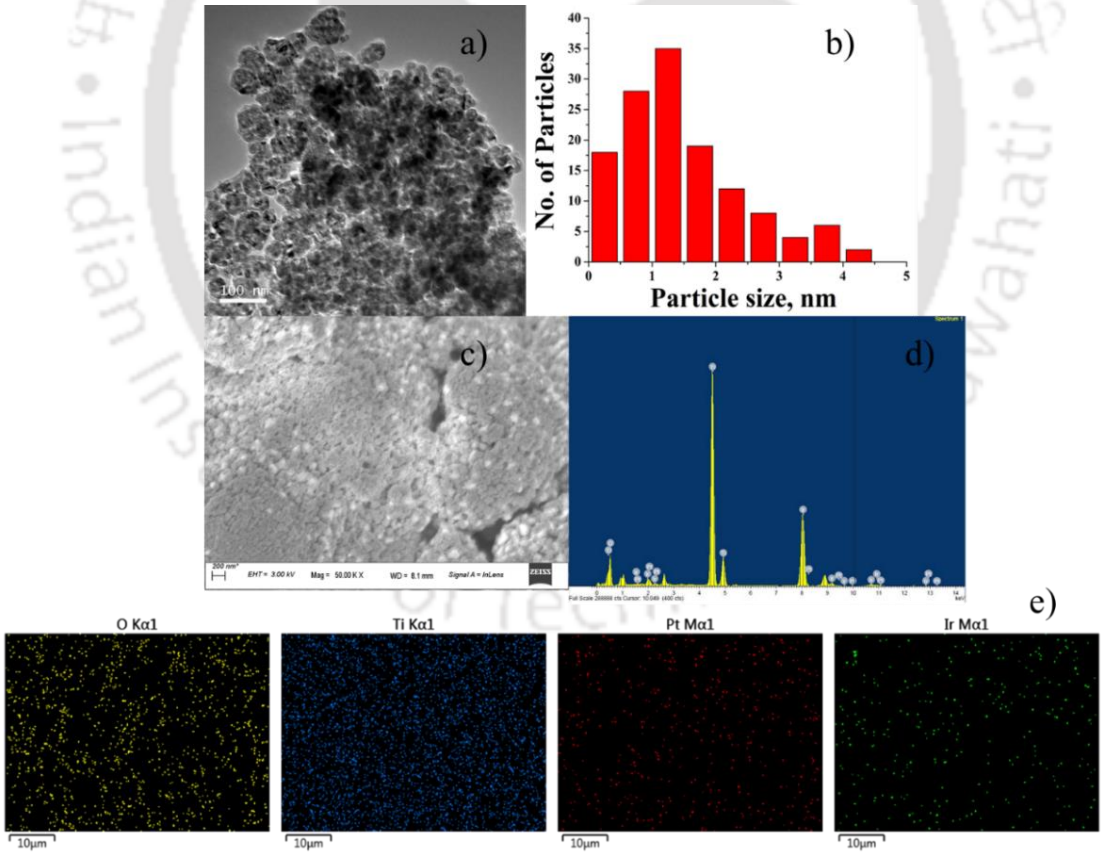

Figure 6.6: (a) Field Emission Transmission Electron Microscopic (FETEM) image, (b) Particle Size Distribution (PSD), (c) Field Emission Scanning Electron Microscopic (FESEM) image, (d) Energy Dispersive X-ray (EDX) survey spectra, (e) EDX elemental mapping of the fresh 2.5IrO_2/0.5Pt/TiO_2 catalyst

6.2.2 POWS activity over $IrO_2/Pt/TiO_2$ photocatalysts

The H_2 and/or O_2 evolution was not observed during the control experiments performed with and without bare TiO_2 using pure DI water as reactant under visible light illumination. The control experiments with Pt/TiO_2 [17] and IrO_2/TiO_2 [19] catalysts showed no activity for POWS into H_2 and O_2 under visible light irradiation. Hence, the following POWS experiments were conducted by dispersing the $IrO_2/Pt/TiO_2$ photocatalysts in pure DI water (no sacrificial agents were added) in the presence of the visible/solar light illumination.

The effect of various parameters such as catalyst loading, cocatalyst loading, stirring speed, and solar simulator (SS) light intensity on the rates of H_2 and O_2 production during POWS are presented in Figure 6.7. Long term stability (LTS) test was also studied for the best catalyst obtained ($2.5IrO_2/0.5Pt/TiO_2$).

The synthesized $IrO_2/Pt/TiO_2$ photocatalysts exhibited activity for POWS indicating the samples are photocatalytically active under visible light illumination. The photocatalytic activity of the $IrO_2/Pt/TiO_2$ catalysts for POWS under visible light irradiation was due to the visible light absorption by the photocatalysts, as confirmed from the UV-Vis spectroscopy. (Fig. 6.2a, b).

6.2.2.1 Effect of catalyst loading

The effect of catalyst loading was studied by varying $0.5IrO_2/0.5Pt/TiO_2$ catalyst amount between 10 – 200 mg at a stirring speed of 500 RPM under visible light (400 W MH lamp) and shown in Fig. 6.7a. It can be seen that the rate of H_2 production (μmol g^{-1} h^{-1}) increased with the catalyst loading up to 50 mg and then decreased with further increase of catalyst loading till 200 mg. The increase in H_2 production rate up to 50 mg catalyst loading is because of the increase in the absorption of the incident light, which in turn results in the increase of number of active sites available for the photocatalytic reaction. Beyond 50 mg catalyst loading, the H_2 production rate decreased. This could be due to the increase in the solution turbidity, which in turn decreases the light absorption, resulting in the less number of active sites available on the catalyst surface.[45–48] At lower loading of 10 mg, no H_2 or O_2 gas was detected, due to a little/no absorption of the incident light. Therefore, 50 mg was the optimum photocatalyst loading at which the maximum H_2 production rate was observed. Although the VB potential of $0.5IrO_2/0.5Pt/TiO_2$ catalyst (E = +1.12 eV) was higher than the water oxidation reaction potential (E = +0.82 eV), the O_2 gas was not detected at the catalyst loadings studied.

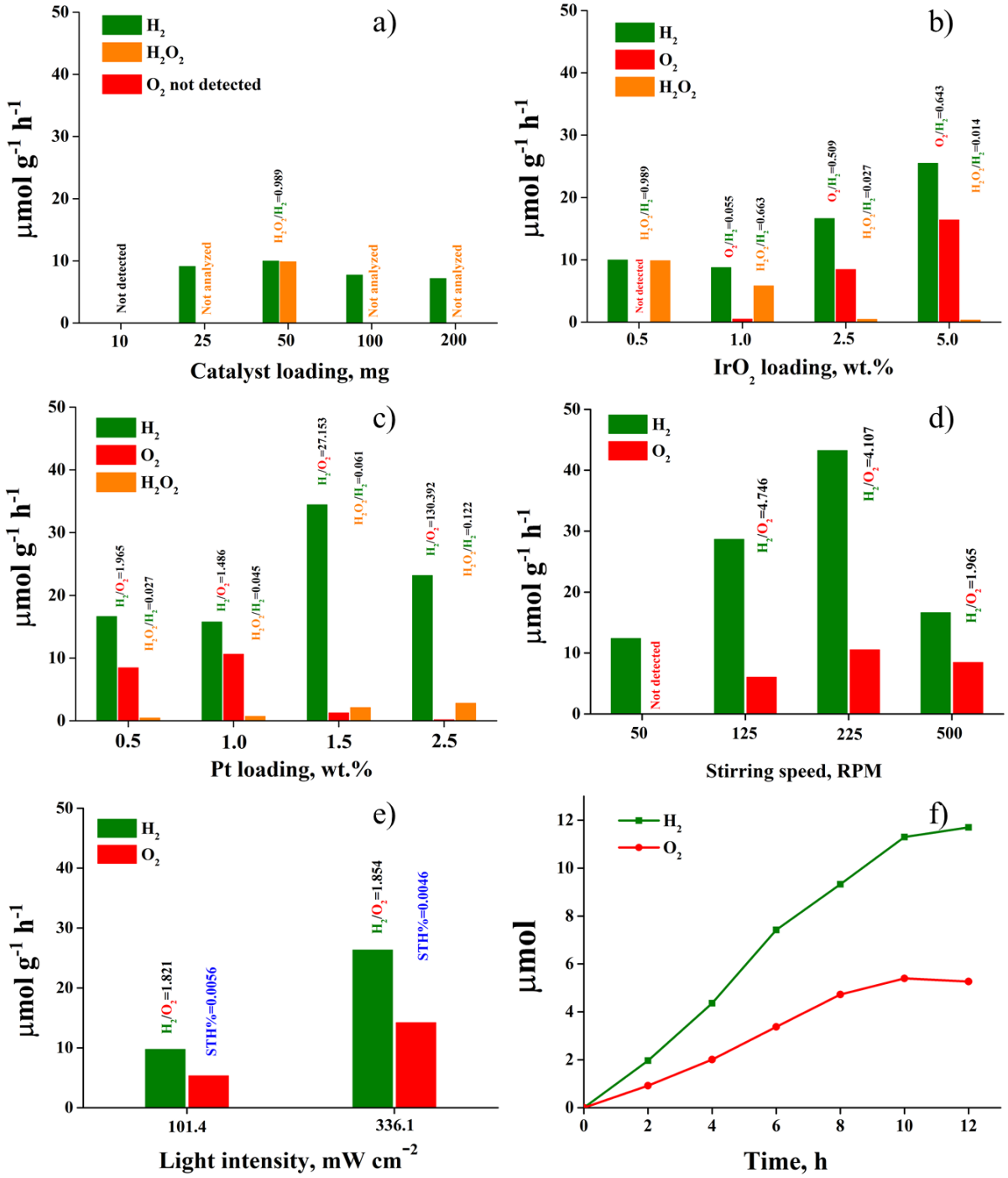

Figure 6.7: a) Effect of catalyst loading (catalyst – $0.5IrO_2/0.5Pt/TiO_2$; stirring speed – 500RPM; 400W MH); b) Effect of IrO_2 cocatalyst loading (catalyst loading – 50mg; Pt loading – 0.5 wt.%; stirring speed – 500RPM; 400W MH); c) Effect of Pt cocatalyst loading (catalyst loading – 50mg; IrO_2 loading – 2.5 wt.%; stirring speed – 500RPM; 400W MH); d) Effect of stirring speed, RPM (catalyst – $2.5IrO_2/0.5Pt/TiO_2$; catalyst loading – 50mg; 400W MH); e) Effect of SS light intensity (catalyst – $2.5IrO_2/0.5Pt/TiO_2$; catalyst loading – 50mg; stirring speed – 500RPM); f) Long term stability (catalyst – $2.5IrO_2/0.5Pt/TiO_2$; catalyst loading – 50mg; stirring speed – 500RPM; 400W MH)

Wenlong et al.[49], developed a novel Z-scheme heterojunction, composed of a phosphatized p-type gallium indium zinc oxynitride (GIZON-P) and a n-type g-C_3N_4 (CN) for the photocatalytic pure water splitting. They reported that H_2 and H_2O_2 were produced over GIZON/CN under visible light irradiation. After phosphorization, the GIZON-P/CN detected the H_2 and O_2 in the stoichiometric ratio of 2:1 under visible light illumination.

In order to identify the H_2O_2 formation during POWS, the suspension after reaction over $0.5IrO_2/0.5Pt/TiO_2$ photocatalyst was filtered out and the liquid solution was analyzed by UV-Vis spectroscopy for the presence of H_2O_2 product. It can be seen that an absorption peak at around 250 nm was obtained (Fig. B.1a in Appendix B), which corresponds to the absorbance of H_2O_2.[50,51] This confirms the formation of H_2O_2 product during POWS.

Further, the amount of H_2O_2 produced during POWS over $0.5IrO_2/0.5Pt/TiO_2$ photocatalyst was quantified from the calibration curve (Fig. B.1c in Appendix B). The calibration curve was obtained by plotting the UV-Vis absorbance of known concentrations of H_2O_2 – DI water samples (Fig. B.1b in Appendix B). The baseline was obtained by using the DI water as reference before analyzing the H_2O_2 samples for absorbance. The H_2O_2 production rate of 9.85 μmol g^{-1} h^{-1}, which is almost same as that of produced H_2 rate of 9.95 μmol g^{-1} h^{-1}. Thus, producing the H_2O_2/H_2 ratio of 0.989, close to stoichiometric value of 1, over $0.5IrO_2/0.5Pt/TiO_2$ photocatalyst, at the catalyst loading of 50 mg and the stirring speed of 500 RPM in the presence of 400 W MH visible lamp. Therefore, the H_2O_2 formation was the reason for not detecting O_2 gas over $0.5IrO_2/0.5Pt/TiO_2$ photocatalyst at the catalyst loadings studied.

Initially, the water oxidation reaction (also called OER) occurs over $0.5IrO_2/0.5Pt/TiO_2$ catalyst producing 1 O_2 molecule and 4 protons (H^+), because the VB potential (E = +1.12 V) is more positive than the water oxidation potential (E = +0.82 V). These 4 H^+ ions convert to form 2 H_2 molecules through proton reduction reaction. Thus, initially forming H_2 and O_2 in the ratio of 2. However, only H_2 gas was identified in GC but not O_2. From the liquid product analysis by UV-Vis spectroscopy, H_2O_2 was identified (Fig. B.1a in Appendix B). This was possible when 1 O_2 molecule reacted with 1 H_2 molecule to form 1 H_2O_2 molecule through oxygen partial reduction (OPR) reaction. The $0.5IrO_2/0.5Pt/TiO_2$ catalyst exhibited CB potential (E = -1.08 V) more negative than oxygen partial reduction potential (E = -0.28 V), allowing OPR reaction to happen. The H_2O_2/H_2 ratio of 0.989 was observed experimentally over $0.5IrO_2/0.5Pt/TiO_2$ catalyst, which is nearly equal to the theoretical value (1.0).

6.2.2.2 Effect of IrO_2 cocatalyst loading

The effect of IrO_2 cocatalyst loading was studied by varying IrO_2 concentration between 0.5 – 5 wt.% (w.r.t the TiO_2 amount) deposited onto 0.5wt.%Pt/TiO_2 ($XIrO_2$/0.5Pt/TiO_2) photocatalysts, at the optimum catalyst loading of 50 mg and stirring speed of 500 RPM under visible light (400 W MH lamp) and shown in Fig. 6.7b. It can be seen that the O_2 production rate increased with increasing the IrO_2 loading. The percentage of the Ir^{4+} phase increased with increasing the IrO_2 loading (see Table B.3 in Appendix B). The increase in the IrO_2 active sites lead to the increase in number of holes captured that subsequently participate in the water oxidation reaction thereby resulting in the increased rates of O_2 production. Also, the VB potentials become more and more positive than water oxidation potential for the successive IrO_2 loading, thereby increasing the affinity towards the O_2 evolution (see Figure 6.5 and Table B.1 in Appendix B). H_2 production rate also increased with increasing the IrO_2 loading. This is because the electrons increase simultaneously with holes, with increasing the IrO_2 loading. Also, the CB potentials are more negative than the water reduction potential (E = -0.41 V) for all the catalysts obtained with varying the IrO_2 loading (see Figure 6.5 and Table B.1 in Appendix B). The PL intensity decreased with increasing the IrO_2 loading (Fig. 6.2e), indicating the separation and transfer of the electron-hole pairs increased. Thus allowing more electrons to get captured by the Pt cocatalyst and concomitant participation in the proton (H^+) reduction reaction to generate more H_2 molecules, and hence the increase in the rate of H_2 production. However, the IrO_2 loading need to be varied further than 5 wt.% to obtain the maximum oxygen activity. The H_2O_2 production rate decreased with increasing the IrO_2 loading. The CB potentials are becoming more positive and closer to the oxygen partial reduction potential (E = -0.28 V) for the successive IrO_2 loading, thereby decreasing the affinity towards the H_2O_2 formation. The O_2/H_2 ratio of 0.509, close to stoichiometric value of 0.5 (Eq. 9), was observed over 2.5IrO_2/0.5Pt/TiO_2 photocatalyst.

6.2.2.3 Effect of Pt cocatalyst loading

The effect of Pt cocatalyst loading was studied by varying Pt concentration in 2.5IrO_2/X Pt/TiO_2 (X = 0.5 – 2.5 wt%). The Pt cocatalyst was deposited before depositing IrO_2. The H_2 production rates increased with increasing the Pt loading till 1.5 wt.% and then decreased (Fig. 6.7c). The percentage of the Pt (Pt^0 + Pt^{2+}) phase increased with increasing the Pt loading (see Table B.3 in Appendix B). The increase in the H_2 production rates with increasing the Pt loading till 1.5 wt.% could be due to the increased Pt active sites capturing more electrons which participate in the water reduction reaction. Moreover, the CB potentials

become more and more negative than water reduction potential with the successive Pt loading, increasing the catalyst affinity for the H_2 evolution (see Figure 6.5 and Table B.1 in Appendix B). However, the H_2 production rate decreased beyond 1.5 wt.%. The excessive Pt loading leads to the coverage of TiO_2 surface with overmuch deposition of Pt, thereby decreasing the light absorption efficiency.[52] This results in the lower activity for H_2 evolution. The O_2 production rate was also increased and then decreased with increasing the Pt loading. The decrease in the O_2 production rate at higher Pt loadings could be because of the shifting of VB potential towards water oxidation potential with increasing Pt loading (Figure 6.5). The excess of Pt favors higher HER activity up to optimum loading (Fig. 6.7c) whereas excess IrO_2 promotes enhanced OER (Fig. 6.7b). It can be observed that there was very little amount of O_2 produced for the photocatalyst $2.5IrO_2/2.5Pt/TiO_2$. The H_2O_2 production rate increased with increasing the Pt loading. This could be due to the shifting of CB potentials further away from the oxygen partial reduction potential (E = -0.28 V) for the successive Pt loading (the CB potentials became more negative with increasing the Pt loading), thereby increasing the affinity towards the H_2O_2 formation. H_2O_2 formation resulted in the deviation of H_2/O_2 ratios from the stoichiometric H_2/O_2 ratio of 2 with varying the cocatalysts (Pt and IrO_2) loadings during POWS reactions. Generation of H_2O_2 during the evolution of H_2 and O_2 from photocatalytic pure water splitting was reported in Refs. [53–55]

6.2.2.4 Formation of H_2O_2 as secondary product during POWS

The reason for the deviations in the observed H_2/O_2 ratios from the stoichiometric value of 2 can be explained based on the bandgap alignment diagram (Figure 6.5) and Equations 1 – 8. All the synthesized $IrO_2/Pt/TiO_2$ photocatalysts have CB potentials higher than the proton (H^+) reduction potential (E = -0.41 V), thus exhibiting H_2 generation (Eq. 7) during POWS. The VB potentials of the $IrO_2/Pt/TiO_2$ photocatalysts are less than the OH radical formation potential (E = +2.32 V). This means that the POWS process does not go through the formation of OH radicals. Thus, the OH radical formation reaction (Eq. 8) can be excluded. All the $IrO_2/Pt/TiO_2$ photocatalysts have VB potentials higher than the water oxidation potential (E = +0.82 V) to form O_2 and water partial oxidation potential (E = +1.35 V) to form H_2O_2, except the photocatalysts $0.5IrO_2/0.5Pt/TiO_2$ and $1.0IrO_2/0.5Pt/TiO_2$ exhibiting VB potentials higher than the water oxidation potential (E = +0.82 V) and lower than water partial oxidation potential (E = +1.35 V) thus have capability to produce O_2 only but the production of H_2O_2 was not possible through water partial oxidation reaction. Producing H_2O_2 from water requires about 530 mV higher potential than producing O_2, making selective production of H_2O_2

intrinsically more difficult, and the water oxidation to produce oxygen, thermodynamically, the most favorable reaction.[42,56] Therefore, the water partial oxidation reaction (Eq. 3) can be excluded, along with hydrogen peroxide (H_2O_2) reduction and oxidation reactions (Eq. 4 & Eq. 5). However, the observed H_2/O_2 ratios for the $IrO_2/Pt/TiO_2$ photocatalysts deviated significantly from the ideal H_2/O_2 ratio of 2. This could be possible when the generated O_2 gas partially or completely reduced to form either H_2O_2 (Eq. 6) or H_2O (Eq. 2). All the $IrO_2/Pt/TiO_2$ photocatalysts have CB potentials higher than the oxygen reduction potential (E = -0.82 V) to form H_2O and oxygen partial reduction potential (E = -0.28 V) to form H_2O_2, except the photocatalysts $2.5IrO_2/0.5Pt/TiO_2$, $5.0IrO_2/0.5Pt/TiO_2$ and $2.5IrO_2/1Pt/TiO_2$ exhibiting CB potentials above the oxygen partial reduction potential (E = -0.28 V) thus having capability to form H_2O_2 only but not H_2O from the oxygen reduction reaction. Again, the oxygen partial reduction to produce H_2O_2 is thermodynamically more favorable than oxygen reduction to produce H_2O, and oxygen reduction reaction (Eq. 2) can be excluded. Therefore, it can be assumed that the generated O_2 gas could have converted to H_2O_2 through oxygen partial reduction reaction (Eq. 6) and resulting in the variation of observed H_2/O_2 ratios for the $IrO_2/Pt/TiO_2$ photocatalysts from the ideal H_2/O_2 ratio of 2. Platinum is also known to be good electrocatalyst for the production of H_2O_2 through partial reduction of oxygen.[57–59] An increase in O_2 evolution was observed with increasing the IrO_2 loading (Fig. 6.7b), which could mean that the activity for the water oxidation reaction to form oxygen (also called OER) increased. The detection of produced H_2O_2 over $0.5IrO_2/0.5Pt/TiO_2$ catalyst indicates that the H_2O_2 decomposition, to further increase O_2, was negligible at the reactor temperature of 60 °C. However, the observed increase in O_2 production rate with increasing IrO_2 loading indicates that the H_2O_2 formation from produced O_2 gas via oxygen partial reduction reaction was suppressed, resulting in the decrease of H_2O_2 production rate. Similarly, the O_2 evolution was decreased and H_2O_2 production increased with increasing Pt loading (Fig. 6.7c). The H_2/O_2 ratio of 1.96, close to stoichiometric value of 2, was obtained for the $2.5IrO_2/0.5Pt/TiO_2$ photocatalyst under visible light irradiation, thus exhibiting ideal POWS (Eq. 9).

Gabriel et al.[60], studied the activity and stability of Pt/IrO_2 bifunctional catalysts for the oxygen evolution/reduction reactions. They reported that the materials' activity toward the ORR was in the order Pt/IrO_2 = 1:1 > Pt/IrO_2 = 3:7 > Pt/IrO_2 = 1:9 and reverse trend was observed for OER. When IrO_2 loading was higher than Pt, ORR on the Pt sites could have been inhibited by the adjacent IrO_2 NPs due to the increased oxophilicity of the Pt NPs because of the Pt-IrO_2

particle – particle interactions.[32] Such interactions were observed for the $IrO_2/Pt/TiO_2$ photocatalysts, from the XPS analysis.

Qin et al.[61], investigated and discussed the causes of visible-light absorption and photoactive enhancement for the $Zn_{1-x}Cd_xS$ solid solution by considering the changes in energy gaps, distributions of charges, and energies of the band edges. They have observed that the CB edge potential becomes more negative with increasing Zn content (i.e., decreasing x value) in the $Zn_{1-x}Cd_xS$ solid solution, indicating that the Zn-dominant solid solution has higher H_2 production capacity than the Cd-dominant solid solution. However, the large band gaps made the Zn-dominant solid solution undesirable compared to Cd-dominant solid solution. Therefore, they attributed the optimal H_2 production activity under visible light irradiation for $Zn_{0.5}Cd_{0.5}S$ to the balance obtained between the light absorption capacity and the H_2 production capacity because of an appropriate band gap and suitable CB edge position. Similarly, the reason for obtaining the optimal H_2 to O_2 ratio of 1.96 (close to the stoichiometric value of 2 for POWS) for $2.5IrO_2/0.5Pt/TiO_2$ catalyst could be because of the balance obtained between the light absorption capacity, and the gas production capacity. The $2.5IrO_2/0.5Pt/TiO_2$ catalyst has the lowest bandgap energy of 2.66 eV among the synthesized photocatalysts, with a CB potential of -0.64eV and VB potential of 2.02eV (Table B.1 in Appendix B).

6.2.2.5 Effect of stirring speed

The effect of stirring speed was studied by varying the stirring speed between 50 – 500 RPM, using the $2.5IrO_2/0.5Pt/TiO_2$ photocatalyst (Fig. 6.7d). The H_2 and O_2 production rates were increased with increasing the stirring speed till 225 RPM and then decreased. With increasing the stirring speed, the probability of the contact between the photocarriers (e^--h^+) and the reactant molecules (H_2O/H^+) at the catalyst surface increases because of the accelerated flowrate of the suspension, and the subsequent mass transfer of the generated H_2 and O_2 gases from the catalyst surface into the solution also increases, resulting in improved production rates. However, further increase in the stirring speed to 500 RPM resulted in the decreased production rates. This could be due to the increase in the turbulence of suspension causing the vortex formation with zero-velocity zone at the center of the reactor thereby decreasing the light absorption.[62,63] At lower stirring speed of 50 RPM, O_2 was not detected. The diffusion of O_2 is much slower than H_2 because an oxygen atom is 16 times heavier than hydrogen atom. Therefore, O_2 is more difficult to escape from the photocatalyst surface than H_2.[39] The mass transfer/diffusion of H_2 and O_2 is significantly improved with increasing the stirring speed, achieving the maximum activity at 225 RPM. Due to the difference in the atomic mass, the

mass transfer/diffusion affected differently with varying stirring speed, resulting in the different H_2/O_2 ratios. The H_2/O_2 ratio of 1.96 (close to stoichiometric value of 2) was obtained at the stirring speed of 500 RPM.

6.2.2.6 Effect of SS light intensity

The effect of SS light intensity was studied at the intensities of 101.4 and 336.1 mW cm^{-2}, over $2.5IrO_2/0.5Pt/TiO_2$ photocatalyst (Fig. 6.7e). The H_2 and O_2 production rates were increased with increasing the solar intensity. The number of incident photons increases with increasing the light intensity, which upon absorption by catalyst generates more (e^--h^+) pairs. This increases the rate of redox reactions resulting in the increased production rates.[17] The H_2 and O_2 production rates increased almost linearly with increasing the solar intensity from 101.4 to 336.1 mW cm^{-2}. Solar to hydrogen conversion efficiency (STH) of ~0.006 % was obtained at the intensity of 101.4 mW cm^{-2}. Although the obtained STH is less than the reported values[17], the synthesized $IrO_2/Pt/TiO_2$ catalysts have significance because of the capability to split the water molecules under solar light without using any sacrificial agents.

The H_2/O_2 ratio of 1.96 and 1.82 under the visible 400W MH and under the SS, close to the theoretical stoichiometric value of 2 for POWS reaction, were obtained over the $IrO_2/Pt/TiO_2$ photocatalyst at the corresponding parameters of 50 mg catalyst loading, 2.5 wt.% IrO_2, 0.5 wt.% Pt and 500 RPM stirring speed.

6.2.2.7 Long-term stability (LTS) test

The long-term stability (LTS) test was conducted over $2.5IrO_2/0.5Pt/TiO_2$ photocatalyst, at the optimum catalyst loading of 50 mg and a stirring speed of 500 RPM under visible light (400 W MH lamp) irradiation (Fig. 6.7f). The H_2 and O_2 production was increased linearly with the reaction time up to 10 h. This indicates that the photocatalyst activity was stable for a period of 10 h. After 10 h, the photocatalyst showed decrease in the activity.

Figure 6.8 shows the color and characterization of the photocatalysts, before and after the LTS test. The color of the photocatalyst changed from yellow for fresh sample (Fig. 6.8a) to dark brown after stability test (Fig. 6.8b), which could mean that the photocatalyst suffered some kind of deactivation. Commercial anatase TiO_2 powder is shown in Fig. 6.8c for reference.

A comparative analysis on the basis XRD, XPS and UV-Vis spectra was carried out for the photocatalyst before (fresh) and after stability test (spent). The XRD pattern shows the presence of anatase TiO_2 phase only and the IrO_2 peaks disappeared (Fig. 6.8d). This indicates that there was a structural change for the spent photocatalyst. The XPS peak fitting shows that there are

Pt^0, Ir^{4+}, and Ir^0 phases in the spent photocatalyst (Fig. 6.8e, f). On comparing the high-resolution XPS spectra of spent photocatalyst with that of fresh photocatalyst (Figure 6.4), it can be observed that the Pt^{2+} phase disappeared and Ir^0 phase appeared (see Table B.4 in Appendix B). The photocatalyst could have underwent reduction in the presence of generated H_2 during the stability test, converting Pt and Ir oxide phases. The BE of Pt4f of Pt^0 phase were shifted to lower values by ~1.2 eV, for the spent photocatalyst (70.7 and 74.0 eV) compared to those of fresh photocatalyst (71.9 and 75.2 eV). The increase in the Pt metallic phase content resulted in the shift towards lower binding energies.[64] The metallic Ir (Ir^0 $4f_{7/2}$) has the binding energy of 59.9 eV, which is close to 60.3 eV reported for the surface Ir atoms.[65] This also suggests that the surface reduction of the IrO_2 to Ir occurred by the accumulation of generated H_2 on the catalyst surface. The surface reduction of the IrO_2 to metallic Ir was reported in Ref [66].

The PtO and IrO_2 were reduced to metallic Pt and Ir by the generated H_2 on the catalyst surface during the course of stability test. A significant decrease in H_2 production was observed after 10 h of stability test. This could indicate that the catalyst surface saturation occurred till 10 h with the accumulation of evolved H_2 causing the reduction of PtO and IrO_2 phases and then activity declined, resulting in the decrease of H_2 and O_2 production. The Pt content increased in lieu of PtO and the IrO_2 content decreased, as observed from the XPS analysis of the spent catalyst. The decrease in O_2 production could be due to the decrease in IrO_2 content. Since the amount of O_2 liberated from the catalyst surface was decreased with decreasing IrO_2 content, the O_2 bubbles could have accumulated on the catalyst surface further affecting the catalyst activity. The backward reaction between H_2 and O_2 to form H_2O (Eq. 2) could be ruled out since the CB potential of $2.5IrO_2/0.5Pt/TiO_2$ catalyst (E = -0.64 V) was lower than the oxygen reduction potential (E = -0.82 V). The IrO_2 and PtO were reduced to metallic Ir and Pt by the product H_2 gas accumulated on the catalyst surface affecting the catalyst activity resulting in the significant decrease of H_2 and O_2 gases after 10 h of stability test over $2.5IrO_2/0.5Pt/TiO_2$ catalyst thereby altering the H_2 to O_2 ratios. The reduction of Pt and Ir oxide phases to Pt and Ir metallic phase affected the light absorption properties of the spent photocatalyst. It can be seen from UV-Vis spectra (Fig. 6.8g) that the absorbance in UV and visible region significantly improved for the spent catalyst due to the presence of the increased metallic Pt and Ir content. However, no shift in absorption edge was observed and the bandgap energy remained the same (Fig. 6.8h). The FESEM image of the spent photocatalyst (Fig. 6.8i) shows that the aggregation of the photocatalyst occurred during the stability test, which decreased the active sites and

thereby active surface area available for the POWS reaction, resulting in the activity decrease. FESEM image of the fresh photocatalyst is shown in Fig. 6.6c.

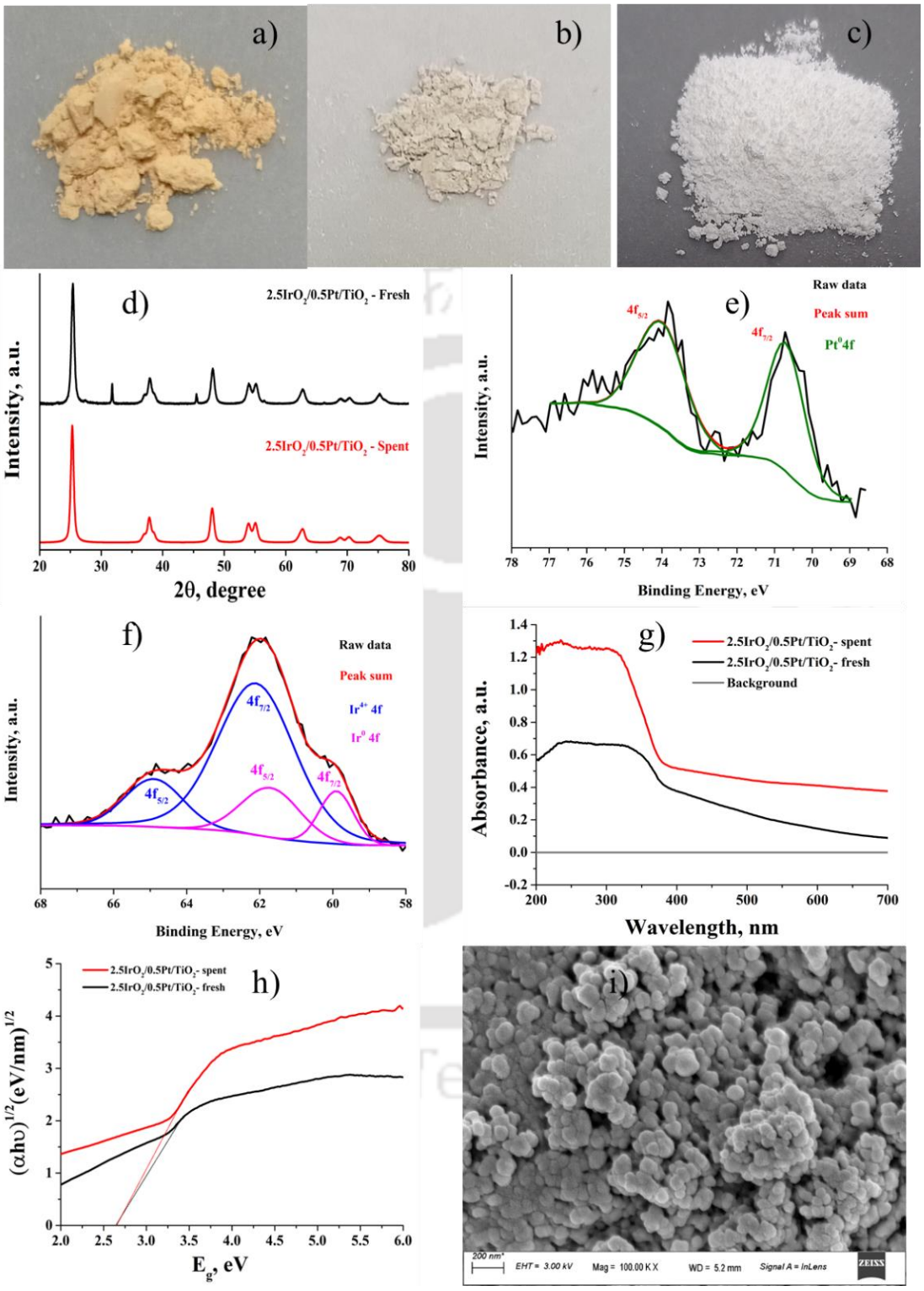

Figure 6.8: (a) Fresh $2.5IrO_2/0.5Pt/TiO_2$, (b) Spent $2.5IrO_2/0.5Pt/TiO_2$, (c) Commercial anatase TiO_2 powder, (d) XRD, (e) High resolution XPS of Pt4f region, (f) High resolution XPS of Ir4f region, (g) UV-Vis spectrum, (h) Tauc plot, and (i) FESEM, of the spent $2.5IrO_2/0.5Pt/TiO_2$ catalyst

Xinyi et al.[67], studied the stability improvement of the Pt/TiO_2 photocatalyst during the photocatalytic pure water splitting under UV light irradiation. They reported that the deactivation of the photocatalyst occurred because of the accumulation of the generated gas on the photocatalyst surface. Gabriel et al.[60], reported that O_2 bubbles accumulation played an important role in the deactivation by blocking the active sites of the catalyst, apart from particle dissolution, growth, coalescence and detachment for the instability of Pt/IrO_2 bifunctional catalysts for the oxygen evolution/reduction reactions. Therefore, the accumulation of the generated gas on the catalyst surface and aggregation of the photocatalyst were found to be the reasons for the activity decrease of the $2.5IrO_2/0.5Pt/TiO_2$ photocatalyst.

6.3 Proposed mechanism of POWS over $IrO_2/Pt/TiO_2$ catalysts

The mechanism for the POWS to produce H_2 and O_2 over $IrO_2/Pt/TiO_2$ was postulated based on the band structure analysis (Figure 6.5) and is shown in Figure 6.9. Upon absorbing the visible light by the photocatalyst, the electrons are excited from the VB to CB of semiconductor and leaving behind vacant holes at the VB. The IrO_2 cocatalyst captures the holes and facilitates the water (H_2O) oxidation to produce O_2 and protons (H^+ ions). Then, the Pt cocatalyst on the TiO_2 surface captures the electrons and facilitates the H^+ reduction to produce H_2. The partial reduction of O_2 to produce H_2O_2 was also promoted over Pt cocatalyst. The transfer pathways of electrons and holes to the Pt and IrO_2 cocatalysts, respectively, were confirmed from the PL analysis.

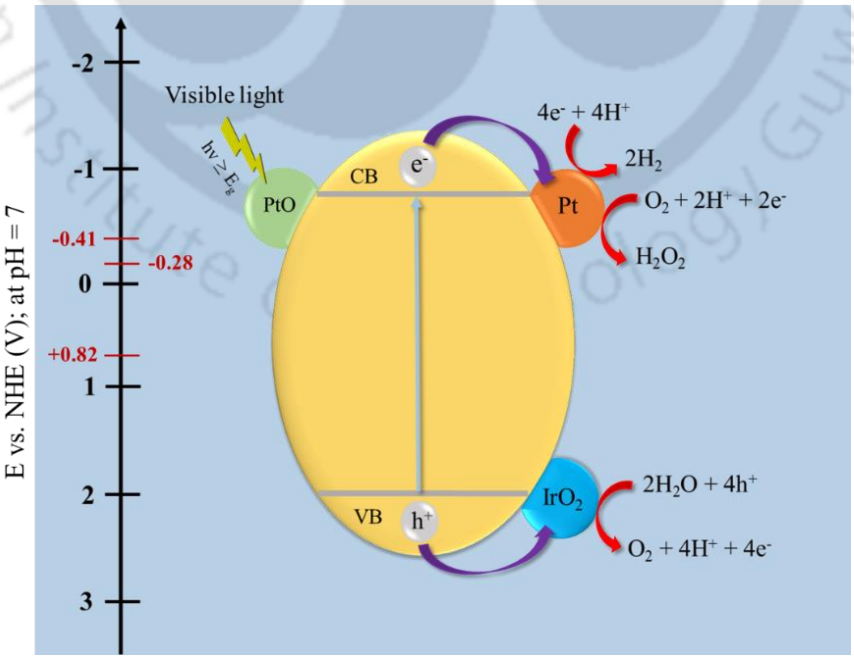

Figure 6.9: Schematic diagram of H_2 and O_2 evolution mechanism from POWS over $IrO_2/Pt/TiO_2$ photocatalyst under visible light irradiation

6.4 Conclusions

The $IrO_2/Pt/TiO_2$ photocatalysts were successfully synthesized by photodepositing the Pt and IrO_2 cocatalysts sequentially onto the commercial anatase TiO_2 powder. The photocatalytic overall water splitting was conducted using the $IrO_2/Pt/TiO_2$ photocatalysts by dispersing in pure water without adding sacrificial agents under visible light illumination. The observed H_2/O_2 ratio for the $IrO_2/Pt/TiO_2$ photocatalysts was significantly deviated from the theoretical value, due to the formation of H_2O_2 as secondary product. The H_2O_2/H_2 ratio of 0.989 (close to theoretical value of 1) was obtained over $0.5IrO_2/0.5Pt/TiO_2$ photocatalyst. While the H_2/O_2 ratio of 1.96 (close to theoretical value of 2) was obtained using $2.5IrO_2/0.5Pt/TiO_2$, at the optimum catalyst loading of 50 mg and stirring speed of 500 RPM under visible light (400W MH). Thus the developed photocatalyst exhibits the overall water splitting activity without any additional sacrificial agents for the production of H_2 and O_2 as well as H_2O_2.

References

(1) Rui, Z.; Chen, L.; Chen, H.; Ji, H. Strong Metal-Support Interaction in Pt/TiO2 Induced by Mild HCHO and NaBH4 Solution Reduction and Its Effect on Catalytic Toluene Combustion. *Ind. Eng. Chem. Res.* **2014**, *53* (41), 15879–15888. https://doi.org/10.1021/ie5029107.

(2) Tian, J.; Zhao, P.; Zhang, S.; Huo, G.; Suo, Z.; Yue, Z.; Zhang, S.; Huang, W.; Zhu, B. Platinum and Iridium Oxide Co-Modified TiO2 Nanotubes Array Based Photoelectrochemical Sensors for Glutathione. *Nanomaterials* **2020**, *10* (3), 522. https://doi.org/10.3390/nano10030522.

(3) Cheng, G.; Xu, F.; Stadler, F. J.; Chen, R. A Facile and General Synthesis Strategy to Doped TiO2 Nanoaggregates with a Mesoporous Structure and Comparable Property. *RSC Adv.* **2015**, *5* (79), 64293–64298. https://doi.org/10.1039/C5RA11099H.

(4) Singh, A.; Kumar, S. Effect of Ag Doping on Phase-Change and Photocatalytic Performance of Rutile–Anatase Mixed-Phase Titanium Dioxide (TiO2) Nanoparticles. *Appl. Phys. A* **2021**, *127* (11), 839. https://doi.org/10.1007/s00339-021-04993-w.

(5) Ginting, M.; Taslima, S.; Sebayang, K.; Aryanto, D.; Sudiro, T.; Sebayang, P. Preparation and Characterization of Zinc Oxide Doped with Ferrite and Chromium. *AIP Conf. Proc.* **2017**, *1862* (1), 30062. https://doi.org/10.1063/1.4991166.

(6) Barpanda, P.; Recham, N.; Chotard, J.-N.; Djellab, K.; Walker, W.; Armand, M.; Tarascon, J.-M. Structure and Electrochemical Properties of Novel Mixed Li(Fe1−xMx)SO4F (M = Co, Ni, Mn) Phases Fabricated by Low Temperature Ionothermal Synthesis. *J. Mater. Chem.* **2010**, *20* (9), 1659–1668. https://doi.org/10.1039/B922063A.

(7) Soundarya, T. L.; Harini, R.; Manjunath, K.; Udayabhanu; Nirmala, B.; Nagaraju, G. Pt-Doped TiO2 Nanotubes as Photocatalysts and Electrocatalysts for Enhanced Photocatalytic H2 Generation, Electrochemical Sensing, and Supercapacitor Applications. *Int. J. Hydrogen Energy* **2023**. https://doi.org/10.1016/j.ijhydene.2023.04.289.

(8) Ramadan, W.; Feldhoff, A.; Bahnemann, D. Assessing the Photocatalytic Oxygen Evolution Reaction of BiFeO3 Loaded with IrO2 Nanoparticles as Cocatalyst. *Sol. Energy Mater. Sol. Cells* **2021**, *232*, 111349. https://doi.org/10.1016/j.solmat.2021.111349.

(9) Dimitrova, N.; Banti, A.; Spyridou, O.-N.; Papaderakis, A.; Georgieva, J.; Sotiropoulos, S.; Valova, E.; Armyanov, S.; Tatchev, D.; Hubin, A.; Baert, K. Photodeposited IrO2 on TiO2 Support as a Catalyst for Oxygen Evolution Reaction. *J. Electroanal. Chem.* **2021**, *900*, 115720. https://doi.org/10.1016/j.jelechem.2021.115720.

(10) Schweinar, K.; Gault, B.; Mouton, I.; Kasian, O. Lattice Oxygen Exchange in Rutile IrO2 during the Oxygen Evolution Reaction. *J. Phys. Chem. Lett.* **2020**, *11* (13), 5008–5014. https://doi.org/10.1021/acs.jpclett.0c01258.

(11) Kuribayashi, K.; Kitamura, S. Preparation of Pt-PtOx Thin Films as Electrode for Memory Capacitors. *Thin Solid Films* **2001**, *400* (1), 160–164. https://doi.org/10.1016/S0040-6090(01)01503-6.

(12) Sta, I.; Jlassi, M.; Hajji, M.; Boujmil, M. F.; Jerbi, R.; Kandyla, M.; Kompitsas, M.; Ezzaouia, H. Structural and Optical Properties of TiO2 Thin Films Prepared by Spin Coating. *J. Sol-Gel Sci. Technol.* **2014**, *72* (2), 421–427. https://doi.org/10.1007/s10971-014-3452-z.

(13) Alrushaid, M.; Nadeem, M. A.; Wahab, K. A.; Idriss, H. Extracting Turnover Frequencies of Electron Transfer in Heterogeneous Catalysis: A Study of IrO2-TiO2 Anatase for Water Oxidation Using Ce4+ Cations. *Catalysts* **2021**, *11* (9), 1030. https://doi.org/10.3390/catal11091030.

(14) Ahmed, L. M.; Ivanova, I.; Hussein, F. H.; Bahnemann, D. W. Role of Platinum Deposited on TiO_2 in Photocatalytic Methanol Oxidation and Dehydrogenation Reactions. *Int. J. Photoenergy* **2014**, *2014*, 503516. https://doi.org/10.1155/2014/503516.

(15) Islam, J.; Kim, S.-K.; Rahman, M. M.; Thien, P. T.; Kim, M.-J.; Cho, H.-S.; Lee, C.; Lee, J. H.; Lee, S. The Effect of Iridium Content in Boron Carbide-Supported Iridium Catalyst on the Activity and Stability of Proton Exchange Membrane Water Electrolyzer. *Mater. Today Energy* **2023**, *32*, 101237. https://doi.org/10.1016/j.mtener.2022.101237.

(16) Zhu, Z.; Chen, J.; Su, K.; Wu, R. Efficient Hydrogen Production by Water-Splitting over Pt-Deposited C-HS-TiO2 Hollow Spheres under Visible Light. *J. Taiwan Inst. Chem. Eng.* **2016**, *60*, 222–228. https://doi.org/10.1016/j.jtice.2015.10.001.

(17) Pala, L. P. R.; Peela, N. R. Green Hydrogen Production in an Optofluidic Planar

Microreactor via Photocatalytic Water Splitting under Visible/Simulated Sunlight Irradiation. *Energy & Fuels* **2021**, *35* (23), 19737–19747. https://doi.org/10.1021/acs.energyfuels.1c02686.

(18) Wang, Y.; Lai, Q.; Zhang, F.; Shen, X.; Fan, M.; He, Y.; Ren, S. High Efficiency Photocatalytic Conversion of CO2 with H2O over Pt/TiO2 Nanoparticles. *RSC Adv.* **2014**, *4* (84), 44442–44451. https://doi.org/10.1039/C4RA07457B.

(19) Pala, L. P. R.; Peela, N. R. Visible Light Active IrO2/TiO2 Films for Oxygen Evolution from Photocatalytic Water Splitting in an Optofluidic Planar Microreactor. *Renew. Energy* **2022**, *197*, 902–910. https://doi.org/10.1016/j.renene.2022.08.017.

(20) Kim, M. G.; Kang, J. M.; Lee, J. E.; Kim, K. S.; Kim, K. H.; Cho, M.; Lee, S. G. Effects of Calcination Temperature on the Phase Composition, Photocatalytic Degradation, and Virucidal Activities of TiO2 Nanoparticles. *ACS Omega* **2021**, *6* (16), 10668–10678. https://doi.org/10.1021/acsomega.1c00043.

(21) Abdullah, B. J. Size Effect of Band Gap in Semiconductor Nanocrystals and Nanostructures from Density Functional Theory within HSE06. *Mater. Sci. Semicond. Process.* **2022**, *137*, 106214. https://doi.org/10.1016/j.mssp.2021.106214.

(22) Ansari, S. A.; Cho, M. H. Highly Visible Light Responsive, Narrow Band Gap TiO2 Nanoparticles Modified by Elemental Red Phosphorus for Photocatalysis and Photoelectrochemical Applications. *Sci. Rep.* **2016**, *6* (1), 25405. https://doi.org/10.1038/srep25405.

(23) Hwang, S. W.; Noh, T. H.; Cho, I. S. Optical Properties, Electronic Structures, and Photocatalytic Performances of Bandgap-Tailored SrBi2Nb2−xVxO9 Compounds. *Catalysts* **2019**, *9* (5), 393. https://doi.org/10.3390/catal9050393.

(24) Yang, Z.; Lu, J.; Ye, W.; Yu, C.; Chang, Y. Preparation of Pt/TiO2 Hollow Nanofibers with Highly Visible Light Photocatalytic Activity. *Appl. Surf. Sci.* **2017**, *392*, 472–480. https://doi.org/10.1016/j.apsusc.2016.09.065.

(25) Wang, D.; Wang, W.; Wang, Q.; Guo, Z.; Yuan, W. Spatial Separation of Pt and IrO2 Cocatalysts on SiC Surface for Enhanced Photocatalysis. *Mater. Lett.* **2017**, *201*, 114–117. https://doi.org/10.1016/j.matlet.2017.04.140.

(26) Zedan, A. F.; Gaber, S.; AlJaber, A. S.; Polychronopoulou, K. CO Oxidation at Near-Ambient Temperatures over TiO(2)-Supported Pd-Cu Catalysts: Promoting Effect of

Pd-Cu Nanointerface and TiO(2) Morphology. *Nanomater. (Basel, Switzerland)* **2021**, *11* (7). https://doi.org/10.3390/nano11071675.

(27) Croy, J. R.; Mostafa, S.; Hickman, L.; Heinrich, H.; Cuenya, B. R. Bimetallic Pt-Metal Catalysts for the Decomposition of Methanol: Effect of Secondary Metal on the Oxidation State, Activity, and Selectivity of Pt. *Appl. Catal. A Gen.* **2008**, *350* (2), 207–216. https://doi.org/10.1016/j.apcata.2008.08.013.

(28) Iemhoff, A.; Vennewald, M.; Artz, J.; Mebrahtu, C.; Meledin, A.; Weirich, T. E.; Hartmann, H.; Besmehn, A.; Aramini, M.; Venturini, F.; Mosselmans, F. W.; Held, G.; Arrigo, R.; Palkovits, R. On the Stability of Isolated Iridium Sites in N-Rich Frameworks Against Agglomeration Under Reducing Conditions. *ChemCatChem* **2022**, *14* (9), e202200179. https://doi.org/10.1002/cctc.202200179.

(29) Zheng, X.; Qin, M.; Ma, S.; Chen, Y.; Ning, H.; Yang, R.; Mao, S.; Wang, Y. Strong Oxide-Support Interaction over IrO(2) /V(2) O(5) for Efficient PH-Universal Water Splitting. *Adv. Sci. (Weinheim, Baden-Wurttemberg, Ger.* **2022**, *9* (11), e2104636. https://doi.org/10.1002/advs.202104636.

(30) Shi, Y.; Ma, Z.-R.; Xiao, Y.-Y.; Yin, Y.-C.; Huang, W.-M.; Huang, Z.-C.; Zheng, Y.-Z.; Mu, F.-Y.; Huang, R.; Shi, G.-Y.; Sun, Y.-Y.; Xia, X.-H.; Chen, W. Electronic Metal-Support Interaction Modulates Single-Atom Platinum Catalysis for Hydrogen Evolution Reaction. *Nat. Commun.* **2021**, *12* (1), 3021. https://doi.org/10.1038/s41467-021-23306-6.

(31) Karakoti, A. S.; King, J. E. S.; Vincent, A.; Seal, S. Synthesis Dependent Core Level Binding Energy Shift in the Oxidation State of Platinum Coated on Ceria–Titania and Its Effect on Catalytic Decomposition of Methanol. *Appl. Catal. A Gen.* **2010**, *388* (1), 262–271. https://doi.org/10.1016/j.apcata.2010.08.060.

(32) Du, J.; Quinson, J.; Zhang, D.; Bizzotto, F.; Zana, A.; Arenz, M. Bifunctional Pt-IrO2 Catalysts for the Oxygen Evolution and Oxygen Reduction Reactions: Alloy Nanoparticles versus Nanocomposite Catalysts. *ACS Catal.* **2021**, *11* (2), 820–828. https://doi.org/10.1021/acscatal.0c03867.

(33) Mendiola-Alvarez, S. Y.; Guzmán-Mar, J. L.; Turnes-Palomino, G.; Maya-Alejandro, F.; Caballero-Quintero, A.; Hernández-Ramírez, A.; Hinojosa-Reyes, L. Synthesis of Cr3+-Doped TiO2 Nanoparticles: Characterization and Evaluation of Their Visible Photocatalytic Performance and Stability. *Environ. Technol.* **2019**, *40* (2), 144–153.

https://doi.org/10.1080/09593330.2017.1380715.

(34) WD, Y.; YD, H.; WC, L.; IL, H. Characterization and Photocatalytic Activity of N and Pt Doped Titania Prepared by Microemulsion Technique. *Adv Mater Sci* **2018**, *3*, 1000144. https://doi.org/10.15761/AMS.1000144.

(35) Dette, C.; Pérez-Osorio, M. A.; Mangel, S.; Giustino, F.; Jung, S. J.; Kern, K. Trellises of Molecular Oxygen on Anatase TiO2(101). *J. Phys. Chem. C* **2019**, *123* (43), 26170–26177. https://doi.org/10.1021/acs.jpcc.9b04314.

(36) Kruse, N.; Chenakin, S. XPS Characterization of Au/TiO2 Catalysts: Binding Energy Assessment and Irradiation Effects. *Appl. Catal. A Gen.* **2011**, *391* (1), 367–376. https://doi.org/10.1016/j.apcata.2010.05.039.

(37) Babelon, P.; Dequiedt, A. S.; Mostéfa-Sba, H.; Bourgeois, S.; Sibillot, P.; Sacilotti, M. SEM and XPS Studies of Titanium Dioxide Thin Films Grown by MOCVD. *Thin Solid Films* **1998**, *322* (1), 63–67. https://doi.org/https://doi.org/10.1016/S0040-6090(97)00958-9.

(38) Abidov, A.; Allabergenov, B.; Lee, J.; Jeon, H.-W.; Jeong, S.-W.; Kim, S. X-Ray Photoelectron Spectroscopy Characterization of Fe Doped TiO2 Photocatalyst. *Int. J. Mater. Mech. Manuf.* **2013**, *1* (3), 294–296. https://doi.org/10.7763/ijmmm.2013.v1.63.

(39) Bie, C.; Wang, L.; Yu, J. Challenges for Photocatalytic Overall Water Splitting. *Chem* **2022**, *8* (6), 1567–1574. https://doi.org/10.1016/j.chempr.2022.04.013.

(40) Koppenol, W. H.; Stanbury, D. M.; Bounds, P. L. Electrode Potentials of Partially Reduced Oxygen Species, from Dioxygen to Water. *Free Radic. Biol. Med.* **2010**, *49* (3), 317–322. https://doi.org/10.1016/j.freeradbiomed.2010.04.011.

(41) Wood, P. M. The Potential Diagram for Oxygen at PH 7. *Biochem. J.* **1988**, *253* (1), 287–289. https://doi.org/10.1042/bj2530287.

(42) Shi, X.; Back, S.; Gill, T. M.; Siahrostami, S.; Zheng, X. Electrochemical Synthesis of H2O2 by Two-Electron Water Oxidation Reaction. *Chem* **2021**, *7* (1), 38–63. https://doi.org/10.1016/j.chempr.2020.09.013.

(43) Byun, M. Y.; Kim, Y. E.; Baek, J. H.; Jae, J.; Lee, M. S. Effect of Surface Properties of TiO2 on the Performance of Pt/TiO2 Catalysts for Furfural Hydrogenation. *RSC Adv.* **2022**, *12* (2), 860–868. https://doi.org/10.1039/D1RA07220J.

(44) She, L.; Zhao, G.; Ma, T.; Chen, J.; Sun, W.; Pan, H. On the Durability of Iridium-Based Electrocatalysts toward the Oxygen Evolution Reaction under Acid Environment. *Adv. Funct. Mater.* **2022**, *32* (5), 2108465. https://doi.org/10.1002/adfm.202108465.

(45) Sane, P. K.; Rakte, D.; Tambat, S.; Bhalinge, R.; Sontakke, S. M.; Nemade, P. Enhancing Solar Photocatalytic Activity of Bi5O7I Photocatalyst with Activated Carbon Heterojunction. *Adv. Powder Technol.* **2022**, *33* (1), 103357. https://doi.org/10.1016/j.apt.2021.11.009.

(46) Zhang, D.; Lv, S.; Luo, Z. A Study on the Photocatalytic Degradation Performance of a [KNbO3]0.9-[BaNi0.5Nb0.5O3−δ]0.1 Perovskite. *RSC Adv.* **2020**, *10* (3), 1275–1280. https://doi.org/10.1039/C9RA07310H.

(47) Reza, K. M.; Kurny, A. S. W.; Gulshan, F. Parameters Affecting the Photocatalytic Degradation of Dyes Using TiO2: A Review. *Appl. Water Sci.* **2017**, *7* (4), 1569–1578. https://doi.org/10.1007/s13201-015-0367-y.

(48) Rafique, M.; Hamza, M.; Tahir, M. B.; Muhammad, S.; Al-Sehemi, A. G. Facile Hydrothermal Synthesis of Highly Efficient and Visible Light-Driven Ni-Doped V2O5 Photocatalyst for Degradation of Rhodamine B Dye. *J. Mater. Sci. Mater. Electron.* **2020**, *31* (15), 12913–12925. https://doi.org/10.1007/s10854-020-03844-3.

(49) Fu, W.; Guan, X.; Wu, H.; Liu, M. Switching from Two-Electron to Four-Electron Photocatalytic Pure Water Splitting via Band Bending Engineering with Boosted Activity. *Appl. Catal. B Environ.* **2022**, *305*, 121054. https://doi.org/10.1016/j.apcatb.2021.121054.

(50) Gill, T. M.; Zheng, X. Comparing Methods for Quantifying Electrochemically Accumulated H2O2. *Chem. Mater.* **2020**, *32* (15), 6285–6294. https://doi.org/10.1021/acs.chemmater.0c02010.

(51) Aye, T. T.; Low, T. Y.; Sze, S. K. Nanosecond Laser-Induced Photochemical Oxidation Method for Protein Surface Mapping with Mass Spectrometry. *Anal. Chem.* **2005**, *77* (18), 5814–5822. https://doi.org/10.1021/ac050353m.

(52) Lin, Y.; Liu, Y.; Li, Y.; Cao, Y.; Huang, J.; Wang, H.; Yu, H.; Liang, H.; Peng, F. Dual Functional CuO1–x Clusters for Enhanced Photocatalytic Activity and Stability of a Pt Cocatalyst in an Overall Water-Splitting Reaction. *ACS Sustain. Chem. Eng.* **2018**, *6* (12), 17340–17351. https://doi.org/10.1021/acssuschemeng.8b04889.

(53) Fu, Y.; Liu, C.; Zhang, M.; Zhu, C.; Li, H.; Wang, H.; Song, Y.; Huang, H.; Liu, Y.; Kang, Z. Photocatalytic H2O2 and H2 Generation from Living Chlorella Vulgaris and Carbon Micro Particle Comodified G-C3N4. *Adv. Energy Mater.* **2018**, *8* (34), 1802525. https://doi.org/10.1002/aenm.201802525.

(54) Shi, W.; Guo, F.; Wang, H.; Guo, S.; Li, H.; Zhou, Y.; Zhu, C.; Liu, Y.; Huang, H.; Mao, B.; Liu, Y.; Kang, Z. New Insight of Water-Splitting Photocatalyst: H2O2-Resistance Poisoning and Photothermal Deactivation in Sub-Micrometer CoO Octahedrons. *ACS Appl. Mater. Interfaces* **2017**, *9* (24), 20585–20593. https://doi.org/10.1021/acsami.7b04286.

(55) Guo, S.; Li, X.; Li, J.; Wei, B. Boosting Photocatalytic Hydrogen Production from Water by Photothermally Induced Biphase Systems. *Nat. Commun.* **2021**, *12* (1), 1343. https://doi.org/10.1038/s41467-021-21526-4.

(56) Zhang, K.; Liu, J.; Wang, L.; Jin, B.; Yang, X.; Zhang, S.; Park, J. H. Near-Complete Suppression of Oxygen Evolution for Photoelectrochemical H2O Oxidative H2O2 Synthesis. *J. Am. Chem. Soc.* **2020**, *142* (19), 8641–8648. https://doi.org/10.1021/jacs.9b13410.

(57) Li, H.; Wen, P.; Itanze, D. S.; Hood, Z. D.; Adhikari, S.; Lu, C.; Ma, X.; Dun, C.; Jiang, L.; Carroll, D. L.; Qiu, Y.; Geyer, S. M. Scalable Neutral H2O2 Electrosynthesis by Platinum Diphosphide Nanocrystals by Regulating Oxygen Reduction Reaction Pathways. *Nat. Commun.* **2020**, *11* (1), 3928. https://doi.org/10.1038/s41467-020-17584-9.

(58) Choi, C. H.; Kim, M.; Kwon, H. C.; Cho, S. J.; Yun, S.; Kim, H.-T.; Mayrhofer, K. J. J.; Kim, H.; Choi, M. Tuning Selectivity of Electrochemical Reactions by Atomically Dispersed Platinum Catalyst. *Nat. Commun.* **2016**, *7* (1), 10922. https://doi.org/10.1038/ncomms10922.

(59) Choi, C. H.; Kwon, H. C.; Yook, S.; Shin, H.; Kim, H.; Choi, M. Hydrogen Peroxide Synthesis via Enhanced Two-Electron Oxygen Reduction Pathway on Carbon-Coated Pt Surface. *J. Phys. Chem. C* **2014**, *118* (51), 30063–30070. https://doi.org/10.1021/jp5113894.

(60) da Silva, G. C.; Fernandes, M. R.; Ticianelli, E. A. Activity and Stability of Pt/IrO2 Bifunctional Materials as Catalysts for the Oxygen Evolution/Reduction Reactions. *ACS Catal.* **2018**, *8* (3), 2081–2092. https://doi.org/10.1021/acscatal.7b03429.

(61) Li, Q.; Meng, H.; Zhou, P.; Zheng, Y.; Wang, J.; Yu, J.; Gong, J. Zn1–XCdxS Solid Solutions with Controlled Bandgap and Enhanced Visible-Light Photocatalytic H2-Production Activity. *ACS Catal.* **2013**, *3* (5), 882–889. https://doi.org/10.1021/cs4000975.

(62) Dai, B.; Zhou, Y.; Xiao, X.; Chen, Y.; Guo, J.; Gao, C.; Xie, Y.; Chen, J. Fluid Field Modulation in Mass Transfer for Efficient Photocatalysis. *Adv. Sci.* **2022**, *9* (28), 2203057. https://doi.org/10.1002/advs.202203057.

(63) Huang, Y.-J.; Lyu, L.-M.; Lin, C.-Y.; Lee, G.-C.; Hsiao, K.-Y.; Lu, M.-Y. Improved Mass-Transfer Enhances Photo-Driven Dye Degradation and H(2) Evolution over a Few-Layer WS(2)/ZnO Heterostructure. *ACS omega* **2022**, *7* (2), 2217–2223. https://doi.org/10.1021/acsomega.1c05756.

(64) Smirnov, M. Y.; Kalinkin, A. V; Bukhtiyarov, V. I. X-Ray Photoelectron Spectroscopic Study of the Interaction of Supported Metal Catalysts with NOx. *J. Struct. Chem.* **2007**, *48* (6), 1053–1060. https://doi.org/10.1007/s10947-007-0170-1.

(65) Martin, R.; Kim, M.; Lee, C. J.; Mehar, V.; Albertin, S.; Hejral, U.; Merte, L. R.; Lundgren, E.; Asthagiri, A.; Weaver, J. F. High-Resolution X-Ray Photoelectron Spectroscopy of an IrO2(110) Film on Ir(100). *J. Phys. Chem. Lett.* **2020**, *11* (17), 7184–7189. https://doi.org/10.1021/acs.jpclett.0c01805.

(66) Fathi Tovini, M.; Damjanovic, A. M.; El-Sayed, H. A.; Speder, J.; Eickes, C.; Suchsland, J.-P.; Ghielmi, A.; Gasteiger, H. A. Degradation Mechanism of an IrO2 Anode Co-Catalyst for Cell Voltage Reversal Mitigation under Transient Operation Conditions of a PEM Fuel Cell. *J. Electrochem. Soc.* **2021**, *168* (6), 64521. https://doi.org/10.1149/1945-7111/ac0d39.

(67) Zhang, X.; Bo, C.; Cao, S.; Cheng, Z.; Xiao, Z.; Liu, X.; Tan, T.; Piao, L. Stability Improvement of a Pt/TiO2 Photocatalyst during Photocatalytic Pure Water Splitting. *J. Mater. Chem. A* **2022**, *10* (45), 24381–24387. https://doi.org/10.1039/D2TA06961J.

Chapter 7

Thesis Conclusions and Recommendations of Future Scope of Work

7.1 Major Findings

i. **TiO_2 thin films**: A uniform and adherent TiO_2 thin films on the glass substrate are successfully prepared by spin coating using sol-gel method. A highly homogeneous TiO_2 thin film is obtained with a sol-gel composition of 0.2 M TTIP, 0.1 M AcAc, 0.09 M AA and 1 g of CTAB per 0.01 mol TTIP. The 4 times coated TiO_2 thin film showed 58.4 % MB degradation at 60 min of photocatalytic reaction.

ii. **Pt/TiO_2 thin films**: An optofluidic planar microreactor was fabricated using Pt/TiO_2 thin films and tested successfully for the photocatalytic water splitting. The highest rate of 16.35 mmol h^{-1} g^{-1} (4.7 µmol h^{-1} cm^{-2}) hydrogen production was obtained on the Pt/TiO_2 film of thickness 1650±119 nm at an optimum reactant (20 vol.% methanol in DI water) flowrate of 0.3 mL min^{-1} under visible light illumination.

iii. **IrO_2/TiO_2 thin films**: The fabricated optofluidic planar microreactor, with IrO_2/TiO_2 film as photocatalyst, has been tested successfully for photocatalytic water splitting. An oxygen evolution rate of ~ 4 mmol h^{-1} g^{-1} (1.84 µmol h^{-1} cm^{-2}) was achieved on the IrO_2/TiO_2 film with a thickness of 3078 ± 362 nm at an optimal reactant (10 mM $NaIO_3$ in DI water) flowrate of 0.3 mL min^{-1} in the presence of visible light irradiation.

iv. **IrO_2/Pt/TiO_2 powder**: The photocatalytic overall water splitting was conducted using the IrO_2/Pt/TiO_2 photocatalysts by dispersing in pure water without adding sacrificial agents under visible light illumination. The H_2/H_2O_2 ratio of 1.01 (close to theoretical value of 1) was obtained over 0.5IrO_2/0.5Pt/TiO_2 photocatalyst. While the H_2/O_2 ratio of 1.96 (close to theoretical value of 2) was obtained using 2.5IrO_2/0.5Pt/TiO_2, at the optimum catalyst loading of 50 mg and stirring speed of 500 RPM under visible light (400 W MH).

v. The Photocatalytic overall water splitting is an important artificial photosynthetic process to produce green hydrogen from pure water. Developing photocatalyst materials with appropriate band edge potentials and band gaps enables the hydrogen and oxygen production activities under visible light illumination. The studies presented in this thesis gave insights on synthesizing the photocatalysts active for the hydrogen and oxygen production from photocatalytic water splitting with and without sacrificial agents under visible light irradiation and the development of optofluidic planar microreactors. For the photocatalytic half reactions performed using planar microreactors, the following scientific insights were highlighted. The rate of hydrogen and oxygen production increased with reactant flowrate reaching a maximum at 0.3 mL

min^{-1} and then decreased. The external mass transfer resistance dominated below 0.3 mL min^{-1} and lower residence times above 0.3 mL min^{-1}. The rate of hydrogen and oxygen production increased with increasing the thickness of the photocatalyst film. The photogenerated carriers (e^--h^+ pairs) increased with film thickness, through the absorption of more photons. In the case of immobilized photocatalytic film, the three competing factors that determine the optimum film thickness are the catalyst surface area, internal mass transfer/diffusion, and absorption of incident light. The initial increase in reaction rates with increasing the film thickness is because of the increase in the active surface area and light absorption. With further increasing the thickness, the reaction rates reach a maximum at a certain value and then decreases. The decrease in the reaction rate is because of the dominance of the internal mass transfer resistance, which reduces the utilization of deeper layers. Moreover, the light absorption also decreases with the increase of film thickness. The increased hydrogen and oxygen production rates with an increase in thickness means that the light absorption increased, and internal diffusional resistance was negligible in the range of thicknesses studied. Recycle tests showed that the Pt/TiO_2-8x and IrO_2/TiO_2-24x films in the planar microreactors exhibited stable hydrogen and oxygen production rates for 4 cycles of 5 h each. Good recycle stability indicates that the catalyst films were adhered firmly onto glass, which is important for the scalability of the planar microreactor. The presence of methanol as SR eliminates the need of H_2/O_2 separation since it avoids the formation of O_2 and increases the safety of the process. The planar microreactor, being a continuous reaction system, has great potential for large scale applications. For the photocatalytic overall water splitting conducted using batch reactor, the rate of H_2 production increased with the catalyst loading up to 50 mg and then decreased with further increase of catalyst loading. The increase in H_2 production rate up to 50 mg catalyst loading is because of the increase in the absorption of the incident light, which in turn results in the increase of number of charge carriers available for the photocatalytic reaction. Beyond 50 mg catalyst loading, the H_2 production rate decreased. This could be due to the increase in the solution turbidity, which in turn decreases the light absorption, resulting in the smaller number of active sites available on the catalyst surface. Increasing the Pt and IrO_2 loadings resulting in the corresponding increase of hydrogen and oxygen production rates. Beyond optimum Pt loadings, hydrogen production rate decreased due to coverage of TiO_2 surface with overmuch deposition of Pt, thereby decreasing the light absorption efficiency. The H_2

and O_2 production rates were increased with increasing the solar intensity. The number of incident photons increases with increasing the light intensity, which upon absorption by catalyst generates more (e^--h^+) pairs. This increases the rate of redox reactions resulting in the increased production rates. Solar to hydrogen conversion efficiency (STH) of ~0.006 % was obtained at the intensity of ~1 sun (101.4 mW cm^{-2}), indicating the significance of the synthesized IrO_2/Pt/TiO_2 photocatalysts capability to split the water molecules under direct sun light without using any sacrificial agents.

7.2 Future scopes

i. Uniform and adherent coatings were obtained by the spin coating method but it is difficult to achieve films with thickness upto 10 µm even after multiple coatings. Drop cast, dip coat and spray coat methods can be tested in order to obtain thick films upto 10 µm with good adherence in a single or fewer coatings.

ii. Good glass bonding using UV curable glue was achieved for the microreactor fabrication. However, the problems such as catalyst blockage, if glue was in excess, were observed. Other methods, such as anodic bonding, can be employed to fabricate microreactor more effectively.

iii. The efficiency of the photocatalytic overall water splitting over IrO_2/Pt/TiO_2 can be improved by fabricating the large scale planar microreactor that can accommodate more catalyst coating area.

iv. The solar to hydrogen conversion (STH) efficiency of the IrO_2/Pt/TiO_2 may be improved by modifying the support structure to obtain more surface area with large number of active sites and by using other deposition techniques to further improve the dispersion of Pt and IrO_2.

Appendix A

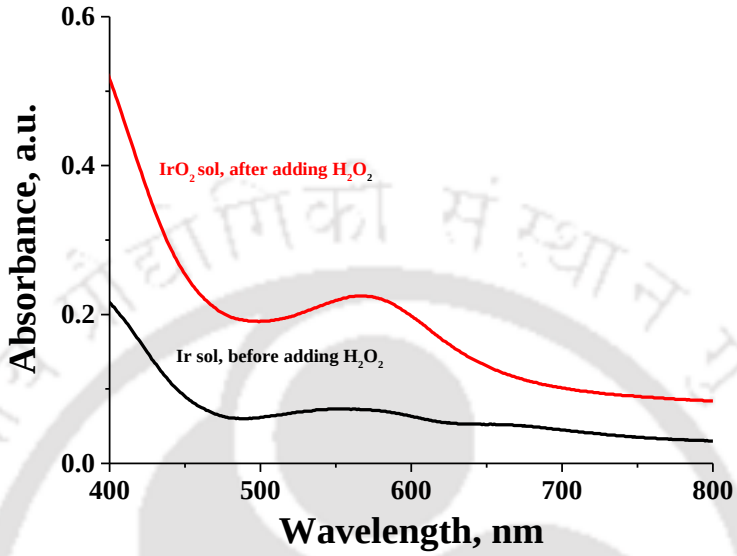

Fig. A.1: UV-vis absorbance spectra of Ir and IrO_2 hydrosols

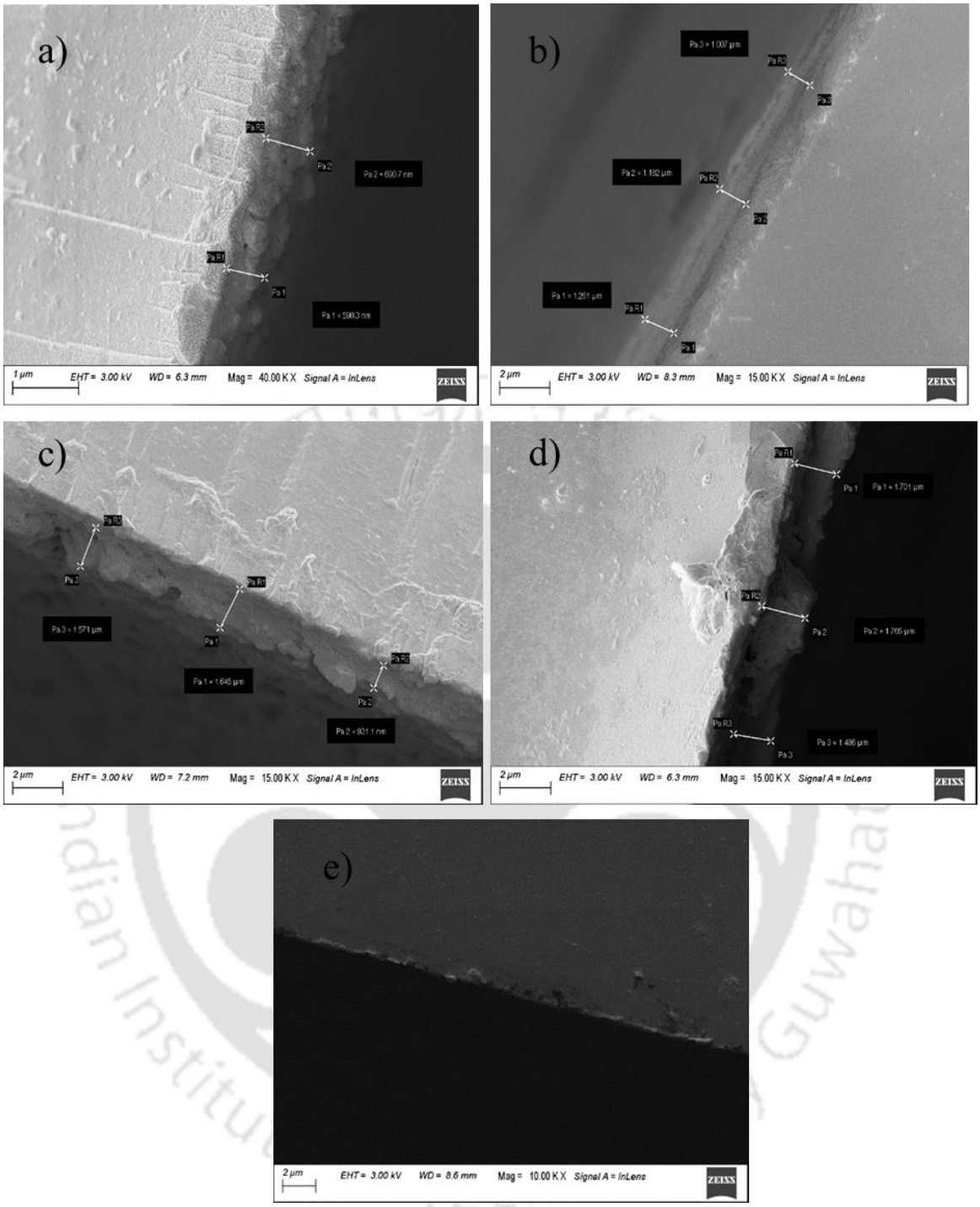

Fig. A.2I: The film thickness measurement using FESEM: a) Pt/TiO_2-2x; b) Pt/TiO_2-4x; c) Pt/TiO_2-6x; d) Pt/TiO_2-8x; and e) Plain glass for reference;

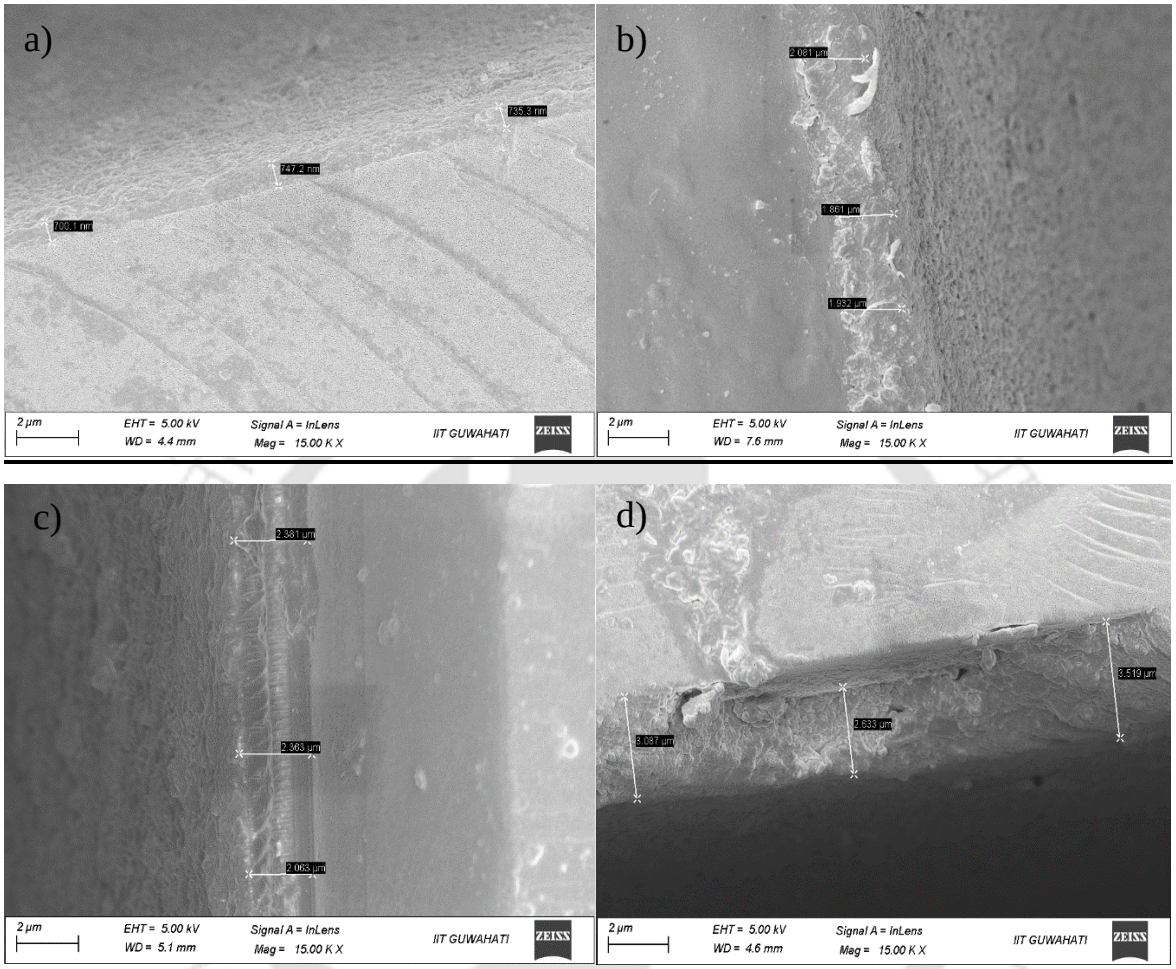

Fig. A.2II: The film thickness measurement using FESEM: a) IrO_2/TiO_2-6x; b) IrO_2/TiO_2-12x; c) IrO_2/TiO_2-18x; and d) IrO_2/TiO_2-24x;

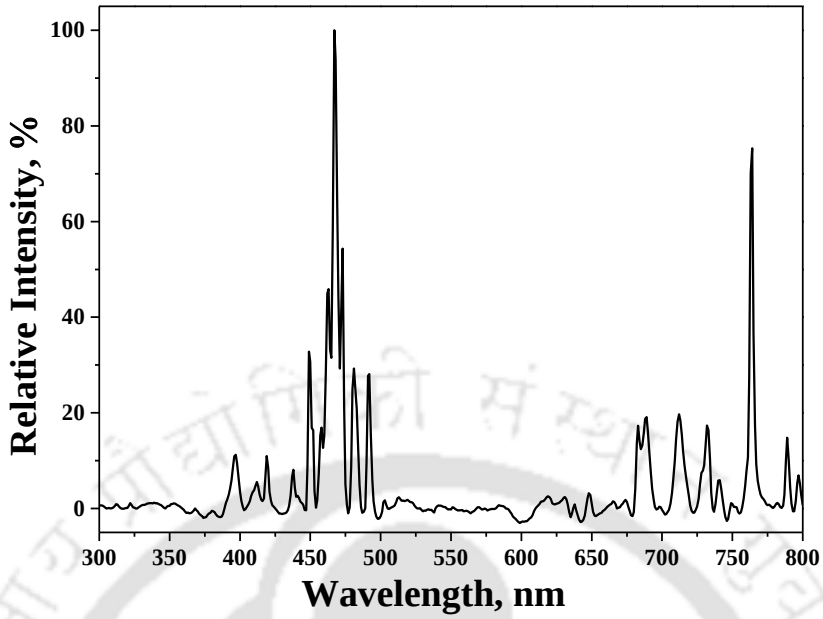

Fig. A.3: Spectral output of the 400 W metal halide lamp (Halonix)

Calculation of 400 W MH lamp intensity:

MH lamp has power of 400 watts.

Distance between the MH lamp and the reactor was maintained at 10 cm. Considering spherical illumination of MH lamp with a radius of 10 cm, the area of illumination is as follow:

Area of illumination = $4\pi r^2 = 4\times3.14\times10^2 = 1256$ cm^2

MH Intensity = Lamp power/ illumination area = 400000/1256 = 318.5 mW/cm^2

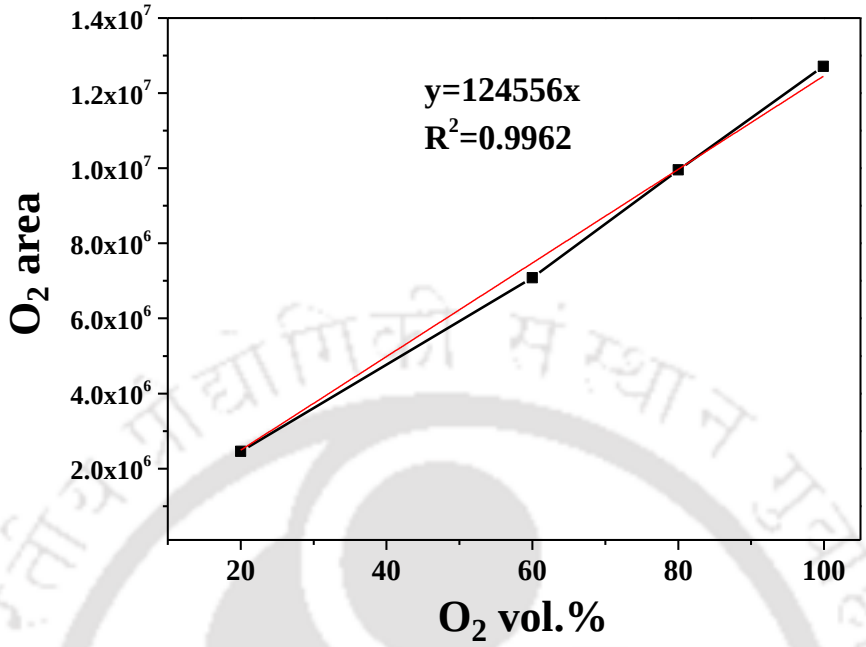

Fig. A.4: Determination of oxygen calibration factor from the calibration curve

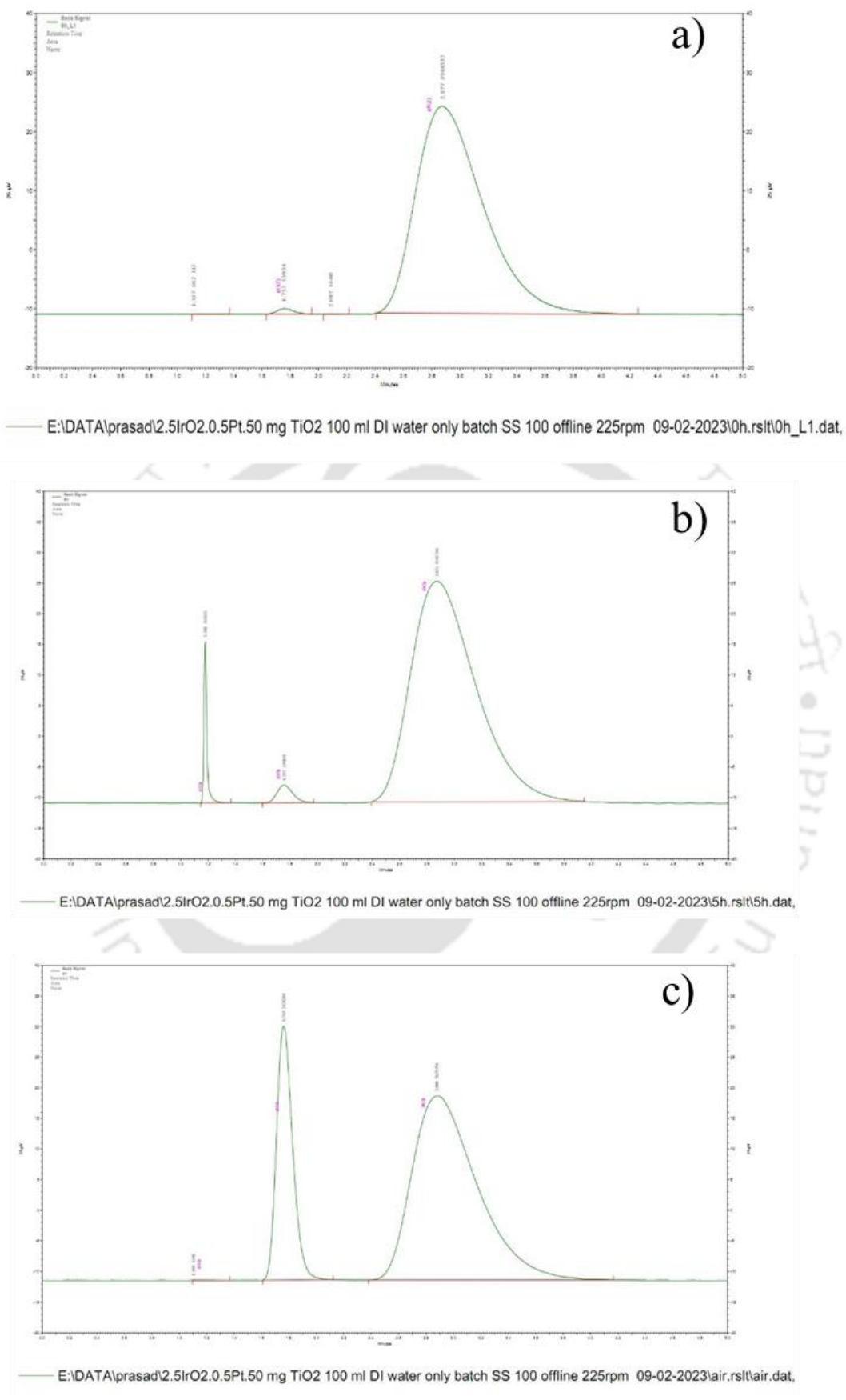

Figure A.5: Chromatographs: a) zero hour; b) five hour; and c) air (ref)

Appendix B

Table B.1: Properties of the synthesized catalysts

S. No.	Catalyst	Crystallite size, nm	Absorption edge, nm	Bandgap energy, eV	VB potential (E_{VB})	CB potential (E_{CB})
1	TiO_2	13.66	392	3.10	2.74	-0.36
2	$0.5IrO_2/0.5Pt/TiO_2$	12.14	406	2.91	1.12	-1.80
3	$1.0IrO_2/0.5Pt/TiO_2$	12.47	415	2.86	1.24	-1.62
4	$2.5IrO_2/0.5Pt/TiO_2$	13.08	448	2.66	2.02	-0.64
5	$5.0IrO_2/0.5Pt/TiO_2$	12.21	421	2.79	2.22	-0.57
6	$2.5IrO_2/1.0Pt/TiO_2$	12.61	426	2.78	2.08	-0.70
7	$2.5IrO_2/1.5Pt/TiO_2$	12.24	422	2.85	1.61	-1.24
8	$2.5IrO_2/2.5Pt/TiO_2$	11.82	410	2.93	1.45	-1.48

Table B.2: Binding energies (B.E) of the synthesized catalysts, obtained from XPS peak fitting

		B.E.				
S. No.	Catalyst	Ir^{4+} 4f (7/2, 5/2)	Pt^0 4f (7/2, 5/2)	Pt^{2+} 4f (7/2, 5/2)	Ti2p (3/2, 1/2)	O1s
1	TiO_2	-	-	-	(458.8, 464.4)	(530, 531.3)
	Rutile IrO_2 [235]	(61.8, 64.8)	-	-	-	-
	Pt [236]	-	(71.2, 74.5)	-	-	-
	PtO [236]	-	-	(72.2, 75.5)	-	-
	$1Pt/TiO_2$ [129]	-	(71.9, 75.2)	(72.9, 76.2)	(458.8, 464.4)	(530, 531.3)
	$5IrO_2/TiO_2$ [18]	(62.1, 64.9)	-	-	(458.8, 464.4)	(530, 531.3)
2	$0.5IrO_2/0.5Pt/TiO_2$	(62.1, 64.9)	(71.9, 75.2)	(72.6, 75.8)	(458.5, 464.2)	(529.7, 531.3)
3	$1.0IrO_2/0.5Pt/TiO_2$	(62.1, 64.9)	(71.9, 75.2)	(72.6, 75.8)	(458.5, 464.2)	(529.7, 531.3)
4	$2.5IrO_2/0.5Pt/TiO_2$	(62.1, 64.9)	(71.9, 75.2)	(72.6, 75.8)	(458.4, 464.2)	(529.6, 531.3)
5	$5.0IrO_2/0.5Pt/TiO_2$	(62.4, 64.9)	(71.9, 75.2)	(72.9, 76.2)	(458.3, 464.1)	(529.5, 531.3)
6	$2.5IrO_2/1.0Pt/TiO_2$	(62.3, 65.2)	(71.9, 75.2)	(72.9, 76.2)	(458.5, 464.2)	(529.7, 531.3)
7	$2.5IrO_2/1.5Pt/TiO_2$	(62.3, 65.2)	(71.9, 75.2)	(72.9, 76.2)	(458.6, 464.3)	(529.8, 531.3)
8	$2.5IrO_2/2.5Pt/TiO_2$	(62.1, 64.9)	(71.9, 75.2)	(72.9, 76.2)	(458.4, 464.1)	(529.6, 531.3)

Table B.3: Surface atomic composition of the synthesized catalysts, obtained from XPS peak fitting

		Surface atomic composition, at.%									
S. No.	Catalyst	Ir^{4+}4f	Pt^0 4f	Pt^{2+} 4f	Ti2p	O1s	Pt4f (Pt^0 4f+ Pt^{2+} 4f)	O1s/Ti2p	O^{2-}/Ti^{4+}	Ir^{4+}4f/IrO_2 loading	Pt4f/Pt loading
1	TiO_2	-	-	-	28.39	71.61	-	2.52	2.19	-	-
2	0.5IrO_2/0.5Pt/TiO_2	0.99	0.14	0.04	27.90	70.94	0.18	2.54	2.05	1.98	0.36
3	1.0IrO_2/0.5Pt/TiO_2	1.16	0.08	0.05	29.82	68.88	0.13	2.31	1.74	1.16	0.25
4	2.5IrO_2/0.5Pt/TiO_2	1.65	0.11	0.06	26.47	71.71	0.17	2.71	2.00	0.66	0.34
5	5.0IrO_2/0.5Pt/TiO_2	2.62	0.15	0.10	17.49	79.63	0.25	4.55	1.40	0.52	0.51
6	2.5IrO_2/1.0Pt/TiO_2	1.61	0.17	0.17	22.68	75.38	0.34	3.32	1.42	0.64	0.34
7	2.5IrO_2/1.5Pt/TiO_2	1.40	0.37	0.14	26.79	71.30	0.51	2.66	1.71	0.56	0.34
8	2.5IrO_2/2.5Pt/TiO_2	1.27	0.64	0.29	26.03	71.78	0.93	2.76	1.92	0.51	0.37

Table B.4: Characteristics of 2.5IrO_2/0.5Pt/TiO_2 catalyst after stability test

Crystallite size, nm	11.87
Absorption edge, nm	448
Bandgap energy, eV	2.66
VB potential (E_{VB})	2.02
CB potential (E_{CB})	-0.64
Ir^{4+} 4f (7/2, 5/2): B.E	(62.1, 64.9)
Ir^0 4f (7/2, 5/2): B.E	(59.9, 61.7)
Pt^0 4f (7/2, 5/2): B.E	(70.7, 74.0)
Ti2p (3/2, 1/2): B.E	(458.8, 464.1)
O1s: B.E	(529.6, 531.2)
Ir^{4+} 4f: At.%	1.02
Ir^0 4f: At.%	0.31
Pt^0 4f: At.%	0.14
Ti2p: At.%	28.6
O1s: At.%	69.93

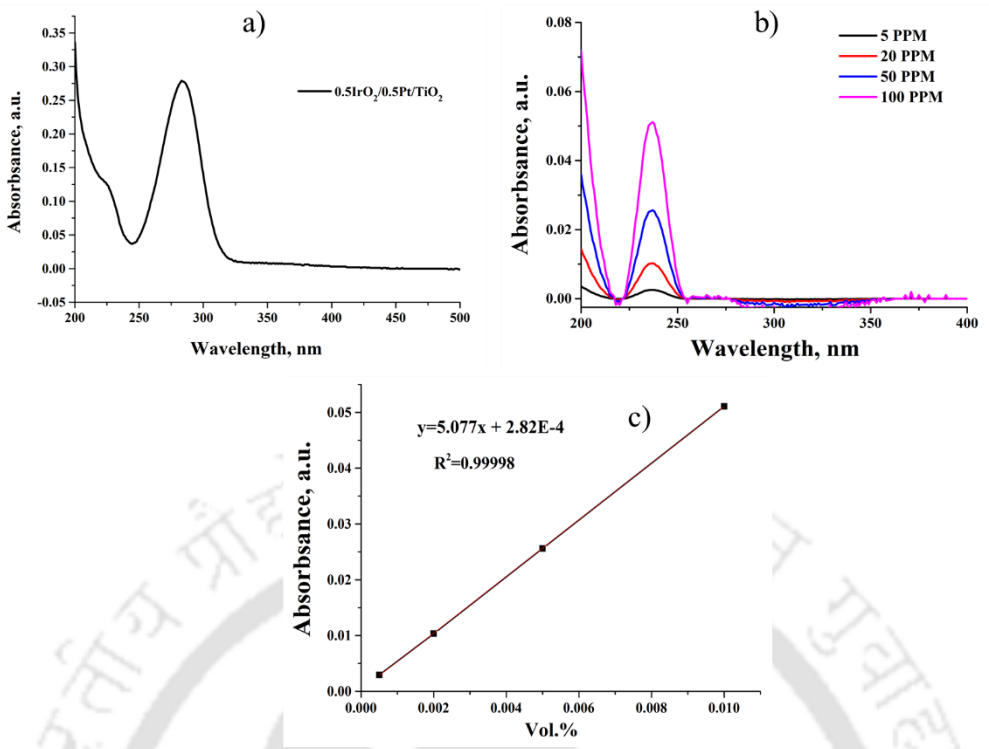

Figure B.1: a) UV absorption spectrum of H_2O_2 product in the aqueous solution after POWS reaction over $0.5IrO_2/0.5Pt/TiO_2$ catalyst; b) UV absorbance of known H_2O_2 concentrations in DI water; and c) H_2O_2 Calibration curve

References

(1) Schweinar, K.; Gault, B.; Mouton, I.; Kasian, O. Lattice Oxygen Exchange in Rutile IrO2 during the Oxygen Evolution Reaction. *J. Phys. Chem. Lett.* **2020**, *11* (13), 5008–5014. https://doi.org/10.1021/acs.jpclett.0c01258.

(2) Kuribayashi, K.; Kitamura, S. Preparation of Pt-PtOx Thin Films as Electrode for Memory Capacitors. *Thin Solid Films* **2001**, *400* (1), 160–164. https://doi.org/10.1016/S0040-6090(01)01503-6.

(3) Pala, L. P. R.; Peela, N. R. Green Hydrogen Production in an Optofluidic Planar Microreactor via Photocatalytic Water Splitting under Visible/Simulated Sunlight Irradiation. *Energy & Fuels* **2021**, *35* (23), 19737–19747. https://doi.org/10.1021/acs.energyfuels.1c02686.

(4) Pala, L. P. R.; Peela, N. R. Visible Light Active IrO2/TiO2 Films for Oxygen Evolution from Photocatalytic Water Splitting in an Optofluidic Planar Microreactor. *Renew. Energy* **2022**, *197*, 902–910. https://doi.org/10.1016/j.renene.2022.08.017.

Research Output

Journal Publications from Doctoral Work

1) **Laxmi Prasad Rao Pala**; Uday, V.; Gogoi, D.; Nageswara Rao Peela; Surface and Photocatalytic Properties of TiO_2 thin Films Prepared by Non-Aqueous Surfactant Assisted Sol-Gel Method. *J. Environ. Chem. Eng.* (**2020)**, *8* (5), 104267. https://doi.org/10.1016/j.jece.2020.104267
2) **Laxmi Prasad Rao Pala**; Nageswara Rao Peela; Green Hydrogen Production in an Optofluidic Planar Microreactor via Photocatalytic Water Splitting under Visible/Simulated Sunlight Irradiation. *ACS Energy & Fuels.* (**2021)** 35:19737–19747. https://doi.org/10.1021/acs.energyfuels.1c02686
3) **Laxmi Prasad Rao Pala**; Nageswara Rao Peela; Visible light active IrO_2/TiO_2 films for oxygen evolution from photocatalytic water splitting in an optofluidic planar microreactor, *Renew. Energy.* 197 (**2022)** 902–910. https://doi.org/https://doi.org/10.1016/j.renene.2022.08.017.
4) **Laxmi Prasad Rao Pala**; Nageswara Rao Peela; Green hydrogen and oxygen production over $IrO_2/Pt/TiO_2$ via photocatalytic overall water splitting under visible light illumination (Renewable Energy, under review 2023)

Publication from collaborative work

1) B. Das; **Laxmi Prasad Rao Pala;** M.K. Mohanta; M. Devi; D. Chakraborty; Nageswara Rao Peela; M. Qureshi; S.S. Dhar; Organic–inorganic hybrid photocatalyst consisting of a highly conjugated metal complex and graphitic carbon nitride for efficient hydrogen evolution and Cr(vi) reduction, *J. Mater. Chem. A.* 10 **(2022)** 23691–23703. https://doi.org/10.1039/D2TA05200H.

Conference Presentations

1) **Laxmi Prasad Rao Pala**; Nageswara Rao Peela; Photocatalytic Degradation of Organic Dye over TiO_2 thin films prepared by non-aqueous surfactant assisted Sol-Gel method. *International Conference on Advanced Materials for Energy Science and Technology (AMEST-2019), Feb 26-28, **2019**, Poster presentation at North-Eastern Hill University, Meghalaya.*
2) **Laxmi Prasad Rao Pala**, Nageswara Rao Peela, 'Photocatalytic Degradation of Organic Dye over TiO_2 thin films prepared by non-aqueous surfactant assisted Sol-Gel method', *Research Conclave'19, March 14-17, 2019, Poster presentation at Indian Institute of Technology Guwahati (IITG), Assam, India*
3) **Laxmi Prasad Rao Pala**; Nageswara Rao Peela; An Optofluidic Planar Microreactor for Green Hydrogen Production via Photocatalytic Water Splitting. *HYPOTHESIS XVI (Hydrogen Power Theoretical & Engineering Solutions International Symposium), Nov 8-10, **2021,** Oral presentation in online mode.*
4) **Laxmi Prasad Rao Pala**, Nageswara Rao Peela; An Optofluidic Planar Microreactor for Photocatalytic Water Splitting Reaction under Visible Light Illumination' *EUROPACAT 2023 (15th European Congress on Catalysis), Aug 27 – Sep 1, **2023**, Prague, Czech Republic, Poster presentation*